FERMILAB-THESIS-2022-10

A Search for Sterile Neutrino Oscillations in the MicroBooNE Experiment Using Deep Learning Reconstruction and Event Selection

A dissertation submitted by

Katie N. Mason

in partial fulfillment of the requirements for the degree of

Doctor of Philosophy

in

Physics

Tufts University

May 2022

Advisor: Dr. Taritree Wongjirad

Abstract

This work presents a search for sterile neutrinos based on the 3+1 model in the MicroBooNE experiment. The 3+1 model examined here expands on the standard model of neutrinos by adding a fourth neutrino flavor. The search presented relies on Deep-Learning-based reconstruction tools and looks for charged current quasi-elastic (CCQE) events kinematically consistent with 2-body interactions.

Along the path to the neutrino oscillation results various reconstruction tools are examined in more detail with a particular emphasis on the reconstruction of electrons and photons. Photons can originate from neutral pion decay; one of the major backgrounds to this analysis. This background source is examined in detail.

Then, using two orthogonal samples of CCQE electron neutrino events and CCQE muon neutrino events, the 3+1 model allowing for electron neutrino appearance, electron neutrino disappearance, and muon neutrino disappearance is tested by comparing to MicroBooNE data.

The 3+1 model oscillation parameter set that best fits this data is found to be a parameter set with high electron neutrino disappearance and little oscillation in the other channels. Wilks' theorem indicates that the null model and the global best fit are excluded at 90% confidence, however initial studies using the Feldman-Cousins' method indicate that neither of these hypotheses are excluded by the data.

Acknowledgements

A big thank you to all of the many people without whom this work would not have been possible. First, I would like to give a huge thank my advisor Dr. Taritree Wongjirad whose advise and guidance throughout my time in graduate school has been invaluable. You have not just taught me about physics, but demonstrated how to be a great mentor.

I also need to thank Dr. Joshua Mills, my fellow Tufts + MicroBooNE graduate student. Since our days back in undergraduate mechanics lab, you have been an amazing source of both physics collaboration and emotional support. This journey would have been much more gloomy without you.

I would like to thank the other members of the Wongjirad research group with whom I have worked over the years: Dr. Ralitsa Sharankova, Dr. Matthew Rosenberg, Polina Abratenko, Zev Imani, Omar Alterkait, and the many undergraduate researchers who have provided assistance and many productive discussions. A big thank you as well to the rest of the Tufts Physics department and specifically the neutrino research group for helping me grow as researcher in my time at graduate school. And thank you as well to my thesis committee: Dr. Hugo Beauchemin, Dr. Janet Conrad, Dr. Hugh Gallagher, and Dr. Peter Love.

Next, I would like to thank the entire MicroBooNE collaboration for the analysis support, review, and all of the resources I utilized. Particularly I would like to thank the rest of the Deep-learning team both past and present whose work contributed to this analysis and members of the Oscillation team who provided critical support: Dr. Janet Conrad, Dr. Ran Itay, Dr. Adrien Hourlier, Dr. Georgia Karagiorgi, Dr.

Michael Shaevitz, Dr. Vic Genty, Dr. Jarrett Moon, Dr. Davio Cianci, Dr. Lauren Yates, Dr. Mark Ross-Lonergan, and Nicholas Kamp. I would also like to thank the editorial board for this analysis Dr. Adi Ashkenazi and Dr. Andrew Mastbaum. I would like to particularly shout out Nicholas Kamp who helped co-write the paper on the shower reconstruction algorithm.

Thank you to my friends and family for providing all the emotional support I could ever need: Dr. Anastasia Yandulskaya-Blue who has been there since day one at Colgate University freshmen and has been an amazing apartmentmate throughout this adventure. I could not have done this without our GBBO and Harry Potter marathons. Also a big shout out to all of my other close friends here in Boston: Terence Blue, Laura Rodríguez-Pérez, Alec Drobac, Hannah Johnston, Dr. Travis Olsen, and Joshua Mills for being the best DND group of all time.

Finally, Mom, Dad, and Ben, thank you for being the best parents and brother and for being there during the long road to get here. Thank you as well to the rest of my big crazy family. You are all amazing and your support has been priceless. And thank you to the various pets over the years, both of the four legged fluffy variety (Cleveland, Savannah, Molly, Sadie, Vixen, Luke, and Leia) and the tiny aquatic variety (Sir Lancelot, Sir Mordred, and Sir Merlin).

This work was performed with the support of US DOE grant DE-SC0019032 and the Tufts Burlingame Fellowship.

Contents

List of Figures

List of Tables

Chapter 1

Introduction

Neutrinos, sometimes referred to a ghost particle, are one of the most abundant particles in the universe. They are called a ghost particle because they are incredibly difficult to detect. Neutrinos are both electrically neutral and extremely light, even at the small scale of other particles. They were originally thought to be mass-less. Even now though many advancements have been made in the field, we have not been able to measure the mass of a neutrino and can only report upper limits. The detectors needed to observe such a particle must be both very large and/or very sensitive.

The story of the neutrino begins in 1930, when Wolfgang Pauli hypothesized a particle to fix a problem of energy conservation in beta decay. Beta decay is a type of radioactive decay where a neutron changes into a proton and releases an electron (or a proton changes to a neutron and emits a positron). If beta decay were simply electron emission, then the energy of the emitted electron should have a particular value. However, a broad distribution of energies was observed suggesting that energy is lost in the process. Pauli proposed that the energy was carried away in the form of a particle that hadn't yet been detected. Enrico Fermi named this particle a neutrino in 1934 in order to describe its lack of charge and incredibly small size.

About 20 years later in 1956, the first experimental evidence of the neutrino was observed at Los Alamos National Laboratory in the first neutrino reactor experiment by observing inverse beta decay reactions caused by neutrinos. Inverse beta decay is a nuclear reaction involving an electron antineutrino scattering off a proton, creating a positron and a neutron. This is a common process used to detect neutrinos. As will be discussed, there are many interactions neutrinos can have with other matter, depending on the type and energy of the neutrino.

There are three types, or flavors, of neutrinos that we can observe: electron neutrino (ν_e), muon neutrino (ν_μ), and tau neutrino (ν_τ). The type of neutrino is determined in experiments based on which other charged particle was involved in the interaction. For example, electron neutrinos are neutrinos which interact with an electron. However, the picture is not quite that simple. Neutrinos actually travel as a mixture of the three flavor states which are known as the mass eigenstates.

This leads to one of their most interesting features. Neutrinos oscillate, or change their observed flavor type, as they travel. The flavor neutrino created by humans or nature is not necessarily the one we observe some distance away. Neutrino oscillations were first predicted by Bruno Pontecorvo in 1957, and the theory was developed further over the years as more flavors were discovered. It took until 1998 (only 24 years ago) for the first evidence of neutrino oscillations to be observed in the Super Kamiokande experiment in Japan and SNO in Canada. This also provided evidence that neutrinos must have non-zero mass. This is striking as the standard model of particle physics predicts that neutrinos are mass-less. Many experiments since that time have further verified three flavor neutrino oscillations and made progress towards determining the parameters governing this oscillation.

However, the observations of some experiments do not fit into the this three flavor picture. Their observations do not agree with what the standard model with three neutrino flavors predicts. These neutrino "anomalies" can be broken into three types: gallium solar neutrino experiments with radioactive source testing, short-baseline reactor experiments, and short-baseline accelerator experiments.

Of particular focus here are the short-baseline accelerator experiments LSND and MiniBooNE. Short-baseline indicates that the detector is located close to the neutrino source. They both observed an excess of ν_e events originating from a primarily ν_μ beam. This excess cannot be explained by the oscillations of three flavors. There are many theories attempting to explain these anomalies. The theory this thesis will focus on is the existence of a fourth flavor of neutrino, which would allow for additional oscillations. The goal is to put constraints on this theory using the MicroBooNE experiment.

The proposed fourth neutrino is sterile, or in other words, does not interact directly with the standard model particles. It would, however, affect neutrino oscillation. In experiments an excess or deficit of expected neutrino of a specific flavor could signal its existence. In this analysis a deficit of ν_μ events expected from the beam, a deficit of ν_e events from the intrinsic beam backgrounds, and/or an appearance of ν_e events from oscillations of the ν_μ 's created in the beam may be observed depending on the oscillation parameters of the sterile neutrino.

The exploration of the current state of neutrino physics starts in Chapter 2 which provides an overview of the standard model of particle physics and introduces neutrino oscillations in the three flavor case. We will also explore various types of neutrino experiments and how neutrinos can interact with a detector. Chapter 3 details the sterile neutrino model under investigation and how it is motivated by experimental anomalies.

To put constraints on the sterile neutrino oscillation parameters, the MicroBooNE detector data is used. The MicroBooNE experiment and data collection process is described in Chapter 5. We will also pause here to discuss the analysis strategy, or how we will determine agreement between the data and this model.

Next we will move into the details of each analysis step. This starts with the deep-learning (DL) and traditional algorithm tools used in neutrino interaction reconstruction in Chapter 6. Chapter 7 and 8 delve into this reconstruction in more detail by examining a possible method of recovering information from non-functional wires in the detector and a validation of the reconstruction of one type of particle respectively. The methods for evaluating and implementing our uncertainties are described in Chapter 9 as well as a breakdown of the uncertainty types. Chapter 10 describes the use of a selection of neutrino events with π^0 particles in the final state as a side check of the main analysis. Then Chapter 11 describes the selection of the specific neutrino events we will use to test the model.

Chapter 12 outlines the 3+1 model sensitivity in MicroBooNE and shows various validations of the method. Chapter 13 shows the results on data. The work shown in this thesis is one step towards an understanding of the experimental neutrino anomalies. Future work will look at these results in comparison to other event selections in MicroBooNE and to results from upcoming detectors as part of the short base-line neutrino program at Fermilab.

Throughout this thesis, I will make use of some abbreviations or technical terms. For example, the model of an additional sterile neutrino flavor is referred to as the 3+1 model. These will be defined the first time they are used, but the reader can refer to Appendix A for a list of some of these commonly used terms. Finally, the development of the test of the MicroBooNE data with the 3+1 sterile neutrino model and the resulting data fit was performed by the author of this thesis. In order to provide a complete picture of the data reconstruction, selection, and uncertainties, work performed by others in the MicroBooNE collaboration is often referred to and summarized. Appendix B lists the analysis steps on which the author was a primary contributor for clarity.

Chapter 2

Neutrino Physics and the Standard Model

Before delving into the details of this analysis, it is important to first review the standard model (SM) of particle physics and the current understanding of neutrinos. This chapter examines standard model neutrinos in Section 2.1 and generally agreed upon physics. Section 2.2 discusses neutrino interactions with a focus on interactions that can occur in the MicroBooNE detector. This is followed by a look at three flavor neutrino oscillations in Section 2.3. Then Section 2.4 presents experimental observations of three flavor oscillations.

2.1 Standard Model

The standard model (SM) of particle physics is a model that is used to describe particles and their interactions. It provides a unified picture where the forces are described by the exchange of particles. Almost all interactions between matter can be described by the electron, electron neutrino, proton, and neutrons interacting via the electromagnetic, strong, and weak forces. The proton and neutron themselves are actually bound states of quarks.

The up quark, down quark, electron, and electron neutrino are known as the first generation particles. Their important characteristics include charge (Q), mass, spin, and color (quarks). These are all believed to be fundamental particles rather than composite particles. These particles are believed to have exactly two other versions that have different masses, but are identical to the first generation in all their other characteristics. Table 2.1 describes these particles.

Table 2.1: The twelve fundamental fermions divided into quarks and leptons. The masses represent the current best experimental measurements. Adapted from Ref. [1].

	Leptons			Quarks		
	Particle	Q	Mass/GeV	Particle	Q	Mass/GeV
1^{st} Gen	electron(e^-)	-1	0.0005	down(d)	-1/3	0.003
	electron neutrino(ν_e)	0	$< 10^{-9}$	up(u)	+2/3	0.005
2^{nd} Gen	muon(μ^-)	-1	0.0105	strange(s)	-1/3	0.1
	muon neutrino(ν_μ)	0	$< 10^{-9}$	charm(c)	+2/3	1.3
3^{rd} Gen	tau(τ^-)	-1	1.7768	bottom(b)	-1/3	4.5
	tau neutrino(ν_τ)	0	$< 10^{-9}$	top(t)	+2/3	174

Particles interact with each other via four fundamental forces: electromagnetism, weak force, strong force, and gravity. Each of the electromagnetism, weak, and strong forces are described by a spin 1 force carrying particle known as a gauge boson. The characteristics of these bosons are summarized in Table 2.2. In a quantum theory of gravity, the force must be carried by a gauge boson as well. No workable quantum theory of gravity has yet been developed, though general relativity dictates that the boson for gravity must be spin 2. As shown in Table 2.2, the strength of gravity is much smaller than the other forces and as such will not have a measurable impact.

Table 2.2: The four known forces of nature. The relative strengths are approximate indicative values for two fundamental particles at a distance of $1fm = 10^{-15}m$ (roughly the radius of a proton). Adapted from Ref. [1]

Force	Strength	Boson	Spin	Mass/GeV
Strong	1	Gluon(g)	1	0
Electromagnetism	10^{-3}	Photon(γ)	1	0
Weak	10^{-8}	W boson($W^{\pm}$)	1	80.4
Weak	10^{-8}	Z boson(Z)	1	91.2
Gravity	10^{-37}	Graviton(?)(G)	2	0

A particle can couple to a force carrying boson only if it carries the charge of the interaction type. These interactions can be written out in the form of Lagrangians. The strong force's charge is called color. This force is not often explicitly examined in this thesis, though it is hidden in the underlying nuclear models used when simulating particle interactions. The electromagnetic force charge is the electric charge. In this thesis the electromagnetic force is necessary in the data readout from the MicroBooNE detector (see Chapter 5). Neutrinos, the primary subject of this analysis, are electrically neutral and have no color charge. Therefore the only interactions between neutrinos and other particles occur via the weak force.

In the SM the masses of fermions come from a Yukawa coupling of the scalar Higgs doublet with the fermion right handed and left handed components. For leptons the coupling is formed by coupling the left handed lepton doublet with the right handed charged lepton fields. Spontaneous symmetry breaking then leads to the charged lepton masses. However, the SM does not contain right handed neutrinos so no such coupling can be built. Neutrinos have only ever been observed as left-handed (and antineutrinos as right-handed). It is known that neutrinos must have some (albeit tiny) mass. Therefore, the SM must be extended in some way to allow for a non-zero neutrino mass. There are a variety of theories attempting to do so. One possibility is that neutrinos are Majorana particles. If this is the case neutrinos are their own antiparticles. This would allow a coupling of the right-handed neutrino fields and left-handed antineutrino-fields which can be added to the SM Lagrangian. This is not seen in other particles as it would violate charge conservation. Regardless of which theory is correct, the end result is that as neutrinos propagate in time they are able to undergo oscillations to different flavor states.

2.2 Neutrino Interactions in MicroBooNE

It is next important to understand the ways neutrinos can interact in matter. Neutrinos interact with other matter via the weak force. These can be broken up further into a variety of interaction types. This section describes some of these interactions which are more relevant in this analysis using the MicroBooNE detector which is filled with liquid argon.

There are two general weak interaction types depending on which of the two bosons is involved. The first are neutral-current (NC) interactions. These occur via the Z^0 boson. As Z^0 is electrically neutral, no electric charge is exchanged in the interaction. The second type are charged-current (CC) interactions. This interaction does exchange charge. When a neutrino is one of the incoming particles, it is changed into it's corresponding charged lepton from the same generation via the exchange of charge through the $W^{\pm}$ boson. Figure 2.1 shows example neutrino NC and CC interaction vertices.

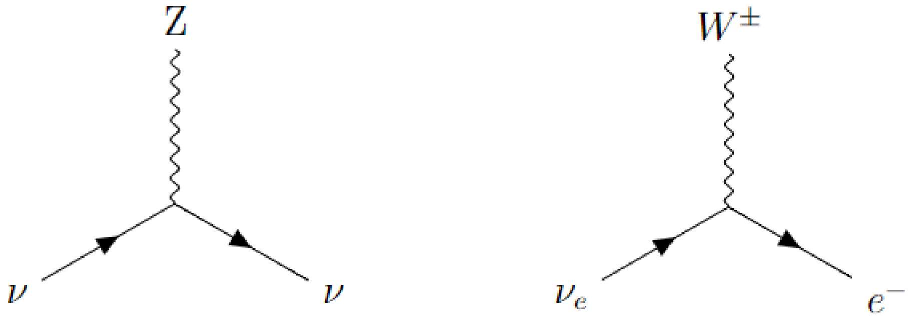

(a) NC interaction vertex (b) CC interaction vertex

Figure 2.1: The neutral-current and charged-current weak interaction vertices (for the 1^{st} generation fermions).

Both CC and NC interactions have a variety of different modes. The mode that occurs is correlated with the neutrino energy. The three most common modes in MicroBooNE are quasi-elastic (QE) scattering, resonant inelastic processes (RES), and deep-inelastic neutrino scattering (DIS). Quasi-elastic scattering (particularly CCQE) is the target interaction type in this thesis. RES and DIS will play a large part in a particular background that is studied in detail in later chapters which is neutrino events containing a π^0 .

Figure 2.2, adapted from Ref [2], shows the relevant contributions of each type to the total ν cross-section per nucleon (and similarly for $\bar{\nu}$). Also shown is the data measurements from a variety of experiments at Argonne National Laboratory and Brookhaven National Laboratory. This figure indicates the neutrino energy range for some accelerator experiments including MicroBooNE. It is clear here that quasi-elastic scattering is dominant at the lowest MicroBooNE energy scales, and that RES have a large contribution at higher energies. DIS is less common at the energy scales of MicroBooNE but still can occur at high energies.

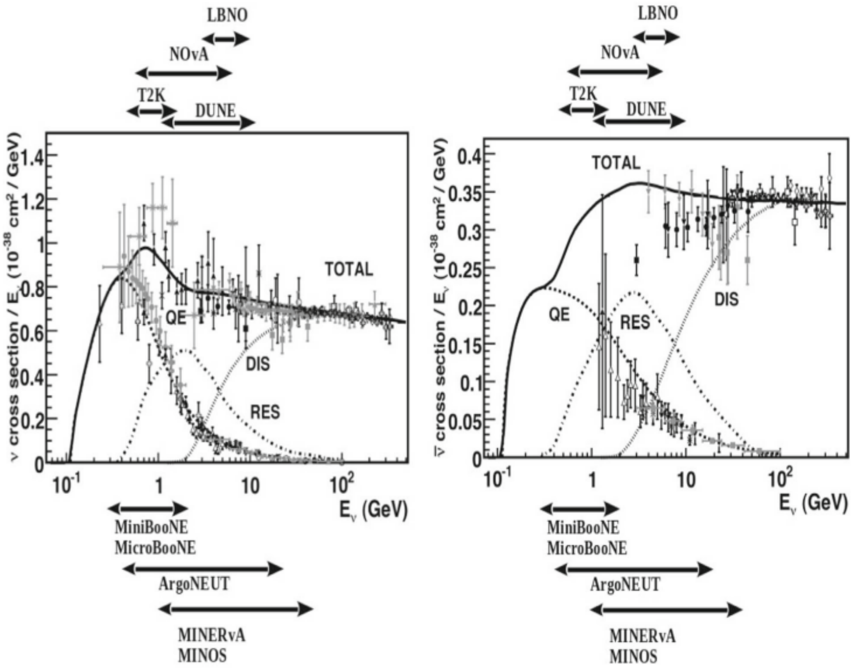

Figure 2.2: CC total scattering cross section per nucleon per unit energy of the incoming particles vs. neutrino (left panel) and antineutrino (right panel) energy for all three processes labeled on the curve along with the total scattering cross sections. Dashed line shows QE scattering, while the dashed-dotted and dotted lines are the inelastic resonance (RES) and deep-inelastic scattering (DIS), respectively. The sum of all the scattering cross sections (TOTAL) is shown by the solid line. Adapted from Ref. [2].

In the discussion of neutrino interactions some terms are used to discuss the characteristics. “Vertex” refers to the interaction point where the boson is exchanged. “Parent particles” are the particles that exist prior to the interaction. In this thesis they are generally the incoming neutrino and the protons, neutrons, and electrons which make up the argon. “Final state particles” are the remaining particles after the interaction and can include a wide variety of particle types depending on the mode.

CCQE is the one of the major interaction contributions at low energies. It is a two-body scatter, ($\nu_e + n \rightarrow e^- + p$ and $\nu_\mu + n \rightarrow \mu^- + p$), where the nucleon recoils elastically from the impact. The Feynman diagrams for these two event types are shown in Figure 2.3. Analogous diagrams could be drawn for the similar NCQE scatters, though those are not generally detectable with the tools in this thesis. These reactions are called quasi-elastic because they assume the nucleus can be treated as quasi-free nucleons. At higher energies, this approximation is no longer valid. These reactions have two form factors. One for vector coupling and one for axial vector coupling. These form factors have a high q^2 (momentum transfer) dependence, so the cross-section drops off at higher energies.

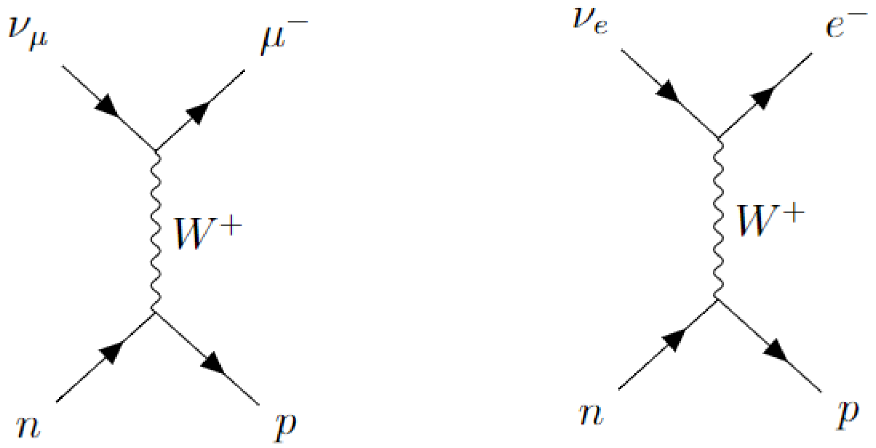

(a) ν_μ CCQE (b) ν_e CCQE

Figure 2.3: Feynman diagrams ν_μ and ν_e CCQE scattering.

Resonant (RES) inelastic processes make up a large portion of interactions at the higher energies of the MicroBooNE energy scale. These are events where the neutrino scatters off of the nucleon. Unlike in QE, there is a high enough momentum transfer to excite the nucleon into a resonant state. These will be discussed further in Chapter 10, as these resonant states often decay into a π^0 . This is one of the major backgrounds to the CCQE events that are the target of the oscillation analysis.

The final type of neutrino interaction in matter relevant to this thesis is deep inelastic scattering (DIS). DIS, in neutrino interactions, is when the neutrino scatters with a quark in the nucleon ($\nu + d \to \mu^- + u$ and $\nu + \bar{u} \to \mu^- + \bar{d}$). Neutrinos could in theory scatter off the higher generation quarks, but the rate is much smaller and they are not statistically relevant in MicroBooNE [3]. Deep refers to the fact that there is high momentum transfer from the neutrino. This destroys the nucleon, resulting in many possible final state topologies.

2.3 Neutrino Oscillations

When observing neutrino interactions in matter, it was discovered that the number of interactions of various modes did not match the number of events expected based on the neutrino source. This led to the discovery of neutrino oscillations which is the only confirmation that neutrinos have mass. Neutrinos having mass in this extended standard model opens the door for neutrino oscillations. This section discusses neutrino oscillation in a vacuum (the formalism changes when neutrinos travel through matter).

The three SM neutrino flavor states (ν_e , ν_μ , and ν_τ) do not exist as unique mass states but instead are a linear combination of three neutrino mass states. The individual flavor states ($\nu_\alpha \in (e, \mu, \tau)$) can then be described in terms of the mass eigenstates ($\nu_i \in (1, 2, 3)$) as:

$$|\nu_\alpha >= \sum_{i}^{N=3} U^*_{\alpha i} |\nu_i > \tag{2.1}$$

U here is the Pontecorvo-Maki-Nakagawa-Sakata (PMNS) matrix which is a 3x3 unitary matrix giving the parameters for lepton mixing.

$$U = \begin{pmatrix} U_{e1} & U_{e2} & U_{e3} \\ U_{\mu 1} & U_{\mu 2} & U_{\mu 3} \\ U_{\tau 1} & U_{\tau 2} & U_{\tau 3} \end{pmatrix} \tag{2.2}$$

A general 3x3 matrix can be described by nine complex numbers, or 18 total parameters. However, U is required to be unitary, or:

$$\begin{pmatrix} U_{e1} & U_{e2} & U_{e3} \\ U_{\mu 1} & U_{\mu 2} & U_{\mu 3} \\ U_{\tau 1} & U_{\tau 2} & U_{\tau 3} \end{pmatrix} \begin{pmatrix} U^*_{e1} & U^*_{\mu 1} & U^*_{\tau 1} \\ U^*_{e2} & U^*_{\mu 2} & U^*_{\tau 2} \\ U^*_{e3} & U^*_{\mu 3} & U^*_{\tau 3} \end{pmatrix} = \begin{pmatrix} 1 & 0 & 0 \\ 0 & 1 & 0 \\ 0 & 0 & 1 \end{pmatrix} \tag{2.3}$$

The unitarity constraint therefore provides nine constraints (i.e $U_{e1}U_{e1}^{*}+U_{e2}U_{e2}^{*}+U_{e3}U_{e3}^{*}=1$), leaving nine independent parameters. If the matrix were real it could be defined just with three rotation parameters and would correspond to the orthogonal rotation matrix. However, since the PMNS matrix is not real there are six additional degrees of freedom which are complex phases. Not all of these phases are actually physically relevant. Generally, with N generations of leptons, there are 2N fields that can be re-phased. That means 2N-1 of these phases can be reabsorbed in a redefinition of the lepton fields. As the standard model has 3 generations of leptons, 5 of the 6 degrees of freedom can be re-phased into one. The PNMS matrix can be then described both in terms of mixing parameters as above, and in terms of three real parameters and a single charge-parity (CP) violating phase. This standard format is used when defining the neutrino oscillation parameters. U is then:

$$\begin{aligned} U &= \begin{pmatrix} 1 & 0 & 0 \\ 0 & c_{23} & s_{23} \\ 0 & -s_{23} & c_{23} \end{pmatrix} \begin{pmatrix} c_{13} & 0 & s_{13}e^{i\delta} \\ 0 & 1 & 0 \\ -s_{13}e^{i\delta} & 0 & c_{13} \end{pmatrix} \begin{pmatrix} c_{12} & s_{12} & 0 \\ -s_{12} & c_{12} & 0 \\ 0 & 0 & 1 \end{pmatrix} \\ &= \begin{pmatrix} c_{12}c_{13} & s_{12}c_{13} & s_{13}e^{-i\delta} \\ -s_{12}c_{23} - c_{12}s_{23}s_{13}e^{i\delta} & c_{12}c_{23} - s_{12}s_{23}s_{13}e^{i\delta} & s_{23}c_{13} \\ s_{12}c_{23} - c_{12}s_{23}s_{13}e^{i\delta} & -c_{12}c_{23} - s_{12}s_{23}s_{13}e^{i\delta} & c_{23}c_{13} \end{pmatrix} \end{aligned} \tag{2.4}$$

where $c_{ij} = cos(\theta_{ij})$, $s_{ij} = sin(\theta_{ij})$, and δ is a CP-violating phase.

As a flavor state evolves through time in the lab frame, it's flavor state becomes:

$$|\nu_{\alpha}(t)> = \sum_{i}^{N=3} U_{\alpha i}^{*} e^{-i(E_i t - p_i \dot{x})} |\nu_i> \tag{2.5}$$

following the Schrodinger picture. The mass and momentum of the given neutrino eigenstate are represented by m and p respectively. As seen here, as the state evolves through time, there is some probability of observing a different neutrino flavor at some time, t. This probability is given by:

$$\begin{aligned} | < \nu_\beta | \nu_\alpha(t) > |^2 &= \textstyle\sum_{ij} U^*_{\alpha i} e^{-itm_i^2/2p} U_{\beta i} U_{\alpha j} e^{itm_j^2/2p} U^*_{\beta j} \\ &= \delta_{\alpha\beta} - \textstyle\sum_{ij} U^*_{\alpha i} U_{\beta i} U_{\alpha j} U^*_{\beta j} (1 - e^{i\Delta m^2_{ij} L/2E}) \end{aligned} \quad (2.6)$$

where $\Delta m^2_{ij} = m_i^2 - m_j^2$. As neutrinos are both light and relativistic the approximations $p \sim E$ and $t = x/c \sim x = L$, can be made using $c = 1$. Based on Eq. 2.6, it can be seen that as long as Δm^2_{ij} is non-zero and the mixing matrix is not diagonal, the probability that ν_β is observed at time t when the neutrino originated as ν_α is non-zero. In other words, a neutrino with energy E, can oscillate through the various flavor states as it propagates over distance L.

It is also noted that from vacuum oscillations alone, the masses of the individual neutrino flavors cannot be determined as they always appear in terms of Δm^2_{ij}. An experimental limit from the KATRIN experiment comes from observing the end point of the electron energy distribution in the nuclear β-decay of tritium. This sets the upper limit of the mass of $\nu_e < 0.9eV$ [4]. Further, from cosmological measurements of the large-scale structure of the universe, $\sum m_{\nu_i} < 1eV$ [1].

The CP-violating phase, the three mixing angles (θ_{ij}), and the two independent mass mixing terms (Δm^2_{12} and Δm^2_{23}) completely describe the extended standard model neutrino oscillations. These parameters can then be used in experimental setups to predict oscillation probabilities which depend on the energy of the neutrino and the distance it travels from the source. Using trigonometric identities, Eq. 2.6 can be written in a more useful form.

$$\begin{aligned} P(\nu_\alpha \to \nu_\beta) &= \delta_{ij} - \textstyle\sum_{ij} U^*_{\alpha i} U_{\beta i} U_{\alpha j} U^*_{\beta j} (2\sin^2(\Delta m^2_{ij} L/4E) + i \sin(\Delta m^2_{ij} L/2E)) \\ &= \delta_{ij} - \textstyle\sum_{ij} 4\Re[U^*_{\alpha i} U_{\beta i} U_{\alpha j} U^*_{\beta j}] \sin^2(1.27\Delta m^2_{ij} L/E) \\ &\quad + \textstyle\sum_{ij} 2\Im[U^*_{\alpha i} U_{\beta i} U_{\alpha j} U^*_{\beta j}] \sin(2.55\Delta m^2_{ij} L/E) \end{aligned} \quad (2.7)$$

where P is the oscillation probability of a given event and the coefficients (1.27

and 2.55) come from reintroducing $\frac{c^3}{\hbar}$ to remove dimensionality for L/E for units of $[m/MeV]$.

Experimental observations have proved that these mass differences are non-zero in neutrinos by observing oscillations as will be discussed in Section 2.4. Therefore we consider three flavors of neutrinos with non-zero mass and resulting oscillations as part of an extended SM. Later in Chapter 3 we will extend this even further by adding a fourth flavor.

2.4 Experimental Oscillation Observations

Three flavor neutrino oscillations have now been observed experimentally from a variety of sources. Specifically oscillations have been observed from studies on solar neutrinos, atmospheric neutrinos, accelerators, and nuclear fission reactors. When looking for neutrino oscillations in these experiments, there are generally two types of signals. The first signal is neutrino flavor appearance. In these observations, a flavor of neutrinos not produced by the source reaction is observed. The second signal is disappearance. In these observations the same flavor produced by the source is observed, but at a reduced rate as some of the produced neutrinos have oscillated into a different flavors. In reality, both can occur concurrently, though may not be observable in a given experiment.

2.4.1 Solar Neutrino Oscillations

Some of the first experiments to observe oscillation were experiments measuring solar neutrinos. Nuclear fusion in the sun produces a large number of ν_e 's through the *pp* chain and the Carbon-Nitrogen-Oxygen (CNO) cycle. The combined reactions result in the overall fusion of protons into He ($4p \rightarrow^4 He + 2e^+ + 2\nu_e$). The average energy of these neutrinos is small: $< E_{2\nu_e} >= 0.59MeV$ [5]. A detailed calculation of the solar neutrino flux has been done using the Standard Solar Model (SSM) [6].

A variety of experiments were used to measure the solar electron neutrino flux. These are summarized in Table 2.3 which was adapted from Ref [6]. These experiments all observed a deficit in the number of observed neutrinos. For example, the latest neutrino flux measured by Super-Kamiokande is (2.345 ± 0.014 ± 0.036)x10$^6 cm^{-2} s^{-1}$ while the prediction of the SSM is (5.46 ± 0.66)x10$^6 cm^{-2} s^{-1}$, or a deficit of $> 50\%$ [6, 7].

Table 2.3: List of Solar Neutrino Experiments from [6]. (LS = Liquid Scintillator)

Name	Target	E Threshold (MeV)	Mass (ton)	Years
Homestake	C_2Cl_4	0.814	615	1970-94
SAGE	Ga	0.233	50	1989-
GALLEX	$GaCl_3$	0.233	100 [30.3 for Ga]	1991-97
GNO	$GaCl_3$	0.233	100 [30.3 for Ga]	1998-2003
Kamiokande	H_2O	6.5	3,000	1987-95
Super-Kamiokande	H_2O	3.5	50,000	1996-
SNO	D_2O	3.5	1,000	1999-2006
KamLAND	LS	0.5/5.5	1,000	2001-07
Borexino	LS	0.19	300	2007-

The solution to these observed deficits was first found by the SNO experiment [5]. SNO was able to observe solar neutrinos via three different interactions. Importantly, this experiment was able to observe both CC and NC events. The NC reaction is sensitive to all three standard model neutrinos providing a measure of the total flux, while the CC reaction is sensitive just to ν_e 's. The same ν_e deficit was seen, but the total flux from the NC interactions matched the flux predicted by the SSM. This indicated that the neutrinos were still present, but had changed flavors [6].

It has been determined that the ν_e disappearance observed by these experiments can be explained by neutrino oscillation in matter or the MSW effect. This oscillation effect is similar to the three oscillation in vacuum but with an extra potential term due to interactions with the particles in the matter. This effect is small for the neutrinos at the energies observed in MicroBooNE, so is not discussed further here, but it provides useful proof that neutrinos can change their flavor as they evolve through time.

2.4.2 Atmospheric Neutrino Oscillations

Atmospheric neutrinos are neutrinos produced by the decay of pions and kaons that are generated when cosmic rays interact in the Earth's atmosphere. They have a broad energy range from 100's of MeV to TeV, and can travel many kilometers before detection (up to 1.3x10^4 km). Detailed atmospheric neutrino flux calculations come from the energy spectrum and composition of primary cosmic rays and their hadronic interactions. While the absolute flux prediction has an uncertainty of 10-20%, the uncertainty on the flux ratio between flavors is <5% [6].

Atmospheric neutrinos oscillation signals can be observed by looking at the ratio of ν_μ to ν_e events observed. The ratio of $\frac{\nu_\mu+\bar{\nu}_\mu}{\nu_e+\bar{\nu}_e}$ is expected to be around 2 at energies of 1 GeV. Near this energy most of the cosmic ray muons interact in the the atmosphere. The rate then decreases at higher energies as more high energy muons make it to the surface of the Earth without interacting [6].

Many detectors observe some amount of atmospheric neutrinos. Notable early experiments are Kamiokande [8], IMB[9], Frejus [10], and NUSEX [11]. Super-Kamiokande was the first to show that neutrino oscillations matched the observations when a deficit of ν_μ events was observed, while the ν_e prediction matched observation [12]. This indicates that for the energy range and travel distance of atmospheric neutrinos, ν_μ's have some probability of oscillating into ν_τ 's.

2.4.3 Accelerator Neutrino Oscillations

The next source of neutrinos are accelerator beams. The neutrino beam used for MicroBooNE is described in more detail in Section 5.1. Generally, neutrino beams are produced by colliding high energy protons onto a target producing pions and kaons which decay into neutrinos. The flux is dominated by ν_μ (and $\bar{\nu}_\mu$). In accelerator experiments, the L/E (baseline/energy) is chosen to maximize the desired oscillation effect. Table 2.4, adapted from [6] is a list of current long-baseline neutrino oscillation experiments. MicroBooNE is what is referred to as a short-baseline experiment. Short-baseline experiments will be further discussed in Chapter 3.

Table 2.4: List of long-baseline neutrino oscillation experiments from [6]

Name	Beam	Detector	L(km)	E_ν(GeV)	Year
K2K	KEK-PS	Water Cherenkov	250	1.3	1999-2004
MINOS	NuMI	Iron-scintillator	735	3	2005-2013
MINOS+	NuMI	Iron-scintillator	735	7	2013-2016
OPERA	CNGS	Emulsion	730	17	2008-2012
ICARUS	CNGS	LArTPC	730	17	2010-2012
T2K	J-PARC	Water Cherenkov	295	0.6	2010-
NOvA	NuMI	Tracking Calorimeter	810	2	2014-

The long baseline accelerator experiments have observed ν_μ and $\bar{\nu}_\mu$ disappearance over long baselines. They have also observed that these ν_μ appear as ν_e . Further, the oscillation parameters found from these results are in agreement with the results for atmospheric neutrinos. There are two future long baseline experiments (DUNE and Hyper-Kamiodande) that will further measure these oscillation parameters, reduce the uncertainties, and look at other neutrino physics.

There are three known oscillation questions that these future long-baseline accelerator experiments are expected to help solve. The first is the value of δ_{CP} which is the CP violating phase. It is still unknown with any sort of confidence as seen in Table 2.7. δ_{CP} could be measured form ν_e appearance measurements. The second unknown is the exact value of $\sin^2(2\theta_{23})$. Current experiments point to this value being maximal ($\theta_{23} \sim 45\,\text{deg}$). If this mixing angle is maximal, it could be an interesting coincidence or it could point to interesting new physics. The third open question is the question of the mass hierarchy or which flavor of neutrino is heaviest. This is discussed further in Section 2.4.5

2.4.4 Reactor Neutrino Oscillations

Nuclear reactors are a source of $\bar{\nu}_e$ in the MeV energy range scale. These are produced via beta-decay from nuclear fission and can be detected via inverse beta-decay in a detector. Liquid scinillator is used as the detector material, though it may be loaded with gadolinium to increase the neutron detection efficiency. The flux can be estimated from the thermal power output and fuel composition of the reactor source. Table 2.5 lists reactor experiments which have observed 3 flavor neutrino oscillations. There are a further subset of reactor experiments which look for oscillations of a proposed sterile neutrino at $\Delta m^2 \sim 1eV^2$ which are discussed further in Chapter 3.

Table 2.5: List of reactor anti-neutrino oscillation experiments from Ref [6].

Name	Reactor Power (GW_{th})	Baseline(km)	Det Mass(t)	Year
Kamland	various	180	1k	2001-
Double Chooz	4.25x2	1.05	8.3	2011-18
Daya Bay	2.9x6	1.65	20x4	2011-
RENO	2.8x6	1.38	16	2011-
JUNO	26.6	53	20k	(2022)

Reactor experiments have observed $\bar{\nu}_e$ disappearance over distances of $\sim$ 200 km and $\sim$ 1.5 km with different probabilities. These mid-baseline reactor experiments agree with the oscillations observed in long-baseline accelerator experiments as they have a similar L/E. The long distance reactor results are consistent with the MSW effect parameters observed in solar neutrino experiments.

2.4.5 Global Picture

As discussed in Section 2.3, there are six oscillation parameters that describe three flavor neutrino oscillations in vacuum. These are: two mass splitting terms, three mixing angles, and a CP-violating phase. Table 2.6 shows how each of the experiment types described above have contributed to the understanding of these parameters.

Table 2.6: Experiments contributing to the present determination of the oscillation parameters. Adapted from Ref [6]. (LBL = long-baseline, MBL = mid-baseline).

Experiment	Dominant	Important
Solar Experiments	θ_{12}	$\Delta m^2_{21}, \theta_{13}$
Reactor LBL	Δm^2_{21}	θ_{12}, θ_{13}
Reactor MBL	$\theta_{13}, \|\Delta m^2_{31,32}\|$	
Atmospheric Experiments		$\theta_{23}, \|\Delta m^2_{31,32}\|, \theta_{13}, \delta_{CP}$
Accelerator LBL (ν_μ ,$\bar{\nu}_\mu$ disappearance)	$\theta_{23}, \|\Delta m^2_{31,32}\|$	
Accelerator LBL (ν_e ,$\bar{\nu}_e$ appearance)	δ_{CP}	θ_{13}, θ_{23}

The current experimental limits on the three flavor oscillation parameters are shown in Table 2.7. Note that these values and their uncertainties are regularly updated as experiments release results.

Table 2.7: Current global best fit oscillation parameters for the three flavor neutrino model for each the normal (NO) and inverted (IO) hierarchy and the 1σ range [13].

Parameter	(NO) Value	(IO) Value
Δm^2_{21} x $10^{-5} eV^2$	7.50 ± 0.22	7.50 ± 0.22
$\lvert\Delta m^2_{32}\rvert$ x $10^{-3} eV^2$	2.55 ± 0.03	2.45 ± 0.03
$\sin^2(\theta_{12})$	0.318 ± 0.016	0.318 ± 0.016
$\sin^2(\theta_{23})$	0.574 ± 0.014	0.578 ± 0.017
$\sin^2(\theta_{13})$	0.0220 ± 0.00069	0.0223 ± 0.00070
δ_{CP}/π	1.08 ± 0.13	1.58 ± 0.16

In Table 2.7, two things are important to note about the mass splittings (Δm^2). The first is that Δm^2_{21} is much smaller than $|\Delta m^2_{32}|$. Therefore it is common to make the approximation ($|\Delta m^2_{32}|$=$|\Delta m^2_{31}|$).

The second thing to notice is that the sign (±) of Δm^2_{32} is not known. Current experiments are not yet sensitive enough to tell the difference. Therefore there are two possible mass hierarchies. $m_3 > m_2$ is referred to as the normal mass hierarchy (NO), while $m_3 < m_2$ is referred to as the inverted mass hierarchy (IO). Figure 2.4 is a figure illustrating the two possible hierarchies. Note that the sign of Δm^2_{21} is known however. This is due to its role in neutrino oscillations in matter in the sun.

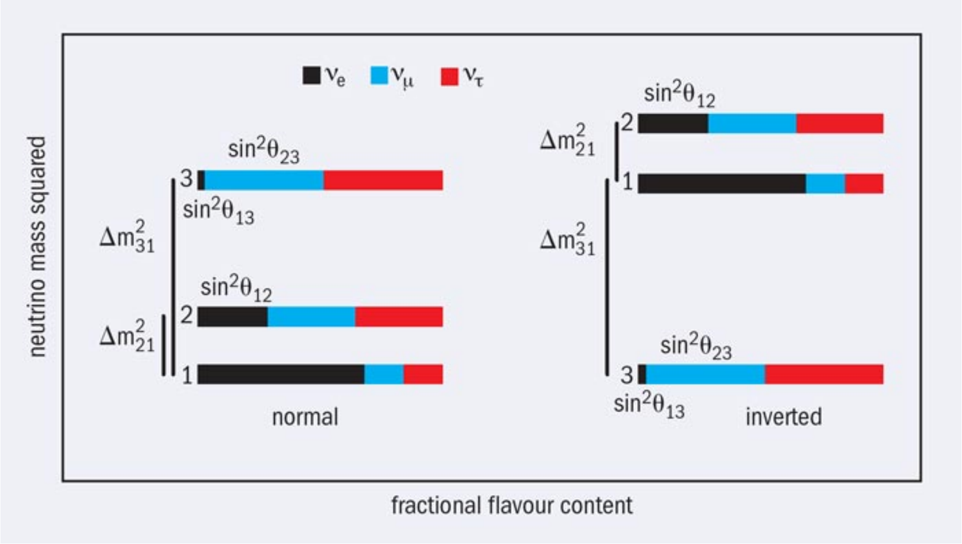

Figure 2.4: Diagram of the relationship between the mass eigenstates (labelled 1, 2 and 3) for neutrinos and the flavour eigenstates (ν_e , ν_μ and ν_τ).The fractional contribution of each flavour to the mass eigenstates is indicted by the coloured bars. Adapted from Ref. [14].

Chapter 3

3+1 Sterile Neutrino Model

Though three-flavor extended standard model oscillation predictions match most experimental evidence, some neutrino anomalies remain which do not fit into this picture. This chapter outlines these anomalies and explores one possible explanation, which postulates an additional neutrino with a higher mass than the standard model neutrino flavors. Section 3.1 describes this model. Section 3.2 outlines the observed anomalous experimental results. Following this discussion, chapter 4 outlines how this model will be tested.

3.1 3+1 Sterile Neutrino Model

The model tested in this thesis is one in which there is one sterile neutrino in addition to the three standard model flavors. Sterile here means that the proposed neutrino does not interact through any of the standard model forces. This proposed neutrino is also referred to as light ($\sim 1eV$) to differentiate it from theoretical models with a larger mass sterile neutrino.

The formalism for determining the four-flavor oscillation probabilities is the same as the three-flavor case discussed in Chapter 2, just now expanded to four flavors and four mass states. The PNMS matrix (from Equation 2.2) is expanded to be:

$$U = \begin{pmatrix} U_{e1} & U_{e2} & U_{e3} & U_{e4} \\ U_{\mu 1} & U_{\mu 2} & U_{\mu 3} & U_{\mu 4} \\ U_{\tau 1} & U_{\tau 2} & U_{\tau 3} & U_{\tau 3} \\ U_{s1} & U_{s2} & U_{s3} & U_{s4} \end{pmatrix} \tag{3.1}$$

As in the three-flavor case, as a neutrino of flavor α evolves through time, the probability that it is some other flavor β at time t is given by:

$$\begin{aligned} | < \nu_\beta | \nu_\alpha(t) > |^2 \quad &= \textstyle\sum_{ij} U^*_{\alpha i} e^{-itm_i^2/2p} U_{\beta i} U_{\alpha j} e^{itm_j^2/2p} U^*_{\beta j} \\ &= \delta_{\alpha\beta} - \textstyle\sum_{ij} U^*_{\alpha i} U_{\beta i} U_{\alpha j} U^*_{\beta j} (1 - e^{i\Delta m^2_{ij} L/2E}) \end{aligned} \tag{3.2}$$

In order for the 3+1 model to best resolve the anomalies seen in the experiments described below, a sterile neutrino mass on the order of $\sim 1\ eV$ is needed [15]. This is far higher than the constraints on the three extended standard model masses. Therefore the assumption is made that the three extended sterile model masses are degenerate at 0 eV relative to the sterile neutrino mass.

$$\Delta m^2_{21} \approx \Delta m^2_{31} \approx \Delta m^2_{32} \approx 0eV^2 \tag{3.3}$$

This assumption can be applied to other experiments with a similar L/E to the existing anomalous signals ($L/E \sim 1m/MeV^2$) and is referred to here as the short base line approximation.

This allows the oscillation probability equations to be written in a simplified form as many terms go to zero. The 3+1 appearance probability is:

$$P(\nu_\alpha \to \nu_\beta) = 4|U_{\alpha 4}|^2 |U_{\beta 4}|^2 \sin^2 x_{41}, \tag{3.4}$$

and the 3+1 survival probability for disappearance measurements is:

$$P(\nu_\alpha \to \nu_\alpha) = 1 - 4|U_{\alpha 4}|^2(1 - |U_{\alpha 4}|^2)\sin^2 x_{41}, \tag{3.5}$$

where $x_{41} \equiv 1.27\Delta m^2_{41} L/E$, and α and β refer to any of the SM neutrino flavors.

The 3+1 sterile neutrino search in MicroBooNE presented in this thesis is sensitive to 3 oscillation channels: $\nu_\mu \to \nu_e$ (ν_e appearance), $\nu_e \to \nu_e$ (ν_e disappearance), and $\nu_\mu \to \nu_\mu$ (ν_μ disappearance). The ν_e content of the beam employed by MicroBooNE is not large enough to observe ν_μ appearance with any statistical significance, as ν_e 's make up $< 1\%$ of the neutrino beam. MicroBooNE is also not sensitive to ν_τ interactions. The oscillation probabilities are:

$$\begin{aligned} P(\nu_\mu \to \nu_e) &= 4|U_{\mu 4}|^2|U_{e4}|^2\sin^2 x_{41} \\ &= \sin^2(2\theta_{\mu e})\sin^2 x_{41} \end{aligned} \tag{3.6}$$

$$\begin{aligned} P(\nu_e \to \nu_e) &= 1 - 4|U_{e4}|^2(1 - |U_{e4}|^2)\sin^2 x_{41} \\ &= 1 - \sin^2(2\theta_{ee})\sin^2 x_{41} \end{aligned} \tag{3.7}$$

$$\begin{aligned} P(\nu_\mu \to \nu_\mu) &= 1 - 4|U_{\mu 4}|^2(1 - |U_{\mu 4}|^2)\sin^2 x_{41} \\ &= 1 - \sin^2(2\theta_{\mu\mu})\sin^2 x_{41} \end{aligned} \tag{3.8}$$

These oscillations have been written in two formats, one using the explicit matrix terms and the other using the mixing angles. For the purpose of the study we will search for the best fit explicit matrix terms. There are three independent parameters that will be fit over: $|U_{e4}|$, $|U_{\mu 4}|$, and Δm^2_{41}. $|U_{e4}|$, $|U_{\mu 4}|$ best fits to the MicroBooNE data can be used to calculate the $\sin^2(2\theta_{ij})$ parameters for comparison to other experiments and current global best fits. The U parameters roughly correspond to normalization parameters on the size of the oscillation. Meanwhile,

Δm^2_{41} corresponds to a term governing the frequency with which oscillations occur for a neutrino with a given E_ν.

3.2 Neutrino Oscillation-like Anomalies

Over the past few decades, some experimental oscillation-like anomalies have been observed which may point to the existence of light sterile neutrinos, including the 3+1 model described above. This mass state is expected to have a small flavor contribution from the standard model neutrino flavors. This is due to experimental bounds as the oscillation amplitudes must be small and at a relatively low L/E $\sim$ 1 m/MeV [16]. These include observations in the ν_e disappearance channel from calibration measurements using the measurement of reactor produced neutrinos with gallium detectors [17, 18], short-baseline reactor based experiments [19], and two short-baseline accelerator experiments [20, 21, 22]. This section examines each of these experimental anomalies.

3.2.1 Gallium Solar Neutrino Experiments

Two Gallium solar neutrino experiments, SAGE and Gallex/GNO, have observed still unexplained anomalies. These are not in the solar neutrino portion of the data. Rather, the anomalies were observed when testing the detectors by using a nearby radioactive source.

The first experiment, SAGE, is a Russian-American experiment designed to measure solar neutrino capture rate on gallium metal. It took data from 1989-2001. The detector was filled with 50 tonnes of gallium heated so it is kept molten. Electron neutrinos are captured via the reaction $^{71}Ga + \nu_e \rightarrow^{71} Ge + e^-$ in the detector. The Ge is regularly extracted and counted to measure the number of reactions. SAGE observed a capture rate of $65.4^{+3.1}_{-3.0}(stat)^{+2.6}_{-2.8}(syst)$ SNU in the solar neutrino experiment which agrees with the three flavor prediction [17].

The GALLEX detector contained 30 tons of gallium in a $GaCL_3$ solution and was located at the Laborati Nazionali del Gran Sasso. It took data from 1991-1997 then was reconstituted under the name GNO and took data from 1998-2003. Likewise to SAGE, the number of neutrino interactions comes from a measure of Ge in the detector after periods of exposure [18]. When measuring the solar neutrino rate, the result is in very good agreement with the prediction [18].

While the solar neutrino observations match up with current standard model predictions and solar flux models, the anomaly for both this experiment and Gallex/GNO was observed when performing calibration/validation studies using reactor neutrinos. For this study, the gallium targets were exposed to a reactor neutrino source whose activity was close to 1 MCi. Gallex performed this twice, using a ^{51}Cr source. SAGE also performed this twice, once using a ^{37}Ar source and the other time using ^{51}Cr. The ν_e flux came out lower than predicted for all four studies with a weighted average ratio value for the four experiments of $R = 0.87 \pm 0.05$. The quality of this fit is quite high with $\chi^2/DOF = 1.9/3$ [17]. While this has a variety of explanations such as an efficiency misunderstanding or mismodelling of the production rate, this could be explained by the hypothesis of a sterile neutrino with $\Delta m^2 \sim 1eV^2$.

3.2.2 Short-baseline Reactor Experiments

Short-baseline reactor neutrino experiments have the same setup as experiments described in Section 2.4.4, but are located close to the source reactor. Recent improved calculations have updated the cross section per fission in the calculation of neutrino flux from nuclear reactors. The new predicted rate is a few percent higher than observed in short-baseline reactor experiments with L$\leq$100 m. This anomaly has been observed by a variety of detectors located <100 m from the reactor core including at ILL-Grenoble, Goesgen, Rovno, Krasnoyarsk, Savannah River, and Bugey. These flux calculation changes were not large enough to have an impact on the mid to long-baseline reactor experiments [19].

The combined ratio of the observed number of events over the standard model prediction from these experiments with the new flux calculations is 0.943 ± 0.023

[19]. It can be explained by a sterile neutrino with the same $\Delta m^2 \sim 1eV^2$. The theory community is investigating the flux predictions, and future experiments with detectors at various baselines will help shed light on this anomaly.

3.2.3 Short-baseline Accelerator Experiments: LSND

There are two notable short-baseline accelerator experiments that have observed anomalies in their neutrino oscillation studies that are not predicted by the standard model: LSND and MiniBooNE. MicroBooNE is part of an effort to further the understanding of this short-baseline accelerator anomaly.

LSND (as well as MiniBooNE, MicroBooNE, and others) is one of this class of short-baseline accelerator experiments. It was located at the Los Alamos Neutrino Science Center. The detector was filled with 167 t of liquid scintillator, and was $\sim$ 30 m from the neutrino source. 1220 8-inch Hamamatsu photomultiplier tubes (PMTs) were placed on the inside surface of the detector and covered $\sim$ 25% of the surface. An active veto shield was used to reduce the cosmic background. The experiment searched for $\bar{\nu}_\mu \rightarrow \bar{\nu}_e$ oscillations. Data was taken from 1993-1998. The beam used was a high intensity proton beam of 798MeV protons. These are sent into a target producing π^+ and other secondary products captured by a beamstop. The resulting neutrino beam primarily consists of ν_μ from $\pi^+ \rightarrow \mu^+\nu_\mu$ and $\bar{\nu}_\mu$ and ν_e from $\mu^+ \rightarrow e^+\nu_e\bar{\nu}_\mu$ [20]. Notably, very few $\bar{\nu}_e$ are produced (1 $\bar{\nu}_\mu$:$\sim 8e10^{-4}\bar{\nu}_e$), making this a good experiment to study $\bar{\nu}_\mu \rightarrow \bar{\nu}_e$ oscillations, though with an irreducible $\bar{\nu}_e$ background.

The neutrino interactions in the detector come from interactions on carbon, free protons, and electrons in the detector liquid. At the energies of the beam neutrinos, the possible neutrinos are ν_e , ν_μ and their corresponding antineutrinos. There are three categories of processes: standard model leptonic processes, inverse β-decay, and semi-leptonic processes. Of these, the third has the highest uncertainty in the cross-sections due to complex nuclear models [20]. The $\bar{\nu}_e$ events investigated for the oscillation study are detected via inverse β-decay ($\bar{\nu}_e + p \rightarrow n + e^-$). The proton is usually a free proton in a hydrogen nucleus in one of the liquid scintillator molecules. The cross section for the process is well modelled. There are two sequential signals. The e^+ produces both Cherenkov and scintillation light which are detected quickly. Then, the neutron is captured by a proton which produces a 2.2 MeV photon which is observed as a delayed signal [20].

LSND observed a total excess of $87.9 \pm 22.4 \pm 6.0$ events which corresponds to an oscillation probability for $\bar{\nu}_\mu \rightarrow \bar{\nu}_e$ of $(0.264 \pm 0.067 \pm 0.045)\%$. The best fit experimental limits on standard model oscillation parameters do not allow for such an oscillation. Figure 3.1 (adapted from Ref. [20]) shows the L_ν/E_ν distribution from LSND along with the best fit oscillation spectrum $(p(\bar{\nu}_\mu \rightarrow \bar{\nu}_e, e^+)n)$.

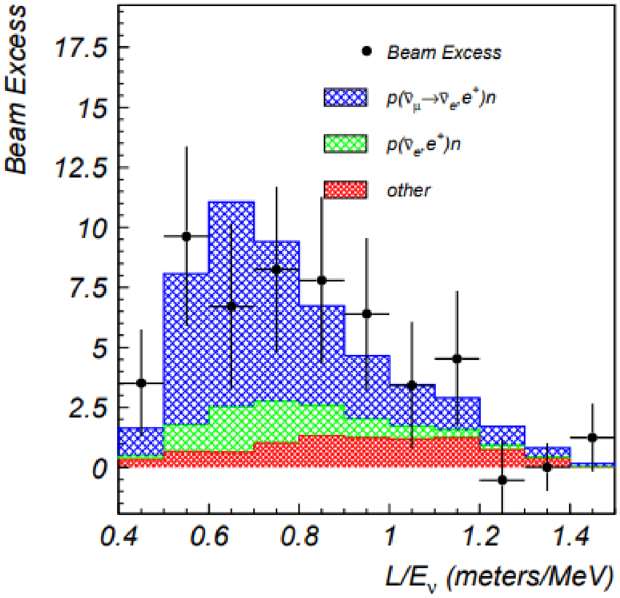

Figure 3.1: The L_ν/E_ν distribution for events with $R_\gamma > 10$ and $20 < E_e < 60 MeV$, where L_ν is the distance travelled by the neutrino in meters and E_ν is the neutrino energy in MeV. The data agree well with the expectation from neutrino background and neutrino oscillations at low Δm^2. Adapted from Ref. [20].

3.2.4 Short-baseline Accelerator Experiments: MiniBooNE

The next short-baseline accelerator experiment to observe an anomaly was MiniBooNE. MiniBooNE was designed with the primary goal of investigating the LSND excess. As such, it was built with a similar L/E in order to be sensitive to the same oscillation parameter. MiniBooNE uses the same boosted neutrino beam as MicroBooNE, which will be described in detail in Section 5.1. It has the capability to run in both neutrino and antineutrino mode. The beam flux is dominated by ν_μ or $\bar{\nu}_\mu$. The flux peaks at 600 MeV in neutrino mode and 400 MeV in antineutrino mode [21].

The MiniBooNE detector is a 12.2 m diameter sphere filled with mineral oil (CH_2) located 541 m from the beam. It is a Cherenkov detector. Neutrino interactions in the detector produce charged particles which in turn produce scintillation and Cherenkov light. This light is detected by 1520 8-inch photomultiplier tubes (PMT's) which line the inside of the detector. The neutrino interactions can be reconstructed from the charge and time information from the PMTs. The total exposure was 11.27 x 10^{20} protons on target in antineutrino mode. Figure 3.2 shows a schematic of the detector enclosure and a cut-away drawing of the the detector. This illustrates the PMT layout and the veto region which contains more PMT's specifically designed to identify and tag cosmic ray background [23].

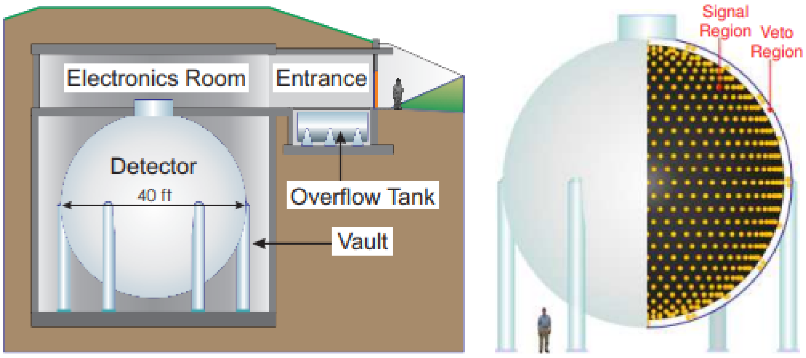

Figure 3.2: The MiniBooNE detector enclosure (left) and a cut-away drawing (right) of the detector showing the distribution of PMT's in the signal and veto regions. Adapted from Ref. [23].

In MiniBooNE, interactions are identified and reconstructed primarily through the Cherenkov light. It generally cannot detect heavy particles such as protons and neutrons. The energy of interactions of the beam neutrinos is primarily below the Cherenkov threshold in mineral oil. The MiniBooNE analysis containing the anomaly focuses on ν_e and ν_μ charged current quasi-elastic (CCQE) events which were described in section 2.2. The light from the outgoing e^- or μ^- respectively is picked up by the PMTs. They can be differentiated by the light patterns. Muons are heavier, and so travel in a straighter line and make a sharper ring of light than electrons. The signal topology for MiniBooNE was defined as 1 lepton + 0 pions + N protons. Pion production channels with nuclear pion absorption is an irreducible background to this signal [24]. The reconstructed E_ν^{QE} then comes from using the reconstructed energy and direction of the outgoing charged particle.

CCQE events are also the main signal for the MicroBooNE analysis presented in this thesis.

MiniBooNE observed an event excess of 78.4 ± 28.5 (2.8σ) in the energy range of $200 < E_\nu^{QE} < 1250$ MeV in antineutrino mode. An $\bar{\nu}_\mu \to \bar{\nu}_e$ oscillation fit to the excess was found to have a probability of 66% and the background-only file has a χ^2 probability over the best fit of 0.5%. In the data taken while running in neutrino mode, an excess was also seen of 162.0 ± 47.8 [22]. Figure 3.3, adapted from Ref. [22], shows this excess, it is notable that the excess appears as low energy peak. The prediction shown in the colored histogram is what the distribution should look like if the only ν_e 's (or $\bar{\nu}_e's$) to interact come from intrinsic beam processes and backgrounds as opposed to oscillation.

MiniBooNE has a variety of important backgrounds. That can create signals that look like ν_e CCQE events. These include ν_μ CCQE, NC π^0 , events external to the detector (dirt), NC Δ, and others as seen in Figure 3.3. Of particular interest to work shown later in this thesis (Chapter 10) is the NC π^0 background. In these events, the π^0 decays into two photons. These photons create a two ring signature in MiniBooNE. If either the direction of the two photons is similar or one photon is not reconstructed for some reason, the reconstructed event can be mistaken for a ν_e CCQE event. MiniBooNE used a sample of NC π^0 events to help constrain this background to the CCQE signal [25].

As with the other anomalies, the MiniBooNE excess could be explained by the existence of light sterile neutrinos. Though, as with the other experiments, there

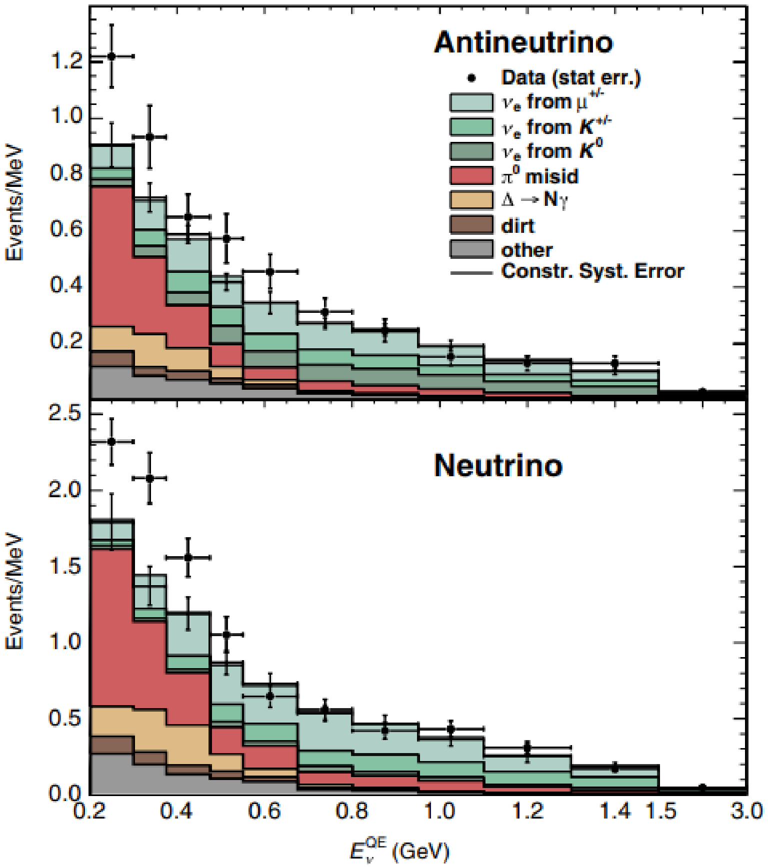

Figure 3.3: The antineutrino mode (top) and neutrino mode (bottom) E_ν^{QE} distributions for ν_e CCQE data (points with statistical errors) and background (histogram with systematic errors). Adapted from Ref. [22].

may be some other explanation. This could include mismodeled backgrounds or some other type of new physics beyond the standard model. Also the excess is not well explained by a light sterile neutrino. Even the best fit oscillation does not fully explain the shape of the excess. Figure 3.4, adapted from Ref. [22], shows the best fit oscillation spectrum as well as example spectra. This doesn't rule out sterile neutrinos, but provides hints that the full picture may be more complicated.

3.2.5 Global Picture

As discussed previously, the existence of light sterile neutrinos may explain these anomalies. Whatever extension is proposed can contain at most 3 light active neutrinos. In principle there are two classes of possible schemes which can explain the results of all of these anomalies. These are (3+1) models, or more generally (3+N),

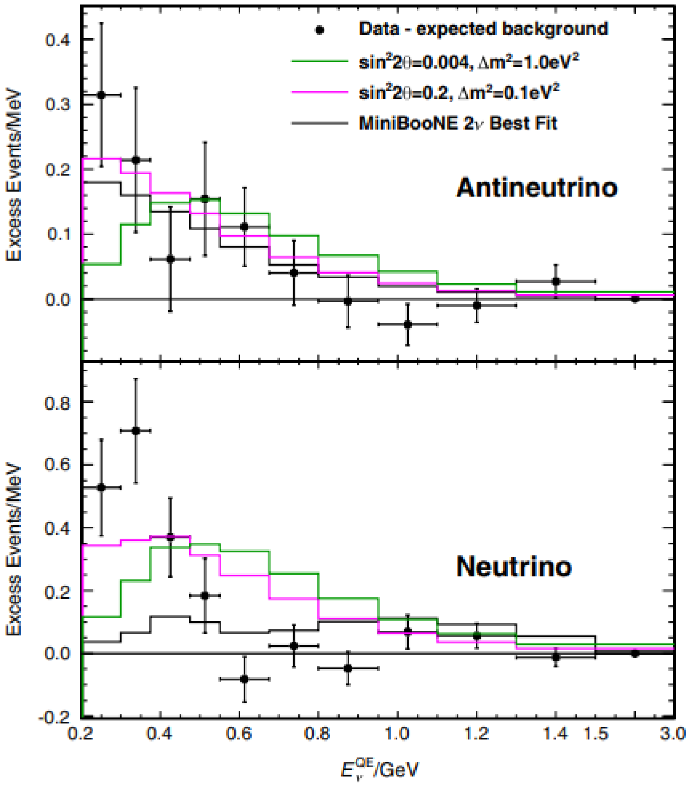

Figure 3.4: The antineutrino mode (top) and neutrino mode (bottom) event excesses as a function of E_ν^{QE}. (Error bars include both the statistical and systematic uncertainties.) Also shown are the expectations from the best two-neutrino fit for each mode and for two example sets of oscillation parameters. Adapted from Ref. [22].

where there is a group of three very light neutrinos which are separated by the other N by a gap of $\Delta m^2 \sim 1eV^2$. The second class are (2+2) where there are two pairs of close masses, though at this point the (2+2) models have been fairly well ruled out [6]. Both of these classes have also been theorized to contain other features beyond the standard model such as neutrino decay. The experiments discussed here have all observed signals over 2σ. Other experiments with similar setups have not observed the same results with the same confidence providing useful experimental limits [15].

Figure 3.5, adapted from Ref. [22], shows the allowed oscillation parameter space found by fitting the LSND and MiniBooNE anomaly results to a two-flavor oscillation equation. The LSND allowed region is shown by the shaded bands. The colored contour lines show the MiniBooNE fit. There is some overlap between the two regions. Also shown are the ICARUS [25] and KARMEN [26] limits, two experiments which did not observe a sterile neutrino signal.

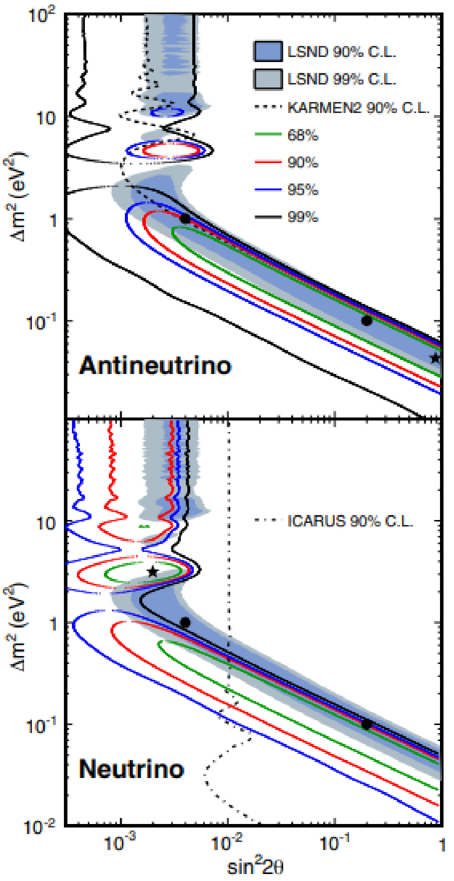

Figure 3.5: MiniBooNE allowed regions in the antineutrino mode (top) and the neutrino mode (bottom) for events with $E_\nu^{QE} > 200MeV$ within a two-neutrino oscillation model. Also shown are the ICARUS [25] and KARMEN [26] appearance limits for neutrinos and antineutrinos, respectively. The shaded areas show the 90% and 99% C.L. LSND $\bar{\nu}_\mu \rightarrow \bar{\nu}_e$ allowed regions. The black stars show the MiniBooNE best fit points, while the circles show the example values used in Fig. 2. Adapted from Ref. [22].

Table 3.1 is one attempt to find a set of global best fit oscillation parameters for different sterile neutrino models. These results from Ref. [15] incorporate both anomalous results and experiments that did not report a signal. This thesis will be fitting to a 3+1 model as it will provide a useful first hint as to whether any oscillations are observable due to sterile neutrinos in MicroBooNE. The values for these global best fits will be useful to compare to when looking at the MicroBooNE sensitivity and data results.

Table 3.1: A summary of best fit parameters found in Ref. [15] for different models involving sterile neutrinos (d=decay).

Global Fit	$\lvert U_{e4}\rvert$	$\lvert U_{\mu 4}\rvert$	$\lvert U_{e5}\rvert$	$\lvert U_{\mu 5}\rvert$	ϕ_{54}	$\Delta m^2_{41}(eV^2)$	$\Delta m^2_{54}(eV^2)$	$\tau(eV^{-1})$
3+1	0.116	0.135	-	-	-	1.32	-	-
3+2	0.106	0.082	0.252	0.060	0.009	1.32	12.6	-
3+1+d	0.428	0.180	-	-	-	0.211	-	1.96

Chapter 4

Analysis Outline

MicroBooNE is part of an effort to further analyze the short-baseline anomaly. It is one of three detectors along the same beamline as MiniBooNE. MicroBooNE, the first of the detectors to take data, has a 470 m baseline. Together with the other two detectors (ICARUS and SBND) they comprise the short-baseline neutrino (SBN) program at Fermilab. ICARUS and SBND have baselines of 600 m and 110 m respectively and will take data in the coming years. Eventually MicroBooNE's results will be combined with the other two detectors to help give a more clear understanding of this anomaly. In particular the rest of this thesis aims to compare MicroBooNE data the 3+1 sterile neutrino model. This chapter outlines the steps needed to go from raw data from the detector to a comparison of the model to provide context. The rest of the chapters will delve into the details of each step.

This oscillation analysis can be broken into four major steps as outlined in Figure 4.1: observation, reconstruction, selection, and model comparison. Observation involves reading in the data from the MicroBooNE detector. When the neutrinos from the beam interact in the detector, the information is collected. Photo-multiplier tubes detect the light from the interaction. A series of 3 wire planes collect the electrons created when charged final state particles ionize the detector medium. The details of this data collection and the beam used to produce the interactions are described in Chapter 5.

The next step is reconstruction. The goal of this step is to take the raw data read

Figure 4.1: A flow chart of the major analysis steps.

out from the detector and determine the physics properties of the neutrino event that occurred. One of the most important properties for the oscillation analysis is the energy of the incoming neutrino. The oscillation probabilities depend on the energy of the neutrino. Once events are reconstructed they are put in histograms based off of their energy. This histogram shows how many events in a given energy bin were observed. It provides a handy framework for comparing the number of observed events in each energy bin to the number of events predicted in that bin by various models. Other kinematic variables of interest will be displayed in a similar fashion.

The reconstruction used here utilizes a combination of deep-learning algorithms and more traditional algorithm. Chapters 6, 7, and 8 describe this reconstruction. Particular attention will be paid to the reconstruction of electron showers as well as the rejection/modelling of π^0 background events as the author was a main contributor to these efforts.

The next major step of the analysis chain is selection. This step involves looking at the properties of all of the reconstructed neutrino events and choosing those which have desired characteristics. (In reality the line between reconstruction and selection is a little more blurry as various reconstruction steps require that the data has certain characteristics as well.)

CCQE events were chosen as the selection target. CCQE events were described in Section 2.2. As in MiniBooNE, the intrinsic ν_e beam backgrounds are irreducible. However other backgrounds, such as single photon events, could be removed by a pure event selection. The selection therefore focuses on selecting ν_e (and ν_μ) CCQE events and rejecting the backgrounds.

The topology of the final state of CCQE events allows for a pure event selection. The specific target topology is 1 charged lepton + 1 proton ($1l1p$). This can be further broken up by lepton type (e^- or μ^-) into $1e1p$ and $1\mu1p$. Searching for a topology containing a proton allows for the rejection of single photon events (which may be mistaken for the electron). In this topology, the charged lepton and the proton for a "vee" shape in the data images as will be discussed in Section 6.5. The kinematics of this "vee" in CCQE scattering are driven by energy-momentum conservation. This means that one can use two-body kinematic scattering constraints to reduce the number of background events selected.

The goal of this particular reconstruction and selection chain is to place strict cuts to isolate a high purity, although statistics-limited, signal from CCQE scatters. The exact selection procedure will be described in chapter 11. A sideband selection of events with a π^0 will also be discussed in chapter 10.

The final step of the analysis is comparison to the model. The model here is a 3+1 sterile neutrino oscillation model with a range of oscillation parameters. This requires accurate predictions from the given model with the given oscillation parameters. In addition to the data from MicroBooNE, the collaboration has created a large collection of simulation samples designed to mimic the data that will be observed. The simulation samples will be discussed in detail in chapter 6, but the general idea is that they provide a way to predict how many events in each energy bin are expected based on the model of interest.

After everything has been run through the reconstruction and selection the result is binned energy histograms for both data and simulation. The simulation counts in each bin can be varied based off the oscillation parameters being tested. We can then test to see how well each simulation model agrees with the data.

In order to measure the scale of the agreement, the uncertainties on the prediction must first be taken into account. The uncertainties are incorporated into this analysis using the covariance matrix formalism. A covariance matrix encodes the variance (σ^2) of the contents of each histogram bin in diagonal entries, and the covariance between the contents of pairs of histogram bins in off-diagonal entries. The covariance matrix M is calculated for any given parameter as:

$$M_{ij} = \frac{1}{N}\sum_{k}^{N}(O_j^{CV} - O_j^k)(O_i^{CV} - O_i^k) \tag{4.1}$$

where N is the number of tested variations for the parameter, O^{CV} is the number of predicted events in the CV (no variation), and O^k is the number of events in the k^{th} variation of different uncertainty parameters. The fractional covariance matrix is used to add the covariance matrices from various parameters. This is defined as:

$$M_{frac,ij} = \frac{M_{ij}}{O_i^{CV} O_j^{CV}} \tag{4.2}$$

Finally in order to illustrate the correlations between bins, correlation matrices are shown:

$$C_{ij} = \frac{M_{ij}}{\sqrt{M_{ii}M_{jj}}} \tag{4.3}$$

The systematic uncertainties will be discussed in detail in chapter 9.

Finally, a log-likelihood metric is used to determine the agreement between observed and expected spectra when performing oscillation fits. The χ^2-CNP metric is also described which is used to further quantify agreement between data and a prediction.

The predicted number of events in each bin, taking into account uncertainties, is distributed as a multivariate Gaussian. This is because the generation of simulation events begins with a sampling from predicted distributions of events based on the flux predictions of each neutrino type. The interaction type is chosen based on GENIE models and the weights are further determined based on the GENIE MicroBooNE tune. In this case, starting with N randomly distributed variables (x_i) and their covariance matrix, M, the probability density function is given by:

$$f(x_1, ..., x_N) = A \exp\,[\sum_i^N (-\frac{1}{2}(x_i - y_i)M^{-1}(x_i - y_i)^T)] \tag{4.4}$$

where (y_i) are the means of the variables, and A is $\frac{1}{(2\pi)^{N/2}\sqrt{|M|}}$, where $|M|$ is the determinant of the covariance matrix M_{tot} determined as in Eq. 9.6.

The likelihood is equal to the probability that a particular outcome μ is observed when the true value of the parameter is θ. Using the above probability density function it is then:

$$L(\theta|x) = A \exp\,[\sum_i^N (-\frac{1}{2}(x_i - \mu(\theta)_i)M^{-1}(x_i - \mu(\theta)_i)^T)] \tag{4.5}$$

where μ is a function of our oscillation parameters ($|U_{e4}|$, $|U_{\mu 4}|$, and Δm^2_{41}) represented by θ and is the expectation. x is the observed distribution (data).

To find the best fit oscillation parameters in this analysis for a given x, we seek the maximum likelihood, or equivalently, the minimum $-\ln(L)$:

$$-ln(L) = \sum_i^N [\frac{1}{2}(x_i - \mu(\theta)_i)M^{-1}_{ij}(x_j - \mu(\theta)_j)] + \frac{1}{2}\ln(|M|) + \frac{N}{2}(2\pi) \tag{4.6}$$

N in this case is the number of bins in reconstructed energy. As $\frac{N}{2}(2\pi)$ is a constant, it can be ignored for the purposes of a fit. We also multiply by a factor of 2 to match up with Wilks' theorem since we use it to determine sensitivity. In our binning scheme our test metric then becomes:

$$-2\ln(L) = \sum_{i,j}^{i=31} [(x_i - \mu(\theta)_i)M^{-1}_{tot,ij}(x_j - \mu(\theta)_j)] + \ln(|M|) \tag{4.7}$$

There are 31 bins coming from the 12 $1e1p$ energy bins and the 29 non-zero $1\mu 1p$ bins. This is the metric that we will use to test agreement to various fit parameters in this analysis.

A second metric will be used on the results to demonstrate the data agreement with the best fit oscillation parameters. This is the χ^2-CNP [27].The χ^2-CNP is defined as:

$$\chi^2_{CNP} = \sum_{i,j}^{i=N} [(x_i - \mu_i) Mij^{-1} (x_j - \mu_j)] \tag{4.8}$$

where x is the predicted number of events, μ is the observed events, and M is the total covariance matrix which includes all of the systematic uncertainties in addition to the CNP term:

$$M_{CNP:i,i} = \frac{3}{\frac{1}{x_i} + \frac{2}{\mu_i}} \tag{4.9}$$

This metric is useful as it can be used to directly determine the p-value of agreement. Even if a set of parameters gives a best fit, that does not mean it is actually a good fit to the data. Chapters 12 and 13 will present various validation studies followed by the result of comparing the MicroBooNE data to predictions.

Chapter 5

The MicroBooNE Experiment

MicroBooNE is a short-baseline accelerator experiment. While it has many goals, the two that are most relevant to this thesis are to develop tools to analyze data in liquid argon time projection chambers (LArTPC) neutrino detectors, and to investigate the MiniBooNE low energy anomaly discussed in Chapter 3. The other major goal of MicroBooNE is to perform a variety of precision cross-section measurements to inform next generation LArTPC experiments.

MicroBooNE is located in Batavia, Illinois at the Fermilab National Accelerator Laboratory (FNAL). It receives neutrinos from the Booster Neutrino Beam (BNB). It has a 470 m baseline, and utilizes the same beam as MiniBooNE. An overhead diagram of the experiment site at Fermilab is shown in Figure 5.1. This shows the close proximity of MiniBooNE and MicroBooNE as well as their location relative to some of the other Fermilab experiments. Section 5.1 describes the BNB and neutrino flux it produces.

Section 5.2 gives an overview of the MicroBooNE detector. This is followed by Sections 5.3, 5.4, and 5.5 which discusses the liquid argon time projection chamber, optical readout system, and electronic readout in more detail. The LArTPC technology used by MicroBooNE is particularly well suited for complicated topologies. With the BNB flux and energy range, many interaction processes (quasi-elastic, resonances, deep inelastic scattering) are possible in the detector. The nuclear effects in neutrino interactions on argon also result in a variety of final states. The detector allows for particle identification and calorimetry.

Finally, Section 5.6 will describe MicroBooNE's data collection and the data that is used is this thesis.

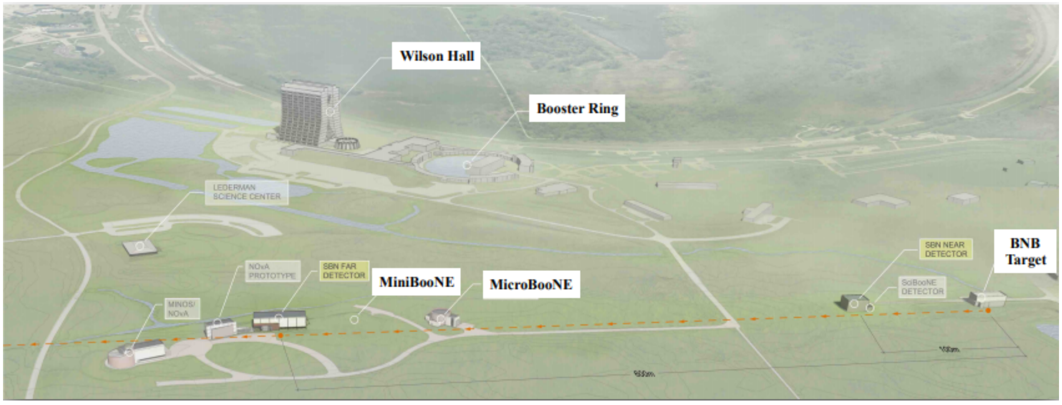

Figure 5.1: Overhead diagram of the Fermilab experiment site, showing the location of MicroBooNE [28].

5.1 The Booster Neutrino Beam

MicroBooNE lies along the Booster Neutrino Beam (BNB). The neutrino beam originates with a proton beam. The proton beam is directed at a beryllium target. This creates secondary mesons, primarily pions and kaons. The beryllium target is inside a pulsed electromagnet which focuses positive secondary particles (or negative when aiming to produce antineutrinos). These secondary particles enter a 50 m decay region where they decay into neutrinos, resulting in a neutrino beam [29]. Figure 5.2 is a cartoon illustrating the generation of the neutrino beam and how ν_μ are produced. This section describes these steps in more detail starting with the proton beam and beryllium target in 5.1.1, followed by the horn and decay pipe in 5.1.2. Finally the resulting beam composition and flux is described in 5.1.3.

5.1.1 The Proton Beam and Beryllium Target

The first step in producing the neutrino beam is the production of a proton beam. Protons originate from the Fermilab Linear Accelerator (LINAC). The LINAC is a 500 ft straight accelerator that creates the proton beam. They are next passed

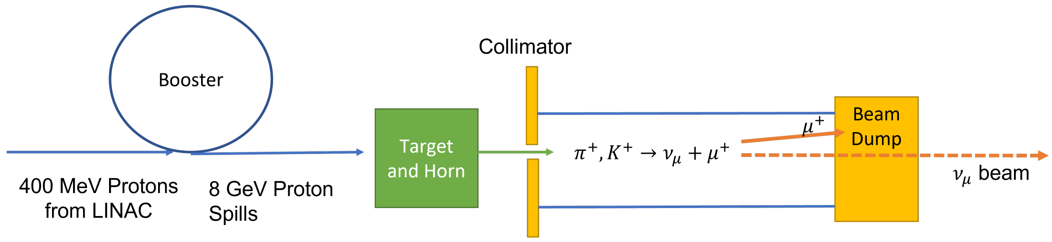

Figure 5.2: A cartoon illustrating the general steps in the Booster Neutrino Beam.

into the Fermilab booster synchrotron which is a 474 m circumference synchrotron operating at 15 Hz. Protons are delivered from the linear accelerator in spills of $\sim 1.6\,\mu s$ duration consisting of 82 bunches of 2 ns width each, with an intensity of 5×10^{12} protons on target (POT) for each beam pulse. The synchrotron serves to accelerate the protons even further. They are injected at 400 MeV and accelerated to 8 GeV kinetic energy (8.86 GeV/c momentum) [29]. The LINAC and booster are used in many other Fermilab experiments including higher energy neutrino experiments, muon experiments, and fixed target experiments. A cartoon of the full layout is shown in Figure 5.3.

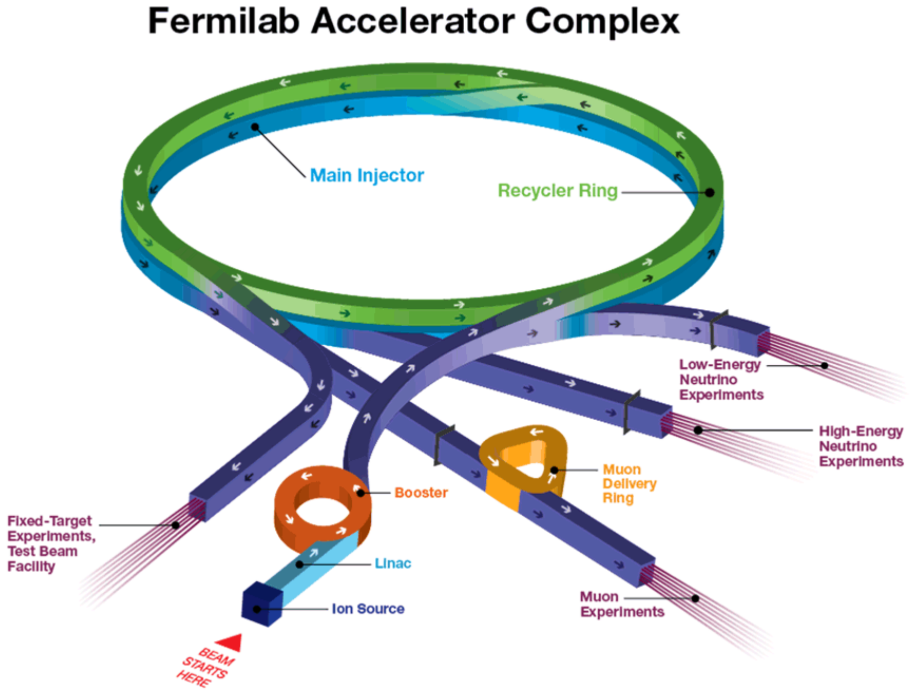

Figure 5.3: A cartoon of the Fermilab Accelerator complex. Adapted from Ref. [30].

These protons are then directed to a beryllium target. The beryllium target for meson production is located inside of the magnetic focusing horn (discussed in the next section). The target is made of seven identical cylindrical slugs of beryllium. These are arranged in a cylinder that is 71.1 cm long with a radius of 0.51 cm. The air around the slugs is circulated to allow for cooling during operation of the beam. Just upstream of the target, the proton beam is monitored using four systems. These are: two toroids measuring the intensity, beam position monitors, a multiwire chamber responsible for the determining the width and position, and a resistive wall monitor which measures the time and intensity of the beam spills [29].

When the protons interact with the beam target it produces predominantly charged pions and kaons that decay in flight. Secondary protons and neutrons are also produced which do not contribute to the beam. MicroBooNE's 470 m beamline is measured from the beryllium target. Later when performing the oscillation measurement, the distance will be taken as the distance from when the charged meson decays into a neutrino to the neutrino interaction point. When neutrino interactions are simulated, this property is included.

5.1.2 The Horn and Decay Region

The beryllium target is encased in an electromagnet called the horn. The purpose of the horn is to focus the charged mesons from the proton interactions into a beam with the requested charge (positive or negative). For this data set, running was taken with magnet polarity that focuses positively charged mesons toward the detector using this horn. The horn used in the BNB beam is a pulsed toroidal electromagnet made of an aluminum alloy. The current is a 143 μs long pulse which has a peak of 170 kA. This peak is timed to coincide with the arrival of the proton beam at the target. In neutrino mode, the current runs along the inner conductor which then folds outwards via the outer conducting cylinder. In the volume between the inner and outer conducting cylinders there is a resulting magnetic field that falls as 1/R.

Figure 5.4 is a schematic of this horn. The outer conductor is shown in gray.

The inner conductor components are in the center in dark green and blue. In this schematic in neutrino mode the positive current flows from left to right along the inner conductor. The current is reversed when the beam is operating in antineutrino mode. This figure was adapted from Ref [29].

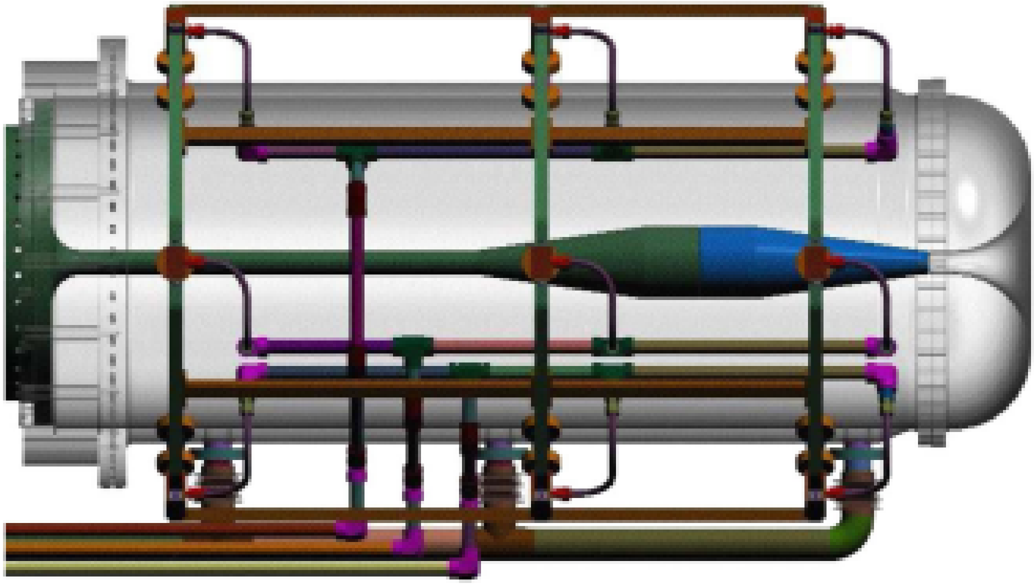

Figure 5.4: A schematic of the pulsed electromagnetic horn used in the Booster Neutrino Beam. Adapted from [29].

These focused charged particles next decay into neutrinos within a 50 m steel decay pipe. The pipe is filled with air that terminates in a beam stop made of steel and concrete, followed by largely undisturbed earth until the neutrino beam hits the detector. A 214 cm long concrete collimator is the entrance to the decay pipe. It absorbs particles that would not contribute to the neutrino flux. It has a narrow opening allowing further focusing of the beam. Charged mesons that are off-axis at this point will be absorbed by the collimator.

The decay pipe itself is filled with air. It has a 3 ft radius and is 45 m long. In this decay pipe, the charged pions will either decay into forward going neutrinos or are absorbed in the steel shell of the decay pipe. The pipe ends in a beam stop made of concrete and steel. Only neutrinos (and some very high energy muons which interact in the surrounding dirt) can pass through this beam stop.

5.1.3 Beam Composition and flux

Figure 5.5 shows the neutrino flux resulting from the BNB when run in neutrino mode [29]. Within this analysis energy range, the neutrino flux is dominated by muon neutrinos (93.6% ν_μ and 5.9% $\bar{\nu}_\mu$) with a small component of electron neutrinos (0.52% ν_e and 0.05% $\bar{\nu}_e$) referred to as "intrinsic ν_e ". The mean ν_μ energy is $\sim 800\,\text{MeV}$ [29, 31].

The beam has an intrinsic component of ν_e coming from the decay of μ^+. Pions very rarely decay directly into electrons + ν_e due to helicity suppression ($\gamma(\pi \rightarrow e\nu)/\gamma(\pi \rightarrow \mu\nu) \sim 1.2x10^{-4}$). The intrinsic ν_e is therefore a small component as most μ^+ produced by the π^+ decay are absorbed by the beam stop or the wall of the decay pipe. These intrinsic ν_e events are an irreducible background to the oscillation study presented in this thesis. The same background was present in MiniBooNE as it is located on the same neutrino beam.

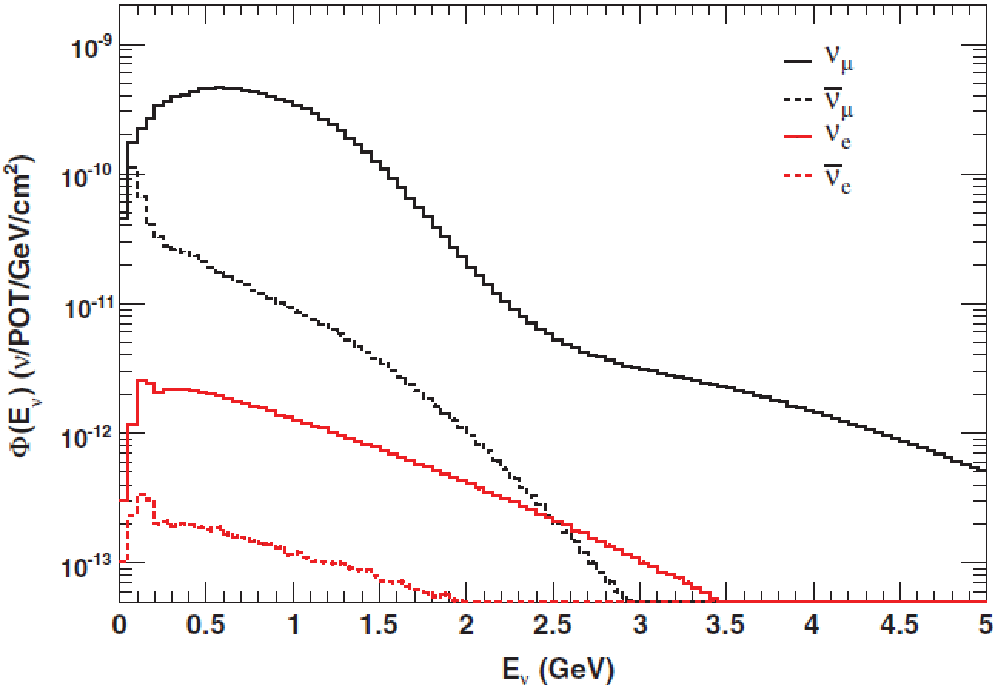

Figure 5.5: Total predicted flux From the BNB by neutrino species when operating in neutrino mode. Adapted from Ref. [29].

The flux can be further broken up by production process. As seen in Figure 5.6, the ν_μ 's are primarily produced by the process $\pi^+ \rightarrow \mu^+\nu_\mu$. This changes at higher neutrino energy, but this analysis cuts off at 2400 MeV. The subdominant contributions come from various kaon ($k^{+/-/0}$) decay channels. The electron neutrinos are primarily produced through the decay chain of $\pi^+ \rightarrow \nu_\mu \mu^+$, followed by $\mu^+ \rightarrow e^+ \bar{\nu}_\mu \nu_e$. Another subdominant process is k^+ decay.

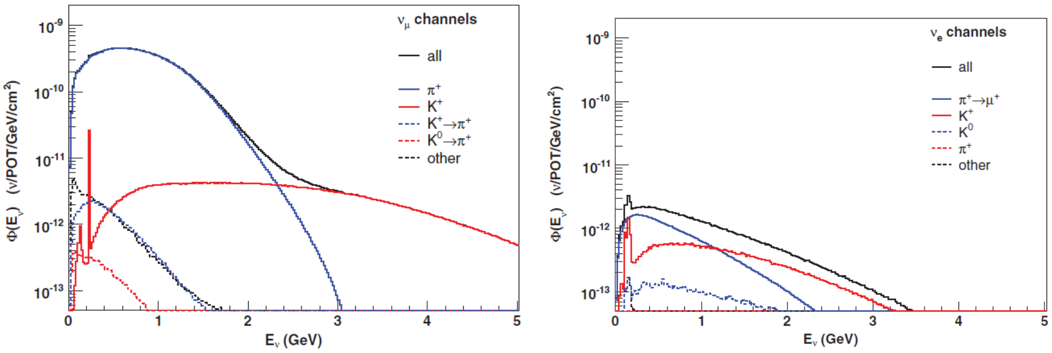

(a) ν_μ Flux (b) ν_e Flux

Figure 5.6: Predicted ν_μ flux (a) and ν_e flux (b) broken up by parent meson. The black line shows the total predicted flux. Adapted from Ref. [29].

5.2 Detector Overview

The MicroBooNE detector consists of a liquid Argon time projection chamber (LArTPC), a light collection system, and an external cosmic ray tagging device. The detector is enclosed within a cryogenic vessel. The TPC employs three wire readout planes which enables 3D position reconstruction. The volume of liquid argon is exposed to an electric field. Particles that move through the detector ionize the argon atoms, leaving behind ionization electrons and produce scintillation light. The ionized electrons drift in the electric fields to the wire readout planes.

The light collection system is a PMT optical system. It collects scintillation light produced in the interaction and is used for beam triggering. The external cosmic ray tagging (CRT) system is composed of an array of scintillator panels surrounding the detector and can be employed to tag thru-going cosmic particles by matching the hits in the CRT in time to the PMT hits. It will not be utilized in the studies presented here as it was not operational for the entire data-taking. [28]. A schematic cross section of the TPC and PMT systems is shown in Figure 5.7.

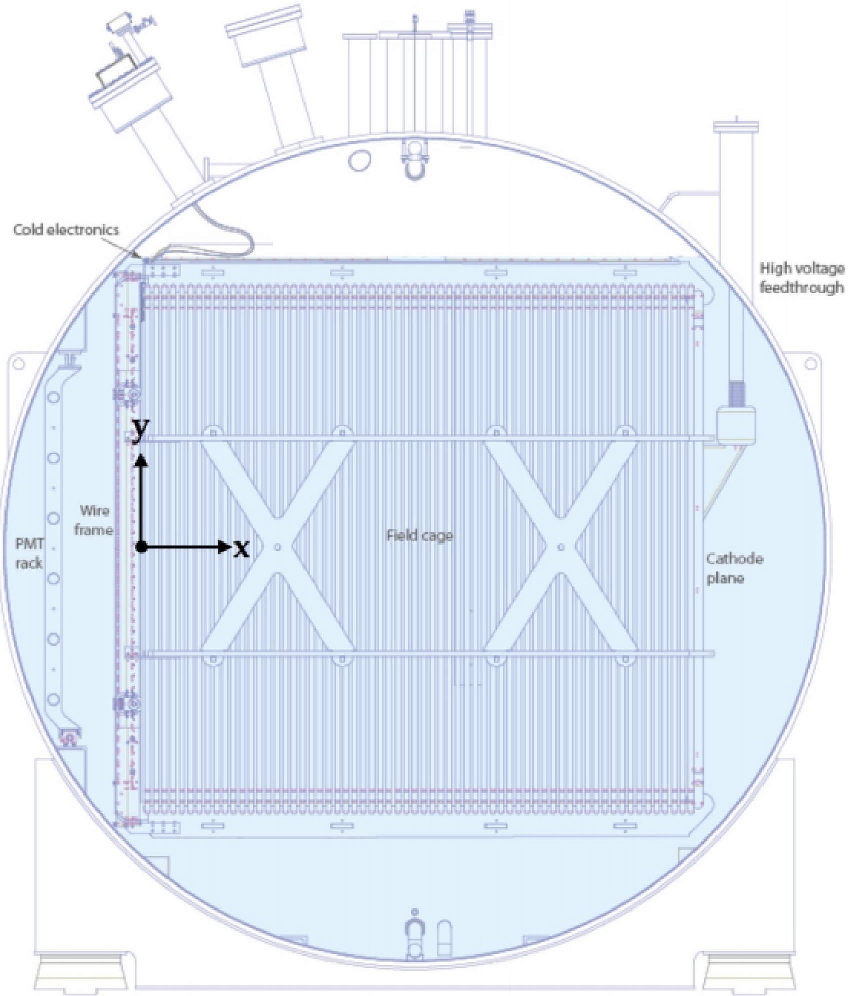

Figure 5.7: Cross section view of the cryogenic vessel containing the LArTPC and the PMT optical system. In this view, the beam direction is out of the page, towards the reader [28].

5.3 The Time Projection Chamber

As charged particles traverse a volume of liquid argon, they leave trails of ionization electrons. A uniform electric field in the detector volume causes these electrons to drift to one side of the chamber. The anode is parallel to the cathode plane and parallel to the beam direction. The applied electric field is 273 V/cm, leading to $\approx 0.11\,\mathrm{cm}/\mu\mathrm{s}$ electron drift velocity.

The argon in the TPC is highly purified which allows these ionization trails to be transported over distances of the order of meters. The ionization electrons drift until they reach the three wire planes located along one side of the active volume at the anode. The plane-to-plane spacing is 3 mm and the wires in each plane are separated by 3 mm. The collection plane is oriented vertically and the induction planes are at ±60° relative to the vertical. The induction planes each have 2400 wires while the collection plane has 3456 wires. Non-uniformities in the electric field, diffusion, recombination, and space charge effects will modify the electrons as they are transported to the wire planes. Taking these effects into account is critical and will be discussed is Chapter 9.

The three wire planes continually read the ionization electrons drifting towards them, though this information is only stored if the data acquisition system (DAQ) is triggered (Section 5.5.2). The process of describing which data is kept is discussed in Section 5.5.2. The electrostatic potentials of the setup results in the ionization electrons passing through the first two (induction) planes. They end their trajectory on the third (collection) plane. The induction planes are named the U and the V planes. The collection plane is the Y plane.

A representative cartoon can be seen in Fig. 5.8. In this cartoon an incoming neutrino interacts in the detector. The resulting charged particles travel through the argon creating ionization electrons. These then drift to the wire planes. The induction planes show a bi-modal waveform from the electron first moving towards, and then away from, the wires. Then the collection plane has a simpler waveform from the stopping of the electron. Due to this difference in waveform, the collection plane (Y) tends to have a cleaner signal.

The coordinate system employed in this analysis is common throughout the MicroBooNE experiment. MicroBooNE employs a right-handed coordinate system to describe the detector, with x-axis toward the cathode, y-axis up, and z-axis downstream from the beam direction. The angle θ is measured from the z-axis, and ϕ is measured from the x-z plane. In the coordinate system the x axis ranges from 0.0 m at the anode to +2.6 m at the cathode. The y-axis is measured from -1.15 m at the bottom of the detector to +1.15 m at the top of the detector. The z-axis ranges from 0.0 m at the upstream end to +10.4 m at the downstream end.

The LArTPC, along with the light collection system (Section 5.4) are contained

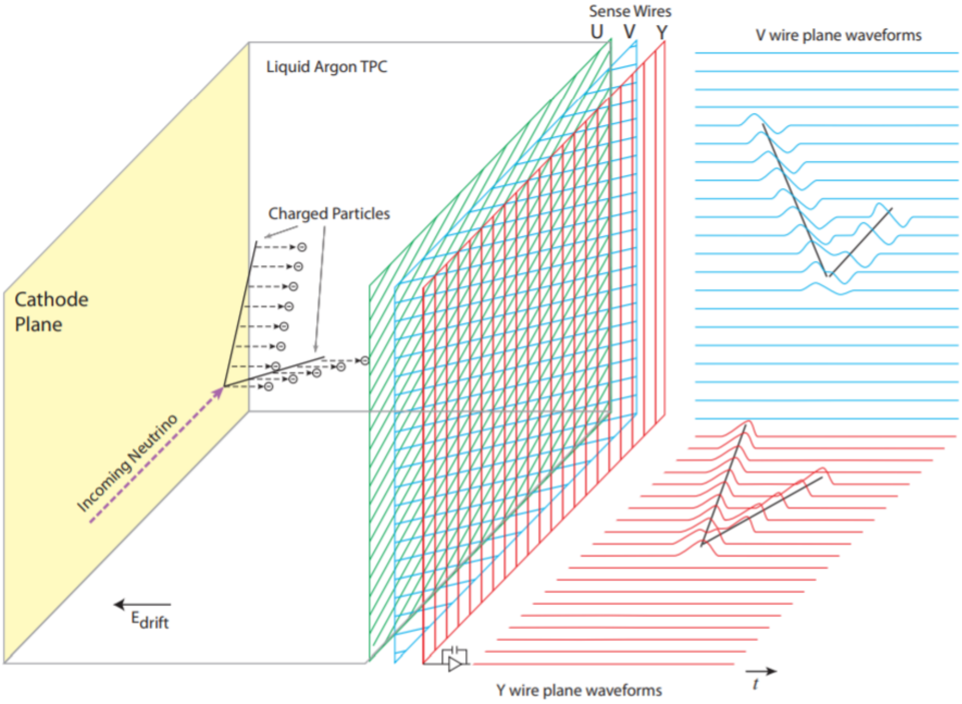

Figure 5.8: Operational Principle of the MicroBooNE detector [28].

in a single walled cyrostat filled with liquid argon. Front end electronics (Section 5.5) are mounted directly on the LArTPC which amplify the wire signals and pass the signals out of the cyrostat for further processing.

5.4 Optical Readout System

The optical readout system is composed of 32 “optical units” in Run 1 and 31 optical units in Runs 2-5 (one of the units became non-functional). Each optical unit consists of an 8-inch Hamamatsu R5912-02mod cryogenic photomultiplier tube (PMT) located behind an acrylic plate coated with tetraphenyl butadiene to shift the 128 nm scintillation photons to the visible range [32]. These PMTs are located behind the wire planes. All of the PMTs are installed inside the cryogenic magnetic field which helps counteract the effect of weak ambient magnetic fields.

An important feature of the PMTs is the time scale they operate on. Prompt scintillation light from the argon is emitted on a 3-6 ns timescale. The drift electrons take milliseconds depending on the location of the interaction. The PMTs operate on a ns timescale. This allows the light to be detected and the data collection system to trigger before the electrons reach the wire planes.

The final component of the optical system are light guide paddles. These are an alternate way to collect the scintillation light. They are not utilized in this analysis, but are a useful test of the technology for future LArTPCs [32].

Figure 5.9 shows the layout of the PMTs (circles) and the light paddles (rectangles). The beam direction in this schematic is left to right. The optical readout system provides the event trigger for the experiment and is also used to reject cosmic rays as discussed in Section 6.2.

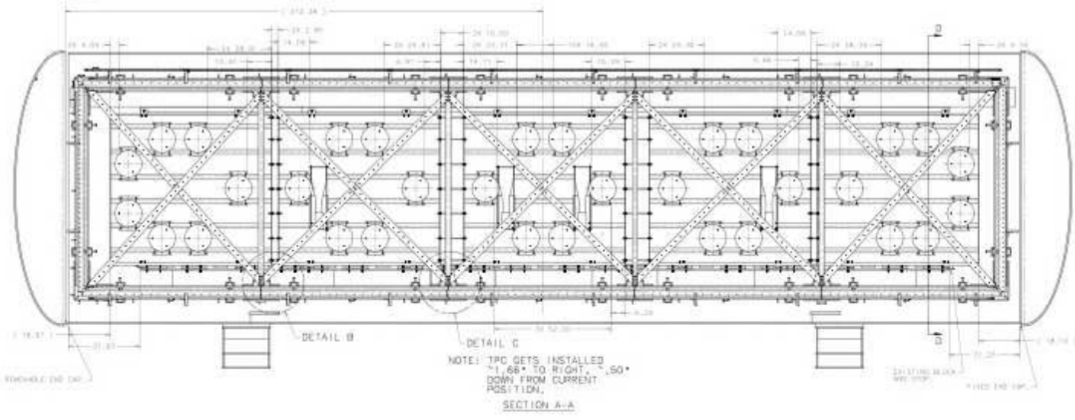

Figure 5.9: A drawing to show the configuration of PMTs and light guide paddles in the MicroBooNE cryostat from [32].

5.5 Electronics Readout

The analog signals that are collected by both the LArTPC and the PMTs next need to be amplified, digitized, and written to disk for use in analyses. MicroBooNE implements custom low-noise electronics which are capable of operating in liquid argon. The data is sent to a readout system which digitizes the signals. These signals are then passed out to a data acquisition (DAQ) system which stores the data to disk if the event trigger is passed. This section delves into a few aspects of this system in more detail. Section 5.5.1 discusses the performance of the wire planes over time, Section 5.5.2 describes the event trigger, and Section 5.5.3 describes the

2D deconvolution of the wire signals into a digital readout.

5.5.1 Wire Performance

An unexpected problem that arose in MicroBooNE is the presence of "dead wires" in the wire readout planes. Dead wires include wires with no readout at all as well as wires that only sometimes have readout. When the wires are not reading out data properly, it can cause gaps in the event images. This complicates the event reconstruction described in Chapter 6. These wires, in each of the three wire planes, are illustrated in Figure 5.10. The larger clusters of dead wires seen in this figure are particularly troublesome in event reconstruction.

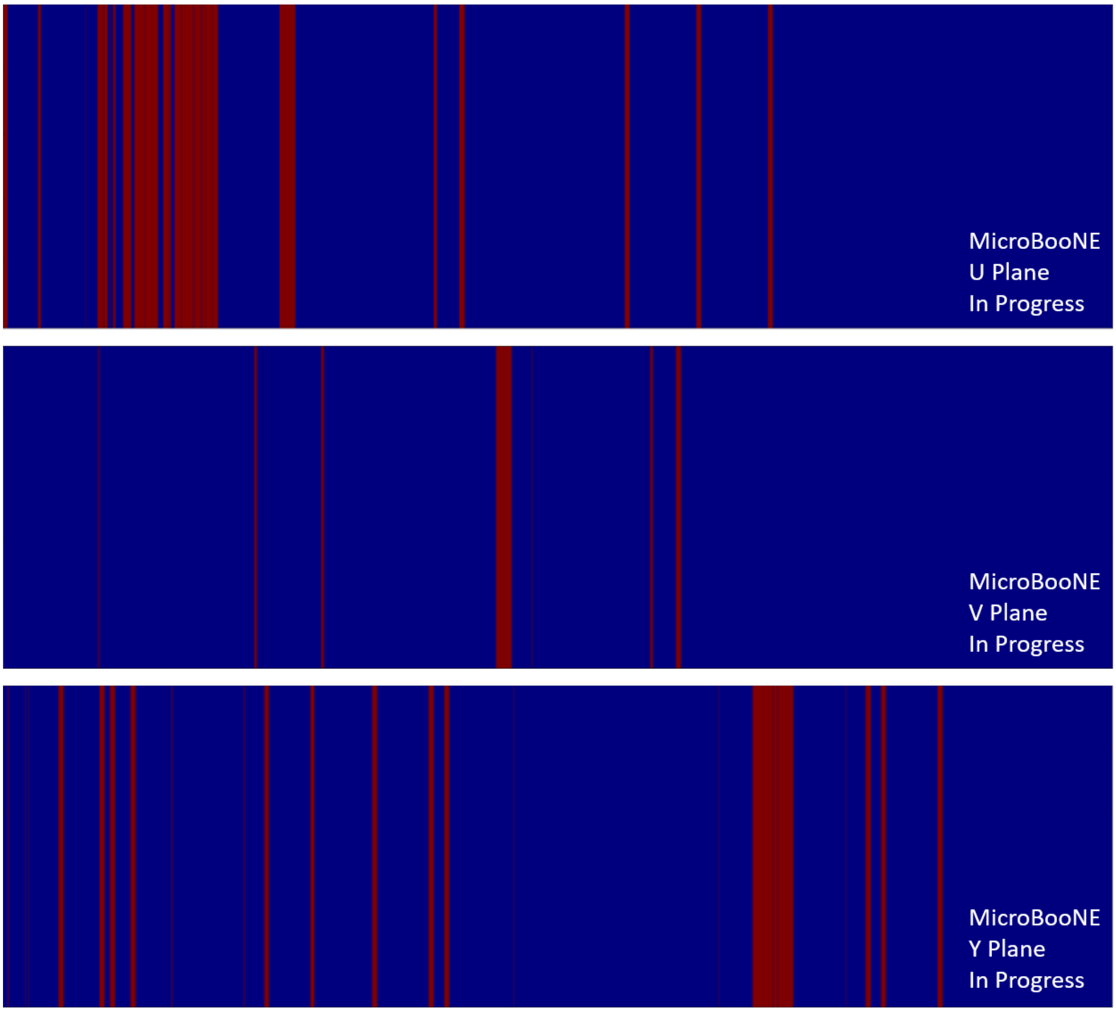

Figure 5.10: This figure shows the channel status for each of the three wire planes in the MicroBooNE detector. The red represents dead wires. The blue represents non-dead wires.

Table 5.1 describes the different types of wires considered dead for this analysis [33]. The main causes of the dead wires are shorted wires and their affected neighboring wires as well as general problems when the detector turned on.

Table 5.1: A summary table of the wires considered to be dead for this analysis. The total number is ~ 862 from all three planes. Adapted from Ref. [33].

Number of ”dead” wires	Reason
20	Over saturation
96	Poor connection to motherboard
304	Problem on detector startup
126	U-Y shorted wires and surrounding wires
287	U-V shorted wires and surrounding wires
36	other noisy wires

Chapter 7 presents a way to reconstruct the information in these dead wires using a deep-learning network. This network is not deployed in this analysis due to computation time and memory restrictions. However, it demonstrates a fix to this problem which may be utilized in future LArTPC experiments

5.5.2 Event Trigger

The MicroBooNE detector sits very close to the Earth's surface and is therefore subject to a large cosmic ray background. In order to reduce the amount of background saved to disk an event trigger is utilized. Later in Section 6.2, reconstruction techniques attempt to remove any remaining cosmic ray background.

The BNB described above produces neutrino spills with a rate of about 5 Hz. Each spill is ~1.6 μs wide. During the rest of the time the beam is active, no data is recorded and saved to tape (except to record off-beam data to understand the cosmic background). In each spill, MicroBooNE receives a trigger from the BNB. This opens up a window of time for which data is recorded. The window includes the a 1.6 ms span covering the beam spill ± 1.6 ms on each side totalling a 4.6 ms total readout window [34, 35].

While the beam triggers on with a rate of 5 Hz to correspond to the beam spills, a neutrino will only interact in about 1 out of every 500 beam spills. The optical trigger is needed to further reduced the saved data volume. The PMTs pick up scintillation light as discussed in Section 5.4. The appearance of this scintillation light is used as another trigger, the details of which are described in Section 6.1.

5.5.3 2D Deconvolution

The final step of data collection is to turn the LArTPC wire readout signal into the number of ionized electrons which passes through the wire planes at any given time. This process is described in detail in Ref. [36] and summarized here. The wire signal comes from not only measuring the charge of the ionized electrons, but from various detector effects such as the electric field and background noise. In order to get the signal from the electrons, deconvolution is used. Deconvolution is a technique to extract a real signal $S(t)$ (which in this case is the charge from the electrons) from a measured signal $M(t_0)$ which is the wire readout. $M(t_0)$ can be written as:

$$M(t_0) = \int_{-\infty}^{+\infty} R(t,t_0)S(t)dt \tag{5.1}$$

where $R(t,t_0)$ is a detector response function. This equation can be solved by a Fourier transform on both sides of the equation.

This works well for the collection plane. However, the induction planes are more complicated. Induction wire planes receive a signal both from electrons passing the wire in question, but also from nearby wires. Therefore in the induction planes a 2D deconvolution is used. In this case Eq. 5.1 is expanded to:

$$M_i(t_0) = \int_{-\infty}^{+\infty} (R_0(t-t_0)S_i(t) + R_1(t-t_0)S_{i+1}(t) + ...)dt \tag{5.2}$$

where S_i is the signal on wire i. This can again be solved with a Fourier transform.

Figure 5.11 shows an example of using 2D deconvolution on an induction plane signal. The image in the right panel is much clearer than the one on the left without any convolution. The 2D convolution process is used on all MicroBooNE data.

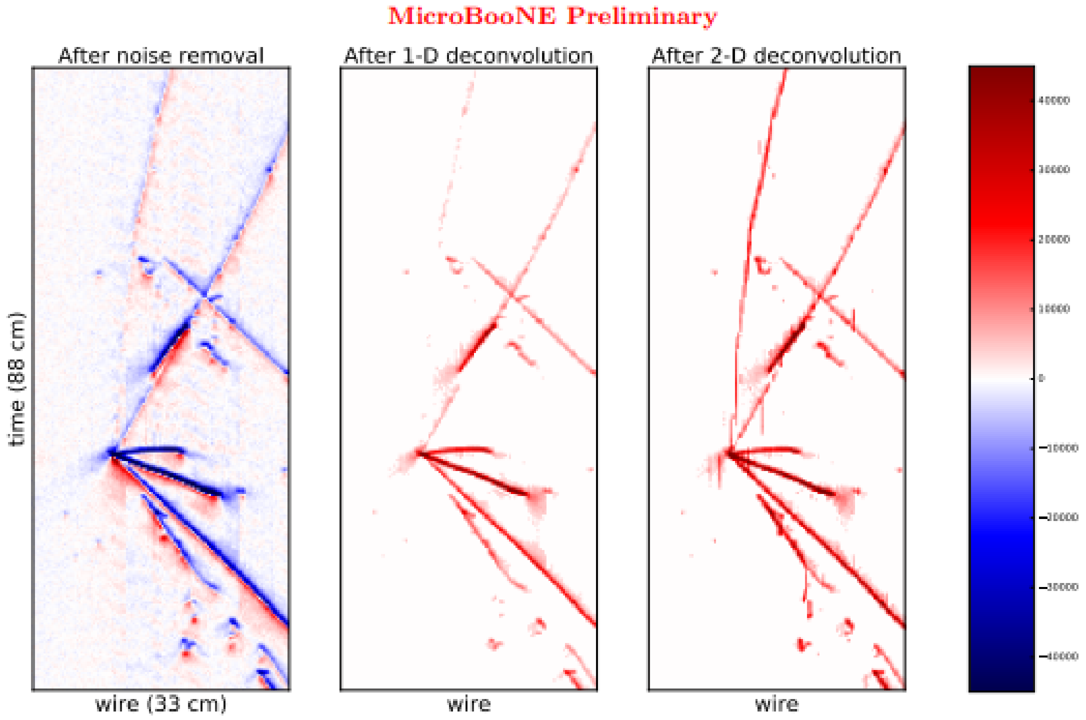

Figure 5.11: An example of 2D deconvolution on the U-plane. Run 3493, sub-run 821, event 41075. The y-axis is the time in ticks and x is the wire number. Adapted from Ref. [36].

5.6 MicroBooNE Data Collection

MicroBooNE began taking data from the BNB in February 2016 and stopped in March 2020. At this point operations were paused due to the global pandemic (though this was only slightly earlier than planned). After this point various other tests were run using the detector. Following these extra tests, the detector was shut down in October 2021.

Table 5.2 summarizes the BNB data taking Runs. Runs refers to the periods of time MicroBooNE was regularly taking beam data. In between these Runs, the detector collected off-beam data or underwent various upgrades such as the addition of the CRT system. Only Runs 1-3 are analyzed in this thesis as the other data has not yet been run through the reconstruction, calibration, and selection. This is simply due to processing time and resource constraints. Protons-on-target (POT) is the number of protons that interact with the beryllium target in the BNB and serves a measure of the beam flux.

Table 5.2: Description of the MicroBooNE Run Periods and the amount of POT delivered after collaboration wide data quality cut. Total good data POT = $12.263e20$

Run	Dates	Total Good POT
Run 1	Feb-Sep 2016	$1.813e20$
Run 2	Oct 2016 - Oct 2017	$3.051e20$
Run 3a	Oct-Nov 2017	$0.442e20$
Run 3b	Dec 2017 - Sep 2018	$2.226e20$
Run 4	Sep 2018 - July 2019	$3.367e20$
Run 5	July 2019 - Mar 2020	$1.365e20$

5.6.1 Blindness to Data

Throughout the development of the analysis presented here, blindness to the data was implemented. Blindness means that as the analysis tools are under construction, the data is not examined. This is to avoid biasing the analysis based on what the data is known to be. The order of the work performed is to first, verify all of the tools on simulation. Using this simulation and the amount of POT from the beam make decisions such as bin size and what methods to use to analyze agreement. Next, the machinery is tested in a variety of ways depending on the context. This may include looking at a small data set that is not large enough to draw conclusions from, analyzing fake data sets, or looking at sideband samples. A sideband is a data sample with different, but similar characteristics to the signal sample. Finally, the full data set is analyzed.

There were two major data un-blinding steps in this work. The first occurred after the reconstruction, selection, and systematic uncertainties were finalized. The purpose of this stage was to specifically look for the MiniBooNE low-energy excess. All of the 3+1 sterile neutrino oscillation framework was then developed and tested while once again being functionally blind (Chapter 12). Functionally blind here indicates that the author had seen the results of the comparison to the MiniBooNE low-energy excess in Ref. [37], but did not use the data in any algorithm until unblinding. The author, to the best of her ability, did not allow this preexisting knowledge to influence analysis choices. This was done by making choices using just the information from simulation and not data.

Chapter 6

The Deep Learning Reconstruction Chain

There are many steps needed to transform the wire pulses recorded in the LArTPC to the physics data about the neutrino interactions. This chapter describes the deep learning reconstruction chain used by this analysis. The chain uses a variety of deep learning tools and traditional algorithms. Figure 6.1 is a flow chart representation of this chain, the steps of which are described throughout the chapter in more detail. Event selection, discussed in Chapter 11, also contains deep learning elements.

6.1 Preparation of Data

The first steps of the reconstruction are common between MicroBooNE analyses. These steps are the common optical filter, good run selection, noise filtering, and signal processing. The common optical filter utilizes the PMT system. The light is collected in time intervals, or “time ticks”, of 15.625 ns. A minimum threshold of 3.5 photoelectrons detected in six time ticks ($\approx$ 100 ns) is first required to trigger and record events. The common optical filter threshold is applied, requiring > 20 photoelectrons detected within any 6 consecutive ticks in the beam spill window, and ≤ 20 photoelectrons detected within 6 ticks in the $2\,\mu s$ period prior to the

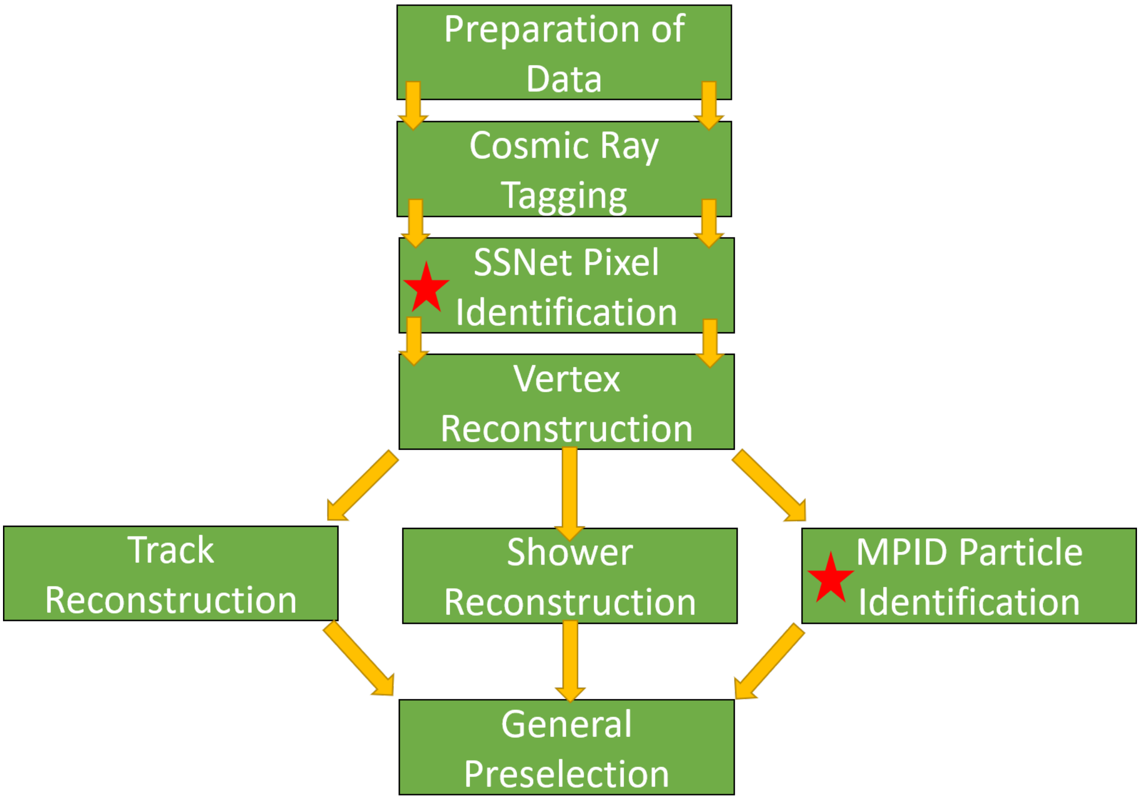

Figure 6.1: A flow chart illustrating the deep learning reconstruction chain. Steps with a red star are currently composed of deep learning tools.

beam window. This helps reduce non-neutrino triggers and is used in nearly all MicroBooNE analyses [38, 39].

The data used through this study was taken from 2016 to 2018 which were recorded over the first three Run periods shown in Table 5.2. Each Run Period contains a large number of smaller sub-runs which span a few hours. After each sub-run the quality is verified by a MicroBooNE shift monitor. The POT in this table is after the good run selection was applied. The good run selection is applied to the data to only originate from good sub-run periods, which are generally periods of good DAQ performance. Other reasons sub-runs may be cut include periods of low argon purity or other temporary detector issues.

Once the data is readout from the detector, it undergoes noise filtering which is discussed in detail in Reference [33]. This noise filtering is used on data for all analyses. The main sources of noise in the data are: low frequency noise from voltage regulator; noise from the HV power supply (which provides power to the cathode);

and 900 kHz burst noise which is expected to be caused by the PMT power supply. Various procedures are used to offset these noise sources.

The data next undergoes signal processing to transform it into images as described in References [40, 41] and summarized in Section 5.5.3. In this process, the raw digitized TPC waveform is converted to the number of ionization electrons passing through a wire plane at a given time. This information is then turned into 2D images representing the 3 different wire planes. The pixel intensity of the images is the integrated reconstructed charge waveforms over six time ticks and is measured in what is referred to here as PIU (pixel intensity units) which represents the amount of charge on a wire over the given time interval. The effective size of each pixel is 3.3 mm along the y-axis (time direction) and 3.0 mm along the x-axis (wire direction) of the image. The pixels have an intensity threshold applied to retain only the major topological features. As the distribution of pixel intensity originating from MIPs peaks at $\sim 40\,\text{PIU}$, a lower threshold of $10\,\text{PIU}$ is applied. Pixels with intensity ≤ 10 PIU are assigned a value of zero.

Next, simulated event samples are generated to compare the data to various physics models. In order to accurately describe the cosmic rays, noise, and unresponsive regions in the detector as a function of time in the simulation, the analysis overlays beam-off data taken throughout the three run periods onto simulated neutrino events. This creates the overlay simulation used throughout the analyses. These simulation samples are used both to test analysis tools and compare data to expectation.

Simulation of events is common throughout analyses performed in the MicroBooNE collaboration. For generating simulated events, the collaboration uses GENIE [42, 43, 44, 45] v3.00.06 and model set G18_10a_02_11a as the primary model. This generator utilized the Valencia CCQE and MEC (2p2h) models [46] and the Local Fermi Gas nuclear model. These were found to give a good description of the MiniBooNE CCQE-like data [47]. The generator also has an improved data-driven final state interaction model and a new tune to bubble chamber data for pion production. To further improve the description, the collaboration undertook a tuning effort utilizing the T2K ν_μ charged current, zero-pion data [48], which is fully described in Ref. [49]. This provides event weights which are referred to as central value, or CV, weights. The propagation of particles in the MicroBooNE detector is simulated using the Geant4 toolkit [50] V10.3.03c.

Events are simulated throughout the total volume of the detector, allowing particles produced upon interactions with argon outside of the active volume to enter it, where they may be mistakenly reconstructed as a neutrino interaction. However, the background rate from these events is found to be negligible at the end of the reconstruction and event selection. Therefore, we explicitly neglect external events in this analysis.

There are a variety of overlay sample types used in this study. These are outlined in Table 6.1 with their simulated POT (along with the data samples). The Data POT in this table is different than in Table 5.2, as this table is the POT of the data that is processed through the entire reconstruction chain. This is also true for the overlay samples. The first ("BNB" sample) is meant to simulate what is expected from the BNB neutrino beam for the set POT. Next there are a variety of specialized samples of uncommon event types in order to have a higher number of events to analyze and reduce the systematic uncertainty. These are "ν_e intrinsic" sample (ν_e events from intrinsic beam background), "CC π^0 " sample, and "NC π^0 " sample. Next there is a sample of just cosmic background events with no neutrino interaction that pass the common optical filter ("ExtBNB" sample). Finally, for the sterile neutrino part of this study a "fullosc" (full oscillation) sample was used. This sample assume that all ν_μ 's at a given POT oscillate into ν_e 's and is used to make oscillation spectra predictions in the case of a sterile neutrino's existence.

Figure 6.2 demonstrates an example of a simulated overlay event. This event is from the CC π^0 run3 simulation sample. This example was chosen as it has multiple particles in the final state of the neutrino interaction which provide a good use case for each reconstruction stage. As various stages throughout the chapter, this event

Table 6.1: The simulation samples used in this study along with the POT for each run. The Fullosc sample is only used in the sterile neutrino oscillation analysis.

	Run 1 POT	Run 2 POT	Run 3 POT
Full Data	1.63e20	2.75e20	2.29e20
Preliminary Data	4.8e19	-	-
BNB	1.34e21	1.30e21	8.88e20
ν_e intrinsic	1.16e23	9.21e22	4.71e22
CC π^0	6.95e20	-	5.92e20
NC π^0	2.90e21	-	2.49e21
ExtBNB	1.05e20	-	1.54e20
Fullosc	2.72e20	3.34e20	2.74e20

will be used as an example. The lower threshold of 10 PIU has been applied in this event image.

Table 6.1 also gives the POT of each type of sample for each run. When comparing to full data, events in a run of a sample are scaled to match the POT of the data. It has been found that Run 2 is very similar to Run 3 [37]. Therefore, due to computing restrictions and few events from these samples appearing in selections, Run3 CC π^0 , NC π^0 , and ExtBNB simulation samples are used to compare to Run 2 data. A sample of preliminary data is also included which is used to validate much of the analysis machinery which is intentionally small to maintain blindness to the full data.

6.2 Cosmic Ray Tagging

The next step of the reconstruction is removing cosmic rays from the data. While most are taken care of by the beam trigger (discussed in Chapter 5) and the common optical filter, cosmic rays concurrent with neutrino interactions still need to be removed. This is done using the Wire-cell charge-light matching algorithm [51, 52]. This algorithm matches charge clusters to flashes of scintillation light recorded by the PMTs. Any charge cluster mapped to optical flashes occurring outside the beam spill are tagged as cosmic. The pixels associated with these clusters are masked off at this point so they are not used in the next stages of reconstruction.

Figure 6.3 shows the effect of this cosmic ray removal on the Y-plane (collection plane) shown in Figure 6.2. To make the display easier to see, the maximum PIU in the image has been set to 100 PIU. It can be seen in the image that almost everything not coming from the neutrino interaction has been removed, though some small pieces of cosmic rays remain.

6.3 Track-like vs. Shower-like particles

As described in Section 5.3, as charged particles traverse a volume of liquid argon they leave a trail of ionized electrons behind which are collected by the wires. Different types of charged particles create a variety of patterns. The reconstruction methods are tuned to expect certain ionization patterns. Therefore, in this reconstruction process, these patterns are separated into two main types. The reconstruction of each particle type is described in more detail later in this Chapter.

The first type are track-like patterns. These are created by heavy charged particles including muons, protons, and charged pions. These particles move some distance though the argon, following a fairly straight path, or track. It generally begins at the neutrino interaction point (or outside the detector in the case of cosmic rays). It extends to the point where the particle does one or several of the following: loses all its energy; interacts again; decays; or exits the detector.

The second type are shower-like patterns. When a high-energy electron interacts in a medium it radiates a bremsstrahlung photon. These emitted photons can then produce an e^+e^- pair or Compton scatter to produce electrons. The same processes repeats again until all energy is deposited in the detector or the process exceeds the detector boundaries. This process forms a branching structure that is referred to as a shower. Reference [53] provides more details on shower characteristics. Figure 6.4 shows an example of how an electromagnetic shower develops.

6.4 SparseSSNet Pixel Identification

The U, V, and Y plane images (without the cosmic rays removed) are passed into a deep learning convolutional neural net, called “SparseSSnet,”which is a semantic segmentation algorithm that labels pixels based on the particle they are from [55]. The network was designed to distinguish pixels coming from track-like versus shower-like particles. SparseSSNet therefore separates the pixels in the data images as either track or shower pixels. This information is later used to separately reconstruct each particle type.

SparseSSNet has a U-ResNet architecture which is a combination of a U-Net [56] and a ResNet [57] architecture. It also makes use of sparse sub-manifold convolutions and sparse data structure. This allows for faster processing speeds with reduced memory usage. This is an improvement from the previous version of the network in Ref [58].

SparseSSNet outputs 5 pixel labels:

1. Heavily ionizing particles (HIP), produced by protons, typically manifest in a short, highly ionized track.
2. Minimum ionizing particles (MIP), produced by muons and charged pions, typically manifest in a longer, fainter (lower dE/dx) track.
3. Showers produced by electrons, positrons, and photons.
4. Delta rays produced from ejected atomic electrons from a hard scattering of other charged particles, mainly muons.
5. Michel electrons produced from a decay at rest of muons.

These labels are then reduced to ”track”(HIP + MIP) and ”shower”(showers + delta rays + Michel electrons) for use in this analysis. Track-like objects and shower-like objects have different topologies which require different reconstruction algorithms which are described in Section 6.6 and Section 6.7 respectively. Table 6.2, adapted from [55], shows the accuracy of SparseSSNet track and shower labels for the SparseSSNet test sample, the BNB overlay sample (primarily ν_μ events) and

Table 6.2: SparseSSNet's track and shower accuracy, for the test sample and the neutrino interaction central value simulation samples. Results are obtained from the collection plane. The number of pixels associated with each class is O(10^7) pixels except for the full-BNB shower which is O(10^5) [55].

	Test	Nue intrinsic	BNB
Track	0.992	0.992	0.998
Shower	0.996	0.859	0.823

the nue intrinsic sample (primarily ν_e events). The track pixel label has an accuracy of $> 99\%$, while the shower accuracy is $> 80\%$. This table is from Reference [55].

Figure 6.5 shows the result of running SparseSSNet on the same simulation events shown in Figure 6.3, but cropped around the neutrino interaction. The pixels labeled as track and shower can be clearly seen. A value of 2 in this image indicates a track, while a value of 1 indicates a shower pixel. Now by eye, it can be seen that this event appears to contain two showers (likely from a π^0 decay as will be discussed in Chapter 10) and three track-like particles.

6.5 Vertex Reconstruction

The next step is the reconstruction of neutrino interaction points, or vertices. Both the $1e1p$ and $1\mu1p$ events selected for this analysis have a topology of two prongs intersecting at the neutrino vertex. The $1e1p$ events consist of one track and one shower, while the $1\mu1p$ events consist of two tracks. The vertex finding algorithm has been optimized to find these topologies as described in detail in [59] and [60], and summarized here.

The vertex algorithm searches for a “vee” shape where two particles meet at a vertex. There are basic selection criteria in order for this algorithm to run which require that the two particles are longer than 3 cm and the opening angle in at least one plane is greater than 10°. Based on the SparseSSnet pixel tagging, the vee may be formed of a “track-track” pair or a “shower-track” pair, allowing for the different event topologies.

More than one vee may be found if there are more than two particles emitted from the interaction point or if cosmic background remains after tagging. This is taken care of in later event selection. Note that in data it is virtually impossible to have more than one neutrino interaction in a given event and in simulation there is only one interaction in each event by construction. Once candidate vertices are found, track and shower reconstruction occurs in two parallel algorithms.

6.6 Track Reconstruction

Track reconstruction is also discussed in detail in Reference [59] and summarized briefly here. The algorithm begins at the reconstructed vertex and follows ionization trails outward in 3D, clustering the pixels with non-zero charge into "prongs." A prong is a collection of continuous charge, either one line or connected branches as is the case for showers. Each prong is assumed to come from one particle. In order to associate a prong with the SparseSSnet identified pixels, the 3D prong is projected onto the 2D images described above. The pixels in this projection are then matched to the prong and each prong is labeled at track-like or shower-like. Shower-like prongs are reconstructed in a separate algorithm discussed in Section 6.7.

The kinetic energies of track-like prongs are calculated using the prong lengths. The direction of track-like particles is also reconstructed. In the case of two track-like prongs, the proton is defined as the prong with the higher average pixel-based ionization density. A fiducial volume containment requirement is enforced on all prongs. This requirement uses the distance of a prong from the edge of the detector as the minimal distance from all the prong's 3D points to a detector edge. It is required that either the distance of both prongs is $> 5\,\mathrm{cm}$ from the edge or else that the combined distance of both prongs is $> 15\,\mathrm{cm}$ from the edge.

6.7 Shower Reconstruction

The electromagnetic shower reconstruction algorithm is used to find any associated shower particles and reconstruct their kinetic energies once a candidate vertex is isolated. The method described here builds on a previous MicroBooNE shower reconstruction in Ref. [53]. The new algorithm retains many vital features of the previous version, especially the use of a semantic segmentation neural network for pixel labeling, but was rebuilt from scratch. Important updates have been added including many simplifications of the algorithm made possible by the improved SparseSSnet described in Sec. 6.4. The work described here was recently published in Reference [61]. Much of this paper and the algorithm it describes was written by the author of this thesis and is repeated here.

6.7.1 Clustering Algorithm

The first step of the reconstruction is to mask the image to only use the pixels identified as shower by SparseSSNet. Pixels with a shower score of >0.5, all other pixels are masked out for the rest of the shower reconstruction. This SparseSSNet masking is a critical step for showers close to or overlapping tracks to ensure only shower pixels are reconstructed.

A template isosceles triangle is placed with its apex at the reconstructed vertex position, pointing in the positive wire direction. The triangle is optimized to choose the shower direction, length, and opening angle for which the triangle contains the most pixels with non-zero charge. These parameters each start at the minimum value shown in Table 6.3. In order to allow for showers that are detached from the vertex, a gap parameter is introduced allowing the triangle to start further from the vertex.

Once a first shower candidate has been found by the reconstruction algorithm, the pixels found in the shower are masked out. If the total amount of PIU remaining passing the cuts of a shower score of >0.5 is $>$ 5000 PIU, the second shower algorithm is run on the masked image. The total range of allowed values for each of the template triangle parameters is shown in Table 6.3. In this table “first shower” refers to the shower found in the first pass of the shower reconstruction which is aimed at finding showers near the reconstructed vertex. “Second shower” refers to the shower found on the second run of the algorithm and has expanded parameters to search for detached showers. In almost every case the first shower is the highest energy of the two as the algorithm is optimized to find the one with the highest number of shower pixels with charge first. The parameters in each case are optimized sequentially in the order of direction, gap size, opening angle, and length.

Table 6.3: Range of parameters for the shower reconstruction algorithm. Parameters are changed in the second shower search to allow for the capture of showers detached from the vertex.

	Minimum value	Maximum value
Direction	0 degrees	360 degrees
Opening angle	17 degrees	75 degrees
Length (first shower)	3 cm	35 cm
Length (second shower)	3 cm	60 cm
Gap Size (first shower)	0 cm	17 cm
Gap Size (second shower)	0 cm	90 cm

Figure 6.6 shows an example display demonstrating the 2D shower reconstruction on a simulated CC π^0 event. This is the same event that is shown in Figures 6.3,6.5. The final optimized showers are shown in red (first shower) and magenta (second shower). In this example, the algorithm found the proper gap of the first shower, but not the second shower. This is acceptable as gap size is not a value that is currently utilized in any other part of the DL analysis.

6.7.2 Shower Energy Reconstruction

The next step is to reconstruct the energy of the shower particles. Energy reconstruction of electromagnetic showers is a crucial component of this analysis for the $1e1p$ selection, which contains electrons from a broad energy range from 35 to 1200 MeV. To determine the energy of each shower, the PIU of all shower pixels enclosed in the Y-view triangle is integrated. This total shower charge will hereby be denoted by Q_{sh}. The Y-view is used because it has the highest signal-to-noise ratio of the three planes as it is the collection plane [33].

To convert the charge to energy, the Q_{sh} in a sample of simulated events is compared to the generated energy of the electrons in the events. A Q_{sh}-to-MeV conversion is determined and shown in Figure 6.7. The simulated electron energy is plotted versus the reconstructed Y-view total shower charge sum for events in the intrinsic ν_e simulation sample selected by the $1e1p$ analysis preselection (which is discussed in Section 6.10). In each vertical bin, a Gaussian fit is performed to find the center point (represented by the black points in Figure 6.7). The edge bins which have smaller statistics are excluded.

Two examples of the Gaussian fits are shown in Fig 6.8. While the Gaussian fits capture the bulk of simulated events well, one can see a tail in each distribution out to higher simulated electron energies which is not captured by the Gaussian. This is expected, as these tails correspond to electron showers which are not fully reconstructed (i.e., showers which pass through dead wires, exit the active volume, or are larger than the shower parameters). The points are then fit to a line. This equation is used for the Q_{sh}-to-MeV conversion. The resulting equation is:

$$\text{Electron: } E \text{ [MeV]} = (1.26 \pm 0.01 \times 10^{-2}) \times Q_{sh} \text{ [PIU]}. \tag{6.1}$$

where the error corresponds to the uncertainty on the linear fit, which represents the statistical error on the simulated electron sample used for the fit. The conversion term of $1.26 \pm 0.01 \times 10^{-2}$ is referred to as m_{e^-} in this thesis.

Using this shower energy calculation, we look at the energy resolution for a sample of simulated CCQE ν_e events containing no final state π^0. This isolates electrons from photons which will be discussed further in Sec. 8.1.1. The following selection criteria are used for this energy resolution:

- Reconstructed vertex is less than 5 cm from simulated neutrino interaction vertex;
- One simulated electron contained in event;

- No simulated final state π^0;
- One reconstructed shower; and
- $1e1p$ Boosted Decision Tree (BDT) score is greater than 0.7 [34] (Chapter 11).

The energy resolution is defined here as:

$$E_{res} = \frac{E_{reco} - E_{sim}}{E_{sim}} \tag{6.2}$$

where E_{sim} is the energy simulated by GENIE. The energy resolution for this sample of simulated events is seen in Fig 6.9. The mean is at -0.07 and the RMS is 0.22.

The shower energy reconstruction has been validated in detail as shown in Chapter 8. As stated earlier, the shower energy is calculated using a MicroBooNE simulation sample comprising of simulated neutrino events overlay with off-beam cosmic ray data. It is therefore notable that the energy calculated with this sample works well when applied to data.

6.8 MPID Particle Identification

The final step in the reconstruction is the MPID network [62]. The MPID network aims to report the particle content of a given event. The input is a cropped image around a reconstructed neutrino vertex. The network structure is a typical convolutional neural network (CNN).

It outputs a score for each of five particle types (p,e^-,γ,μ^-,$\pi^\pm$) indicating how likely it is that the particle is in the event. As there is generally more than one particle in each event, the network outputs an individual score for each type. For example, a $1e1p$ event is expected to have both a proton and electron score close to 1. This network is utilized in separation of CC and NC π^0 events in Chapter 10. It is also used for the final cuts for the ν_e CCQE and ν_μ CCQE selections which will be discussed further in Chapter 11.

6.9 CCQE Neutrino Energy Reconstruction

Recall the target signal events for this oscillation ($1e1p$ and $1\mu 1p$ events) are CCQE. In principle these are a two-body interaction with fully constrained kinematics, even when realistic effects are introduced, assuming the target nucleon is at rest. For these events, energy and momentum conservation constraints allow the neutrino energy to be determined completely from the lepton energy and angle, the proton energy and scattering angle, or a combination of the final-state lepton and proton measurements.

The neutrino energy can be reconstructed in three ways:

$$E_\nu^{\text{range}} = \mathrm{K}_p + \mathrm{K}_\ell + M_\ell + M_p - (M_n - B), \tag{6.3}$$

$$E_\nu^{QE-p} = \left(\frac{1}{2}\right) \frac{2 \cdot (M_n - B) \cdot E_p - ((M_n - B)^2 + M_p^2 - M_\ell^2)}{(M_n - B) - E_p + \sqrt{(E_p^2 - M_p^2)} \cdot \cos\theta_p}, \tag{6.4}$$

$$E_\nu^{QE-\ell} = \left(\frac{1}{2}\right) \frac{2 \cdot (M_n - B) \cdot E_\ell - ((M_n - B)^2 + M_\ell^2 - M_p^2)}{(M_n - B) - E_\ell + \sqrt{(E_\ell^2 - M_\ell^2)} \cdot \cos\theta_\ell}, \tag{6.5}$$

where K is kinetic energy determined from the track length or charge clustered into the electromagnetic shower depending on the particle type; θ is measured with respect to the beam axis; M is mass; p is proton in nucleus; n is neutron in nucleus; and B is the average binding energy, assumed to be 40 MeV [63]. For the oscillation analysis presented in this thesis, the reconstructed neutrino energy used is $E_\nu \equiv E_\nu^{\text{range}}$ as in Equation 6.3. However, if a selected CCQE event is well reconstructed, the three energy calculation methods should be in agreement, within some variation due to unknown nuclear momentum. A consistency check of the three energy methods given by:

$$\Delta^{QE} = \sqrt{(E_\nu^{range} - E_\nu^{QE-p})^2 + (E_\nu^{range} - E_\nu^{QE-\ell})^2 + (E_\nu^{QE-\ell} - E_\nu^{QE-p})^2} \tag{6.6}$$

is a useful handle for the selection CCQE events and is used in the Boosted decision trees for both the $1e1p$ and $1\mu 1p$ event selection discussed in chapter 11.

6.10 General Preselection

The reconstructed objects describe here are next utilized in various event selections which will be described in more detail as they are used in the following chapters. However, some basic preselection criteria are first applied to data and simulation which are common between the selections.

First, a note on some jargon used throughout the rest of this thesis. An image is a 2D representation of of time vs. wire for a specific wire plane as described in Section 6.1. An event refers to a single neutrino interaction. The true vertex is the 3D point at which the neutrino interaction occurs. A reconstructed vertex is a 3D vertex found by the algorithm defined here.

When performing selections the target is a reconstructed vertex that is at a true neutrino interaction point of whatever interaction mode is under investigation. Therefore all selection requirements are placed on a reconstructed vertex and the reconstructed tracks and showers associated with it. Sometimes, the selection requirements will be satisfied by more than one vertex in an image. In this case a final requirement is placed to pick just one vertex. The requirement depends on the desired signal, but is used because it is extremely unlikely that two neutrino interactions occur in the same time window. Further, none of the simulation samples include such a scenario.

After the reconstruction is complete, there are a set of preselection criteria which are common between all selections. Some have already been described, but are repeated here for clarity. They include:

- common optical filter applied;
- part of a good run;
- at least one vertex;
- two reconstructed prongs at the vertex;
- the vertex is in the fiducial volume;
- the vertex is away from the edge of the active volume and outside of a dead-region in z located at $\sim 700\,\mathrm{cm}$;

- events are required to be "well-contained" in the active volume *i.e.* to not pass close to or across the edge of the active volume;
- an event must be "boostable" to the nucleon rest frame (i.e $0 < \beta < 1$ for the boost);
- electron kinetic energy > 35 MeV ($1e1p$ only);
- proton and kinetic energy > 50 MeV; and
- the proton cannot be backwards going relative to the beam direction.

Next, an "orthogonality cut" is used to divide the events into two non-overlapping $1l1p$ samples: $1e1p$ and $1\mu1p$. This makes use of the pixel labeling from SparseSSNet. The fraction of shower pixels for each of the two particles is calculated, and the maximum shower fraction for the two is found. The orthogonality cut uses the maximum shower fraction to separate $1e1p$ ($>$ 20% shower fraction) from $1\mu1p$ candidates ($<$ 20% shower fraction).

An additional containment cut is applied to the $1e1p$ sample that removes showers that are partially or fully located in a diagonal region of the detector with poor charge response. For the $1e1p$ sample, shower energy must be consistent between the three planes as defined by [37]:

$$\frac{\sqrt{(E_e^U - E_e^V)^2 + (E_e^U - E_e^Y)^2 + (E_e^V - E_e^Y)^2}}{E_e^Y} < 2 \tag{6.7}$$

6.11 The Total Reconstruction Chain

After all of the steps outlined in this chapter, the reconstructed data that will be used in the selection stage for each event consists of: neutrino interaction location, number of and type of prongs, kinematic variables for both track and shower particles, neutrino energy, and MPID scores. These events have all undergone a basic preselection which divides out candidates for the three different selections. Data which does not pass any of the preselection criteria is no longer considered.

Now that there is a clear picture of the general event reconstruction chain used in this analysis, a more in depth look at various aspects of the reconstruction is provided before proceeding on to the $1l1p$ event selection and its use in 3+1 sterile neutrino search. The next chapters review work by the author of this thesis searching for improvements, verifying parts of the reconstruction, and analyzing samples which are backgrounds to the main $1l1p$ event selection. Chapter 7 presents a deep learning neural network that was explored to reconstruct dead channels in MicroBooNE. Chapter 8 describes the verification of the shower reconstruction using selections of both π^0 events and Michel electron events. Then Chapter 10 examines the use of the same sample of a π^0 as a sideband to the 1l1p event selection.

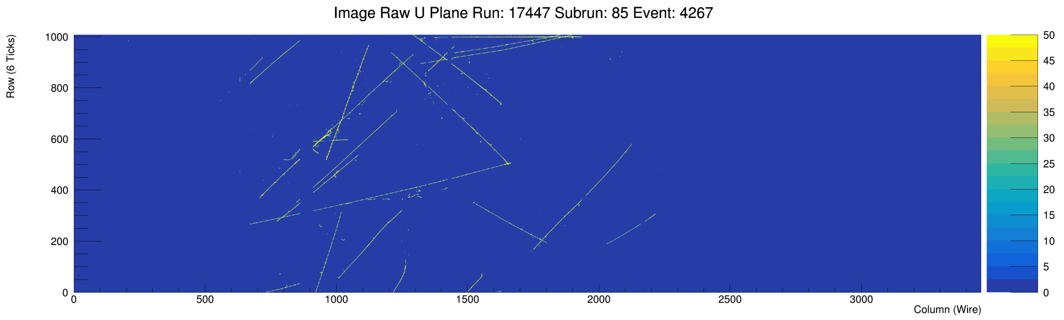

(a) U-Plane Image

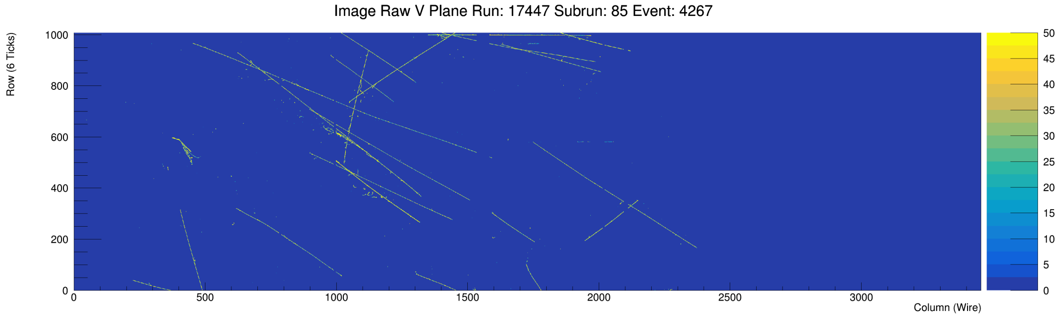

(b) V-Plane Image

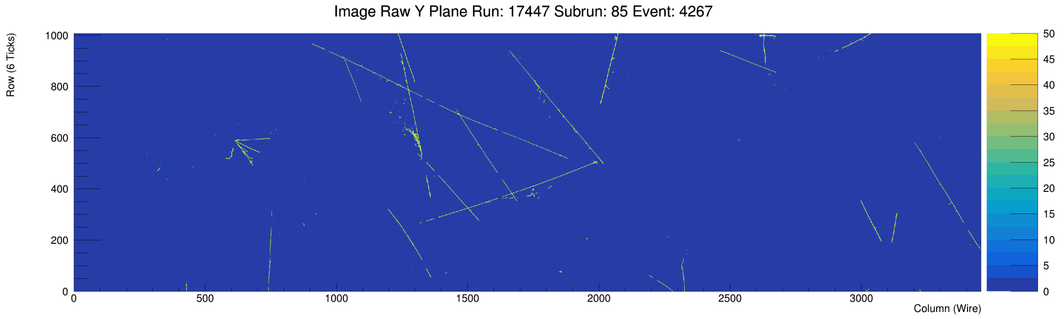

(c) Y-Plane Image

Figure 6.2: An example of a simulated overlay event at the start of the reconstruction chain in all three MicroBooNE wire planes. The x-axis corresponds to the wire number, the y-axis corresponds to time ticks, and the z-axis is PIU (capped at 50 for visualization purposes).

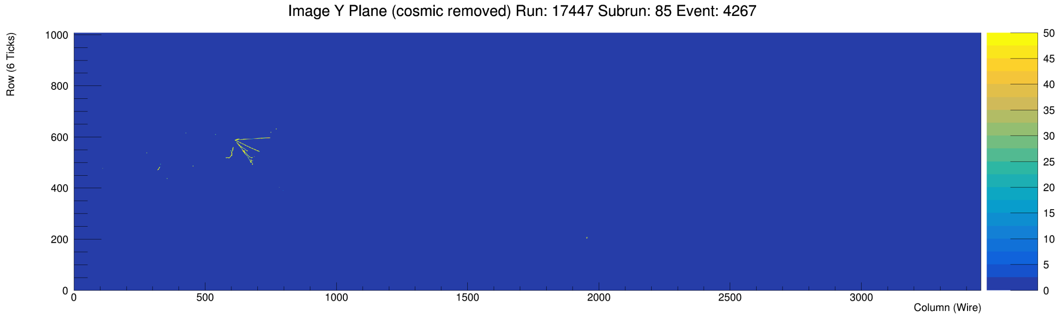

Figure 6.3: An example of a simulated overlay event in the collection plane after cosmic background has been removed. The x-axis corresponds to the wire number, the y-axis corresponds to time ticks, and the z-axis is PIU with a maximum of 50 PIU for visualization.

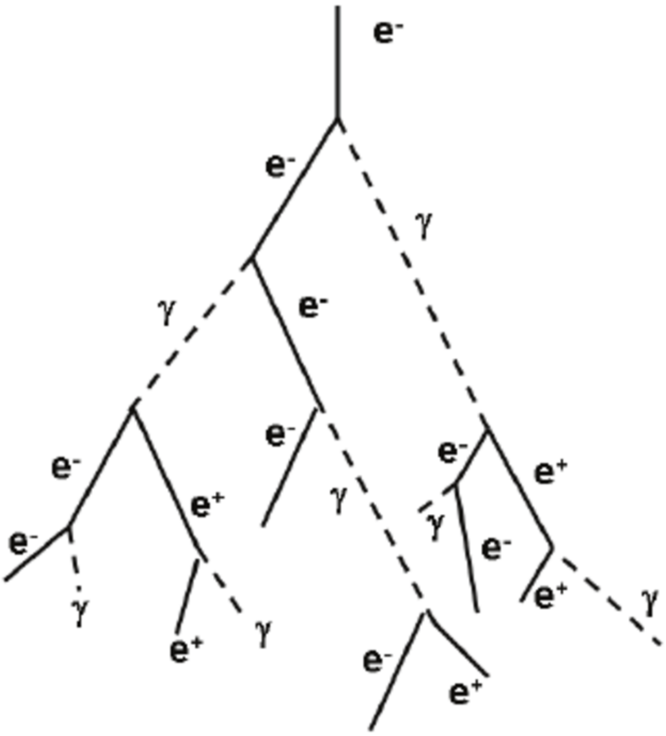

Figure 6.4: An example of an electromagnetic shower process. Adapted from Ref. [54].

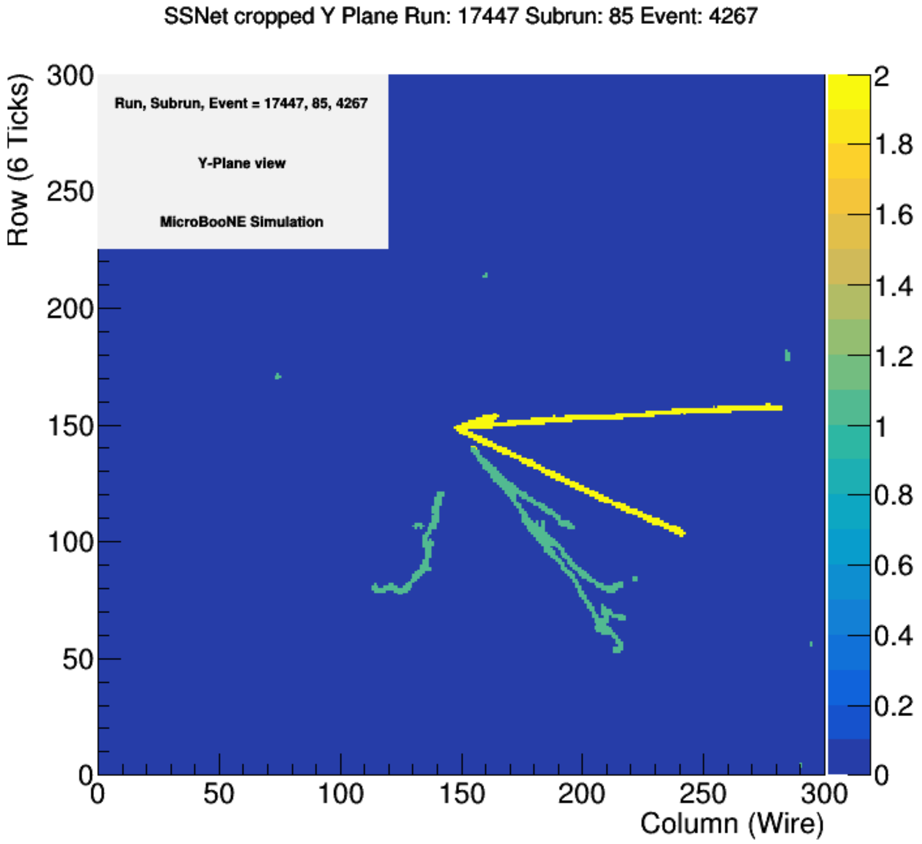

Figure 6.5: An example of a simulated overlay event in the collection plane after SSNet has been run. The x axis corresponds to the wire number, the y axis corresponds to time ticks, and the z axis is SSNet category. The image has been cropped to be around the simulated neutrino interaction.

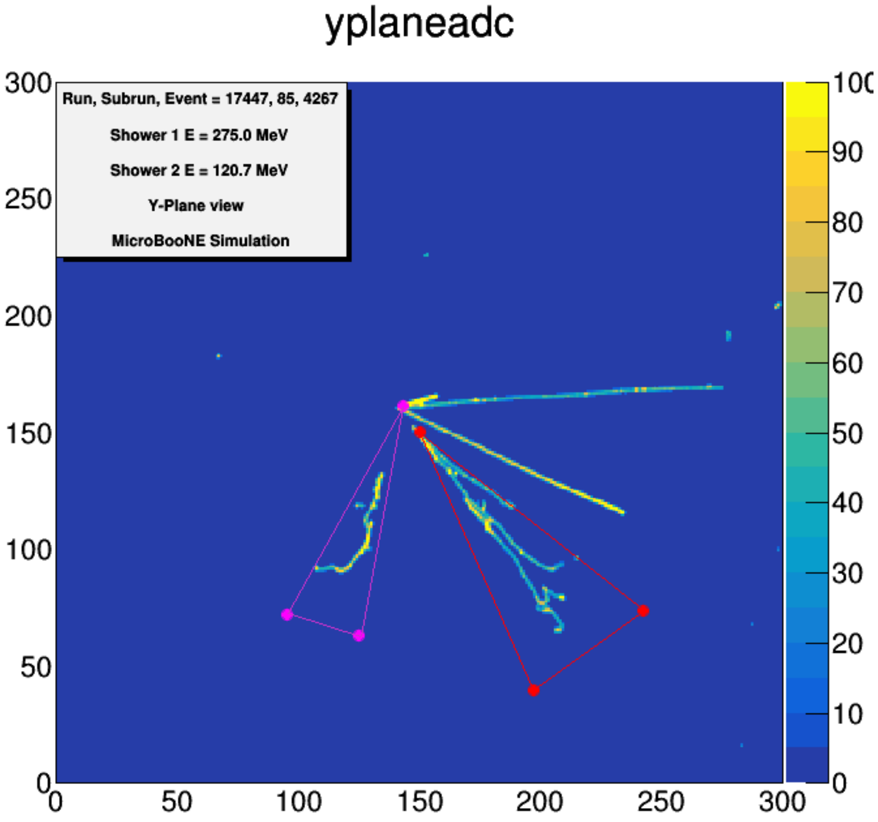

Figure 6.6: Event displays of a simulated CC π^0 event showing the raw PIU image. The leading reconstructed photon is represented by the red triangle and the subleading reconstructed photon is represented by the magenta triangle.

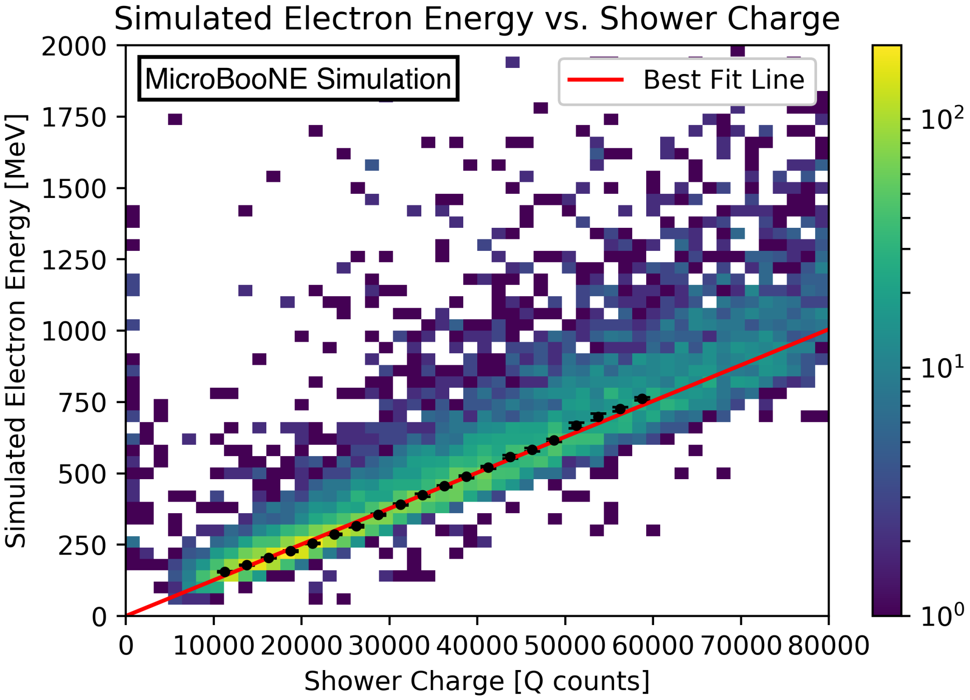

Figure 6.7: Simulated electron energy vs Q_{sh} for a sample of generated $1e1p$ events. The linear fit is used in the shower energy calculation.

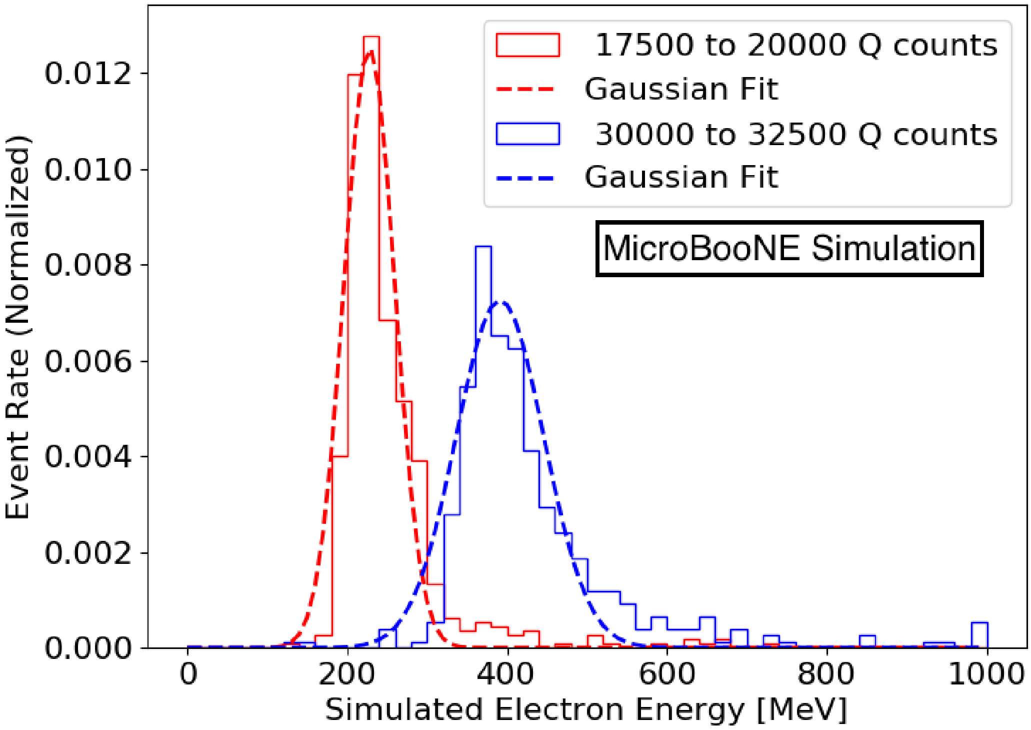

Figure 6.8: Example distributions of simulated electron energies (solid lines) and corresponding Gaussian fits (dashed lines) within two different shower charge sum ranges. The means of the Gaussian fits are used to generate the black points in Figure 6.7.

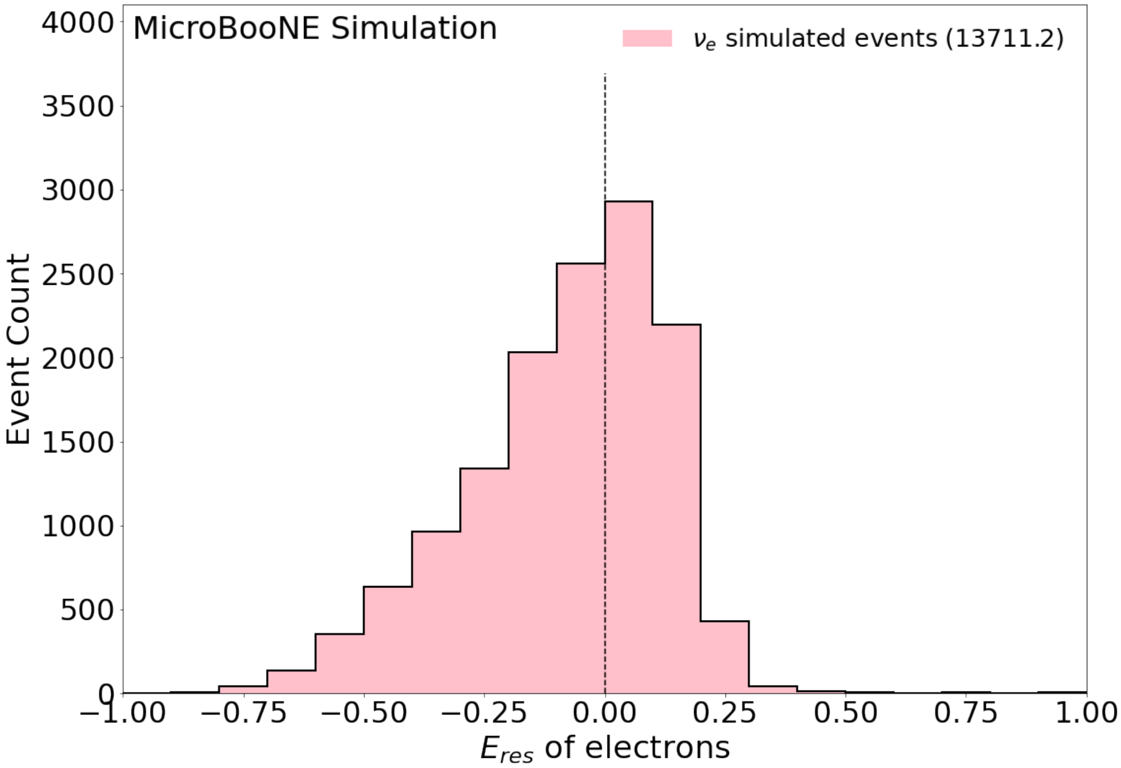

Figure 6.9: The energy resolution for a sample of simulated electrons as described by Equation 6.2. The y axis has the raw number of simulated events without scaling. The dashed vertical line is included at $E_{res} = 0.0$ for reference.

Chapter 7

Recovering Trajectories in Unresponsive Channels using a Convolutional Neural Network

Recall that MicroBooNE reads in data from 3 wire planes in a LArTPC. As presented in Section 5.5.1, these wire planes suffer from dead wires, oversaturated wires, and noisy wires. (For the purpose of this network, all of these categories in Table 5.1 are labeled as ”dead”.) To try to address the problem of these dead wires, a convolutional neural network (CNN) has been developed that recovers the trajectories of particles that pass through these wires.

Convolutional neural nets have been used in the field of deep learning to search for patterns in images and to alter images. This chapter presents the results for training a generative convolutional neural network, referred to as the “Infill” network, that reconstructs the PIU values in simulated dead wires for a LArTPC detector output. While the results of this network are not used in the rest of the analysis presented in this thesis, it shows that machine learning methods can be utilized to solve this problem. Future MicroBooNE analyses using more machine learning methods, as well as future LArTPC experiments, can make use of this fact.

7.1 Network Training Images

As discussed in Chapter 5 and summarized here, the MicroBooNE experiment contains three wire-readout planes (U,V,Y). Images are created for each of the three planes that show the amount of charge deposited on each wire in the plane over readout time window. The wire and time information is transformed into row and column number where the value of each pixel corresponds to the amount of charge deposited or PIU value. The operating status of each wire is known.

This network has been trained on data events rather than simulation. This is a great advantage as no simulation can perfectly model data. The Infill network's function is to reconstruct dead wires. By overlaying regions with no dead wires with "fake" dead wires, training on data instead of Monte Carlo simulation becomes feasible. This is beneficial when the network is deployed on data as it does not suffer any penalties due to inconsistencies between data and simulation.

The data for this network is prepared in the same way as the data that is fed into the deep learning reconstruction, but no further reconstruction is performed. This network is designed to be inserted at the start of the chain. The data samples used in this training are from a sample of off-beam data events ("ExtBNB" in Table 6.1). This means the events are unlikely to contain neutrino events and instead contain cosmic ray background. To create images necessary for training, a crop with no dead regions is taken from a full plane.

The crops have size 512x496 pixels. The width was chosen as the largest region of the U plane without any dead wires. The height was chosen to work well in the network structure ($512 = 2^9$, allowing for many decoding layers which decrease image size by a factor of 2). For consistency, crops from the other planes are the same size. This crop becomes the "true" PIU image needed for training.

To create the network input image with dead wires, the true image is overlay with a dead wire pattern from a different part of the plane. All PIU values in the specified wires are set to zero. This means that the dead channel pattern on the images is as realistic as possible. The network's main goal is to predict whether or not there should be non zero values in the dead wires, as this will aid in topological reconstruction methods. A secondary goal is to predict the PIU values that are as close to the true values as possible.

7.2 Sparse Network Structure

The network is a sparse network created using Facebook's SparseConvNet [64]. SparseConvNet makes use of submainfold convolutions in order to handle sparse data, or data with a large number of zero pixels like the MicroBooNE images. Submanifold convolutions are different from regular convolutions in that output features from non-active sites are discarded. In other words, an output pixel will be nonzero if and only if the central pixel of the convolved field is nonzero in the inputs. The sparseness of the data is therefore retained through a convolution, while a classic dense convolution will spread information to pixels which originally contained no information which leads to image dilation and an increase in memory usage. Similarly, activation functions, batch normalization, and pooling layers are restricted to active sites. In the case of the Infill network, active sites are pixels which either have non-zero PIU or are located in the dead regions.

The SparseConvNet operates on sparse data which only includes a subset of the pixels in the image. For the Infill network the pixels that are used are all non-zero pixels as well as pixels in dead wires. The input image and true image are transformed from 2D matrices to a sparse matrix of size Nx3, where N is the number of pixels saved. The first two columns represent the row an column value of the pixel. The third represents the PIU value. The network can only generate PIU values for pixels saved at this stage. This results in matrices with far fewer pixel values saved. In the U-plane, $\sim 40\%$ of values are kept. In the V and Y planes, which have fewer dead wires, $\sim 10\%$ of values are kept. However, these percentages vary wildly depending on how many dead wires are in a given cropped image as well as the number and energy of cosmic rays in the event.

Using a sparse network instead of a traditional dense network has two main

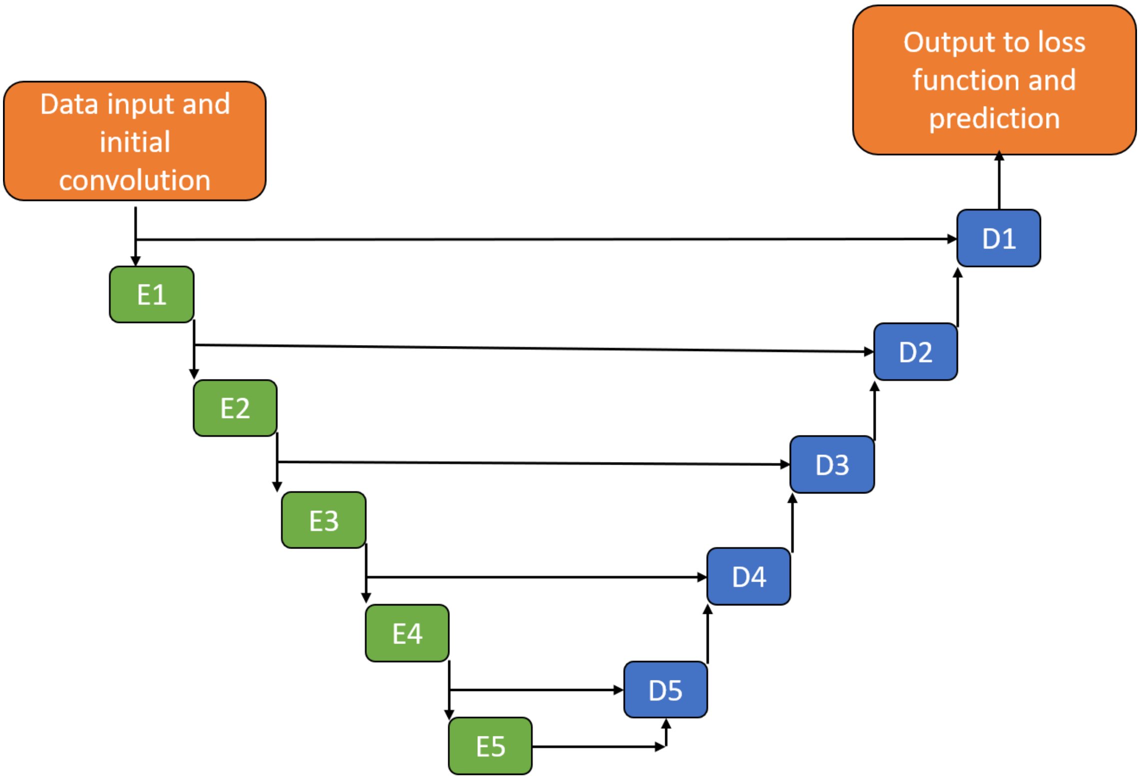

Figure 7.1: A flowchart illustrating the Infill network structure where E is an encoding layer and D is a decoding layer. The final output image has the same spatial dimensions as the original sparse image.

advantages. The sparse nature allows for faster processing speeds. In a previous dense version of this network, an image took 2 seconds to process on a GPU. With the sparse network the time has been reduced to 0.6 seconds. Secondly, each image takes up significantly less memory. This allows for larger batch size while training.

The Infill network is a UResNet structure consisting of five encoding layers and five decoding layers [56]. This is the same structure as SparseSSNet [55, 58], which was described in Section 6.4. A diagram of the network layers is shown in Figure 7.1. An encoding layer consists of 1/2 down-sampling and sparse ResNet convolutions, while the decoding layers consist of x2 up-sampling with sparse ResNet convolutions. The arrows in the flow chart represent connections between layers. The horizontal arrows in particular represent the concatenations that combine the outputs of the convolution layers from the encoding to the decoding side. The output is a sparse image with a generated PIU value at each location. It has the same spatial size as the input.

The loss function is an L1 loss with weights. This loss function gives a measure of how closely the output of the network matched the "true" image. There are five different weights utilized:

A: non-dead region,

B: pixels in dead wires with $0 <$ true PIU < 10;

C: pixels in dead wires with $10 <$ true PIU < 40;

D: pixels in dead wires with $40 <$ true PIU < 70;

E: pixels in dead wires with true PIU < 70.

The loss is then given by:

$$L = \frac{A|T_a - P_a|}{N_a} + \frac{B|T_b - P_b|}{N_b} + \frac{C|T_c - P_c|}{N_c} + \frac{D|T_d - P_d|}{N_d} + \frac{E|T_e - P_e|}{N_e} \tag{7.1}$$

where, A,B,C,D,E represent weights, T_i are the true PIU values for the category, P_i are the network predicted PIU value for the category, and N_i are the average number of pixel per image in the given category taken over 228 test images. Weights were adjusted during training in order to increase performance in the various pixel value classes. Classes (C) and (D) were given the highest weights as the network displayed a bias towards predicting PIU values on the extreme of the distribution.

The network uses the RMSProp optimizer function [65]. The learning rate was decreased as training progressed. The decision to lower the learning rate was based off of visual inspections of the loss function. When the loss leveled off, the learning rate was decreased.

7.3 Network Results

The network has been trained on a set of 160,000 crops for each plane of the detector. Each plane was trained independently. The U-plane was trained for three

Table 7.1: The accuracy when testing the network on 228 test crops for each plane, measuring how close the PIU of the output pixel is to the true value. The first four rows are measured only in dead wires and only where the true value is greater than zero. The last row is measured over the entire dead region.

	U-Plane	V-Plane	Y-Plane
< 2 PIU	27.24%	20.22%	25.20%
< 5 PIU	45.33%	37.36%	43.83%
< 10 PIU	66.82%	56.37%	66.73%
< 20 PIU	84.47%	75.14%	84.88%
Binary Accuracy	98.40%	99.13%	99.16%

epochs, the V-plane for three epochs, and the Y-plane for four epochs. (In one epoch, the network sees each training image once). Results from deploying the network on 228 cropped images (test sample) for each plane which it had not encountered in training are shown in Table 7.1. The test sample is a set of images not used in training. Testing over previously unseen examples ensures that the network is not simply memorizing the training set.

For each plane, the accuracy is calculated for various thresholds for pixels in the dead wires where the true PIU value is greater than zero. To better understand the impact of the PIU scale, the process of MicroBooNE shower reconstruction can be used. As discussed, in Section 6.7 a shower's energy is reconstructed from the total PIU of the shower object. This PIU is then converted to an energy using a scale factor of 0.01256 MeV/PIU in Eq. (6.1). This means that 20 PIU in a shower object corresponds to 0.2512 MeV of deposited energy. So, even the largest range in the accuracy table results in a small change in energy.

Additionally, a binary accuracy is calculated in the dead wires based on whether or not the network placed either less than ten PIU or greater than ten PIU charge correctly. (Ten PIU is chosen because anything less is removed from the final reconstruction techniques in Section 6.1). As seen in the binary accuracy of Table.7.1, the network fairly accurately places PIU charge over threshold where there should be charge, while not adding charge where there should not be charge.

Figure 7.2 shows the comparison between the true PIU value and the value predicted by the network. Each pixel contained in a dead region with non-zero true PIU has been plotted. The histogram contains the results from the entire test sample. A red line representing y=x has been included for visual comparison. It should be noted that the final images have thresholds of 10 PIU, so large differences for PIU less than 10 will have no impact on the final product.

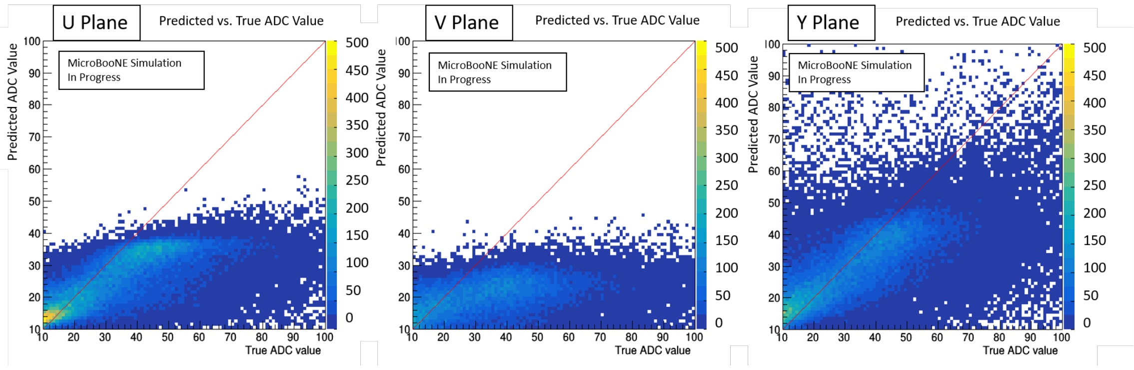

Figure 7.2: The results of running the network on the test sample, for each of the three planes. The predicted PIU value vs. the true PIU value is shown for each pixel in the dead channel. The red line represents y=x for reference.

Figure 7.3 shows the PIU distribution for both the set of true test images and the set of corresponding network outputs. Once again, only pixels in the dead wires are plotted. Both of these figures show the best performance in the y-plane. This plane begins with the best signal quality and is the main plane used in the DL reconstruction chain described in Chapter 6.

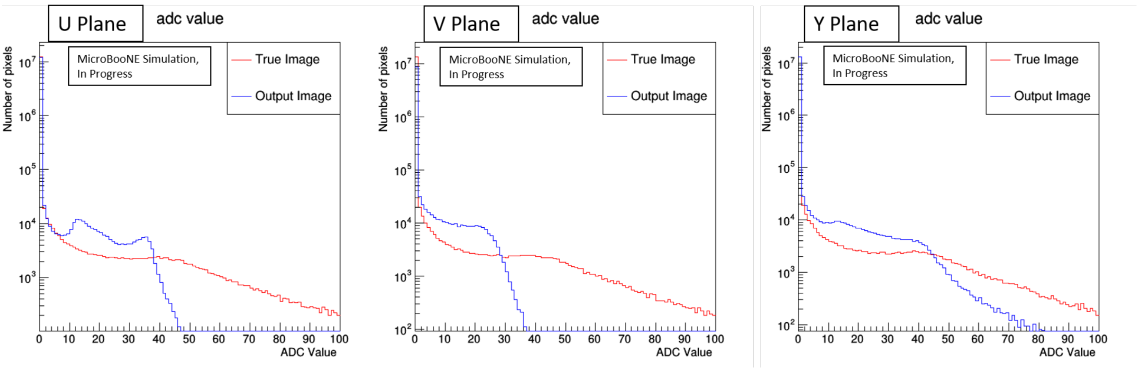

Figure 7.3: This set of figures shows the PIU distributions for the test crops in each of the three planes (note ADC = PIU). The distributions of both the true image and the network output image are shown. The PIU distribution is plotted only for the dead wires.

Once an image is fed into the network, the output is overlaid on the input image, but only in the dead wires. This ensures that the network does not alter non-dead regions. The entire image has a threshold of 10 PIU. This output image is then passed into the other networks in the chain. Figure 7.4 shows event displays for each plane corresponding to the network input image, network output image, and true image. As in previous event displays in Chapter 6, the x-axis of these images is the wire direction and the y-axis is the time dimension. The pixel value corresponds to the the PIU (or predicted PIU).

Overall, the network performs well when placing non-zero PIU. This should be helpful as inputs for other reconstruction algorithms that are primarily topology based. However, the accuracy in generating the precise PIU is too low to use this network in applications requiring an accurate PIU (i.e. in shower energy calculations).

7.4 Future Applications

The Infill network has not yet been incorporated into the total reconstruction chain. However, it is a demonstrated deep-learning solution for a hardware problem. Future LArTPC experiments may encounter a similar problem. If that occurs, the network structure could be used with a different data set as one possible solution.

Due to computing resource restriction it has not yet been run over the full MicroBooNE simulation and data. A new and improved second generation reconstruction is currently under development. The Infill network is one possible step that is under consideration for the next generation of tools.

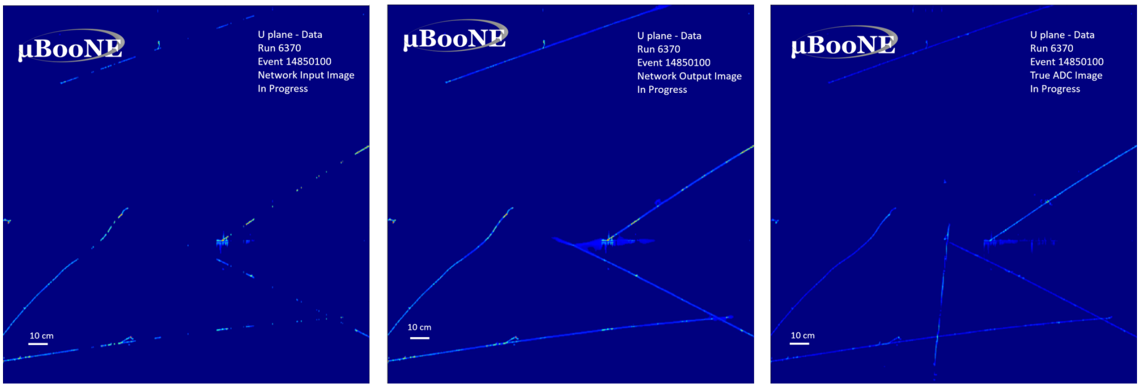

(a) U-plane

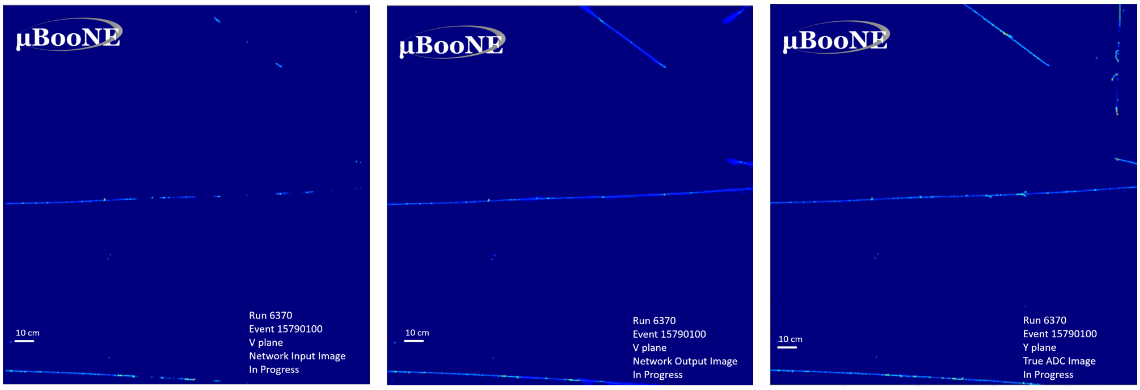

(b) V-plane

(c) Y-plane

Figure 7.4: This figure shows an example set of event displays from the U-plane (a), V-plane (b), and Y-plane(c). The first image is the network input image with dead wires. The second image is the Infill output image after thresholds are applied and after being overlay with the network image. The third image is the true PIU image for reference.

Chapter 8

Verification of Shower Energy Reconstruction on Data

The next reconstruction step that was examined in more detail by the author of this thesis is the shower energy calculation discussed in Section 6.7.2. Shower reconstruction is a critical part of reconstructing the CCQE $1e1p$ events utilized in this analysis. Extensive work was performed to ensure the validity of using the simulation-derived energy calculation. Note that as with the shower reconstruction, the work described here was recently published in Reference [61]. Much of this paper and the algorithm it describes was written by the author of this thesis and is repeated and adapted here.

To verify this shower energy calculation, two event selections have been used. The first is a selection of π^0 events described in Section 8.1. The second is a selection of Michel electrons in neutrino events described in Section 8.2. For each of these selections a best fit PIU-to-energy conversion value is found for both simulation and data. Section 8.3 combines these results and shows that the use of the simulation-derived energy calculation is valid.

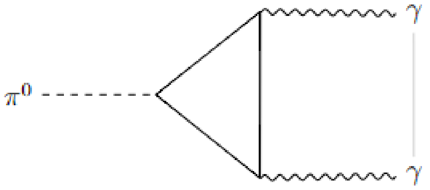

Figure 8.1: The dominant Feynman diagram describing $\pi^0 - > 2\gamma$.

8.1 The π^0 Sideband Sample

The first sample used to analyze the performance of the shower reconstruction is a sample of π^0 events which decays into two photons as shown in Figure 8.1. The π^0 interactions are discussed in more detail as a sideband to the $1l1p$ events in Chapter 10.

The selection of this sample includes the preselection common across all of the event selections utilizing this reconstruction chain that was presented in Section 6.10. The reconstruction chain was not optimized to reconstruct every possible event containing a π^0 . The events selected here must start from the two-prong vertices. Therefore, the bulk of π^0 events selected for this analysis are one of two topologies. The most prevalent topology in this study is from charge current (CC)π^0 events where the scattered muon and the proton from the Δ decay form the vertex, and there are two additional disconnected electromagnetic showers from π^0 decays. The second is from neutral current (NC)π^0 where one photon converted within the 0.3 cm wire spacing and thus forms can form a reconstructed vertex proton, while the second photon is displaced from the vertex. As a result, contributions to the π^0 selection discussed here will come from NC π^0 and CC π^0 , as well as CCπ^- and CCπ^+ events where the π^+/π^- undergoes charge exchange within the nucleus. The π^0 itself is invisible in the MicroBooNE detector as it is electrically neutral. However it then decays into two photons. These photons can produce an e^+e^- pair or Compton scatter which produces showers. From these photons the momentum and energy of the π^0 can be reconstructed.

The identification and reconstruction of π^0 events is presented here. This is followed by both a verification of the Q_{sh}-to-MeV conversion value agreement to data and simulation, and a verification of agreement between data and simulation. Recall Q_{sh} represents the PIU sum of the SparseSSNet tagged shower pixels enclosed in the reconstructed shower. This is accomplished by using a well-measured physical quantity: the π^0 invariant mass (135 MeV/c^2 [6]).

8.1.1 π^0 Event Selection

Before proceeding to event selection, an extra reconstruction step is needed for events with a π^0 . The reconstruction of π^0 events relies on the 2D shower reconstruction described in Section 6.7. For this study, this is extended by introducing a simple 3D shower reconstruction. This is necessary to reconstruct the 3D direction and therefore the kinematics of the π^0 event. These quantities are essential for reconstructing the π^0 invariant mass which is used to test the shower reconstruction.

In order to characterize a full 3D shower, 2 2D projections on different planes that match in time are needed. So, the 2D reconstructed showers on the different wire planes are compared for overlap in time. The overlap fraction is defined as:

$$F_{overlap} = \frac{N_{overlap}}{N_{tot}} \tag{8.1}$$

where $N_{overlap}$ is the number of pixels in the Y-plane shower that overlap in time with shower pixels from a 2D shower in another plane and N_{tot} is the number of pixels in the Y-plane shower. The U and V planes are considered separately. If the overlap fraction is > 0.5 in either or both planes, the pixels that overlap between the collection plane shower and the shower in another plane with the highest overlap fraction are used to calculate a cluster of 3D shower points. The 3D shower direction is found by using the calculated center of the 3D point cluster and the event vertex.

This 3D reconstruction leads to what is referred to as the “shower quality cuts”. These are requirements that are necessary in order to reconstruct two 3D showers for the π^0 selection.

- Two collection plane showers, each with reconstructed energy greater than 35 MeV;
- Both collection plane showers have an overlap fraction with a shower in another plane greater than 0.5; and
- The two collection plane showers cannot match to the same shower in another plane.

If a collection plane shower matches with showers in both the U and V planes, the one with the highest overlap fraction is chosen.

After the preselection (described in Section 6.10) and shower quality cuts have been applied, some of the remaining events have showers that are poorly reconstructed. The sample also contains a large number of backgrounds such as cosmic muons. To improve the selection, the following requirements are introduced that remove events with poor reconstruction and remove backgrounds. These are referred to as "box cuts" as they are hard cuts designed to remove background events at the tails of the distributions of various variables.

One of the variables used in these "box cuts" is a Δ mass test variable and requires a bit more calculation than others to obtain. The 4-vector of the reconstructed showers are used along with the 4-vector of the proton-like track as described in section 6.6. These three objects are assumed to have come from a Δ decay and are therefore used to reconstruct a Δ rest mass. The tails of this distribution are comprised of poorly reconstructed π^0 events and cosmic muon backgrounds which allows for another box cut. The box cuts are performed at a vertex level and are defined to be:

- Reconstructed π^0 mass is less than 400 MeV/c^2;
- Reconstructed energy of the leading photon is greater than 80 MeV/c^2;
- The charge sum of all pixels (both track and shower) within 2 cm of the vertex $>$ 250 PIU counts;
- Leading photon reconstructed angle w.r.t. beam direction $<$ 1.5 radians;
- The angle between the two photons $<$ 2.5 radians; and

- Δ mass test variable is between 1000 and 1400 MeV.

Figure 8.2 shows the distributions from which these cuts were chosen. These distributions of box-cut variables are made at the preselection stage which were used to determine the π^0 box cuts. These distributions are compared to the preliminary data sample (Table 6.1) as this was used to make the cut decisions. The cut values are indicated with dashed black lines. These plots only contain statistical error. The main backgrounds these sought to remove were cosmic rays (bright pink) and mis-reconstructed π^0 events (dark green). The well reconstructed π^0 events are in light green (CC π^0) and light blue (NC π^0).

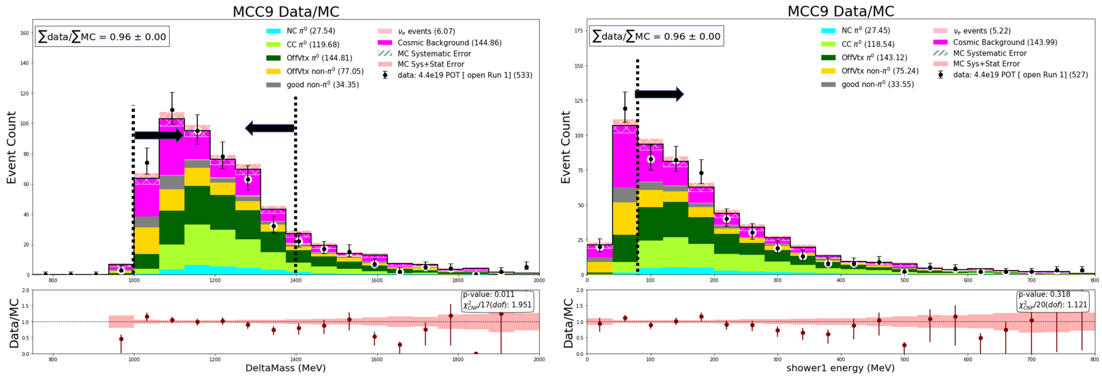

(a) π^0 Mass $[MeV/c^2]$ (b) Leading E_γ $[MeV/c^2]$

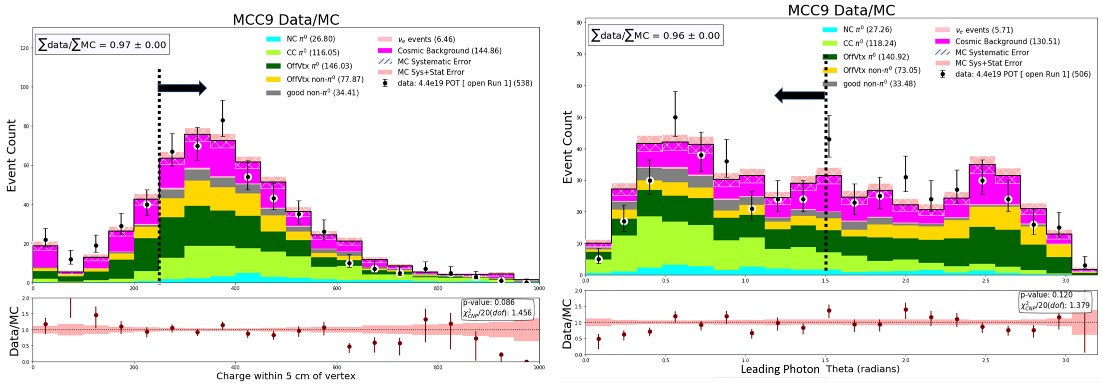

(c) PIU sum around vertex (d) Leading θ_γ [rad]

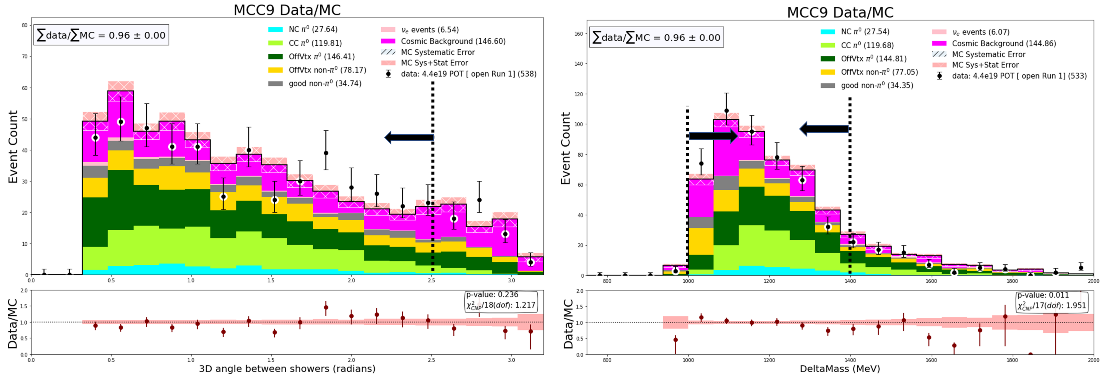

(e) γ Opening Angle [rad] (f) Δ Mass $[MeV/c^2]$

Figure 8.2: Kinematic distributions at the preselection stage for preliminary data for variables used in the π^0 box cuts. The error bars are statistical only. The black dashed line indicates the cut value. The black arrow indicates the side of the cut that is kept. The simulation has been scaled to match the preliminary data POT.

Here, “leading photon” refers to the simulated photon with the highest energy. The reconstructed “leading photon” is determined to be the shower with the highest PIU sum. An additional requirement on the DL 1e1p BDT of < 0.7 is further added at this stage to maintain blindness to the LEE for this study as was described in Section 5.6.1 [34]. This requirement has a flat $\approx 3\%$ effect across the energy spectrum. The effect of this cut is shown in Figure 8.3. As shown in the plot, the cut removes very few events. If more than one reconstructed vertex remains at this point, the vertex with the highest leading-photon energy is chosen.

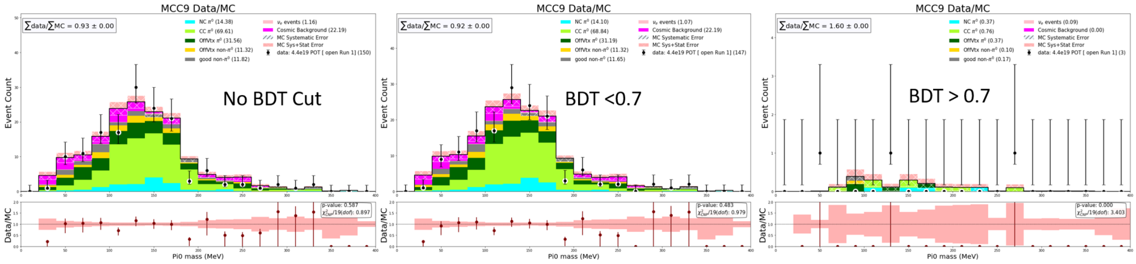

Figure 8.3: The π^0 mass distribution of the preliminary data with three versions: no 1e1p BDT cut, 1e1p BDT < 0.7 (used in analysis), and 1e1p BDT > 0.7. All other π^0 "box-cuts" have been applied.

The efficiency of each cut stage is seen in Figure 8.4. A sample of events with a true π^0 in the final state, the neutrino vertex in the fiducial volume, and with both decay showers starting in the fiducial volume is used to test the efficiency. The numerator is the number of events remaining after each cut stage. The efficiency is shown as a function of the simulated neutrino energy. The biggest drop in efficiency just comes from finding a vertex with one reconstructed shower. This is because the vertex finding algorithm was not designed with π^0 events as the primary target.

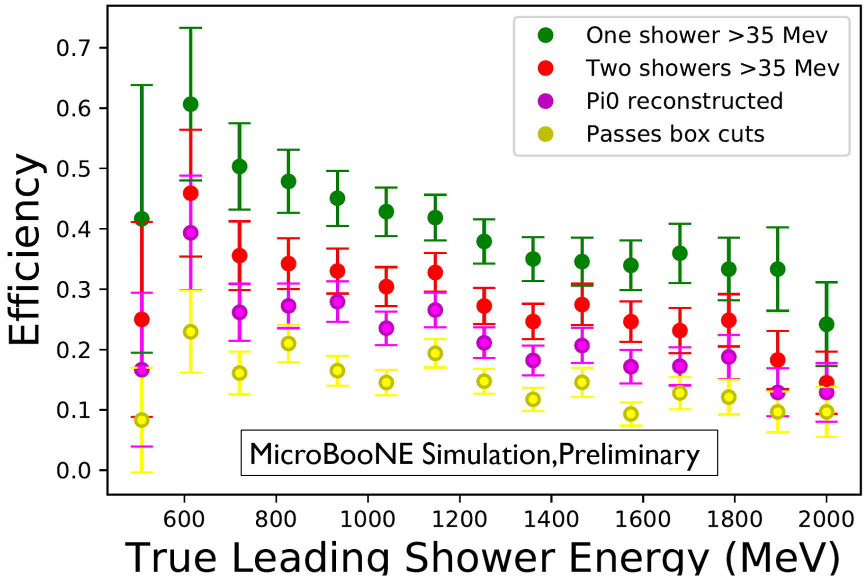

Figure 8.4: The efficiency of the π^0 selection at various cut stages.

For the purpose of studying this sample in the next sections, the simulation has been broken into various categories. “NC π^0 ” are neutral current π^0 events with a well reconstructed vertex, which is a vertex within 5 cm of the true generated vertex. “CC π^0 ” are defined similarly for charged current π^0 .“Offvtx π^0 ” are π^0 events with poorly reconstructed vertices. The reconstructed vertex is further than 5 cm from a true generated neutrino vertex (often placed instead at a shower start). If the vertex is in the wrong position, the 3D shower directions of both showers cannot be trusted, nor any quantities built from these. “Non π^0 ” events are broken into on and off vertex as well. ν_e events are all events that originated from a ν_e . Cosmic background events also remain after selection. In some discussions the exact type of background is not necessary to differentiate. In these cases all events without a π^0 in the final state are simply referred to as “background”.

8.1.2 Decay Photon Energy Reconstruction

Using the shower energy calculation from the electron sample on both electron and photon showers assumes that the energy of both shower types is reconstructed the same way. To demonstrate that this assumption is valid, the same simulated energy vs Q_{sh} plot and fit (as was used in Section 6.7.2) is performed on two samples of photons: leading and sub-leading photons from a sample of simulated CCπ^0 events. To ensure this fit is performed only over well-reconstructed events, the π^0 box cuts are applied. This is shown in Figure 8.5. The resulting fit equations are:

$$\text{Leading Photon: } E\ [\text{MeV}] = (1.25 \pm 0.02 \times 10^{-2}) \times Q_{sh}\ [\text{PIU}]. \tag{8.2}$$

$$\text{Sub-leading Photon: } E\ [\text{MeV}] = (1.20 \pm 0.02 \times 10^{-2}) \times Q_{sh}\ [\text{PIU}]. \tag{8.3}$$

It is seen from the fit results that the leading photon fit matches the electron fit as expected while the sub-leading photon fit does not match as within the statistical error. This is due to the worse reconstruction in the sub-leading photon. However it is a difference of $< 6\%$ which is well below the energy resolution for both electrons (shown Figure 6.9) and photons (shown in Figure 8.6). The energy reconstruction

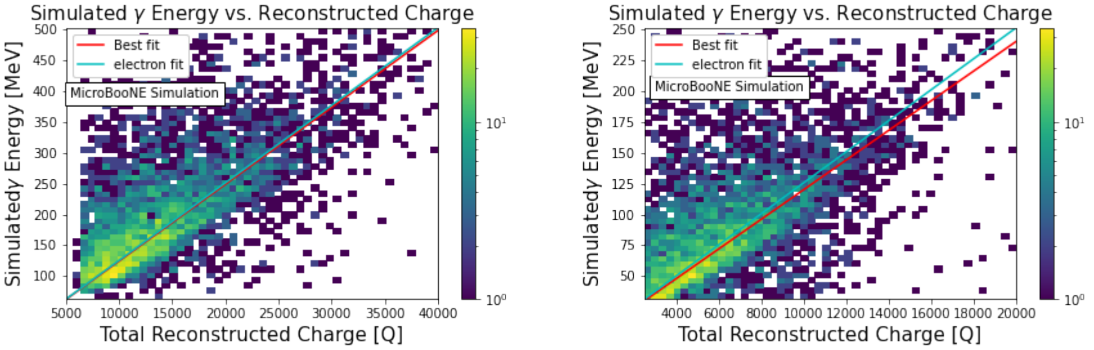

(a) Leading Photon (b) Sub-leading Photon

Figure 8.5: Simulated photon energy vs Q_{sh} for a sample of generated CC π^0 events with the π^0 box-cuts applied. The best fit is shown for this sample as well as the best fit from the electron fit. (a): leading photon, (b): sub-leading photon.

of all showers therefore uses the charge-to-energy (Q_{sh}-to-MeV) conversion value found for the simulation electron sample, $m_{e^-} = 1.26 \times 10^{-2}\ MeV/PIU$.

Simulated energy resolution of the decay photons is presented in Figure 8.6, where resolution is defined in Eq. 6.2. This plot is made using the specialized high POT CCπ^0 and NCπ^0 simulation samples. For the purpose of scaling the different samples and background contributions, the events are POT scaled to match the total data POT. This distributions in this plot have all of the π^0 selection cuts applied. The energy resolution is shown separately for the leading (highest energy) photon and sub-leading photon.

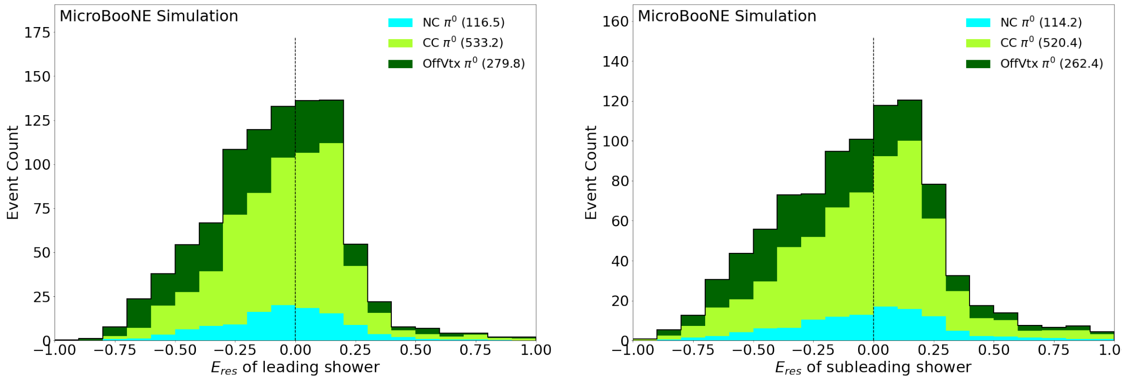

(a) Leading Photon (b) Sub-leading Photon

Figure 8.6: The energy resolution for each of the decay photon in the selected π^0 sample. The leading photon is shown in (a) and the sub-leading photon is shown in (b). The events have been scaled to match the total data POT of 6.67×10^{20}. Resolution is defined in Eq. 6.2. The dashed vertical line is included at $E_{res} = 0.0$ for reference.

Table 8.1 shows the mean and RMS of the distributions shown in Figures 8.6 and 6.9 for comparison. Both the leading and sub-leading photon E_{res} mean is close to zero for all samples. The leading photon has a smaller RMS than the sub-leading photon, which is more broad and has a larger tail. The resolution of photon energy from π^0 decay is worse than that seen in the electrons, but they have similar bias as indicated by the mean.

There are two main causes for the difference between leading and sub-leading photons. The first is that the sub-leading photon is generally the lower energy of the two. Failing to reconstruct a small number of pixels will have a larger effect on a lower energy shower which has fewer true shower pixels associated with it. The other cause are events where the leading and sub-leading shower are close together. Part of the sub-leading shower is reconstructed as part of the other shower as the leading shower is prioritized. Of these two sub-leading photon reconstruction failure modes, the first is dominant. Some of the other poorly reconstructed photons in both the leading and sub-leading plot are caused by mistakes in SparseSSNet, overlapping cosmic rays that were not removed properly, and dead wires in the collection plane. These common mistakes also effect electron reconstruction.

Table 8.1: Characterization of the resolution distributions shown in Figure 6.9, Figure 8.6, and Figure 8.8 .

	Mean E_{sim}	Mean E_{res}	RMS of E_{res}
Electron	744.8 MeV	-0.07	0.22
Leading Photon	230.3 MeV	-0.07	0.36
Sub-leading Photon	98.8 MeV	0.04	0.69
	Mean θ_{sim}	Mean θ_{res}	RMS of θ_{res}
Between two photons	54.1°	0.05	0.50

Figure 8.7 shows a data to MC simulation comparison of the reconstructed photon energies in the π^0 sample. The uncertainty bars on the simulation distribution represent the statistical uncertainty based on the number of simulated events. The total number of simulation events has been scaled to match the total number of data events for this chapter to remove any effect due to π^0 rate modeling. This a notoriously difficult problem and will be discussed further in Chapter 10 . This

plot uses the BNB simulation samples combined with the high POT π^0 simulation samples and the ν_e intrinsic sample, and data as described in Section 6.1. The χ^2 which is reported in the caption of this plot is a combined Neumann-Pearson (CNP) χ^2 [27] which is discussed in great detail in Chapter 12.

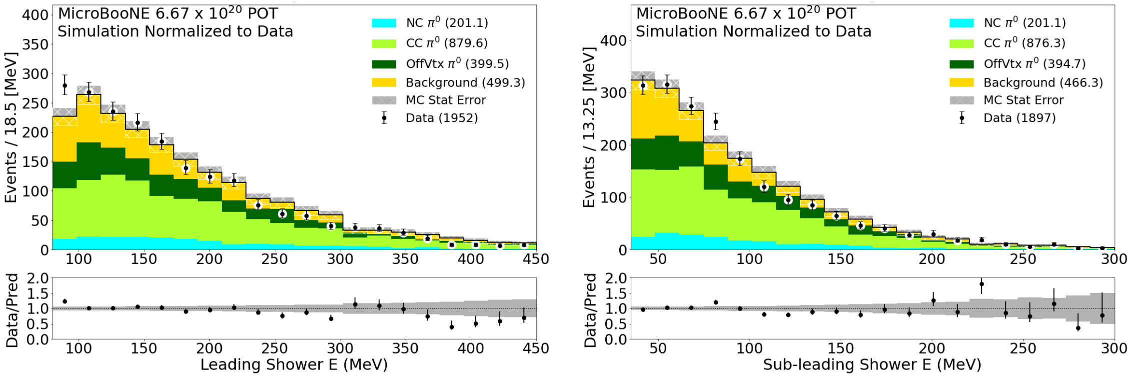

(a) Leading Photon

(b) Sub-leading Photon

Figure 8.7: The reconstructed photon energies for events passing all selection cuts. The leading photon is shown in (a) and the sub-leading photon is shown in (b). The MC simulation samples have been normalized to the total number of data events. The data events are shown by black points. The number of events in each category is shown in the legend in parentheses. The $\chi^2_{CNP}/19(dof) = 1.267$ with a p-value of 0.193 for the leading shower and the $\chi^2_{CNP}/19(dof) = 0.973$ with a p-value of 0.491 for the sub-leading shower.

The spectra seen in Figure 8.7 closely mirror the shower energy scale of the MiniBooNE LEE [21]. This makes the π^0 sample ideal for verifying the simulation-derived shower energy calculation is valid on data.

8.1.3 π^0 Rest Mass Reconstruction

In order to further verify the shower energy calculation, it is necessary to use a known physical quantity. For the π^0 sample that quantity is the π^0 rest mass of 135 MeV/c^2 [6]. The π^0 mass can be calculated using the equation:

$$M_\pi^0 = \sqrt{4\sin^2(\frac{\theta}{2})(E_1)(E_2)} \tag{8.4}$$

where E_1 is the leading photon energy and E_2 is the sub-leading photon energy. The 3D opening angle between the photons is θ.

Figure 8.8 shows the resolution of θ. The opening angle resolution is defined as:

$$\theta_{res} = \frac{\theta_{reco} - \theta_{sim}}{\theta_{sim}}. \tag{8.5}$$

This figure uses the same simulation samples as Figure 8.6 with all of the π^0 box cuts applied. The distribution is characterized in Table 8.1. The mean is close to zero indicating little bias.

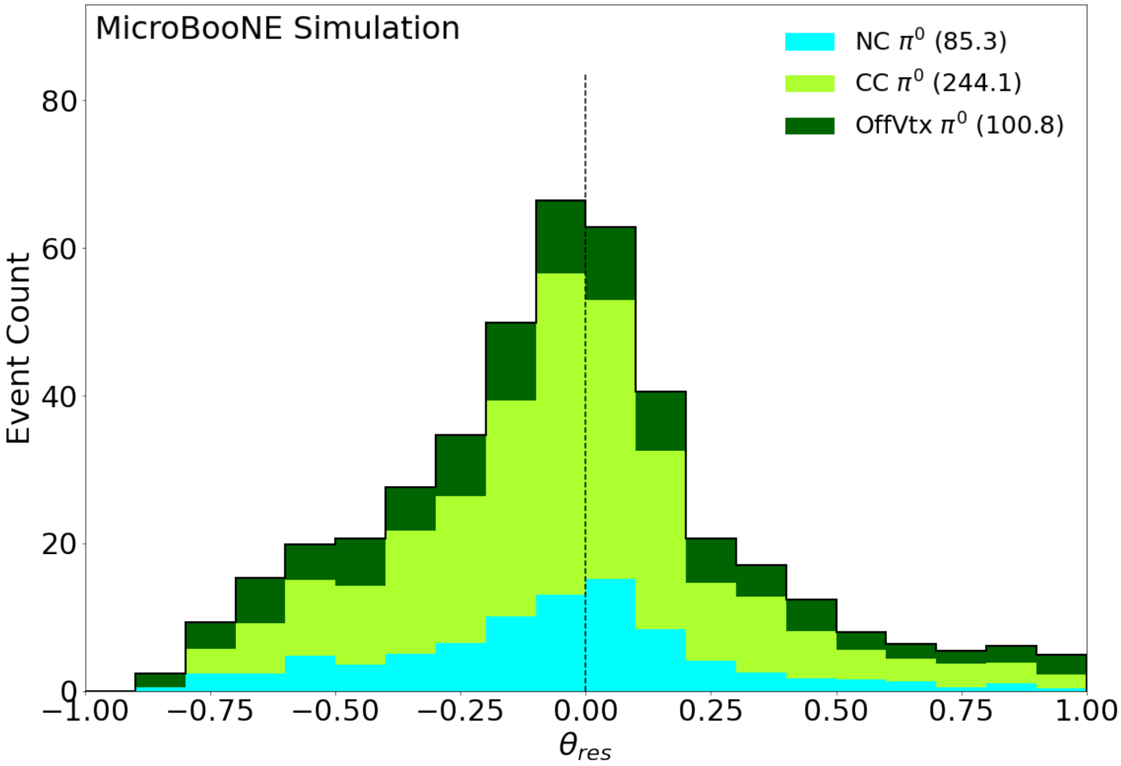

Figure 8.8: The opening angle (θ) resolution of the decay photons in the selected π^0 sample. The events have been scaled to match total data POT of 6.67×10^{20}. Resolution is defined in Eq.8.5. The dashed vertical line is included at $\theta_{res} = 0.0$ for reference.

The π^0 invariant mass can now be reconstructed. The result of this reconstruction is shown in Figure 8.9. As in Figure 8.7, the total number of simulation events has been scaled to match the total number of data events. A Gaussian fit to the simulation gives a mean of 132.39 ± 1.716 MeV/c^2 and a width of 39.8 ± 1.724 MeV/c^2. A Gaussian fit to the data gives a mean of 137.51 ± 2.585 MeV/c^2 and a width of 48.96 ± 2.631 MeV/c^2, both of which match the true value of 135 MeV/c^2 within uncertainty and overlap with each other within uncertainty. This indicates good initial agreement between the data and simulation.

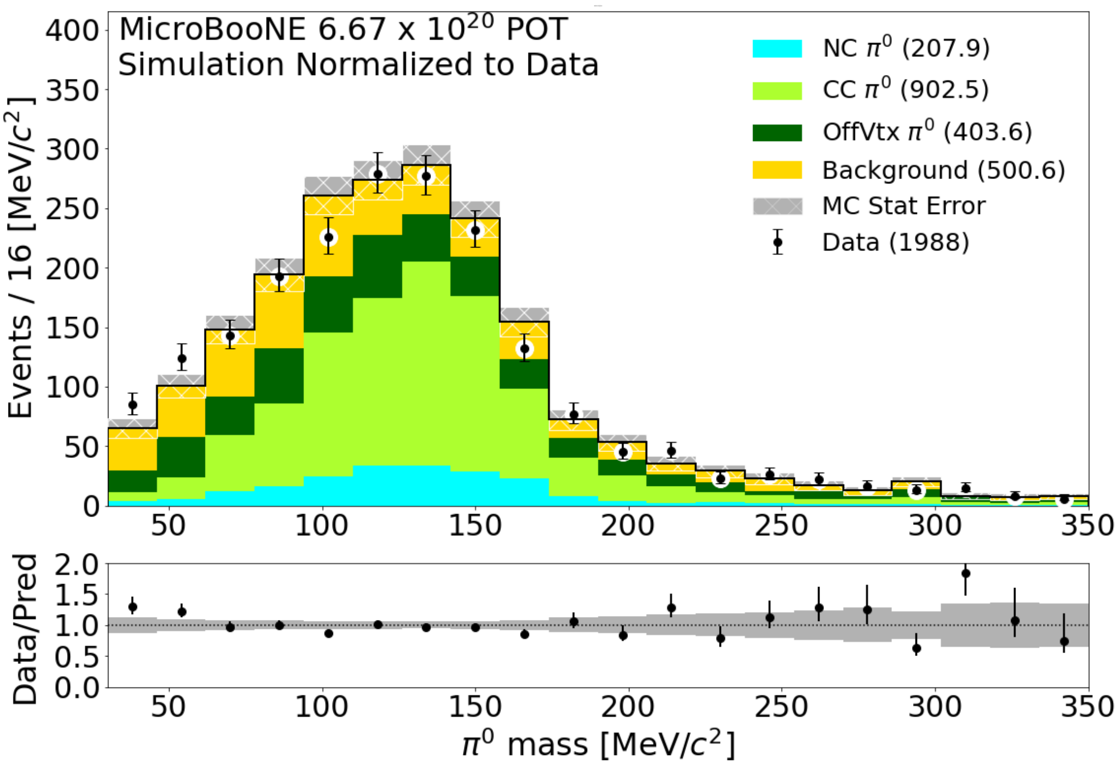

Figure 8.9: The calculated π^0 mass for events passing all selection cuts. The MC simulation samples have been normalized to total number of data events. The data events are shown by black points. The number of events in each category is shown in the legend in parenthesises. The $\chi^2_{CNP}/19(dof) = 0.976$ with a p-value of 0.486 for the MC prediction.

8.1.4 Best-Fit Shower PIU-to-energy Conversion Points

The π^0 sample is next used to verify the agreement in data and simulation of the shower energy scale using the known π^0 invariant mass M_{π^0}. Instead of simply using the Q_{sh}-to-MeV factor derived from simulated electrons, test points are found representing which Q_{sh}-to-MeV conversion factor (m) gives the best fit to $M_{\pi^0} = 135$ MeV/c^2. This is done for a sample of each simulation and data. The goal for each is to find the value of m that yields a π^0 mass distribution that peaks closest to the true value of 135 MeV/c^2. This value of m is then compared between data and simulation and to the electron value found in Section 6.7.2 denoted here by m_{e^-}.

To find the optimal m for the sample, the following χ^2 formula is minimized:

$$\chi^2 = \sum_i \left(\frac{(135[MeV/c^2] - M^i_{\pi^0})}{dM} \right)^2. \tag{8.6}$$

where i is each π^0 event in the given sample, dM is 29.8 MeV/c^2 based on the width of a Gaussian fit to the good simulation π^0 distribution (the NC π^0 and CC π^0 categories in Figure 8.9). $M^i_{\pi^0}$ represents the π^0 mass and is given in this case by:

$$M^i_{\pi^0} = \sqrt{4\sin^2(\frac{\theta}{2})(m \times (Q_{sh})_1)(m \times (Q_{sh})_2)} \tag{8.7}$$

where Q_{sh} is the reconstructed shower charge and θ is the reconstructed opening angle between the two showers.

The same χ^2 formula is minimized for both MC simulation and data. The 1-σ range is calculated on these fit points by looking at the range of m values for each data and simulation which give a χ^2 value satisfying the Wilks' theorem condition $|\chi^2(m) - \min_m[\chi^2(m)]| < 1$ [66]. The χ^2 distributions can be found in Figure 8.10 for simulation (a) and data (b). The resulting best fit m values can be seen in the first two rows of Table 8.2. Agreement is seen between the data and the simulation best fit points indicating that the simulation derived shower conversion factor is valid to use on data.

Another important consideration is how closely the best fit m values derived here match m_{e^-} in Eq. (6.1). The best fit value of m derived from the π^0 sample has the potential to be affected by many factors. The largest of these factors is the amount of background events selected. The π^0 selection contains many background events, which should not necessarily reconstruct as a π^0 mass of 135 MeV/c^2. To account for this background in simulation a second fit is performed only using good simulation events. In this instance good simulation is defined as simulated events that pass all π^0 cuts, have a simulated final state π^0 , and have a reconstructed vertex within 5 cm of the true simulated neutrino interaction vertex. A further cut of π^0 mass < 200 MeV is added to prevent poorly reconstructed events from having

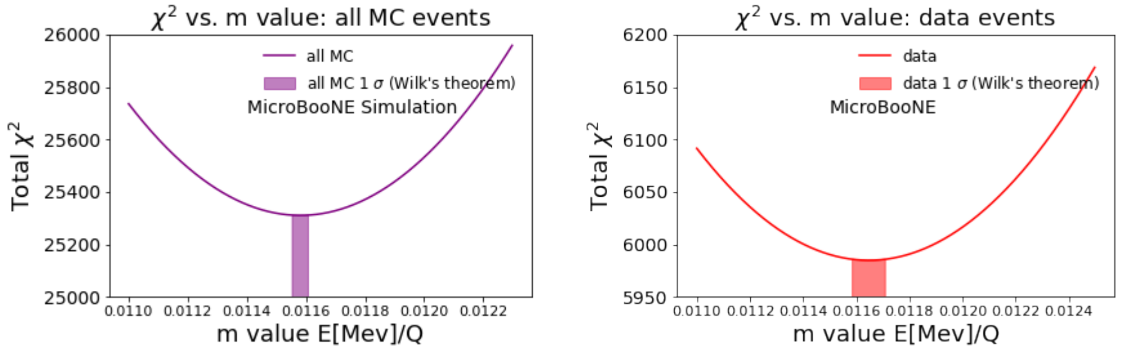

(a) Fit to all selected MC simulation events

(b) Fit to selected data events

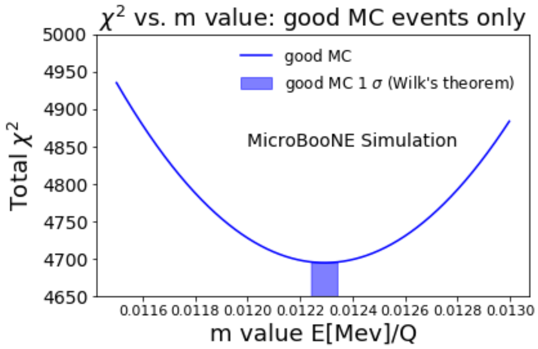

(c) Fit to good selected MC simulation events

Figure 8.10: Total χ^2 vs. m distributions for all MC simulation(a), data(b), and good MC simulation(c) that pass the π^0 selection criteria.

a large effect on the χ^2.

To account for the background events in data, the optimal m found previously is next shifted by the same amount that the MC m is shifted when backgrounds are included (7.11×10^{-4}) as seen the last two rows in Table 8.2. Data (un-shifted) are the results from minimizing Eq. 8.6 over all data points. Data (shifted) shows the results of applying the shift found by comparing the fit over all simulation to the fit over good simulation. This shift retains the excellent data and simulation agreement. The shifted result on data only differs by 1.6% from the value seen in Eq. 6.1. This indicates that, at the photon energy scale seen in the π^0 sample, the charge-to-energy conversion factor is valid. The disagreement seen between the un-shifted data best fit and m_{e^-} is therefore interpreted to be due to the purity in the sample. Data and simulation agreement of these results and agreement to m_{e^-} is discussed further in Section 8.3 and examined in combination with the results from the Michel e^- sample.

Table 8.2: The best value of m (MeV/Q_{sh}) for each data and MC simulation sample and the range found using Wilks' theorem. Results are shown before accounting for background (top two rows) and after (bottom two rows).

Sample	m [MeV/Q]	m range	χ^2/NDF
All MC	1.159×10^{-2}	$[1.156 \times 10^{-2}, 1.160 \times 10^{-2}]$	$25310.3/9473 = 2.7$
Data (un-shifted)	1.165×10^{-2}	$[1.159 \times 10^{-2}, 1.170 \times 10^{-2}]$	$5984.7/1973 = 3.0$
Good MC	1.230×10^{-2}	$[1.225 \times 10^{-2}, 1.234 \times 10^{-2}]$	$4694.9/3039 = 1.5$
Data (shifted)	1.236×10^{-2}	$[1.230 \times 10^{-2}, 1.241 \times 10^{-2}]$	$5984.7/1973 = 3.0$

8.2 The Michel Electron Sideband Sample

To validate the shower energy reconstruction at lower energy showers, a sample of Michel electrons is used. Michel electrons are electrons resulting from muon decay as shown in Figure 8.11. As discussed in Section 6.5, the DL vertices search for the intersection of two ”prongs”. A muon decay into a Michel electron forms this pattern and is therefore often reconstructed at the initial vertex stage of the event reconstruction. Muons in MicroBooNE result from both the cosmic background and CC ν_μ events. This selection will focus on electrons from CC ν_μ events. In order to compare the simulation to data, Michel electrons coming from cosmic background are treated as background to the desired selection.

This is the first time a Michel sample has been reconstructed in a LArTPC which is dominated by Michels from ν_μ interactions. As in Section 8.1, the event selection criteria for this sample is described first. Next, the data/simulation agreement in the Michel shower energy spectrum is examined. Finally, the agreement of the Michel sample with the physical Michel cutoff of $m_\mu/2 = 52.8$ MeV is assessed through a fit procedure analogous to that performed in Section 8.1.4. The data and MC simulation results of this fit agree, validating the use of the ν_e simulation-derived Q_{sh}-to-MeV on data. Both the data and ν_e simulation fits also show consistency between the simulation-derived Q_{sh}-to-MeV conversion value validating the absolute shower energy scale of the reconstruction in the low energy region ($\lesssim 50$ MeV).

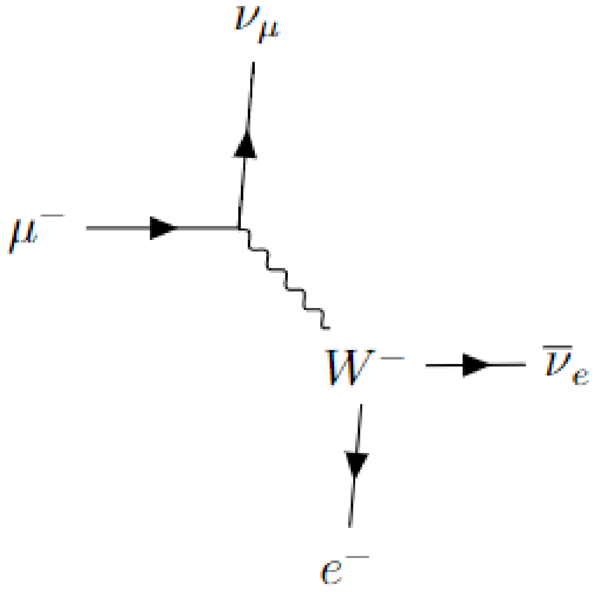

Figure 8.11: The dominant Feynman diagram describing μ^- decay.

8.2.1 Michel Electron Event Selection

The Michel electron sample has been chosen in order to validate the reconstructed energy scale of lower-energy electrons. This scale below the energy of most electrons in the DL-LEE search. Previous work has been performed in MicroBooNE using a larger sample than presented here, as seen in Ref. [67]. The study presented here uses a different selection and is designed to test the reconstruction of showers used in the $1e1p$ selection utilized in this thesis.

Muon-Michel vertices are identified through the following requirements which treat the longer of the two prongs as the candidate muon and the shorter as the candidate electron.

- Two prongs at the vertex;
- Long prong track-length $>$ 100 cm;
- Short prong track-length $<$ 30 cm;
- Long track consists of $<$ 20% SparseSSNet shower-like pixels;
- Short track consists of $>$ 80% SparseSSNet shower-like pixels; and

- $\phi_\mu < 0.5$ radians,

where ϕ_μ is the azimuthal angle of the muon with respect to the horizontal plane, where $\phi_\mu = 0.5\,\text{rad}$ corresponds to downward-going muons.

The last requirement is particularly useful in removing cosmic backgrounds as they are predominantly downward moving as seen in Figure 8.12. Lastly, in events with more than one selected vertex, only the first vertex is kept.

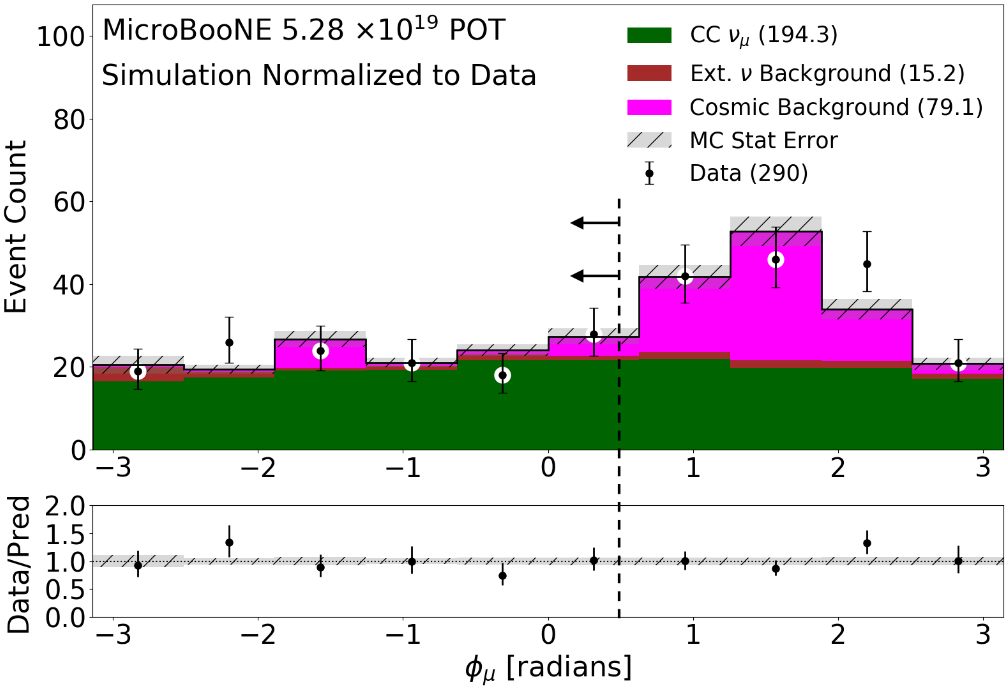

Figure 8.12: ϕ_μ distribution for selected events in both data and MC simulation, corresponding to $\approx 5.3 \times 10^{19}$ POT. The selection cut requiring $\phi_\mu < 0.5$ radians is indicated by the dotted line. The MC simulation samples have been normalized to total number of data events. The data events are shown by black points. The number of events in each category is shown in the legend in parentheses. The uncertainty bars are statistical only. The $\chi^2_{CNP}/9(dof) = 0.822$ with a p-value of 0.596 for the MC prediction.

For Michel electrons in events passing these cuts, the electromagnetic shower reconstruction algorithm from section 6.7.1 is applied to find Q_{sh}. This is then converted to a shower energy via Eq. 6.1. Figure 8.13 shows the shower energy distribution for Michel electrons in both data and simulation using this conversion. Note that data here comes from the preliminary data set to ensure blindness to the low-energy signal region at the time this analysis was performed. The simulated events are broken into various categories to indicate which type of event caused the muon. This selection is the only one presented in this thesis which cannot discount external neutrino events. These are neutrino interactions occurring outside the detector volume where the final state particles travel into the detector. A muon from such an event can decay into a Michel electron in the active volume. This appears in the figures as "Ext. ν Background".

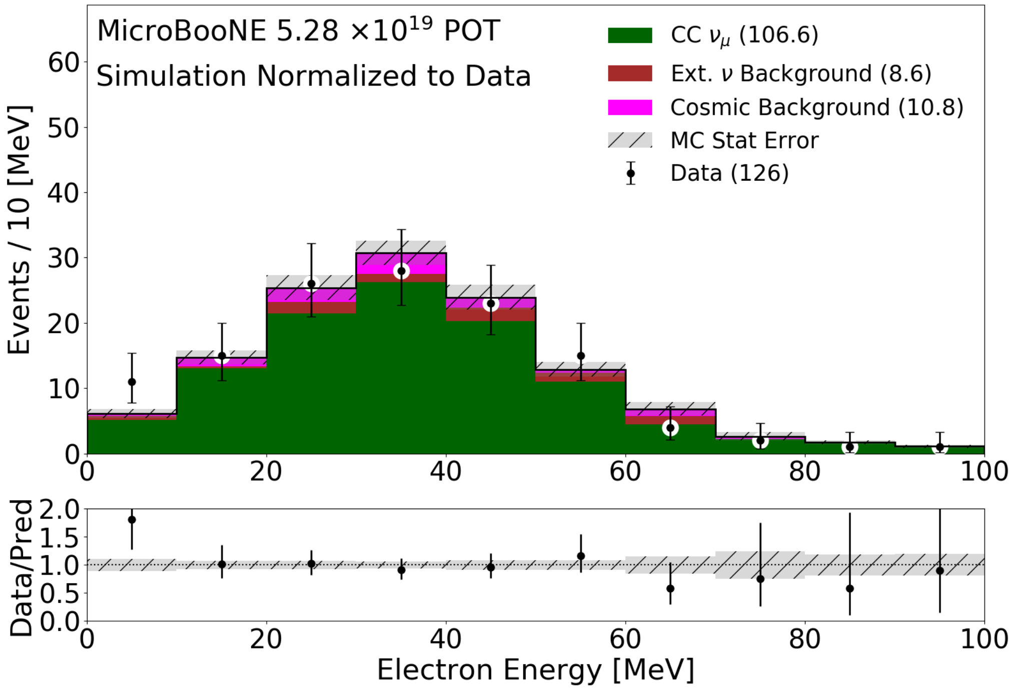

Figure 8.13: Electron energy distribution for Michels in both data and MC simulation after all selection criteria have been applied, corresponding to $\approx 5.3\times10^{19}$ POT. The MC simulation samples have been normalized to total number of data events. The data events are shown by black points. The number of events in each category is shown in the legend in parenthesises. The uncertainty bars here are statistical only. The $\chi^2_{CNP}/9(dof) = 0.608$ with a p-value of 0.857 for the MC prediction.

One can see that the high-end tails for the shower energy distribution in both data and simulation fall off around 60 MeV. The high energy tail above the true value of 52.8 MeV likely is due to over estimation of shower energy reconstruction seen in Figure 6.9. The shower energies of this sample are much lower than those seen in the π^0 sample. The good data/simulation agreement within statistical uncertainty indicates that the shower algorithm performs well down to low energies.

8.2.2 Best-Fit Shower PIU-to-energy Conversion Points

A validation of the absolute shower energy scale is now performed and the data/simulation agreement with the Michel sample is analyzed in a manner analogous to the π^0 study described in Section 8.1.4. In this case, instead of fitting to a single value, the spectrum is fit to function. The Michel spectrum cutoff is used as the known physical quantity. The Q_{sh} (reconstructed shower charge) spectrum shown in Figure 8.14 is fit to the following five-parameter function representing this cutoff:

$$f(x = \frac{Q_{\mathrm{sh}}}{Q_{\mathrm{cutoff}}}; \sigma, N) = N \int_0^1 (3y^2 - 2y^3) \frac{1}{\sqrt{2\pi\sigma^2}} \exp \frac{-(x-y)^2}{2\sigma^2} dy \tag{8.8}$$

where:

$$\sigma = y\sqrt{r_1^2 + \frac{r_2^2}{yQ_{\mathrm{cutoff}}} + \left(\frac{r_3}{yQ_{\mathrm{cutoff}}}\right)^2}. \tag{8.9}$$

Here, $f(x)$ represents a parameterization of the true Michel spectrum convoluted with a Gaussian representing charge resolution [68]. N is a floating normalization parameter, and $\{r_1,\ r_2,\ r_3\}$ represent contributions to the charge resolution corresponding to a constant noise term, a statistical charge-counting term, and a Gaussian noise term, respectively. Q_{cutoff} represents the cutoff of the Michel shower energy spectrum, which, after the Q_{sh}-to-MeV conversion, should correspond to the Michel energy cutoff of $m_\mu/2 \approx 52.8$ MeV. The integration over the variable y represents a scan over the simulated shower charge spectrum. The expression is invariant under $\int_0^1 I(y)dy \to Q_{\mathrm{cutoff}}^{-1} \int_0^{Q_{\mathrm{cutoff}}} I(Q_{sh}^*/Q_{\mathrm{cutoff}})dQ_{\mathrm{sh}}^*$, where $I(\dots)$ represents the integrand in Eq. 8.8.

There are five parameters $(Q_{\mathrm{cutoff}}, N, r_1, r_2, r_3)$ that need to be determined, making this fit more complicated than the π^0 version. $f(x)$ is fit to the Michel spectrum in data and simulation by varying all five parameters. This is done by minimizing the χ^2 which has a similar structure to the π^0 fit:

$$\chi^2(Q_{\text{cutoff}}, N, r_1, r_2, r_3) = \sum_i \left(\frac{(O_i - f(x = \frac{(Q_{\text{sh}})_i}{Q_{\text{cutoff}}}; N, r_1, r_2, r_3)}{\sigma_{\text{i,stat.}}} \right)^2 \tag{8.10}$$

where O_i is the number of observed Michel events in Q_{sh} bin i and $\sigma_{\text{i,stat.}} = \sqrt{O_i}$ is the Poisson error. The 2D confidence regions for Q_{cutoff} versus the different resolution parameter are found in Ref. [61]. They are calculated by fixing the remaining three parameters at their best fit values and using Wilks' theorem for two free parameters. (Note that Wilks' theorem confidence levels are discussed in great detail in Chapter 12). In data, the 1σ r_1 contour prefers a fractional resolution of ≈ 0.3, while the 1σ r_2 and r_3 contours are both consistent with zero. In simulation, the 1σ r_1 contour prefers a fractional resolution of ≈ 0.25. The 1σ r_3 contour is consistent with zero, but the 1σ r_2 contour prefers a value of ≈ 13 $[\text{PIU}]^{1/2}$.

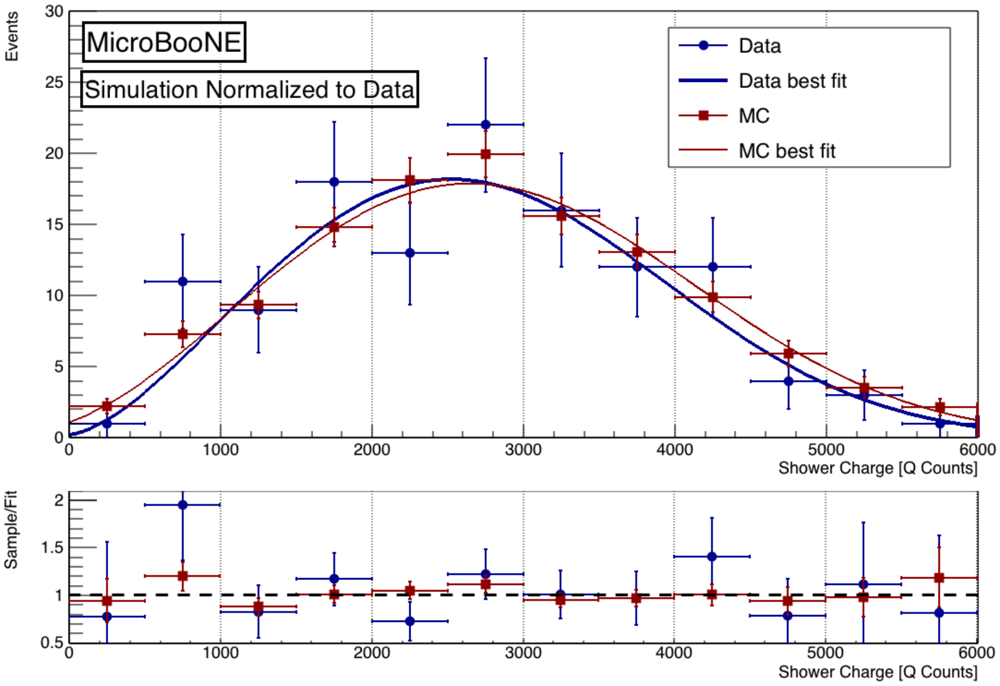

Figure 8.14: **Top**: Michel shower charge sum spectrum in data and MC simulation along with the corresponding best fit to eq. (8.8) (allowing only Q_{cutoff} to vary in the fit). This sample corresponds to $\approx 5.3 \times 10^{19}$ POT. **Bottom** Ratio of the data/simulation to the corresponding fit. The MC simulation and fit result here have been normalized to match the data.

Next, the parameters $\{N, r_1, r_2, r_3\}$ are fixed at the minimum χ^2 values (respectively for data/simulation) and a χ^2 scan over Q_{cutoff} is performed, this time only including the tail of the Q_{sh} spectrum ($Q_{\text{sh}} > 3000$ PIU). The purpose of this one-dimensional scan is to obtain the χ^2 minimum and corresponding 1σ interval on Q_{cutoff} using Wilks' theorem for one fit parameter [66]. Figure 8.14 shows the observed Michel shower charge spectra in data and simulation along with their respective best fits from the 1D scan.

Figure 8.15 shows χ^2 as a function of Q_{cutoff}. The Wilks' theorem 1σ interval on Q_{cutoff} corresponds to the points for which $\chi^2(Q_{\text{cutoff}}) - \min\{\chi^2; Q_{\text{cutoff}}\} \leq 1$. In order to get the charge to energy conversion factor m from Q_{cutoff} , $m = \frac{52.8 \text{ MeV}}{Q_{\text{cutoff}}}$. The best fit and 1σ intervals for m are given in Table 8.3 along with the χ^2/NDF of the best fit. One can see excellent agreement between data and simulation, demonstrating the consistency of the shower reconstruction. The data/simulation agreement and consistency with Eq. (6.1) demonstrated by this study are discussed further in Section 8.3 in combination with the results from the π^0 sample.

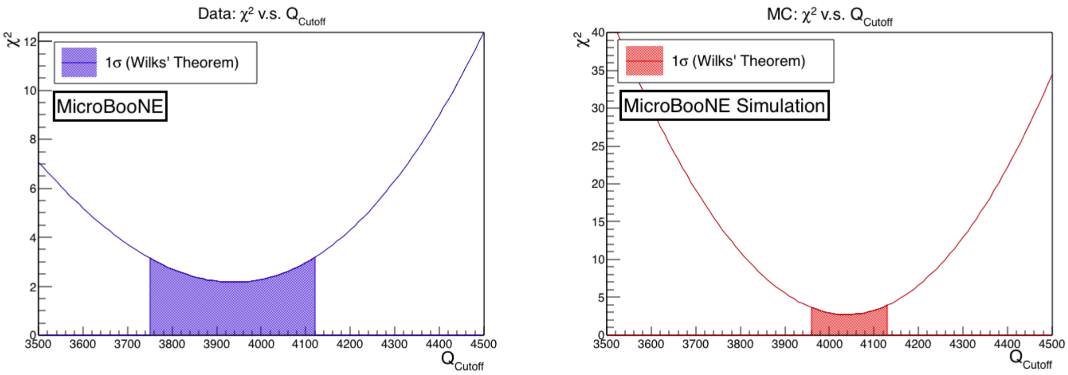

(a) (b)

Figure 8.15: χ^2 from (8.10) as a function of Q_{cutoff}, for data (a) and MC simulation (b). This sample corresponds to $\approx 5.3 \times 10^{19}$ POT. The 1 σ allowed regions from Wilks' theorem are shown in shaded regions below each curve.

Table 8.3: The best fit values and 1σ ranges (via Wilks' theorem) for m along the χ^2/NDF of that fit given by eq. (8.10) for both data and MC simulation. The fit here is the one-dimensional scan over Q_{cutoff} transformed into m as described in the text.

Sample	m [MeV/Q]	m range	χ^2/NDF
Data	1.341×10^{-2}	$[1.282 \times 10^{-2}, 1.401 \times 10^{-2}]$	$2.17/6 = 0.4$
MC	1.308×10^{-2}	$[1.279 \times 10^{-2}, 1.334 \times 10^{-2}]$	$2.73/6 = 0.5$

8.3 Final Verification of the Shower Energy Calculation

Both the data/simulation agreement of the shower reconstruction and the absolute scale of the ν_e simulation-derived Q_{sh}-to-MeV conversion are validated by utilizing the π^0 invariant mass of ≈135 MeV and the Michel electron spectrum cut-off at ≈52.8 MeV. Comparison points were obtained separately for data and simulation in each sample. These points are shown with statistical uncertainties in Figure 8.16. The Q_{sh}-to-MeV conversion factor or m values found in Section 6.7.2 for electrons, leading photons, and sub-leading photons are shown by shaded bands in Figure 8.16. In principle, one expects agreement between the points and the electron and leading photon calibration line. The 1σ ranges in the m value from both the data/simulation Michel cutoff study and the data/simulation π^0 mass study agree well with the best-fit m values from simulated electrons and leading photons. Agreement with the sub-leading photon line is not necessarily expected because of the reconstruction failure cases discussed previously.

Table 8.4 shows the agreement of data and MC simulation for each point, as well as the agreement of each data and simulation point to the electron best fit value from Eq. (6.1). It is seen here that the best fit m values agree between data and simulation for each sample. This validates the use of the same simulation-derived Q_{sh}-to-MeV conversion value (m_{e^-}) for both data and simulation. While the best fit m values for each sample do not exactly match m_{e^-} within statistical uncertainty, there are factors that may affect this value. These include: detector response modeling, sub-leading photon reconstruction in the π^0 sample, and backgrounds in the Michel

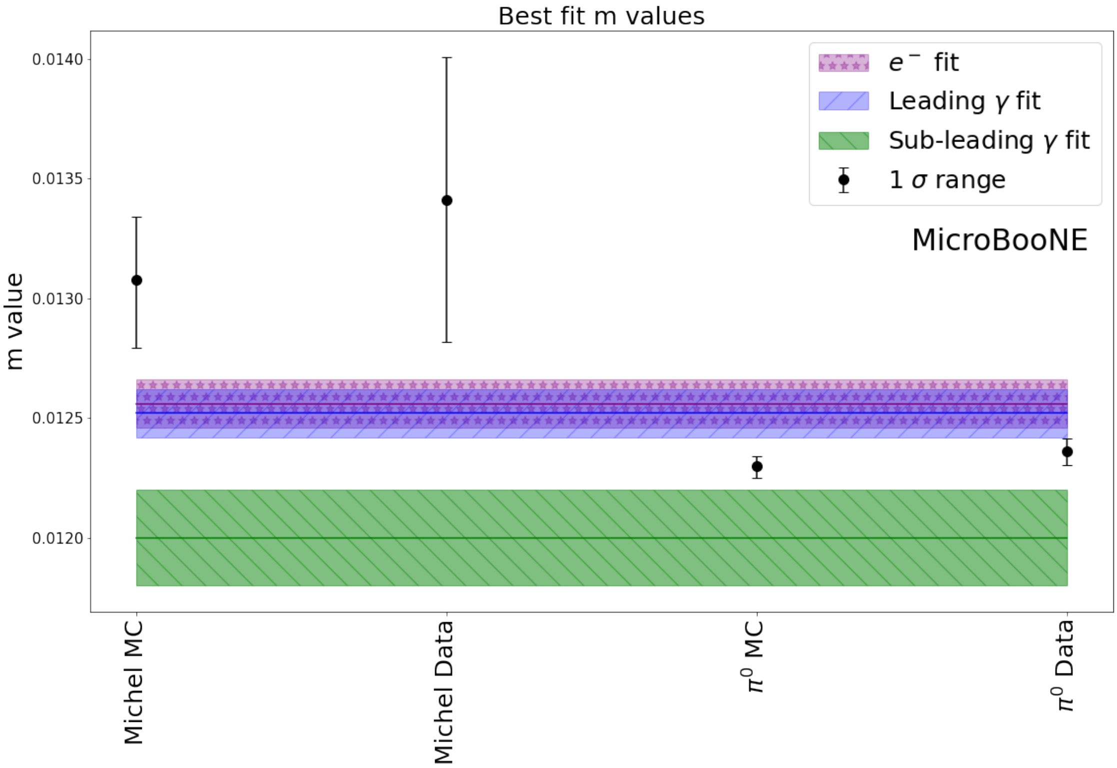

Figure 8.16: The data and MC simulation points from each the π^0 sample and the Michel e^- sample are compared with the Q_{sh}-to-MeV electron calibration line used in the DL analysis from eq. 6.1. The Q_{sh}-to-MeV photon calibration lines (eq. 8.2 and eq. 8.3) are also included for reference. The shaded regions represent the statistical uncertainty of this given calibration line.

$e-$ sample. Therefore, the 2-6% difference gives an estimate of the scale of the possible data to simulation bias on the shower energy reconstruction. This size effect is acceptable for use in this thesis analysis. The $< 6.5\%$ difference between each (m_{MC}, m_{Data}) and m_{e^-} gives the scale of the detector systematic uncertainty in this reconstruction process.

Table 8.4: Data and MC simulation best fit m values from each sample and comparison to the charge-to-energy conversion factor from eq. (6.1) ($Q_{\text{sh}} - to - MeV = m_{e^-} = 1.26 \pm 0.01 \times 10^{-2}$). Uncertainties in ratios are calculated from the 1 σ range of each value. The background adjusted values are used for the π^0 sample.

Sample	m_{MC} [MeV/Q]	m_{Data} [MeV/Q]	m_{Data}/m_{MC}	m_{MC}/m_{e^-}	m_{Data}/m_{e^-}
π^0	$1.230^{+0.004}_{-0.006} \times 10^{-2}$	$1.236^{+0.005}_{-0.006} \times 10^{-2}$	$1.005^{+0.006}_{-0.006}$	$0.984^{+0.009}_{-0.009}$	$0.979^{+0.008}_{-0.009}$
Michel e^-	$1.31^{+0.03}_{-0.02} \times 10^{-2}$	$1.34^{+0.06}_{-0.06} \times 10^{-2}$	$1.025^{+0.051}_{-0.049}$	$1.038^{+0.022}_{-0.024}$	$1.064^{+0.048}_{-0.048}$

In addition, as shown in Figure 8.7 and Figure 8.13, the showers found in the two samples are at different energy ranges. The assumption has been made in this analysis that the Q_{sh}-to-MeV factor does not change with shower energy. The samples cover the range of values of interest for the DL 1e1p analysis. The Q_{sh}-to-MeV value given in Eq. 6.1 is valid for EM showers in both data and simulation at the energy ranges and precision relevant for the oscillation search presented in later chapters.

Chapter 9

Detector Effects and Systematic Uncertainties

The predicted event spectra used throughout this work have a range of associated uncertainties that correspond to how well various aspects of the experiment are known. These generally arise from five sources: the beam flux prediction, the neutrino–nucleus interaction model, the hadron re-interaction model, the detector simulation, and the finite statistics in the samples used to form the prediction. As discussed in chapter 4, this analysis makes use of the covariance matrix (Eq. 4.1). This chapter details the various uncertainties used in the analysis. For each type, the covariance matrix and correlation matrix (Eq. 4.3) are shown for both null oscillation and maximum oscillation.

The beam flux prediction uncertainties, the neutrino–nucleus interaction model uncertainties, and the hadron re-interaction model uncertainties are reweightable. Variations can be produced that are changes to the parameters in the model. These variations are used to assigned a relative probability of each event in the sample. This means that any variations of these types result in the same observed events, but with different probabilities that the event occurs based on the underlying truth information. Meanwhile the detector variations are non-reweightable, as they have the potential to change how the events are reconstructed. This can also lead to changes in which events are selected depending on how these values shift. A large category of this type of uncertainty is changes in the waveform read by the wires. This can lead to variations in the reconstructed energy. These two major types of systematic uncertainty are evaluated in different ways.

The systematic uncertainties used in this analysis use the same scheme as that presented in Ref [37] (the deep-learning LEE paper) and Ref. [69]. However there are a few key differences from the LEE analysis that affect the systematic uncertainties. These are:

1. Change in 1e1p binning (discussed in Appendix D);
2. Weight capping of high systematic weights (discussed in Section D);
3. changing the $1\mu1p$ selection to include the high stats π^0 samples (change is within simulation statistical error); and
4. removal of the background fitting performed on the ν_μ background to the $1e1p$ selection (the largest change).

The removal of the background fitting in the $1e1p$ selection was necessary as the backgrounds would need to be refit at each oscillation parameter. As a result the background spectrum in the $1e1p$ sample is affected by statistical fluctuations and the systematic covariance matrix for some variations has large bin to bin fluctuations.

There are many studies throughout this thesis that use systematic uncertainty and have their own covariance matrix with the events binned in the kinematic variable under investigation, but the general process is always the same. For illustration purposes, the covariance matrices shown here are those used in the 3+1 sterile neutrino search. Events are binned by reconstructed neutrino energy for the ranges $1e1p$: [200-1200] in 100 MeV bins + 1200-1600 MeV + 1600-2400 MeV and $1\mu1p$:[250-1200] in 50 MeV bins. It should also be noted that as the oscillation prediction changes, the contributions to the covariance matrix from the different event types changes. To illustrate this, both the null oscillation and maximum oscillation covariance and correlation matrices are shown in this chapter. The next sections detail how each type of systematic uncertainty is calculated. Section 9.6 then describes how all the types of systematic uncertainty are combined to make a total covariance matrix.

9.1 Flux Modeling and Uncertainties

The systematic uncertainties on the flux prediction can be grouped into three main sources: hadron production in the target, secondary hadron interactions, and the properties of the magnetic focusing horn. The flux re-weighting method is based on the techniques previously developed by the MiniBooNE collaboration [29] and adapted to the MicroBooNE detector location [31].

The hadron production parameters comprise of changes to the rate and spectrum of the hadrons that are produced when the proton beam interacts with the target. The secondary hadron interaction parameters allow for variation in the cross sections for the hadrons interacting with the target and focusing horn. The focusing horn properties that are allowed to vary are the electric current and resulting magnetic field of the horn.

Figures 9.1(a) and (b) show M_{flux} for the bins used in the 3+1 sterile neutrino oscillation analysis. These matrices are presented in terms of reconstructed bins where bins 0-9 are the original bins of the $1e1p$ selection used in the MiniBooNE LEE analysis (Chapter 11 indicated by red line), bins 10-11 are the additional high energy $1e1p$ bins (indicated by white line), and bins 12-30 are the $1\mu1p$ bins. Figures 9.1(c) and (d) represent the corresponding correlation matrices.

9.2 Interaction Model Systematic Uncertainties

The neutrino interaction model is made up of a wide variety of re-weightable parameters that can be broken down into two broad categories: parameters associated with each interaction type, and parameters for final state interactions (FSI) that affect all neutrino interaction modes. Each interaction type has a set of parameters that depends on the cross section model used. This set of uncertainties can also be

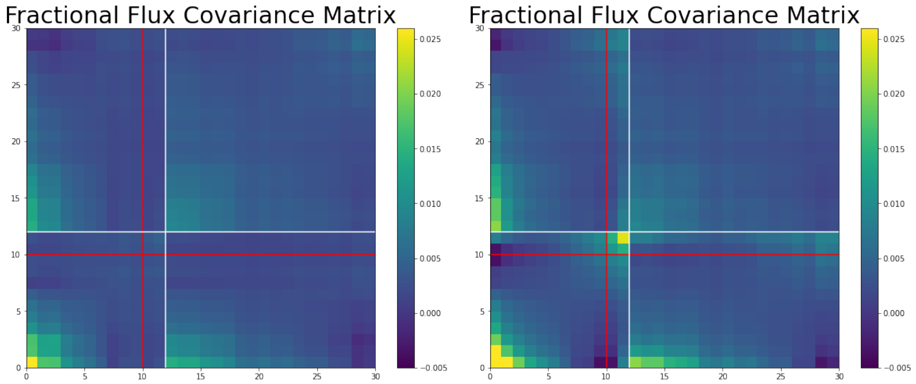

(a) covariance matrix, no osc (b) covariance matrix, max osc

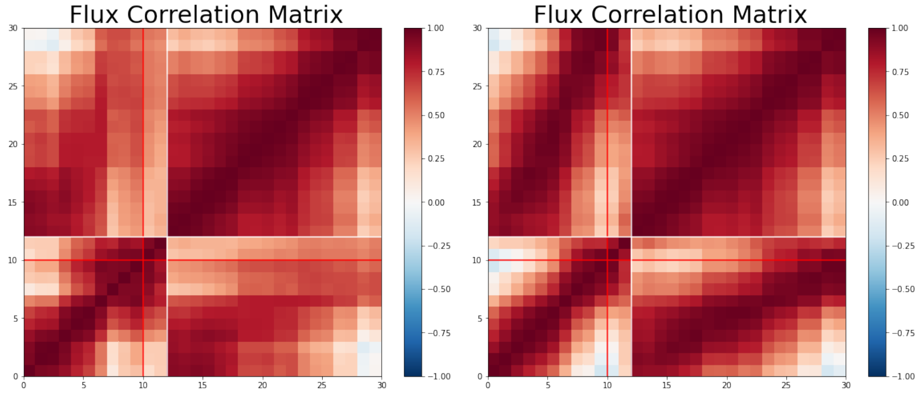

(c) correlation matrix, no osc (d) correlation matrix, max osc

Figure 9.1: Flux fractional covariance matrices for (a) null oscillation and (b) maximum oscillation, and the corresponding correlation matrices (c) and (d). Bins 0-9 are the original bins of the 1e1p selection (indicated by red line). Bins 10-11 are the additional high energy 1e1p bins (indicated by white line). Bins 12-29 are the 1μ1p bins. The z-axis has been capped to be consistent with each other for comparison.

thought of as the uncertainties on our neutrino background estimate and uncertainty on the signal.

Events are re-weighted according to the properties of the neutrino's interaction with the nucleus and the interactions of the resulting particles as they exit the nucleus. These parameters and their uncertainties are described in detail in Refs. [49, 69]. The majority of GENIE model parameters are varied together using a single weight calculator. The remaining parameters are:

- strength of the RPA effect in the Valencia CCQE model;
- shape of the CCQE cross section due to the axial form factor;
- shape of the CCQE cross section due to the vector form factor;

- angular distribution of decaying nucleon pairs in MEC events;
- shape of the CC MEC cross section in $q^0 - q^3$;
- angular distribution of decaying nucleon pairs in MEC events;
- two parameters for the angular distribution in Δ decays;
- two parameters for the normalization of CC/NC coherent pion production; and
- two parameters for corrections to the neutrino–nucleon elastic scattering form factors.

The largest uncertainties on the interaction model come from the variations related to CCQE and final state interactions (FSI). These are all encompassed in the GENIE weight calculator. The machinery for performing the re-weighting for the interaction model systematic uncertainties relies on code provided by GENIE which was combined with code developed in MicroBooNE [43, 45, 49]. The covariance and correlation matrices from the neutrino interaction model uncertainties are shown in Figure 9.2.

9.3 Hadron Re-Interaction uncertainties

The systematic uncertainties on hadron re-interactions consider variations in the hadron–argon interaction cross sections for protons, π^+, and π^-. These are uncertainties on any secondary interaction of these particles after they leave the nucleus. Hadron re-interaction systematic uncertainties are evaluated by re-weighting events according to the Geant4 truth information that describes the trajectories of the hadrons after they leave the argon nucleus [70].

The covariance and correlation matrices from the re-interaction model uncertainties are shown in Figure 9.3. The contribution from this type of uncertainties is sub-dominant when compared to the other systematic contributions.

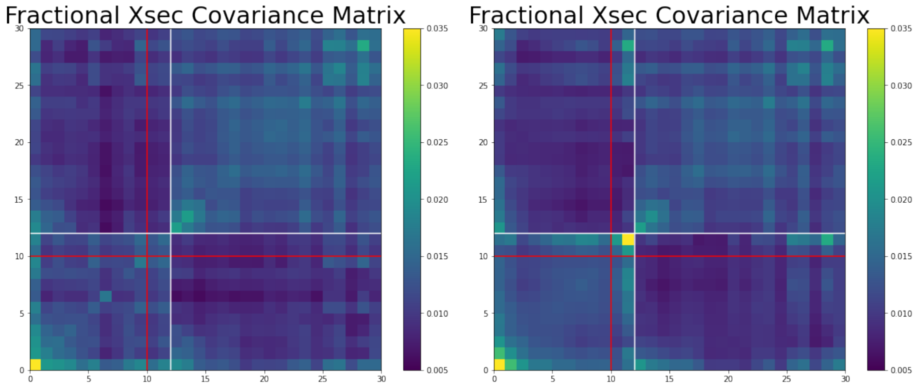

(a) covariance matrix, no osc (b) covariance matrix, max osc

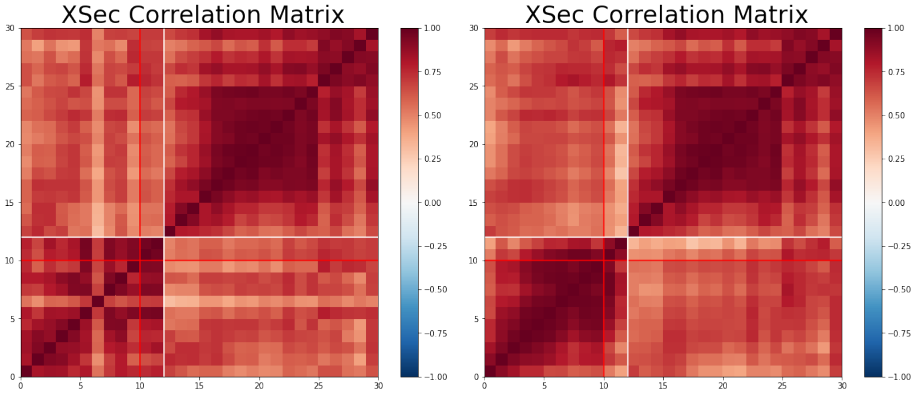

(c) correlation matrix, no osc (d) correlation matrix, max osc

Figure 9.2: Neutrino interaction model fractional covariance matrices for (a) null oscillation and (b) maximum oscillation, and the corresponding correlation matrices (c) and (d). Bins 0-9 are the original bins of the 1e1p selection (indicated by red line). Bins 10-11 are the additional high energy 1e1p bins (indicated by white line). Bins 12-29 are the 1μ1p bins. The z-axis has been capped to be consistent with each other for comparison.

9.4 Detector Variations

The detector-related systematic uncertainties are evaluated using a set of samples in which the detector simulation has been varied. Comparisons between these modified samples and the nominal simulation are used to estimate the uncertainty on the prediction. The variations include:

1. modifications in the amplitude and width of signals on the wire waveforms as a function of x position;
2. (y, z) position and detector angles θ_{XZ} and θ_{YZ} of the local particle trajectory [71];
3. variations in the electron-ion recombination parameters;

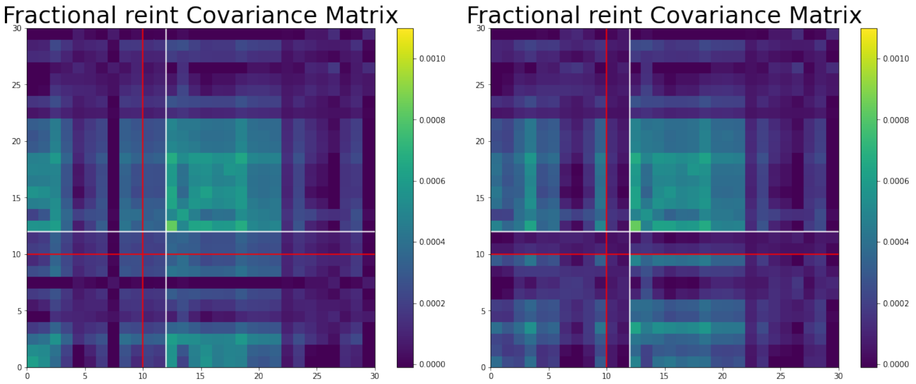

(a) covariance matrix, no osc (b) covariance matrix, max osc

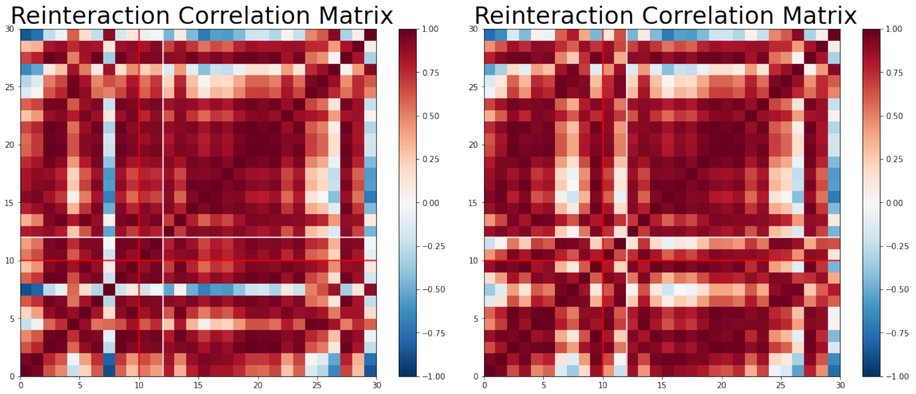

(c) correlation matrix, no osc (d) correlation matrix, max osc

Figure 9.3: Re-interaction fractional covariance matrices for (a) null oscillation and (b) maximum oscillation, and the corresponding correlation matrices (c) and (d). Bins 0-9 are the original bins of the 1e1p selection (indicated by red line). Bins 10-11 are the additional high energy 1e1p bins (indicated by white line). Bins 12-29 are the 1μ1p bins. The z-axis has been capped to be consistent with each other for comparison.

4. an alternative electric field map in the TPC; and variations in the light yield, the light attenuation, and the Rayleigh scattering length.

The total detector covariance matrix is the sum of the matrix from each variation. The samples used to evaluate these uncertainties have high statistical uncertainty. To get around that, this analysis uses a method to reduces the statistical fluctuations.

The underlying true spectra (e.g., the neutrino energy spectrum) are expected to be smooth, so a kernel density estimator algorithm [72] is used to estimate most contributions to our detector variation predictions. For a given detector variation sample, each event is assigned a kernel function with some width, and the final spectrum for this variation is obtained by summing all kernels. This is given by:

$$f(x) = \frac{1}{Nh}\sum_{i}^{N} K(x - x_i; h) \tag{9.1}$$

where K is the kernel function, h is the bandwidth of the Kernel, and x_i is the value of the data point in the sample. N is the number of simulated events. KDE smoothing works well if N is $O(5k)$. The kernel used here is the Epanechnikov kernel as it gives the smallest mean squared error.

$$K(x; h) = \begin{cases} \frac{3}{4}(1 - \frac{x^2}{h^2}) & -h < x < h \\ 0 & otherwise \end{cases} \tag{9.2}$$

This allows a reduction of the effect of the statistical fluctuations in the spectrum obtained from each detector variation sample without making any other assumptions about the impact of the variation on our analysis variables.

Figure 9.4 shows the effect of this smoothing on one variation (Run 3 variations on the space-charge effect with the $1e1p$ selection applied). The reconstructed energy distribution of selected events in the sample (POT scaled) is shown in (a) along with the smoothed version. Then the resulting covariance matrix for this variation is shown.

The only case where KDE smoothing is not used for evaluating the detector response uncertainties is the misidentified ν_μ backgrounds to the $1e1p$ prediction. The limited statistics in the detector variation sample combined with the high purity of the $1e1p$ selection leave us with too few events to obtain robust results from the KDE algorithm. A 20% systematic uncertainty is instead assessed on these backgrounds, based on the magnitude of the differences observed in the detector variation samples within the limited statistics available. This uncertainty is treated as uncorrelated between the analysis bins. This will have a small effect compared to the $\mathcal{O}(100\%)$ Poisson statistical errors on the number of muon neutrino and neutral current events in each $1e1p$ analysis bin. The covariance and correlation matrices

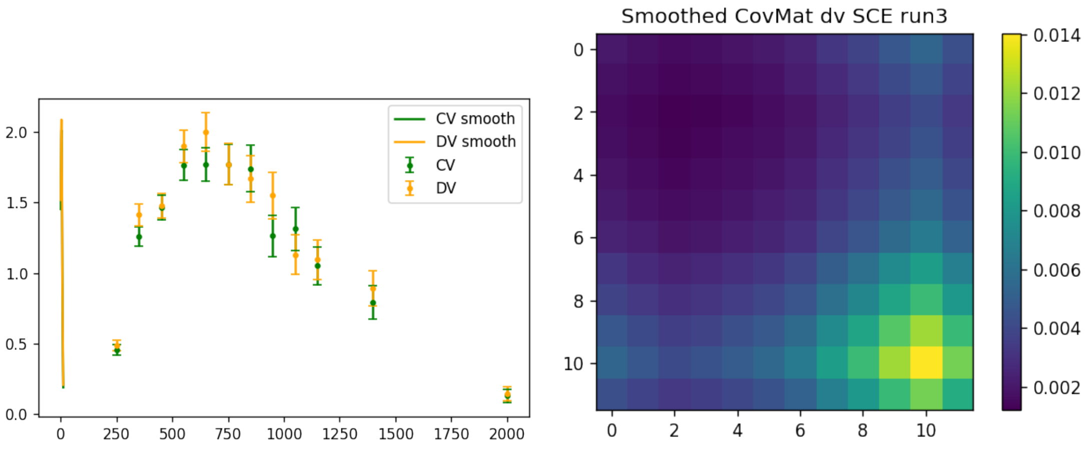

(a) Reconstructed E_ν (MeV) (b) covariance matrix

Figure 9.4: An example use of KDE smoothing using the Run 3 SCE effect sample. This sample has the $1e1p$ selection applied and uses the reconstructed E_ν (MeV) as the variable of interest.

from the detector variations are shown in Figure 9.5.

9.5 Uncertainty from Finite Statistics

The predicted spectra are also subject to statistical uncertainties due to finite statistics in the samples used to form the prediction. The statistical uncertainty in each bin is calculated as

$$\sigma_{\text{pred stat}} = \sqrt{\sum_i w_i^2} \tag{9.3}$$

where the sum runs over all of the events in the bin and w_i is the weight of each event, including the scaling factor needed to match the data POT, the cross section model tune weight, and the π^0 weights where applicable. The covariance and correlation matrices from the simulation statistical uncertainties are shown in Figure 9.6.

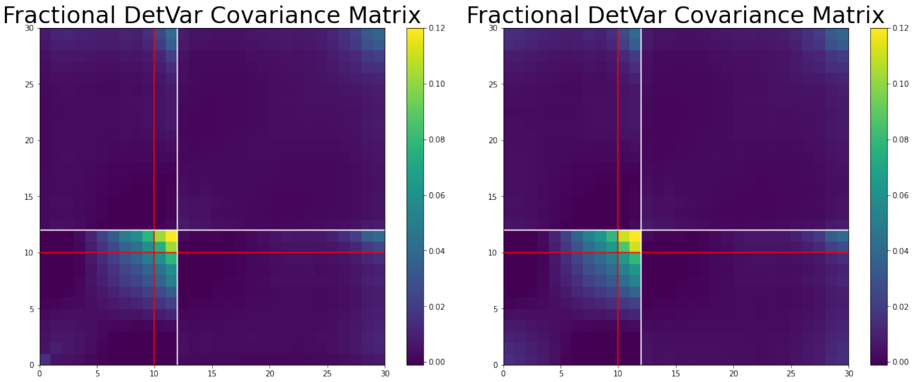

(a) covariance matrix, no osc (b) covariance matrix, max osc

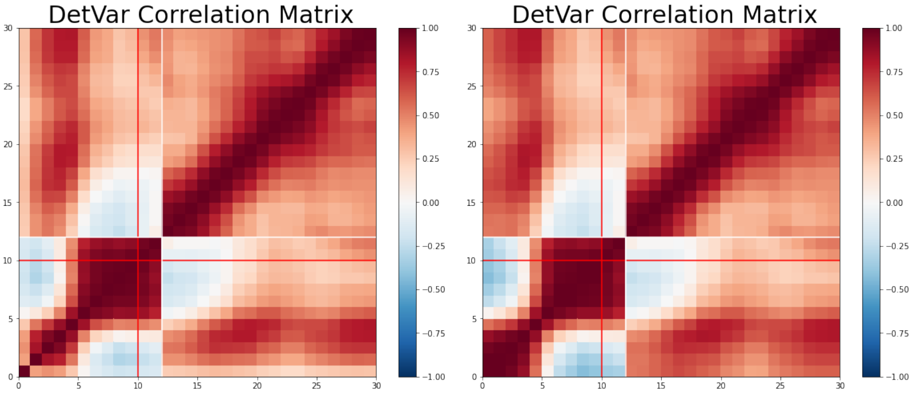

(c) correlation matrix, no osc (d) correlation matrix, max osc

Figure 9.5: Detector variation fractional covariance matrices for (a) null oscillation and (b) maximum oscillation, and the corresponding correlation matrices (c) and (d). Bins 0-9 are the original bins of the 1e1p selection (indicated by red line). Bins 10-11 are the additional high energy 1e1p bins (indicated by white line). Bins 12-29 are the $1\mu1$p bins. The z-axis has been capped to be consistent with each other for comparison.

9.6 Total Covariance Matrix

The total fractional covariance matrix is then a sum of the covariance matrices for each type of uncertainty and is:

$$M_{frac} = M_{flux} + M_{xsec} + M_{reint} + M_{det} + M_{stat} \tag{9.4}$$

where $M_{flux}, M_{xsec}, M_{reint}, M_{det}, M_{stat}$ are the contributions from the flux, neutrino interaction, hadron re-interaction, detector variations, and limited statistics respectively. This total fractional covariance matrix is shown in Figure 9.7.

The contributions of each type of uncertainty to the total spectrum is shown in

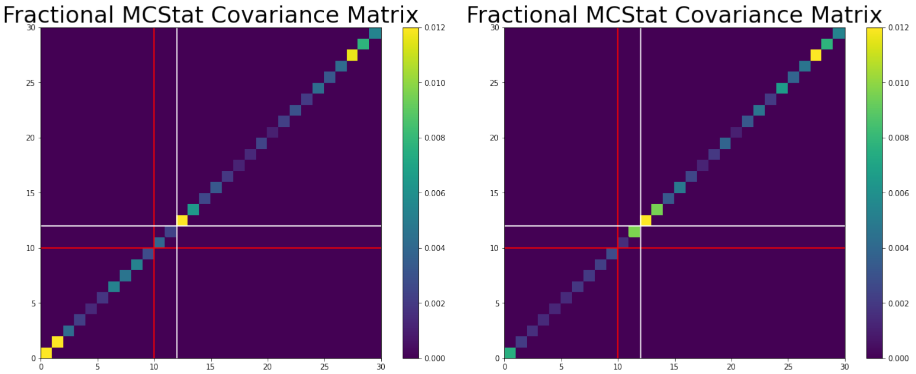

(a) covariance matrix, no osc (b) covariance matrix, max osc

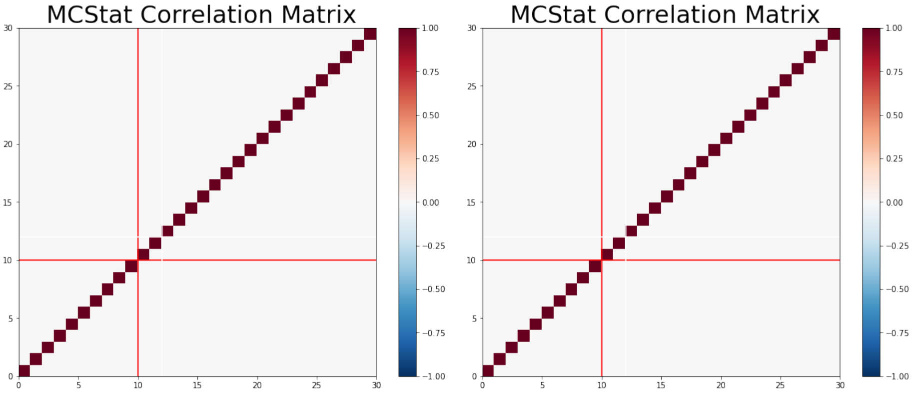

(c) correlation matrix, no osc (d) correlation matrix, max osc

Figure 9.6: Simulation statistical fractional covariance matrices for (a) null oscillation and (b) maximum oscillation, and the corresponding correlation matrices (c) and (d). Bins 0-9 are the original bins of the 1e1p selection (indicated by red line). Bins 10-11 are the additional high energy 1e1p bins (indicated by white line). Bins 12-29 are the 1μ1p bins. The z-axis has been capped to be consistent with each other for comparison.

Figure 9.8. This has been broken up into the $1e1p$ and $1\mu 1p$ spectrum. The result is shown for both no oscillation and maximum oscillation. The dominant uncertainties are detector variations, flux uncertainty and neutrino interaction (Xsec in the figure legend) uncertainty.

The total systematic covariance matrix (M) can be calculated by:

$$M_{sys} = \sum_{i,j} M_{frac,ij}\mu_i\mu_j \tag{9.5}$$

where μ_i is the expected number of events in the bin.

To account for the statistical error between the observation and the prediction, the Combined Neyman-Pearson method is used [27]. This method has been shown

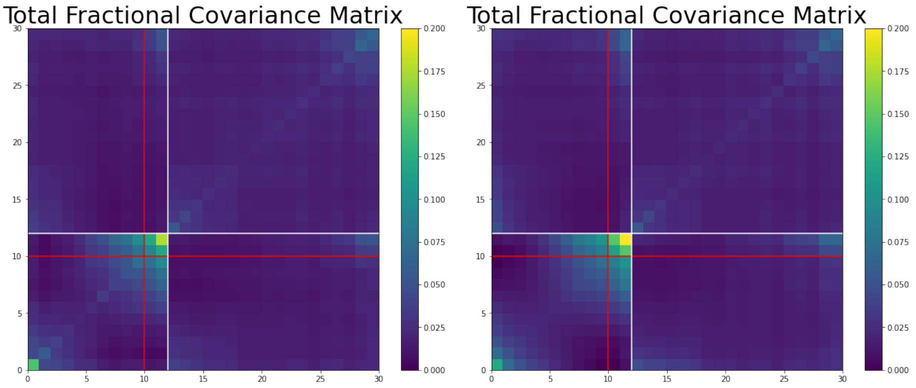

(a) covariance matrix, no osc (b) covariance matrix, max osc

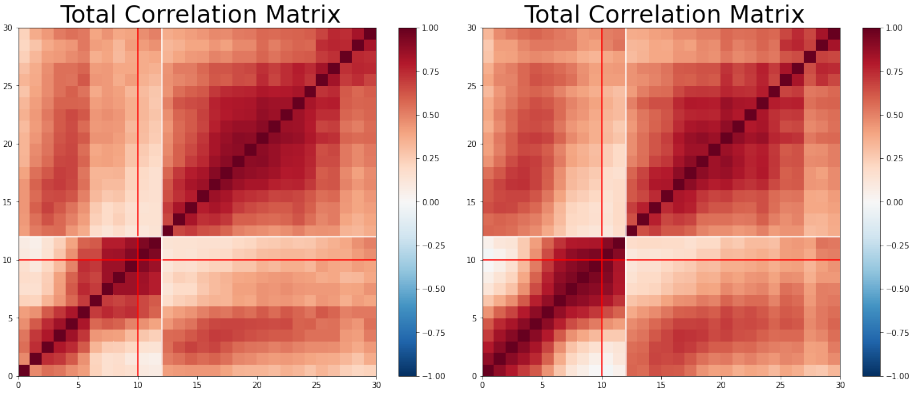

(c) correlation matrix, no osc (d) correlation matrix, max osc

Figure 9.7: Total fractional covariance matrices for (a) null oscillation and (b) maximum oscillation, and the corresponding correlation matrices (c) and (d). Bins 0-9 are the original bins of the 1e1p selection (indicated by red line). Bins 10-11 are the additional high energy 1e1p bins (indicated by white line). Bins 12-29 are the 1μ1p bins. The z-axis has been capped to be consistent with each other for comparison.

to reduce bias in cases of low event statistics when used in goodness of fit tests when compared to the individual Neyman or Pearson methods. Therefore the total covariance matrix becomes:

$$M_{tot} = M_{sys} + M_{stat} \tag{9.6}$$

where M_{stat} is zero except for the diagonal. The diagonal terms are:

$$M_{stat:i,i} = \frac{3}{\frac{1}{x_i} + \frac{2}{\mu_i}} \tag{9.7}$$

where x_i is the observed number of events. This M_{tot} is the covariance matrix form used throughout this analysis.

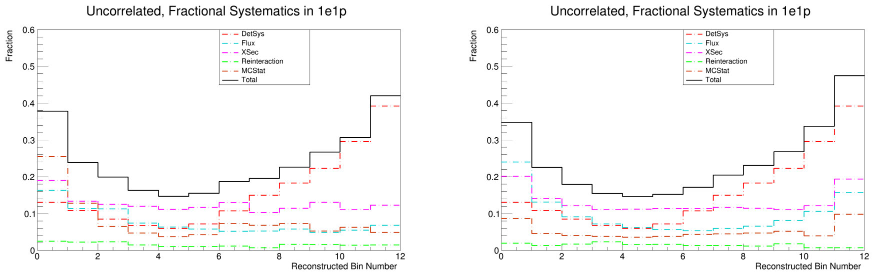

(a) $1e1p$ selction, no osc (b) $1e1p$ selction, max osc

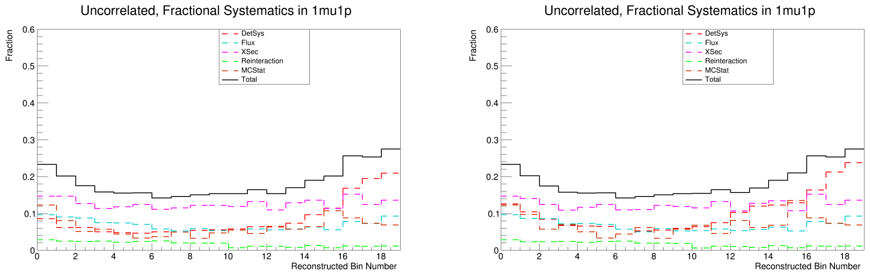

(c) $1\mu1p$ selction, no osc (d) $1\mu1p$ selction, max osc

Figure 9.8: Systematic uncertainties to the $1e1p$ selection (a,b) and the $1\mu1p$ selection (c,d) broken up by contribution type. The y axis has been set to the same value (0.6) in all plots.

The process outlined here is used in the rest of this thesis to apply uncertainties to the simulation for a variety of selections and reconstructed variables. Additionally, in the 3+1 oscillation study, it must be recalculated for each set of oscillation parameters as different contributions will have different event probabilities. The contributions from the flux, neutrino–nucleus interaction model, and the hadron re-interaction model need to be re-scaled depending on the relative contributions of the different neutrino interactions at different parameters.

Chapter 10

The π^0 Background to ν_e CCQE 1e1p

Chapter 8 described the π^0 selection and used it to verify the shower reconstruction on data. However in that study, all distributions shown were area-normalized to the number of data events. The π^0 sample has further use to the analysis as it is an important background to the $1e1p$ selection. Events with one decay photon close to the neutrino interaction vertex and one further away may be mis-reconstructed as 1e1p.

Section 10.1 describes events with a π^0 in the final state. Section 10.2 shows the π^0 selection again but without normalization of the prediction and with the systematic errors applied as described in Chapter 9. Then Sections 10.3, 10.4, 10.5, and 10.6 show the use of this sample as a sideband including: determining π^0 event weights due to disagreement between data and prediction, a cross check of the MPID network, and modeling $1\gamma 1p$ events.

10.1 π^0 events in MicroBooNE

Figure 10.1 shows the different mechanisms that create π^0 's in MicroBooNE. Simulation events with a simulated π^0 from the BNB simulation sample that pass the π^0 selection were analysed for this plot. There are five different mechanisms at play: quasi-elastic scattering, resonant production, deep-inelastic scattering, coherent production, and meson exchange current interactions. Some of these interaction types were described in Section 2.2, but are discussed here in the context of events creating a π^0 .

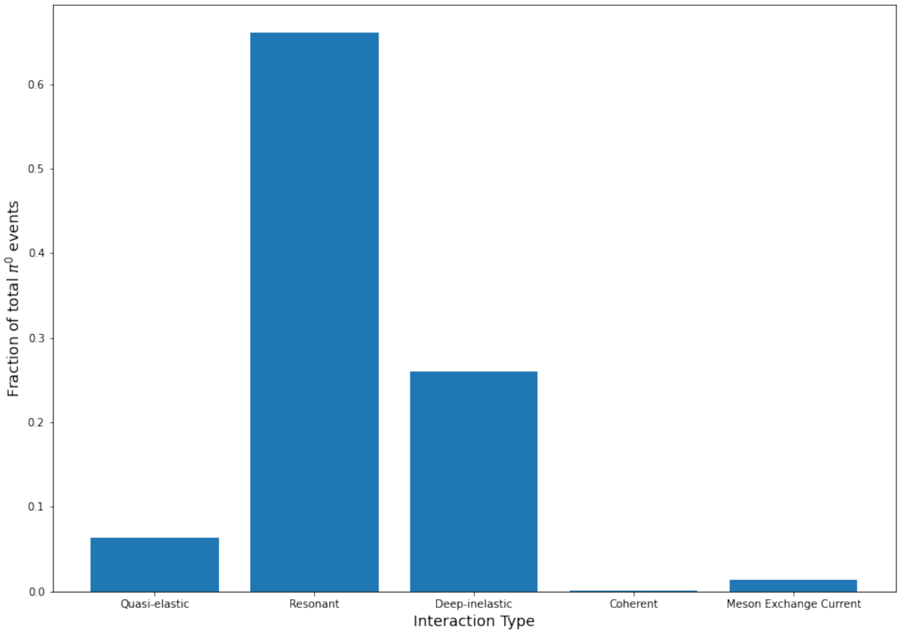

Figure 10.1: Bar graph illustrating the interaction types which produce π^0 's in MicroBooNE.

π^0 events here are classified as any event with a π^0 . Therefore a subset of events may also come from $\pi^{\pm}$ events that charge-exchange into a π^0 . These are the quasi-elastic and meson exchange current interactions, which make up a relatively small contribution of selected events. The π^0 events are primarily produced through the Δ resonance (hence the use of reconstruction of the Δ invariant mass as a π^0 selection cut in Section 8.1.1). In resonant π^0 production, a neutrino interacts with a neutron or a proton which excites the nucleon into a Δ^0 or Δ^+. This delta then decays back into a neutron or proton, emitting a π^0 [73]. This mechanism is:

$$ResonantNC : \nu N \to \nu \Delta^0 \to \nu \pi^0 N \tag{10.1}$$

$$ResonantCC : \nu(n/p) \to \mu^- \Delta^{+/-} \to \mu^- \pi^0 (p/n) \tag{10.2}$$

Figure 10.2 shows the Feynman diagrams for the NC π^0 resonant and CC π^0 resonant channels.

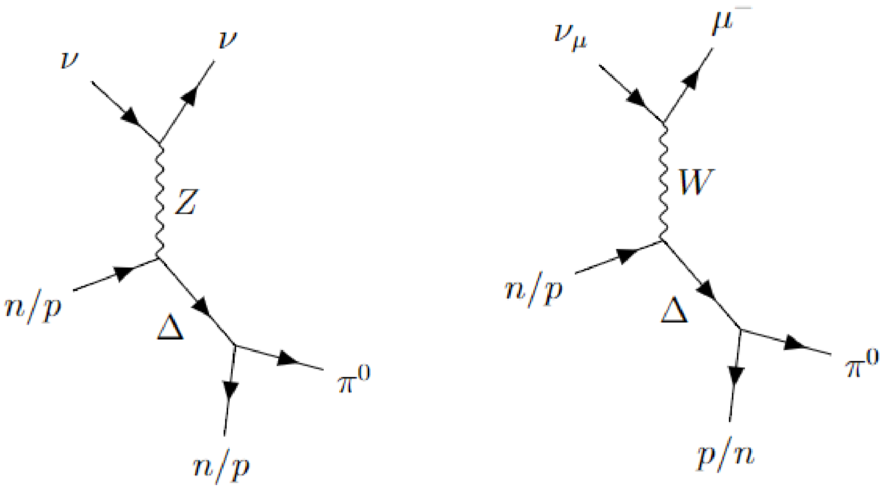

(a) NC (b) CC

Figure 10.2: Feynman diagrams showing the π^0 resonant channel

The second largest source of π^0 events are deep inelastic scattering events (DIS) [74]. DIS was discussed in Section 2.2. The complicated final state topologies may include π^0 's. This cross-section is difficult to model as it involves complicated nuclear effects. More experimental data is needed to fully model this process, though recent progress has been made based on results from the MINERvA collaboration [75].

The final mechanism for NC π^0 events is coherent production. In this case a π^0 is created from the sum of scattering from all the nucleons

$$Coherent : \nu A \rightarrow \nu A \pi^0 \tag{10.3}$$

This makes up a small fraction of the simulated events.

Regardless of how the π^0 is produced, it very quickly decays into two photons ($\tau_{\pi^0} \sim 8e10^{-17}\ s$ [73]). These decay photons may be mistakenly identified as a single electron if one shower is mis-reconstructed or one shower exits the detector making this an important background to model correctly. This chapter shows the use of the π^0 selection as a sideband in the $1e1p$ selection, the calculation and applications of π^0 events in simulation, and a study of 1γ1p-like π^0 events. Note that much of the work described here was recently published in Reference [37]. The relevant sections of that paper were written by the author of this thesis and are repeated here with additional details.

10.2 The π^0 Sideband

The first use of this sample is to check the agreement of simulation with data. Using the selection presented in Section 8.1.1, the simulation events are POT scaled to match the data POT. Here and in other comparisons to data, the simulation has been tuned within the MicroBooNE collaboration using fits to the T2K “CCpi0” ν_μ data. The ν_e cross section assumes the same underlying cross section parameters; hence it differs from the ν_μ cross section mainly due to lepton-mass threshold effects [49].

The resulting π^0 mass peak is shown in Figure 10.3 with flux, cross-section, and detector systematics as described in Chapter 9. Both the standard simulation samples and the high POT π^0 samples are used. These samples were described in detail in Table 6.1. The standard simulation events that match the type of events in the π^0 sample are removed and replaced with those from the high POT sample. This prevents overlap between the types of events in each sample. If this step was not taken, some π^0 events would essentially be double counted. The POT of each simulation sample is independently POT scaled to match the data. Adding in the high POT π^0 sample therefore has no impact on the shape of the distributions, but decreased the simulation statistical error.

The simulation has been broken into various categories based off the type of interaction. As in Section 8.1.1,"NC π^0 " are neutral current π^0 events with a well reconstructed vertex, which is a vertex within 5 cm of the true generated vertex. "CC π^0 " are defined similarly for charged current π^0 . "Offvtx π^0 " are π^0 events with poorly reconstructed vertices. There are 4 background categories without a true π^0 . These are divided into Offvtx, ν_μ backgrounds, ν_e backgrounds, and cosmic backgrounds. These have been separated in some figures to make the contribution

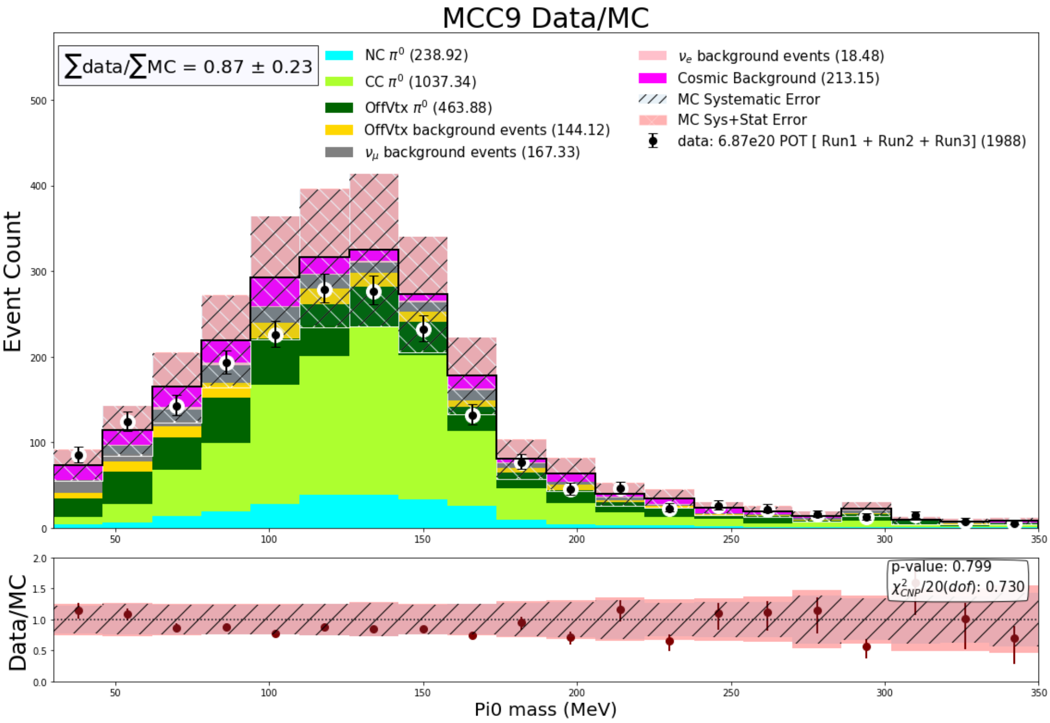

Figure 10.3: Shows the calculated π^0 mass for events passing all selection cuts. The simulation has been normalized to the run 1,2, and 3 data POT. Flux, cross-section, and detector systematics are included. The top panel shows the event count histogram while the bottom shows the ratio of data/simulation(MC) in each bin.

of each type clear. Figure 10.3 also shows the full systematic uncertainty on the simulation.

One can further test the reconstruction quality by reconstructing the Delta baryon invariant mass as resonant interactions are the dominant interaction types. This variable is used in the π^0 selection (Section 8.1.1). Recall that the Δ can decay into a proton+π^0 . The reconstructed neutrino vertices used in this analysis target events with two prongs. In a resonant event those two prongs may be the proton + one decay photon. This reconstruction of the Δ invariant mass is then performed by finding the invariant mass of the 4-vector of the π^0 from the reconstructed photons, and the track identified as the proton by 3D reconstruction. The result is shown in Figure 10.4. A convincing peak is observed. There is a tail of high invariant mass that represents poorly reconstructed events and events from other interaction types.

In each of these distributions, the ratio of the number of data events over the number of simulation events is 0.87 ± 0.23. This agrees with 1.0 within uncertainty,

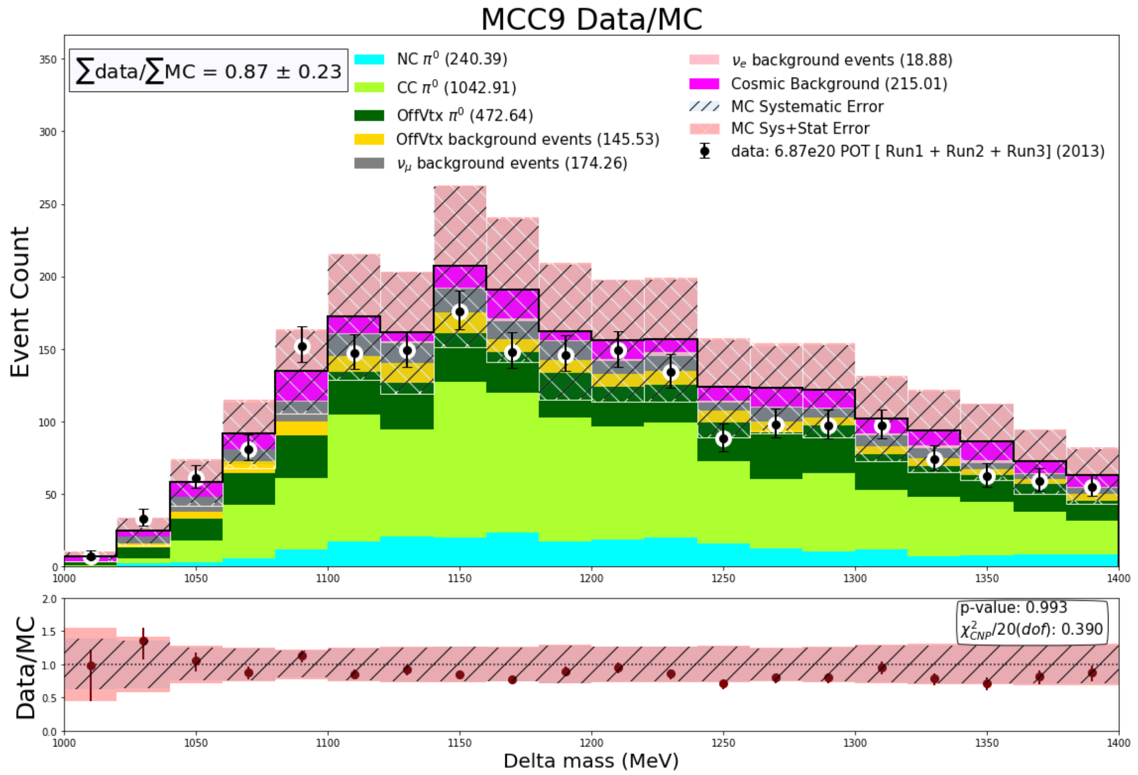

Figure 10.4: Shows the calculated Delta baryon mass for events passing all selection cuts. The simulation has been normalized to the run 1,2, and 3 data POT. Flux, cross-section, and detector systematics are included. The top panel shows the event count histogram while the bottom shows the ratio of data/simulation(MC) in each bin.

but is low. It can be seen in the lower ratio plot that the ratio in each bin also agrees with 1.0 within uncertainty. As this effect is seen across various MicroBooNE analyses [76], this indicates that there is a real effect due to π^0 production mis-modeling. In order to account for this here, a re-weighting scheme has been applied. Simulated π^0 events have been scaled based on the true π^0 momentum of the event.

The reconstructed π^0 momentum distribution is shown in Figure 10.5. In the bottom panel it is noted that as momentum increases, the ratio in general decreases. This further motivates the use of π^0 momentum for determining weights that can be used to correct the simulation prediction.

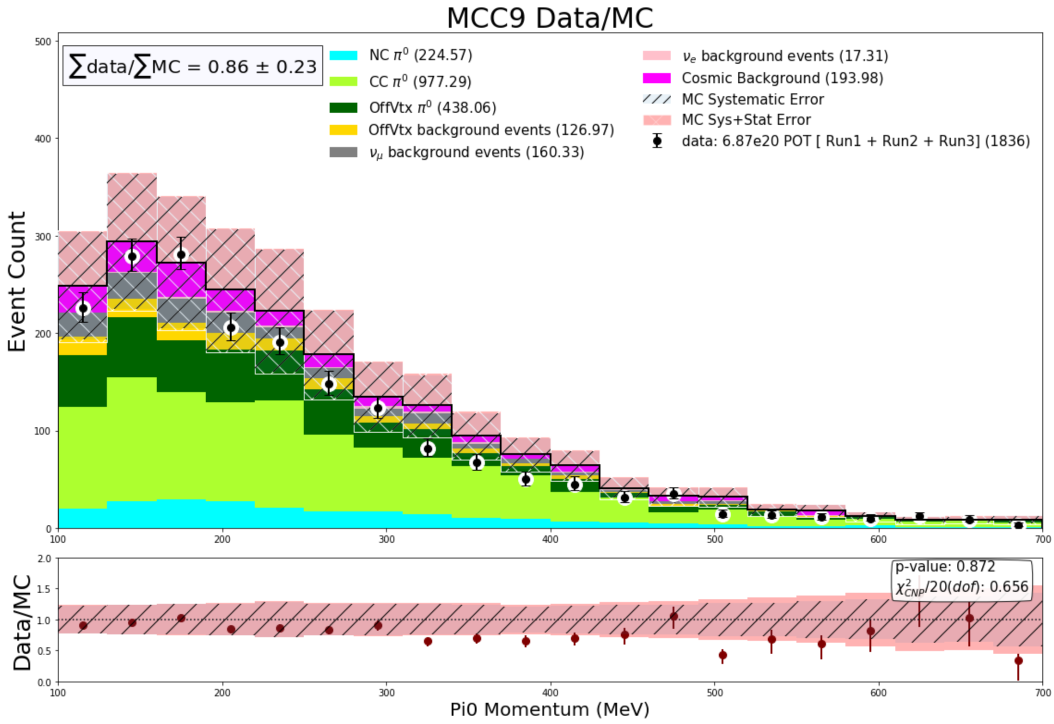

Figure 10.5: Shows the calculated π^0 momentum for events passing all selection cuts. The simulation has been normalized to the run 1,2, and 3 data POT. Flux, cross-section, and detector systematics are included. The top panel shows the event count histogram while the bottom shows the ration of data/simulation in each bin.

10.3 Determination of π^0 weights

As the weighting is performed in terms of π^0 momentum, it is important to first look at the performance of this reconstructed kinematic variable. Fig 10.6 shows the momentum resolution of selected π^0 events. This distribution gives confidence in using this variable, even though the sub-leading photon energy is often under reconstructed as shown in Figure 8.6. The resolution is symmetric.

The first step in this process is to break the sample up into CC and NC events as one cannot assume the weights are the same. This is done by making use of the MPID network described in Section 6.8. The MPID muon score is used here to separate out the CC and NC π^0 events. Figure 10.7 shows this score distribution. The NC π^0 distribution peaks near zero in this variable, while the CC π^0 distribution peaks near one making this a useful variable to separate them.

A cut on the MPID muon score can then be used to differentiate the two samples. Figure 10.8 shows what the purity of each sample is as the cut value is changed.

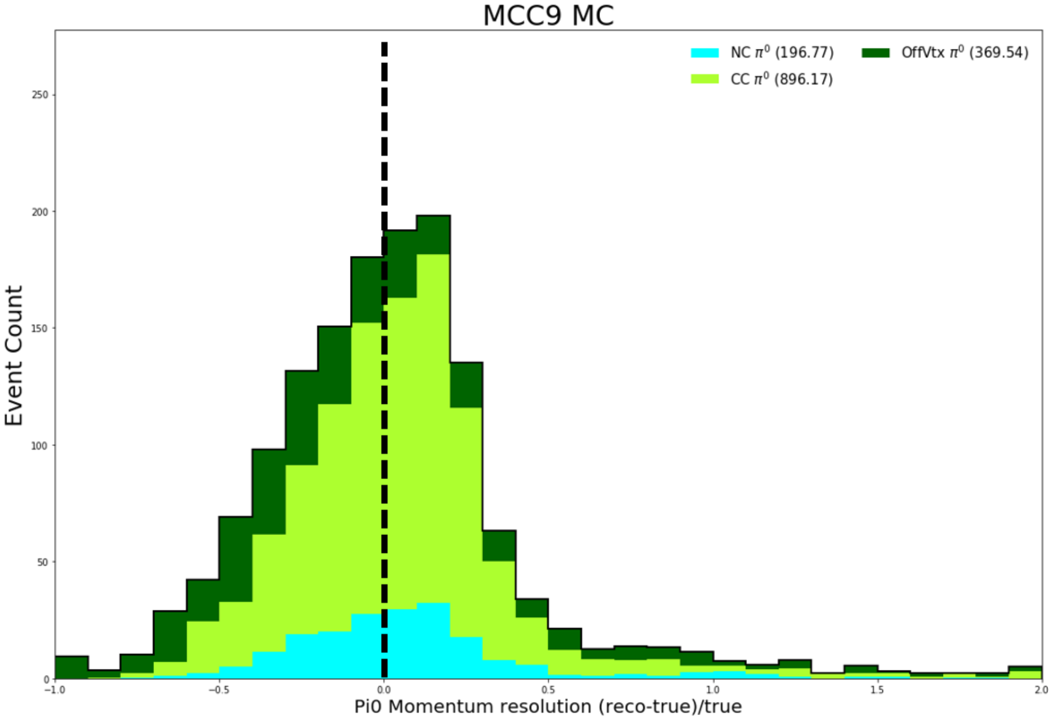

Figure 10.6: The pi0 momentum resolution (reconstructed - true)/true for runs 1+2+3 simulation samples. The black dashed line indicates resolution equals 0.0 to help guide the eye.

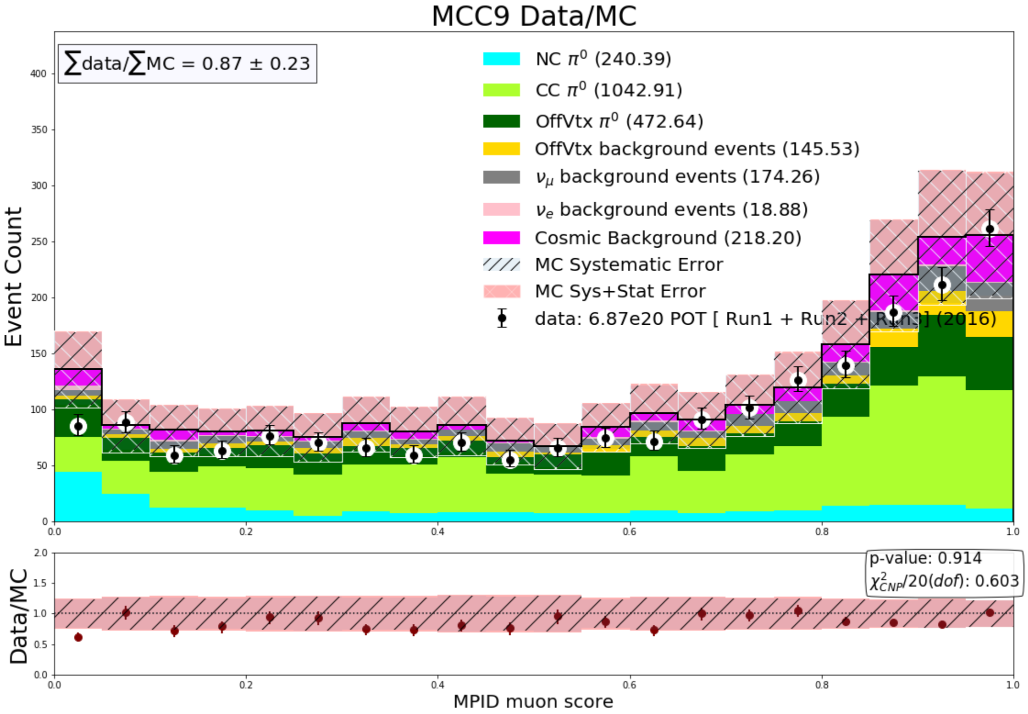

Figure 10.7: This plot shows the MPID muon score for run 1, 2, and 3. The simulation POT is normalized to the POT of the data. Flux, cross-section, and detector systematics are included. The top panel shows the event count histogram while the bottom shows the ratio of data/simulation in each bin.

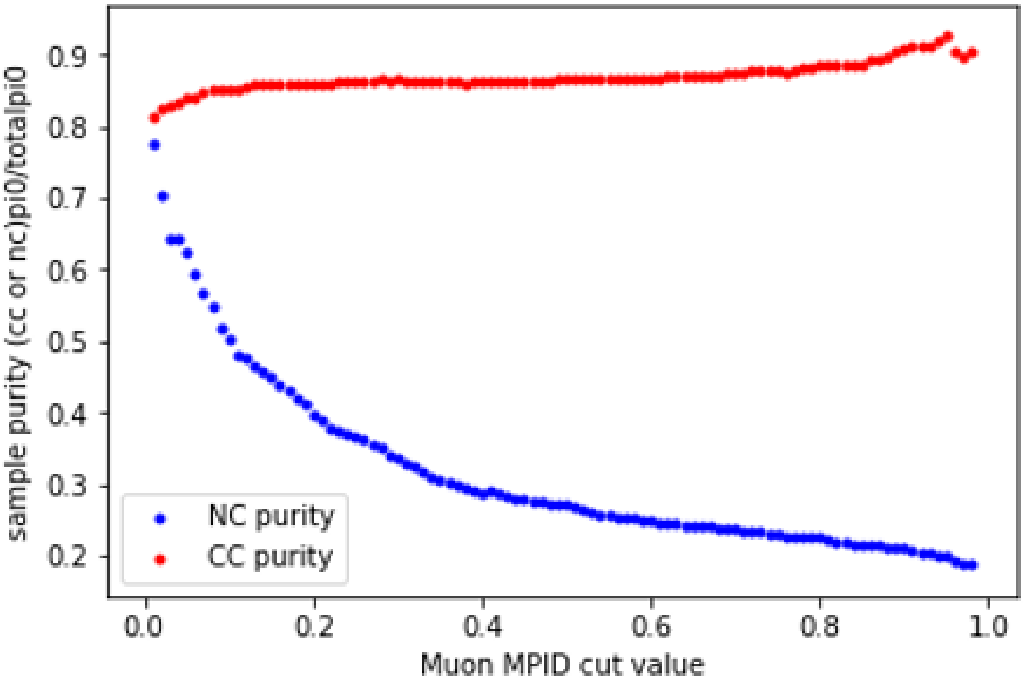

Figure 10.8: This plot shows the purity ((CC or NC π^0)/total π^0) of both the NC and CC pi0 samples at various cut values of the MPID muon score.

Here purity is the number of CC or NC events out of all of the selected π^0 events with the given cut value. A cut value of 0.05 was chosen as this keeps the purity of both samples above 0.60. Events below this value are considered to be the NC sample and events above make up the CC sample. The CC and NC samples are then treated separately to determine the simulation weighting.

The simulation in each sample is then broken into two categories: good and background. Good simulation events for the purpose of this re-weighting study includes all selected events which contain a true π^0 in the final state. Simulation and Data from runs 1, 2, and 3 are used in this process as well as the specialized high POT π^0 samples. The final re-weighting is done based on a fit to the distribution R in π^0 momentum. R is defined as:

$$R = \frac{\text{(Data - background) : unfolded reco momentum}}{\text{(Good simulation Events): true momentum}} \tag{10.4}$$

The numerator represents ”good” data events, with the reconstructed distribution unfolded back to truth. To get the data minus background reconstructed

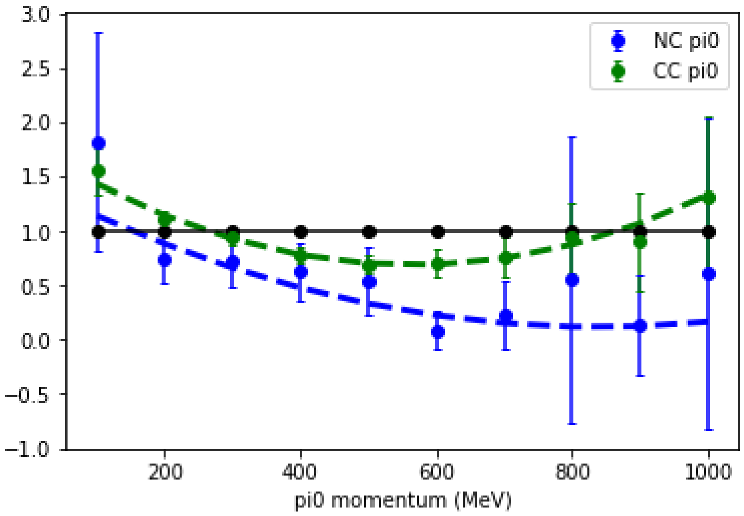

Figure 10.9: This plot shows the R distribution in terms of π^0 momentum for each the NC π^0 and CC π^0 samples. The best fit polynomials from equations 10.5 and 10.6 are shown. The error bars are statistical only.

momentum distribution, the expected background based of simulation is removed from each bin. In simulation, "good" events are considered to be all those with a true π^0 in the final state, both on and off vertex.

Unfolding was performed using the RooUnfold package [77]. The Bayes method is used with 4 iterations. The unfolding matrix was constructed using the simulation events. The resulting R distribution is shown in Figure 10.9. A polynomial has been fit to each distribution. These fits give re-weighting formula where p is the true π^0 momentum in MeV. The resulting formulas are:

$$CC \quad Weight = (3.43e10^{-6})p^2 - (0.0039)p + 1.784 \tag{10.5}$$

$$NC \quad Weight = (1.89e10^{-6})p^2 - (0.0032)p + 1.442 \tag{10.6}$$

The weight formula is then applied to every simulation event that contains a true π^0 . The resulting π^0 reconstructed mass distribution is seen in Figure 10.10. The reconstructed π^0 momentum is shown separately for the NC π^0 and CC π^0 samples in Figure 10.11. These figures were created for use in Ref [37]. The weighted simulation is indicated by the red dashed line on the plot. Additional π^0 kinematic plots with the weights applied can be seen in Appendix C.

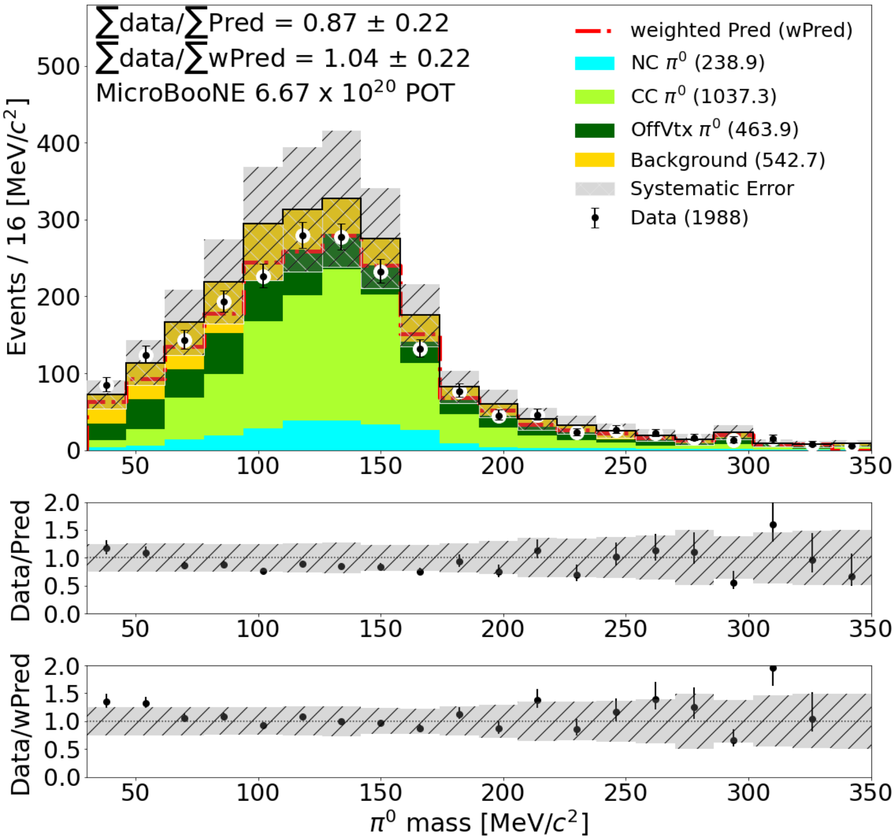

Figure 10.10: The reconstructed π^0 mass variable for events passing the π^0 selection criteria. The colored stacked histograms represent the standard simulation (MC) prediction. The red dashed line is the total weighted (wMC) prediction. The data points are shown by the black points. The lower two panels show the data/MC ratio and data/wMC ratio respectively. The $\chi^2_{\mathrm{CNP}}/20(dof) = 0.709$ with a p-value of 0.821 for the MC prediction. The $\chi^2_{\mathrm{CNP}}/20(dof) = 0.778$ with a p-value of 0.744 for the wMC prediction [37].

A Gaussian fit to the weighted Monte Carlo simulation in Figure 10.10 gives a mean of 136.18 ± 1.716 and a width of 41.09 ± 1.724. A Gaussian fit to the data in Figure 10.10 gives a mean of 129.59 ± 2.585 and a width of 43.83 ± 2.631. Additionally, a p-value of 0.757 is calculated, indicating good agreement between data and MC. This weight formula will further be applied to selected $1e1p$ and $1\mu1p$ events which contain a true π^0 in the final state. Further studies on the weights used can be found in Appendix C.

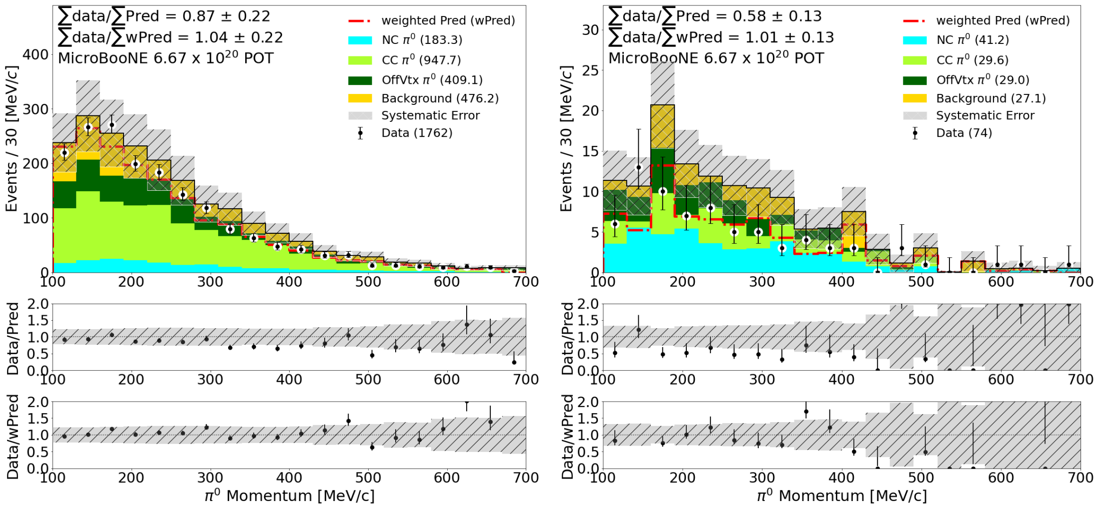

(a) CC Sample (b) NC Sample

Figure 10.11: Reconstructed π^0 momenta for the CC (a) and NC (b) samples. The colored stacked histograms represent the standard simulation (MC) prediction. The red dashed line is the total weighted (wMC) prediction. The data points are shown by the black points. The lower two panels of each figure show the data/MC ratio and data/wMC ratio respectively. In the CC sample, the $\chi^2_{\mathrm{CNP}}/20(dof) = 0.619$ with a p-value of 0.902 for the MC prediction and the $\chi^2_{\mathrm{CNP}}/20(dof) = 0.405$ with a p-value of 0.991 for the wMC prediction. In the NC sample, the $\chi^2_{\mathrm{CNP}}/20(dof) = 0.555$ with a p-value of 0.944 for the MC prediction and the $\chi^2_{\mathrm{CNP}}/20(dof) = 0.490$ with a p-value of 0.972 for the wMC prediction [37].

10.4 Application of π^0 weights

The π^0 weights described above are applied to all events with a true π^0 in the final state in all three selections: the $1\mu 1p$ selection, the $1e1p$ selection, and the π^0 selection. Note that in the $1\mu 1p$ selection, π^0 events are a very small background so the effect is negligible.

Figure 10.12 shows the effect of the different NC π^0 fit functions on the $1e1p$ backgrounds. Appendix C shows studies into the use of these alternate fit functions. ”Standard” here refers to the 2^{nd} degree polynomial that was chosen. The total number of backgrounds with different fitting schemes are (run 1+2+3 POT scaled) are:

- 10 bin 2^{nd} degree polynomial: 1.03
- 5 bin 2^{nd} degree bolynomial: 1.29

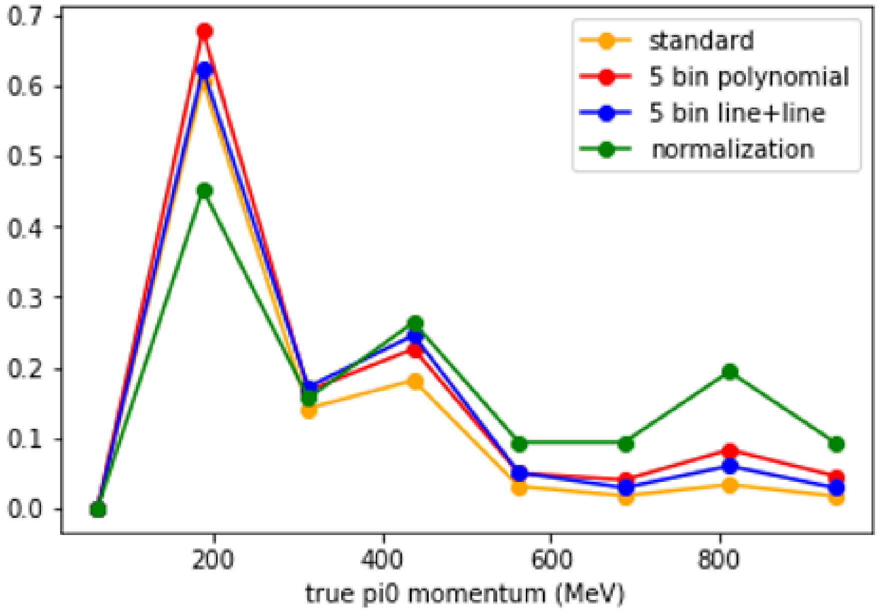

Figure 10.12: Effect of different NC π^0 fit functions on the NC π^0 backgrounds to the 1e1p

- 5 bin line+line: 1.21
- Normalization: 1.35

In the case of more than one π^0 , the particle used in determining the weight is that of the highest momentum. π^0 weights have been applied to all distributions for both $1\mu 1p$ and $1e1p$ selections (and side bands) throughout this document unless otherwise noted.

Further, while it is possible in principle to reduce the uncertainties on events with a π^0 in the final state when the weighting is performed it is not necessary to do at this point. This is because the uncertainty is currently dominated by flux and cross section systematics, so reducing the uncertainty in the fit values will have a small impact on the total uncertainty. The $1e1p$ selection is also limited by statistical uncertainty.

10.5 Muon MPID distribution cross-check

Another use of the π^0 sideband is to examine the effect on π^0 events of one of the specific cuts in the $1e1p$ selection (Chapter 11). This cut is the use of the ratio of MPID image scores for photons and electrons to identify potential background events with π^0 's in them for the purpose of the $1e1p$ selection. Specifically,the goal of this selection criteria is to help remove the π^0 events that did not have a second reconstructed shower from the $1e1p$ selection.

The distribution of the score ratio of $\gamma/(\gamma+e)$ is in Figure 10.13 for events in the π^0 selection. The cut value that will be used will remove events in the $1e1p$ selection with this ratio is > 0.67 (shown on the plot). The value of the cut was chosen based on MPID simulation results, not on the π^0 sample. It is implemented as removing events with $\gamma/e > 2$, but since the γ/e tail is long leading to many empty bins, it is more convenient to present the ratio $\gamma/(\gamma+e)$ to demonstrate the data-to-simulation agreement. This is a very loose criteria, and one can see that many π^0 's actually pass this cut. This is likely due to the presence of delta rays or Michel electrons in the event image. Figure 10.13 is a useful reference to see data/simulation agreement in this variable. There are also no unexpected features. There is good shape-agreement between data and simulation.

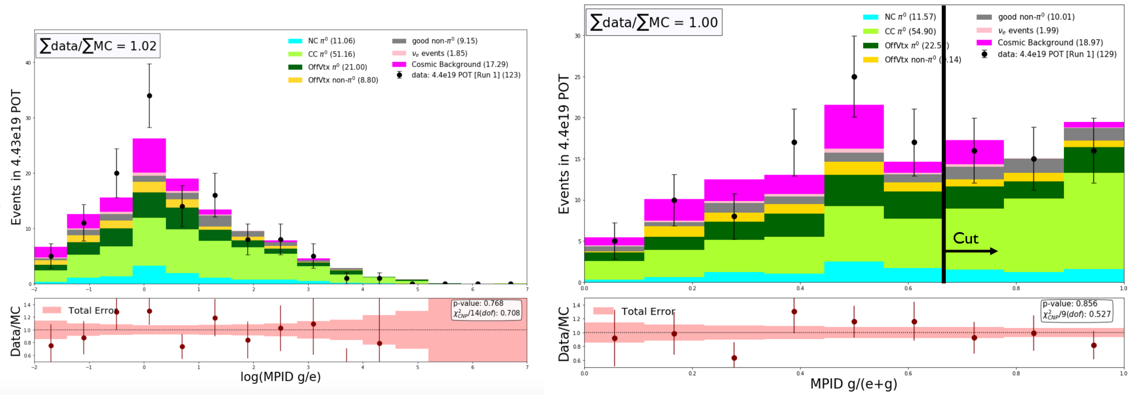

(a) $\log(\gamma/e)$

(b) $\gamma/(\gamma+e)$

Figure 10.13: The distributions of MPID image scores presented as $\log(\gamma/e)$ (a) and $\gamma/(\gamma+e)$ (b) for events passing the π^0 selection. simulation has been normalized to the data in for the purpose of determining shape agreement.

10.6 Isolating Events Similar to 1e1p

The π^0 sample finally provides a useful check of our reconstruction for events with a proton and a shower attached at the vertex. This is done by applying a cut on the muon MPID score < 0.1. The muon MPID distribution can be found in the above section (Figure 10.7). The DL reconstruction finds events with two prongs at the vertex. In the case of the π^0 selection, the majority of events have a muon produced in a CC neutrino interaction. The DL vertex finding algorithm. then often finds 1 muon and 1 of the 2 photons connected at the vertex, with the other reconstructed photon disconnected from the vertex. A small proton is often missed in these events. In other cases a muon and proton are found with 2 disconnected showers.

Once these types of events are removed by removing events with a muon, the selection is then dominated by events with 1 proton and 1 photon connected at the vertex. This topology matches the $1e1p$ topology and therefore allows us to isolate these events and analyze the data/simulation agreement. This sample is similar to the NC sample used to determine the π^0 weights. Due to the reconstruction process the NC π^0 reconstructed events often have the topology of 1γ1p at the vertex, with a second disconnected γ.

First, the proton energy and the energy of the leading shower is examined. The proton is the track reconstructed in the event, since events with muon tracks were removed. π^0 weights discussed above are applied to the simulation, and only simulation stat errors are used. There is excellent data/simulation agreement for both the proton in Figure 10.14 and the leading shower in Figure 10.15.

Next, treating the leading shower as the electron, ignoring the second shower, and using the proton, the energy of the neutrino is reconstructed as though it were a $1e1p$ event using E_ν^{range} as discussed in Section 6.9. The result can be seen in Figure 10.16. There is agreement across the full energy spectrum. This study gives us further confidence in our ability to reconstruct the energy of low-energy $1e1p$ events.

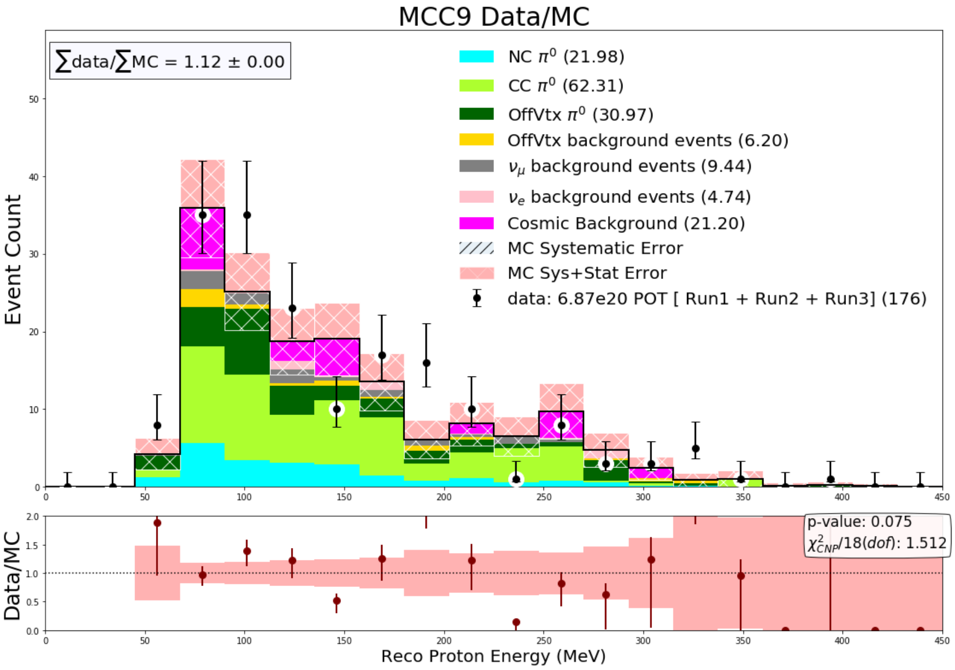

Figure 10.14: The calculated proton energy for events passing all selection cuts. The simulation POT has been normalized to the run 1,2, and 3 data sets POT and then re-weighted in true π^0 momentum.

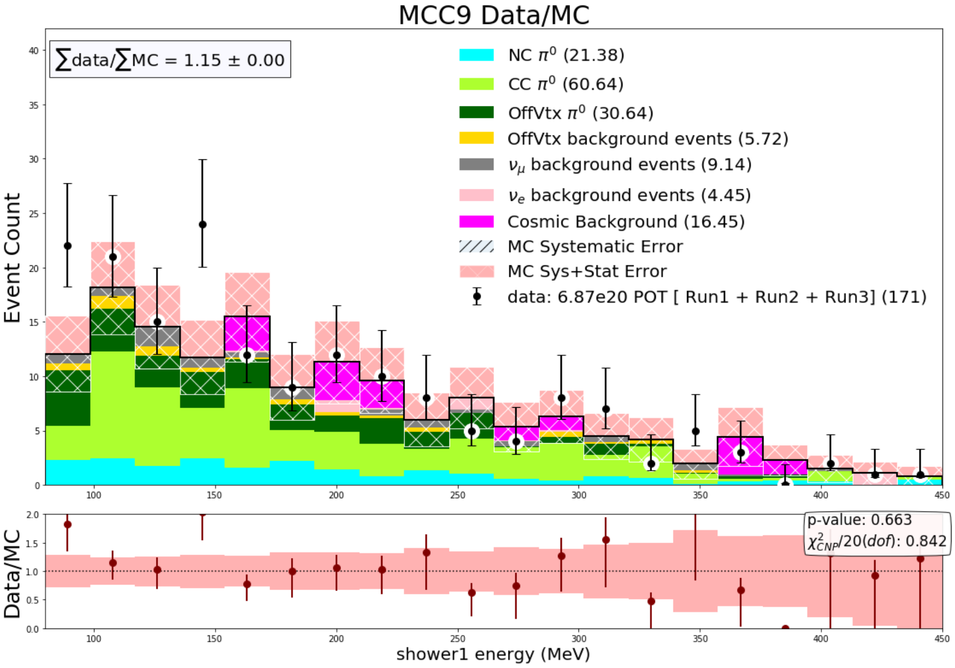

Figure 10.15: The calculated electron energy for events passing all selection cuts. The simulation POT has been normalized to the run 1,2, and 3 data sets POT and then re-weighted in true π^0 momentum.

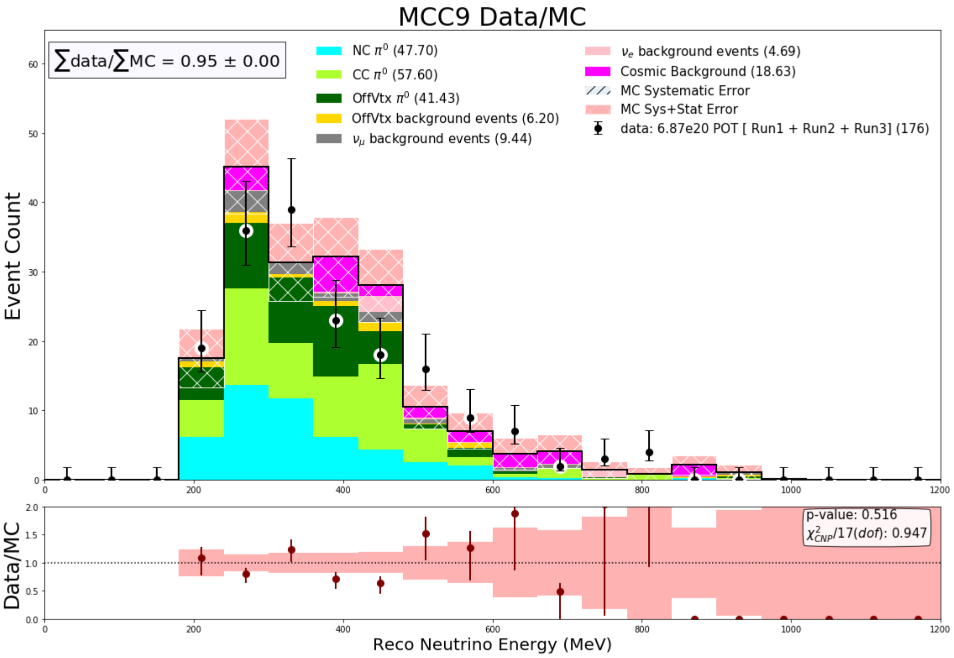

Figure 10.16: The calculated neutrino energy for events passing all selection cuts (treating the event as a 1*e*1*p* event). The simulation POT has been normalized to the run 1,2, and 3 data sets POT and then re-weighted in true π^0 momentum.

Chapter 11

ν CCQE 1l1p Selection

Now that the reconstruction is complete and there is a more complete understanding of the backgrounds and systematic uncertainty, we can proceed on to the target event selection. This chapter outlines the selection and shows a comparison of the data to the MiniBooNE low-energy excess (LEE). Section 11.1 describes the BDT ensemble formalism used to make the selections. Section 11.2 describes the selection itself. Finally, Section 11.3 compares these data selections to a specific MiniBooNE low-energy excess model.

11.1 The BDT Ensemble

The selections shown here utilize Boosted Decision Trees (BDTs). Decision trees are a machine learning model. It has a flowchart like tree structure. Each node denotes a feature of the data set and each decision make can be thought of as a branch. In the application used here the output is a score from 0 to 1 indicating the probability that a given event is the sought after type ($1e1p$ or $1\mu1p$ final state topology). The "boosted" part of a BDT means that instead of a single tree, inside the algorithm a series of decision trees are used. The first tree is trained on all the events, then a second tree is trained on a smaller sample, half of which were classified by the first tree [78]. The next tree is trained on examples where the first two give differing results, and so on. This method has been used in many HEP experiments, including MiniBooNE [79].

One of the main problems that arises with BDTs is over-fitting. This means that the BDT has memorized the content of the training set, but hasn't actually learned any features. So, when it is given a new example not in the training set it fails. An ensemble of BDTs is one way to combat this. In an ensemble, a number of BDTs are trained in parallel where each BDT is trained on a random subset of the simulation sample. This reduces both bias and variance in the final results when compared to a single BDT [80].

This implementation of BDTs is performed using Python XGBoost library [81]. Both selections are trained independently on each of the three runs resulting in six BDT ensembles. The $1\mu1p$ BDTs contain 10 individual trees and the $1e1p$ BDTs contain 20. Each individual tree is trained on 50% of the simulation samples for that run presented in Table 6.1. The $1e1p$ ensembles are also trained on a sample of high stats low energy ($E_\nu < 500\ MeV$) ν_e intrinsic events with: Run 1 = 6.05 $\times10^{23}$ POT, Run 2 = 7.49 $\times10^{23}$ POT, and Run 3 = 5.97 $\times10^{23}$ POT. This was done to enhance performance in the MiniBooNE excess range. Data is run through all trees in a sample and the score is taken as the average from each tree. When using the ensemble on simulation samples, only BDTs that don't contain a given event in its training sample are included when calculating the average BDT score.

11.2 $1l1p$ Selection

The next step is to perform a selection on the simulation samples and data to isolate the two samples of $1e1p$ and $1\mu1p$ events. Recall in Section 6.10, a general preselection has been applied to both the data and simulation samples at this point and the $1e1p$ and $1\mu1p$ selections have been broken up by an orthogonality cut. Following the preselection, each use ensembles of BDTs trained independently for each date run for each selection.

Each BDT categorizes events on the basis of kinematic measurements. These variables are related to transverse momentum, energy, angle, and combinations that test the correlations between these variables. Four measurements related to ionization charge are also included: total charge within 5 cm of the vertex (both), shower pixel fraction in the electron prong (1e1p only), shower pixel fraction in the proton prong (1e1p only), and the ratio of the number of shower pixels in the image to the number of shower pixels connected to the electron prong(1e1p only) . The 1μ1p BDT ensemble has an additional transverse ϕ angle variable in order to capture information on planarity of the event. Table 11.1 lists all of these variables and defines which selection the variable is used in. They have been grouped by type.

The BDT selection relies heavily on the kinematic variables. These help select specifically for two-body scattering. Table 11.2 defines many of the variables used in the BDTs. Figure 11.1 shows the importance of various BDT training variables in each selection for Run 1 (similar behaviour was seen for Runs 2 and 3). Variables with a higher importance have more impact on the final BDT ensemble score of an event.

The most important variables in the $1e1p$ BDT have to do with the shower variables. Importance here means having the largest effect on the BDT scores. This is likely due to to a large number of backgrounds not containing a well reconstructed shower. Meanwhile, the most important variable in the $1\mu1p$ BDT ensemble is the transverse momentum ratio. The next two important variables are x_{Bj} and QE consistency. The transverse momentum ratio is expected to be near zero for two-body scattering since the neutrino enters along the z axis. Similarly, x_{Bj} and QE consistency are dependent on how well two-body scattering describes the event, making them powerful variables.

The BDT scores are normalized to the range $[0, 1]$, where higher values indicate a higher probability for the event to come from a true interaction of the type targeted for the selection. The analysis requires the average BDT score within the ensemble to be > 0.95 for the 1e1p ensemble BDT and > 0.50 for the 1μ1p BDT.

Finally the selections have one more set of final selection criteria designed to remove common backgrounds that pass the BDTs:

Table 11.1: The suite of BDT training variables. Variables used in the $1\mu1p$ BDTs and the $1e1p$ BDT are noted. The analysis has been designed with substantial variable overlap. If a $*$ appears, the variable is used in the boosted frame.

Variable	Used in $1\mu1p$ BDT	Used in $1e1p$ BDT
Variables Used in BDTs, Based on Ionization		
Charge within 5 cm of vertex	Yes	Yes
Shower charge in event image / shower charge clustered as electron	No	Yes
Proton shower fraction	No	Yes
Electron shower fraction	No	Yes
Variables Used in BDTs, Related to Energy Measurements		
Neutrino Energy	Yes	Yes
Energy of electromagnetic shower	No	Yes
Lepton length	Yes	Yes
Proton length	No	Yes
$p_z - E_\nu$	No	Yes
Variables Used in BDTs, Related to 2-Body Scattering Consistency		
Bjorken's x	Yes *	Yes *
Bjorken's y	Yes *	Yes *
QE Consistency	Yes *	Yes *
Q_0	Yes	Yes
Q_3	Yes	Yes
Variables Used in BDTs, Related to Transverse Momentum		
α_T	Yes	Yes
Event p_T	Yes	Yes
Event p_T/p ("PTrat")	Yes	Yes
ϕ_T	Yes	No
Variables Used in BDTs, Related to Angles		
Proton ϕ	Yes	Yes
Proton θ	Yes	Yes
Lepton ϕ	Yes	Yes
$\phi_p - \phi_\ell$	Yes	Yes
$\theta_p + \theta_e$	No	Yes
Variables Useful for Comparison, Not Used in Either BDT		
η (Norm. Avg. ionization difference)	No	No
Opening Angle	No	No
x Vertex	No	No
y Vertex	No	No
z Vertex	No	No

1. $M_{\pi^0} < 50\,\mathrm{MeV}/c^2$ (1e1p);
2. the MPID γ/e image score ratio < 2 (1e1p);
3. the MPID muon interaction score < 0.2 if $E_e > 100\,\mathrm{MeV}$ (1e1p);

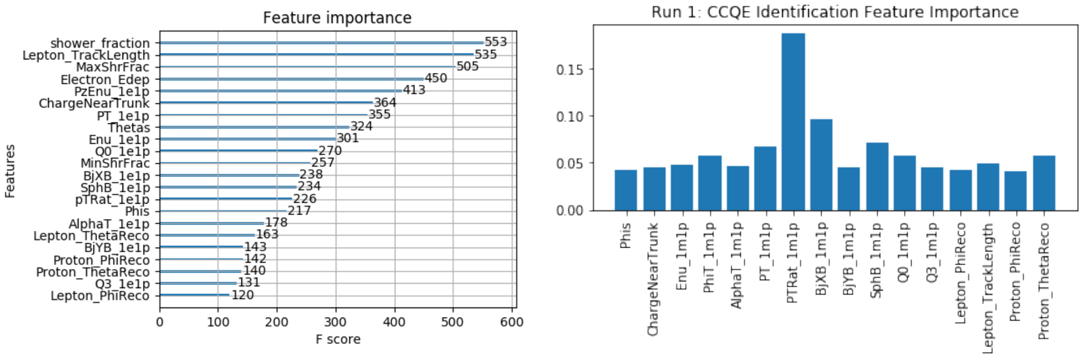

(a) $1e1p$ (b) $1\mu 1p$

Figure 11.1: The Importance of various variables in the BDT ensemble for Run 1 for both the $1e1p$ selection(a) and $1\mu 1p$ selection(b). Note that for the $1\mu 1p$ plot, the importance is normalized to 1.0.

Table 11.2: Summary table of important kinematic variables derived from the reconstruction code used in this analysis and used in the BDT's.

Variable Name	Definition
K_p	Kinetic energy of proton [59]
K_l	Kinetic energy of charged leptons [59, 61]
M_l, M_n, M_p	Masses of the lepton, neutron and proton [6]
$\cos\theta_p$, $\cos\theta_\ell$	p_p^z/p_p, p_ℓ^z/p_ℓ
ϕ_p, ϕ_ℓ	$atan^2(p_p^y, p_p^x),\ \ atan^2(p_\ell^y, p_\ell^x)$
$P_p = (E_p, p_p)$	4-vector of the proton
$P_\ell = (E_\ell, p_\ell)$	4-vector of the lepton
B	Binding Energy for Ar=40 MeV [63]
E_ν^{range}	(Default value of E_ν) Eq.6.3
E_ν^{QE-p}	Eq.6.4
$E_\nu^{QE-\ell}$	Eq.6.5
Δ^{QE}	2-Body scattering Consistency: Eq.6.6
Q^2	$2E_\nu^{range}(E_\ell - P_\ell^z) - M_\ell^2$
Hadronic Energy (E$_{had}$)	$E_\nu^{range} - E_\ell$
Björken's Scaling x (x$_{Bj}$)	$Q^2/2M_n E_{had}$
Björken's Scaling y (y$_{Bj}$)	E_{had}/E_ν^{range}
Opening angle	$\cos^{-1}(\hat{p}_\ell \cdot \hat{p}_p)$
p_T	$\sqrt{(p_\ell^x + p_p^x)^2 + (p_\ell^y + p_p^y)^2}$
p_L	$p_p^z + p_\ell^z$
α_T	$\cos^{-1}\left(-\dfrac{\vec{P}_T^l \cdot \vec{P}_T}{\lvert\vec{P}_T^l\rvert\lvert\vec{P}_T\rvert}\right)$
ϕ_T	$\cos^{-1}\left(-\dfrac{\vec{P}_T^l \cdot \vec{P}_T^p}{\lvert\vec{P}_T^l\rvert\lvert\vec{P}_T^p\rvert}\right)$
p_{fermi}^T	$p_p^T + p_\ell^T$
p_{fermi}^z	$p_p^z + p_\ell^z - E_\nu^{range}$

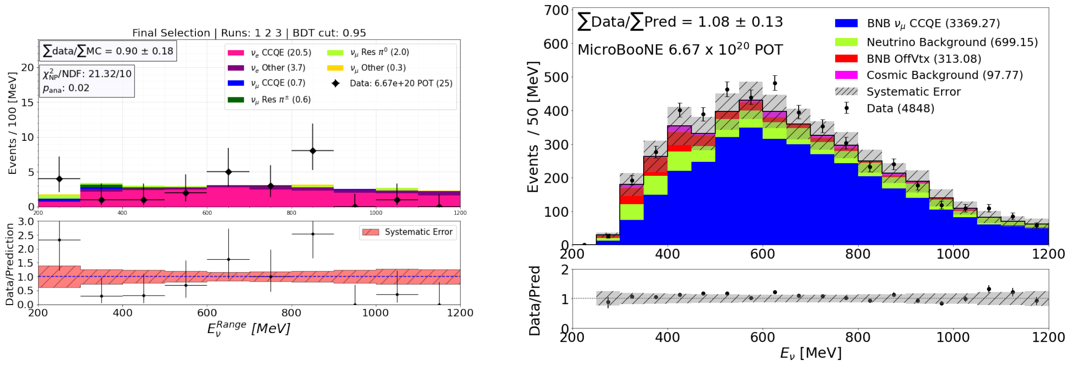

(a) $1e1p$ (b) $1\mu1p$

Figure 11.2: Predicted E_ν^{reco} spectrum for the full 1e1p (a) and 1μ1p(b) selections, with the data selection shown represented by black points. Adapted from Ref [37].

4. the MPID proton score < 0.9 if $E_\nu < 400\,\text{MeV}$ (1μ1p).

Then, for both selections in events with more than one identified vertex passing all the other criteria only the vertex with the highest BDT score is considered.

Figure 11.2 shows the results of applying the selection to both MC and data as used in Ref [37]. The MC has been scaled using the CV weights, the π^0 weights [37], and POT weights to match the data POT. These weights have no sterile neutrino signature. The uncertainties were calculated as discussed in chapter 9. Note that the data is shown here as the plots were taken from [37], but is not yet considered throughout the rest of the this study.

11.2.1 $1e1p$ background fitting

Note that the results shown in the rest of this chapter employ a method to smooth the ν_μ background spectrum to the $1e1p$ spectrum as described in Ref. [37]. This is performed to reduce statistical uncertainty in the predicted spectrum. This method will not be used in the following chapters discussing the 3+1 sterile model search. It would require refitting the ν_μ background spectrum at each set of oscillation parameters as the spectrum may change. This fit would need to be well verified which is not feasible when 25x25x25 parameters sets are tested.

11.3 Comparison to the MiniBooNE LEE

The first use of these selections is to compare the result to the MiniBooNE LEE anomaly. This is shown in Ref. [37] and is summarized here. The model used for comparison in this Section is based off the MiniBooNE LEE signal observed in Ref. [82]. Obtaining this model was not straight forward as there is no consensus on the cause of the anomaly. MicroBooNE developed a purely-phenomenological, simplified model for the LEE. This MicroBooNE LEE signal prediction is obtained by unfolding MiniBooNE simulated and measured neutrino spectra with reconstructed neutrino energy >200 MeV [82] producing a "true" underlying ν_e flux distribution. The revised flux is then applied to ν_e events in the MicroBooNE simulation at truth-level. This LEE signal contribution is added to the beam-intrinsic CC ν_e and misidentified background prediction from the standard simulation to obtain the total predicted event rate under this model.

In this model, there is no observable change in the $1\mu1p$ spectrum. This selection is then used as a constraint using the method originally developed for MiniBooNE [83]. The result is an updated prediction for the $1e1p$ selection and an associated updated covariance matrix incorporating the information provided by the data observation in the $1\mu1p$ compared to its prediction. 25 data $1e1p$ events are selected, while a total of $29.0 \pm 1.9_{\text{(sys)}} \pm 5.4_{\text{(stat)}}$ ($27.4 \pm 3.8_{\text{(sys)}} \pm 5.2_{\text{(stat)}}$) events are predicted for the analysis range (200–1200 MeV) with (without) the $1\mu1p$ constraint. Note that since the 3+1 search performed in this thesis is a joint fit with the $1e1p$ and $1\mu1p$ channels, it does not implement this method.

In Ref. [37], the agreement of the $1e1p$ observation with two different hypotheses (the standard model, SM, and the LEE model) is detailed. Three statistical tests are used. The first is to check the goodness of fit between each model and the data. This is performed using the χ^2-CNP method described in chapter 4, eq. 4.8. [27]. This metric will also be used when examining the results of the 3+1 model fit in Chapter 13. A frequentist method is then used to determine the corresponding p-value.

The frequentist studies are performed using 10^5 pseudo-experiments that are generated from the given model under investigation. The method of generating pseudo-experiments is discussed further in Chapter 12, and is performed in the SBNFit software package [84]. These pseudo-experiments are used to create probability distributions for the χ^2-CNP for the given hypothesis. The value of the χ^2-CNP in data is compared to this probability distribution in order to determine the p-value. This test found a p-value for the comparison between the $1e1p$ observation and the expected background prediction to be 0.014 for the SM prediction this indicating a 2.5σ tension with the SM. However, the agreement with the LEE was even worse with a p-value of 5.0x10$^-$4.

The second set of statistical test is two-hypothesis test which determines compatibility between the observed $1e1p$ data and the H_0 (SM) and H_1 (LEE) hypotheses.The test statistic is:

$$\Delta\chi^2 = \chi^2_{H_0} - \chi^2_{H_1} \tag{11.1}$$

where each χ^2 is computed using the χ^2-CNP formalism. This $\Delta\chi^2$ is as an approximation of the log-likelihood ratio. The sensitivity to exclude H_1 if H_0 is true is based on the probability that a $\Delta\chi^2$ from the H_1 pseudo-experiments is less than the median $\Delta\chi^2$ from the H_0 experiments.

The $\Delta\chi^2$ for the data between the H_0 and H_1 predictions is found to be -11.08. The observed $\Delta\chi^2$ is significantly below the median of both distributions. This is a result of the observation being generally lower than the H_0 prediction as seen in Figure 11.2(a). The probability that a $\Delta\chi^2$ value sampled from the H_0 distribution is smaller than the observed $\Delta\chi^2$ is 0.020. This indicates 2.1σ tension between the data and the H_0 (SM) hypothesis. Further, the probability that a $\Delta\chi^2$ value sampled from the H_1 distribution is smaller than the observed value is 1.6×10^{-4}. This test therefore rejects the H_1 (LEE model) hypothesis with a significance of 3.6σ. As shown by this test, the data agrees better with the SM than with the specific MiniBooNE LEE model that was tested. However, the possibility remains that some set of 3+1 oscillation parameters may give a better fit to the data than the SM hypothesis.

The third statistical test that we consider is a fit for the LEE signal strength parameter, x_{LEE}. This checks for agreement with different normalization scaling of the LEE model. A best fit scaling is found by minimizing χ^2_{CNP} using the Feldman-Cousins method [85] (discussed further in Chapter 12). The best-fit value is found to be $x_{\text{LEE}} = 0$. Using the Feldman–Cousins procedure, confidence intervals on the signal strength were found. The 90% confidence interval has an upper bound at $x_{\text{LEE}} \leq 0.25$, and the 2σ ($\sim$95%) interval has an upper bound at 0.38. These results are unsurprising given the results of the other tests. Figure 11.3 shows the results of this test. The confidence intervals of 1 and 2 σ are shown to have no overlap with the allowed MiniBooNE LEE model with a scaling of 1.0 even with both statistical and systematic uncertainty included.

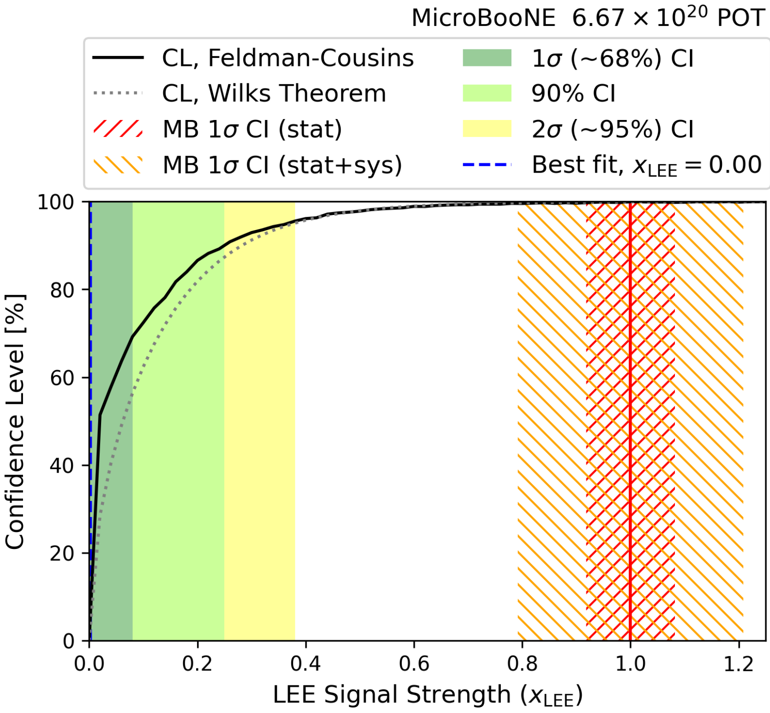

Figure 11.3: Confidence level at which values of the LEE scaling are ruled out based on the Feldman-Cousins procedure (solid black) and Wilk's theorem (dotted gray curve). The shaded regions are the different Feldman-Cousins confidence intervals. The hashed region is the confidence intervals on the MiniBooNE LEE model with a scaling of 1.0. Adapted from Ref. [37].

This analysis was one of multiple investigating this specific MiniBooNE LEE model. One looking for specifically a photon-like excess is shown in Ref. [76] and also saw better agreement with the SM than with an LEE model. There were also three more analyses looking for an electron-like excess using different reconstruction tools and target signals [38, 39]. No MiniBooNE-like excess was seen in these analyses either [86]. Figure 11.4 shows the results of these different analyses. The selection utilized in this thesis is in the first bin of the figure (indicated by the blue circle). Three of the four eLEE analyses shown heavily favored the standard model over the LEE. The fourth did not have strong discrimination power between the two models.

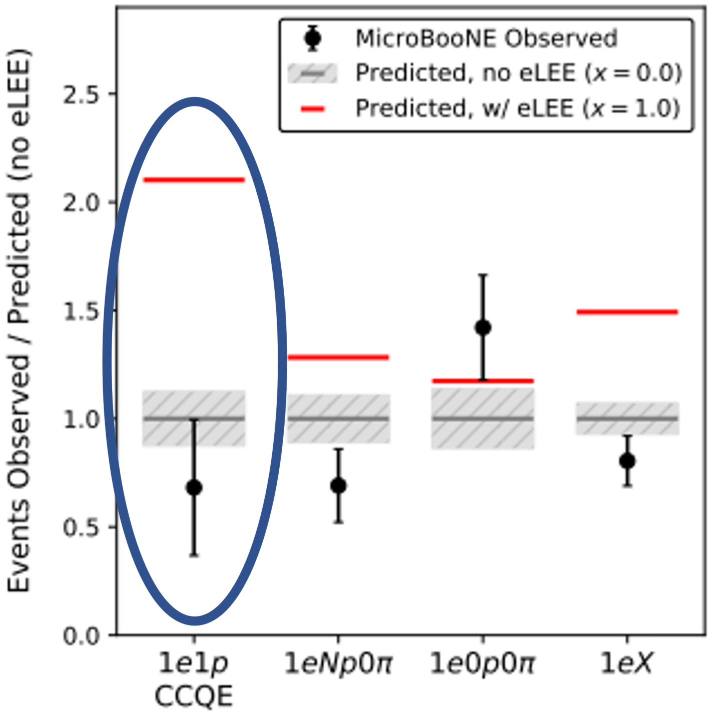

Figure 11.4: Ratio of observed to predicted ν_e candidate events in each analysis's energy range. Statistical errors are shown on the observations (black), while systematic errors are shown around the prediction (gray). The expected ratio assuming the MiniBooNE-like eLEE signal model with its median signal strength is also shown (red). The Reconstruction and selection utilized in this thesis comprises the first bin of this plot. Adapted from Ref. [86].

As has been shown in this section, the observed selected data agrees more closely with the standard model than with the unfolded MiniBooNE LEE model. However, that does not rule out sterile neutrino oscillations completely, especially as there is a remaining tension with the standard model. Fewer events were observed in the $1e1p$ channel than are predicted in the SM. The following chapters will test the agreement of these data selections with a 3+1 light sterile neutrino model.

Chapter 12

3+1 Oscillation Search Strategy and Sensitivity

The final step of this analysis is comparing the $1l1p$ CCQE MicroBooNE data to the 3+1 sterile neutrino model described in Chapter 3. This analysis combines the $1e1p$ selection with the $1\mu1p$ selection in a joint fit and tests three oscillation channels concurrently. ν_e appearance (Eq. 3.6), ν_e disappearance (Eq. 3.7), and ν_μ disappearance (Eq. 3.8) are all allowed to occur. There are three independent parameters that will be fit over: $|U_{e4}|$, $|U_{\mu4}|$, and Δm^2_{41}.

One change has been made to the selection presented in previous chapters. In order to search for the MiniBooNE low-energy excess, the binning for the 1e1p selection was set to be 200-1200 MeV in 100 MeV bins (here referred to as LEE binning). The lower bound was set due to reconstruction efficiencies at low energies. The higher bound was set based off where the prediction matching the MiniBooNE low-energy excess went to zero. However for this study, the prediction does not necessarily go to zero depending on the oscillation parameters used. A test was performed to determine the best binning to use for this analysis as described in Appendix D. The binning scheme used in this study is 200-1200 MeV in 100 MeV bins 1 bin from 1200-1600 MeV + 1 bin from 1600-2400 MeV.

The true neutrino energy spectra for the simulation samples used in this analysis is shown in Figure 12.1. This is broken up into $1e1p$ with no sterile oscillation (a), the spectrum of maximum BNB $\nu_\mu \rightarrow \nu_e$ oscillation to illustrate the shape (b), and the $1\mu1p$ selection with no sterile oscillation (c). The baseline for the same samples is shown in Figure 12.2. This baseline is the total travel distance in meters from the meson decay in the decay pipe of the beam to the interaction point in the detector. The two truth variables are used in determining the oscillation probability.

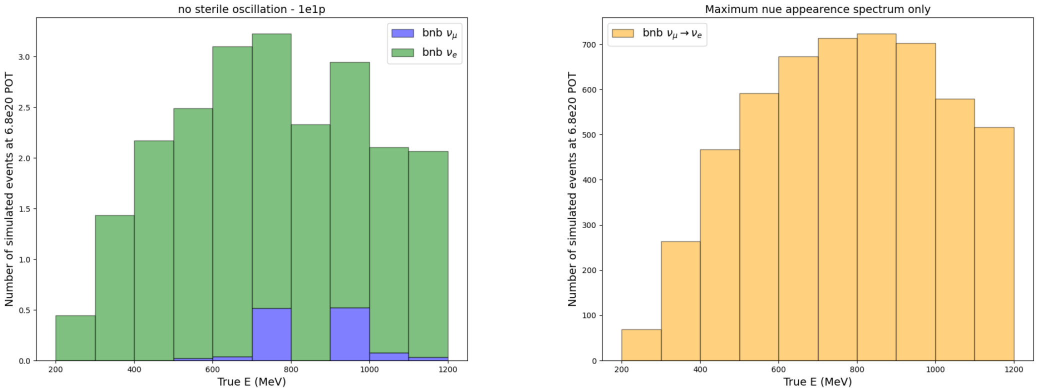

(a) $1e1p$, no sterile osc (b) $1e1p$, maximum BNB $\nu_\mu \rightarrow \nu_e$ oscillation

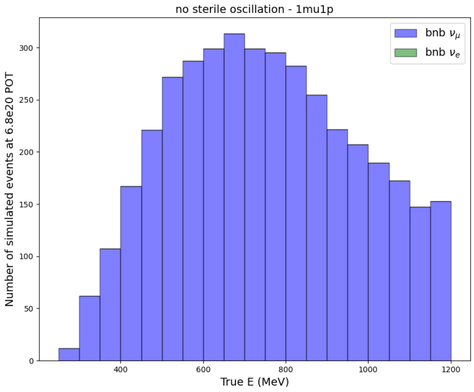

(c) 1μ1p, no sterile osc

Figure 12.1: The true neutrino energy (MeV) spectrum of $1e1p$ with no sterile oscillation (a), the spectrum of maximum BNB $\nu_\mu \rightarrow \nu_e$ oscillation to illustrate the shape (b), and the $1mu1p$ selection with no sterile oscillation (c).

When the predicted spectra for a given set of oscillation parameters, the starting point is the predicted spectra shown in Figure 11.2 (though with an extended energy range). The events in each simulation sample starts with a weight incorporating POT scaling to match data, GENIE interaction weights based on the cross section model, and π^0 weights described in Chapter 10. This is what is referred to as the

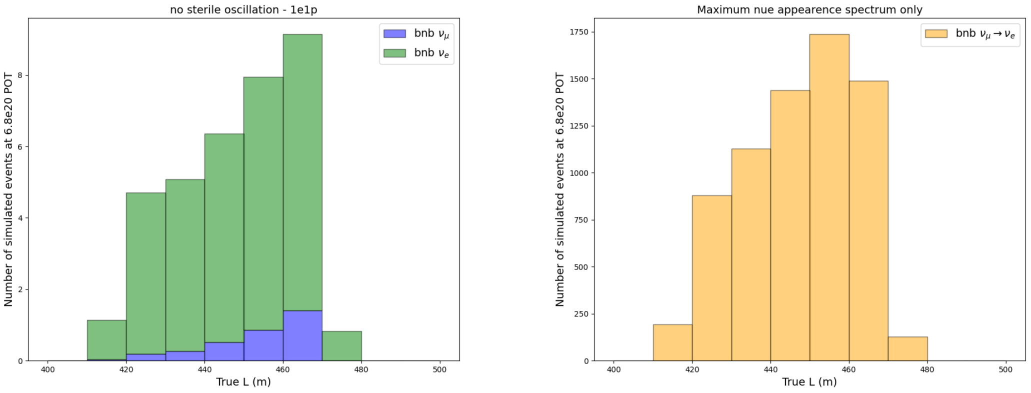

(a) $1e1p$, no sterile osc (b) $1e1p$, maximum BNB $\nu_\mu \rightarrow \nu_e$ oscillation

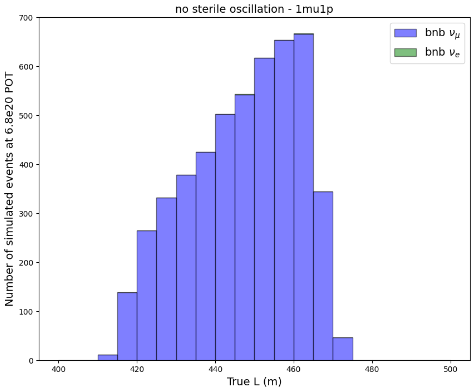

(c) 1μ1p, no sterile osc

Figure 12.2: The true neutrino travel distance (m) spectrum of $1e1p$ with no sterile oscillation (a), the spectrum of maximum BNB $\nu_\mu \rightarrow \nu_e$ oscillation to illustrate the shape (b), and the $1mu1p$ selection with no sterile oscillation (c).

null model. This oscillation fit is performed in bins of E_ν^{range} (MeV) as determined in Section 6.9.

Next, each event is assigned a weight equal to the oscillation probability for a given set of 3+1 parameters, using the simulation E_ν and baseline. The oscillation equation used depends on the event. All of the simulation sets described in Table 6.1 are used. If the event is a ν_μ event from the BNB, Eq. 3.8 for ν_μ disappearance is used. If the event is part of the intrinsic BNB ν_e background, Eq. 3.7 for ν_e disappearance is used. Finally a simulation sample not previously utilized is used to model ν_e appearance. This is the FullOsc sample from Table 6.1. This sample is from a simulation assuming the entire BNB ν_μ flux oscillated into ν_e . These events have all the standard weights applied. In the null model the oscillation probability is zero, so they are not included in the spectra. However in a 3+1 model, the event weights are multiplied by weights representing the oscillation probability based on Eq. 3.6.

This chapter describes the fit strategy and sensitivity before moving on to data results in Chapter 13. Everything shown in this Chapter was performed while remaining functionally blind to the data. Section 12.1 explains the method used to determine sensitivity using Wilks' theorem. Section 12.2 describes how the best fit oscillation parameters will be found between observation and data for a given observation. This is followed by Section 12.3 which provides the results of this sensitivity study. Section 12.4 demonstrates a simple signal injection test. Finally, Section 12.5 shows a test of this machinery on two fake data sets.

12.1 Wilks' Theorem Sensitivity Method

Recall that the test metric used to determine the agreement of the model with data is $-2ln(L)$ as outlined in Chapter 4. The sensitivity of the $1l1p$ selection in MicroBooNE to the 3+1 sterile model under investigation can be determined using this metric. The sensitivity that will be investigated is the exclusion sensitivity. This test determines which 3+1 oscillation parameters will be excluded if the data matches the null model exactly.

The method used to determine this exclusion sensitivity in this study utilizes Wilks' theorem [66]. Wilks' theorem states that, as long as some general conditions are satisfied, $-2ln(L)$ approaches a χ^2 distribution in the limit where the data sample is large [6]. In other words, if the data x is distributed according to the likelihood function for model parameters θ, the maximum ln likelihood ratio (R) follows a χ^2 distribution with n degrees of freedom (DOF). R, which is defined here as:

$$R = -2\ln\frac{L(\theta|\mu)}{L(\theta_{bf}|\mu)} \tag{12.1}$$

goes as:

$$R \sim \chi^2_n \tag{12.2}$$

as long as N is large, where L is given by equation 4.5, $L(\theta)$ is L for a given set of oscillation parameters, and $L(\theta_{bf})$ is the L for the best fit oscillation parameters. R written out fully for this analysis is therefore:

$$\begin{aligned} R = &\sum_{i,j}^{i=N}[(x_i - \mu(\theta)_i)M(\theta)^{-1}_{tot,ij}(x_j - \mu(\theta)_j)] + \ln(|M(\theta)|) \\ - &\sum_{i,j}^{i=N}[(x_i - \mu(\theta_{bf})_i)M(\theta_{bf})^{-1}_{tot,ij}(x_j - \mu(\theta_{bf})_j)] - \ln(|M(\theta_{bf})|) \end{aligned} \tag{12.3}$$

To build the Wilks' theorem exclusion sensitivity, R is calculated at each point in parameter space in a scan with $\mu(\theta)$ and $M(\theta)$ as the expected number of events and covariance matrix for the parameters. x is the null oscillation spectrum, and $\mu(\theta_{bf})$ and $M(\theta_{bf})$ are the oscillation parameters giving the minimum $-2\ln(L)$ when compared to the null oscillation.

As R can be treated like a χ^2 under Wilks' theorem, the value can be compared to the χ^2 distribution. Figure 12.3(a) shows the χ^2 distribution for various degrees of freedom. If the value of R is greater than some percentile in this distribution it is chosen to be excluded. The 90% level was chosen for this analysis as it is subject to large statistical uncertainty (especially in the $1e1p$ channel). For 3 DOF (corresponding to the three free oscillation parameters in this study), the 90% exclusion value is 6.251 [87]. Figure 12.3(b) shows the χ^2 distribution for 3 DOF and shows where the 90% percentile is.

At each point in parameter space under investigation R is compared to this value. If R at the point is greater than 6.25, it is considered to be part of the excluded region. This sensitivity test shows that in this analysis, if the data matches the null oscillation exactly, which region of parameter phase space will be excluded under Wilks' theorem with 90% confidence.

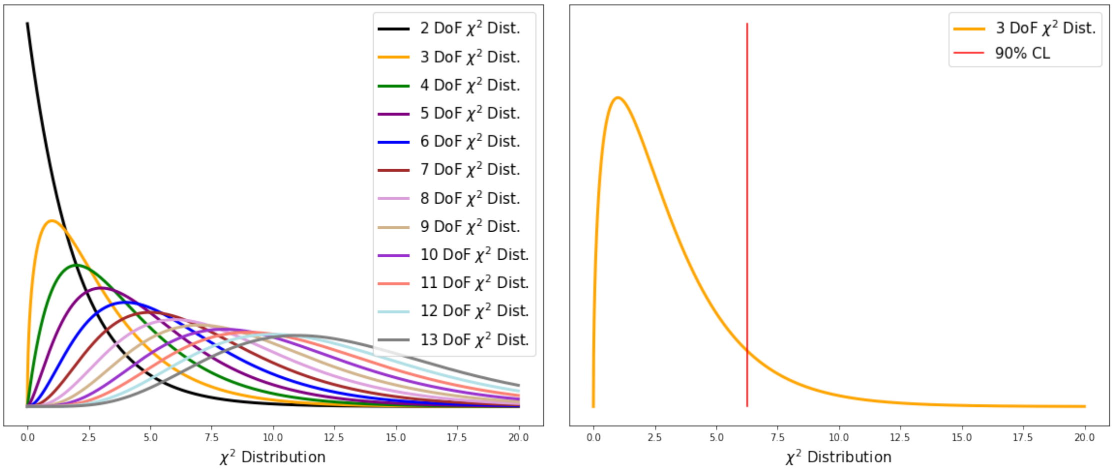

(a) N DOF (b) 3 DOF

Figure 12.3: The χ^2 distribution for various degrees of freedom (a) and 3 degrees of freedom with the 90^th percentile highlighted.

12.2 Determining the Best Fit Model Parameters

A grid scan is a method in which the oscillation parameters come from a set list of allowed values. This breaks up the smooth parameter space into a coarse grid. The resolution of a grid scan can be increased by decreasing the step size in parameter values which increases the total number of parameters. The amount of computation time required increases as a function of number of oscillation points tests. Increasing the resolution of a grid scan with 3 oscillation parameters quickly becomes computationally prohibitive. Therefore in this analysis, a relatively coarse grid of 25x25x25 is used.

A grid scan over the parameters will work well to determine Wilk's theorem excluded parameter ranges. However, in order to determine the best fit parameters with data, this analysis will use a minimizer in order to achieve a more fine resolution for the best fit. A minimizer is an algorithm that minimizes a given function which in this case find the oscillation parameters which minimize $-2\ln(L)$ for the observed data.

The 90% confidence levels will then be found via a more coarse grid search method. This best fit point represents the bf, or best fit terms used in equation 12.1. Then, the likelihood L is calculated at each point in the grid search parameter space and used to find R at that point. If the resulting R value is > 6.251, that point will be considered excluded with 90% confidence. This Section describes the use of the minimizer and validates its use. The method is illustrated in Section 12.5 using a fake data set and used in the final results in Chapter 13.

The minimizer utilized in this study is TMinuit from Root [88]. It was run in "SEEk" mode which causes a Monte Carlo minimization of the function. Random values of the variable parameters are chosen uniformly over a hypercube centered at the current best value. The hypercube size was set to be 3 standard deviations.

The minimizer requires specification of a start point, or initial parameters to fit with. Based on a handscan of a few test runs, the best performance is found when the starting point is the minimum from a grid search. When instead starting at the null oscillation point it was found that the minimizer often became stuck in a local minimum. Due to this issue it was decided that the best use of the minimizer is to use it in conjunction with a grid search. To find the best fit oscillation parameters for a given spectrum, a standard grid search is run first to find the grid point in parameter space with the lowest $-2\ln(L)$. This is then fed to the minimizer algorithm as a test point. This process allows for a finer resolution when finding the best fit oscillation. The parameter values tested in the initial grid search are:

- Δm^2_{41}, 25 logarithmic spaced values, range: [0.01,100] MeV^2;
- U_{e4}, 25 logarithmic spaced values, range: [0.01,0.5];
- $U_{\mu 4}$, 25 logarithmic spaced values, range: [0.01,0.5].

and discussed further in Section 12.3. The resulting 3D grid is the 25x25x25, or 15625 test parameter sets.

One complication that needed to be addressed was the speed with which the minimizer algorithm runs. With each iteration or step of the minimizer a new expectation spectrum with the test oscillation parameters is needed. The minimizer often requires ~ 300 iterations before converging. This is computationally fast when changing just the two U parameters as they create a scaling effect in the spectrum.

However, when changing Δm^2_{41} every simulation event needs to be re-weighted (as opposed to changing the size of the entire bin). Recomputing the spectrum at each Δm^2_{41} is computationally expensive. The workaround this analysis uses is:

1. Pre-generate 400 spectra with Δm^2_{41} logarithmically spaced between 0.01-100 MeV^2. U parameters are set to the maximum.
2. Find the Δm^2_{41} from the spectra library that is closest to the value tested by the minimizer.
3. Re-weight the pre-generated spectra based on the $U_{e4}, U_{\mu 4}$ values being tested in each minimizer step.

The result is that the minimizer is only allowed to test certain Δm^2_{41} values, resulting in a step-like phase space. However using 400 values still allows for more resolution in this parameter than provided by the grid search alone.

To illustrate the performance of this process, 1000 pseudo-data sets were thrown from various 3+1 oscillation test points. To generate each pseudo-experiment, the multivariate normal distribution is sampled from as defined by the mean prediction that test point and the associated covariance matrix. The pseudo-data set generation is carried out in the SBNfit software package, which provides support for such calculations [84]. In each bin, we then sample from a Poisson distribution defined by the rate parameter (mean) that is equal to the value sampled from the multivariate normal distribution. This gives a pseudo-observation that has integer numbers of events in each bin and incorporates both systematic and statistical uncertainties. The SBNfit software package also contains many libraries that are critical to oscillation studies and the generation of systematic covariance matrices and is utilized behind the scenes throughout much of this thesis [84].

The minimum $-2\ln(L)$ was found for each pseudo-experiment from both the grid search only and the grid search with the additional minimizer. The test points used were smallest oscillation ($\sim$ null oscillation), maximum oscillation, and the global best fit.

Fig. 12.4 shows R for each pseudo-experiment for each of these test points which is the difference between the $-2\ln(L)$ at the point the pseudo-experiment was thrown from and the minimum $-2\ln(L)$ for that data set. Both the grid search only and the grid search + minimizer are shown. The corresponding vertical lines represent the value for which 90% of R values are below for that test point. This value is referred to as R_{crit}. Also shown is 6.251 which is the 90% confidence level (CL) according to Wilks' theorem.

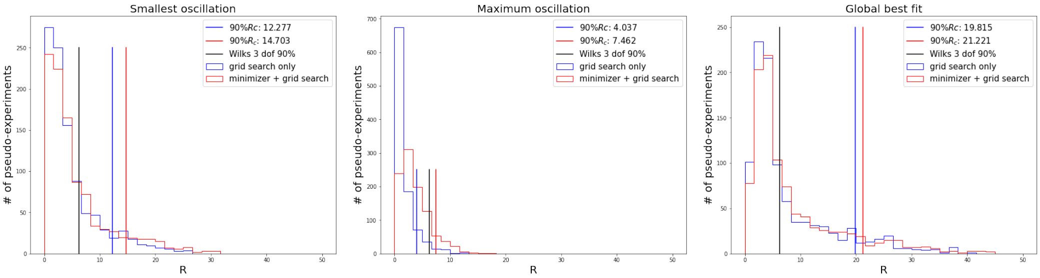

(a) Null Oscillation (b) Maximum Oscillation (c) Global best fit

Figure 12.4: The R distribution for 1000 pseudo-experiments thrown from the specified set of oscillation parameters. The red spectrum is the result using only a grid search. The blue spectrum is the result of using a grid search followed by the minimizer. The Wilks' theorem 90% confidence level value is shown and compared to the 90% R_{crit} from the given spectrum.

There are two important features to note. The first is that for each test point, R_{crit} of the combined grid search and minimizer is higher than the grid search on its own. This verifies that the minimizer is performing as expected and finding a lower $-2\ln(L)$ than the grid search alone and validates the use of the combined grid search and minimizer to find the best fit parameters to a given observation.

Additionally, the Wilk's theorem 90% confidence level value for 3 degrees of freedom (6.251) is shown as a black vertical line. Another common oscillation analysis method is to use a Feldman-Cousins method to determine the exclusion contours [85]. In the Feldman-Cousins method, instead of comparing to the χ^2 distribution, 90% R_{crit} would be determined based on what R value 90% of pseudo-experiments are less than. This method is discussed further in Section 13.2.

Figure 12.5 again shows the minimizer test with the global best fit oscillation parameters. The χ^2 distribution for 3 DOF is now shown. There is fairly good agreement between the χ^2 distribution and the minimizer with a grid search R distribution. This good agreement is not seen at all test points.

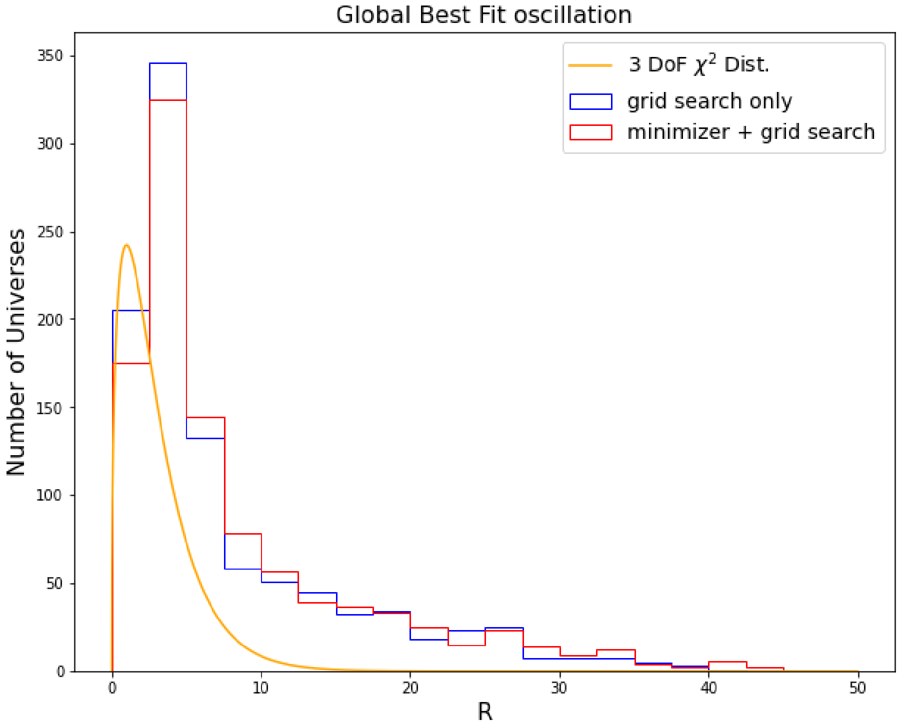

Figure 12.5: The R distribution for 1000 pseudo-experiments thrown from the specified set of oscillation parameters. The red spectrum is the result using only a grid search. The blue spectrum is the result of using a grid search followed by the minimizer. The orange line shows the 3 DOF χ^2 distribution for comparison.

12.3 Wilks' Theorem Sensitivity Results

Finally, using the chosen binning along with the well-vetted reconstruction and analysis, the Wilks' theorem exclusion sensitivity can be determined. This follows the method described in Section 12.1. The parameter values tested are the same as in Section 12.2. The ranges were chosen to be consistent with the SBND prospects study in Ref. [89]. The only exception is the minimum U_{e4} and $U_{\mu 4}$ which were chosen to give oscillation amplitudes $\sim 10^{-4}$. Observing oscillation any lower than this is not statistically possible in our analysis.

Out of the 15625 sets of parameters tested in this study, 1474 parameters sets are excluded if the observation matches the null prediction. This translates to 09.56% of the parameters. This is not the same as the percentage of the parameter space as the grid points are logarithmically spaced.

As confidence levels in 3D parameter space are not intuitive to visualize, the sensitivity result is instead displayed in 2D slices at each of the 25 parameter values tested for each of the 3 parameters. The result is shown in Figures 12.6, 12.7, and 12.8 for Δm^2_{41}, $|U_{e4}|$, and $|U_{\mu4}|$ respectively. For a given value of a parameter, the 2D confidence level in terms of the other 2 parameters is shown. The color scale represents the R value at each parameter grid point and has been capped at 20.0 to allow for better visualisation for R close to 6.25 (Wilks' 90% exclusion level for 3 degrees of freedom). The confidence level is indicated by the white contour lines.

As the value of a given parameter increases, the size of the excluded region in the 2D parameter space slice also increases. Another interesting feature is that for the highest parameter values tested, the entire 2D slice is not excluded. For example with maximum U_{e4}, a region of low Δm^2_{41} is still allowed as this results in small oscillation probabilities.

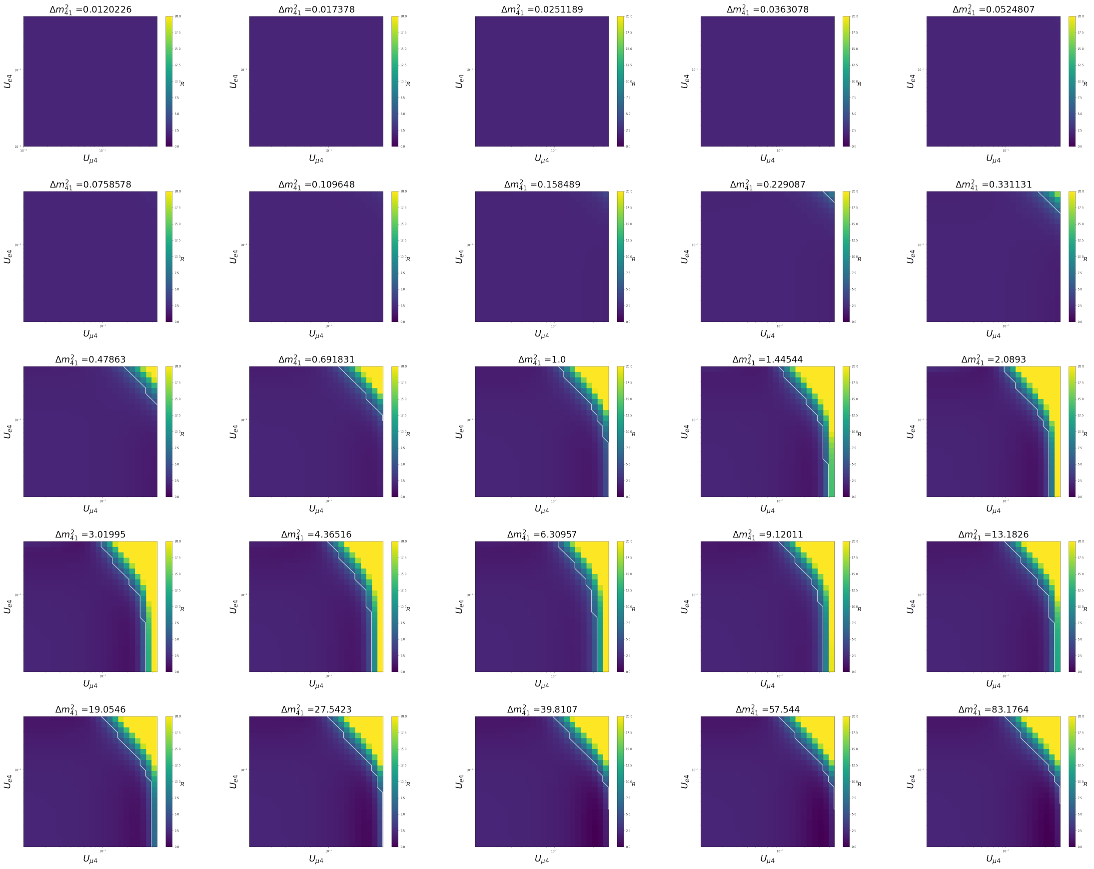

Figure 12.6: 2D slices for each Δm^2_{41} value tested to construct the Wilks' 90% confidence excluded region (Δm^2_{41} value indicated by the plot title).

A region of particular interest to analyze is the global best fit 3+1 oscillation parameters (from Table 3.1 in Chapter 3). The 2D slices for these parameters are

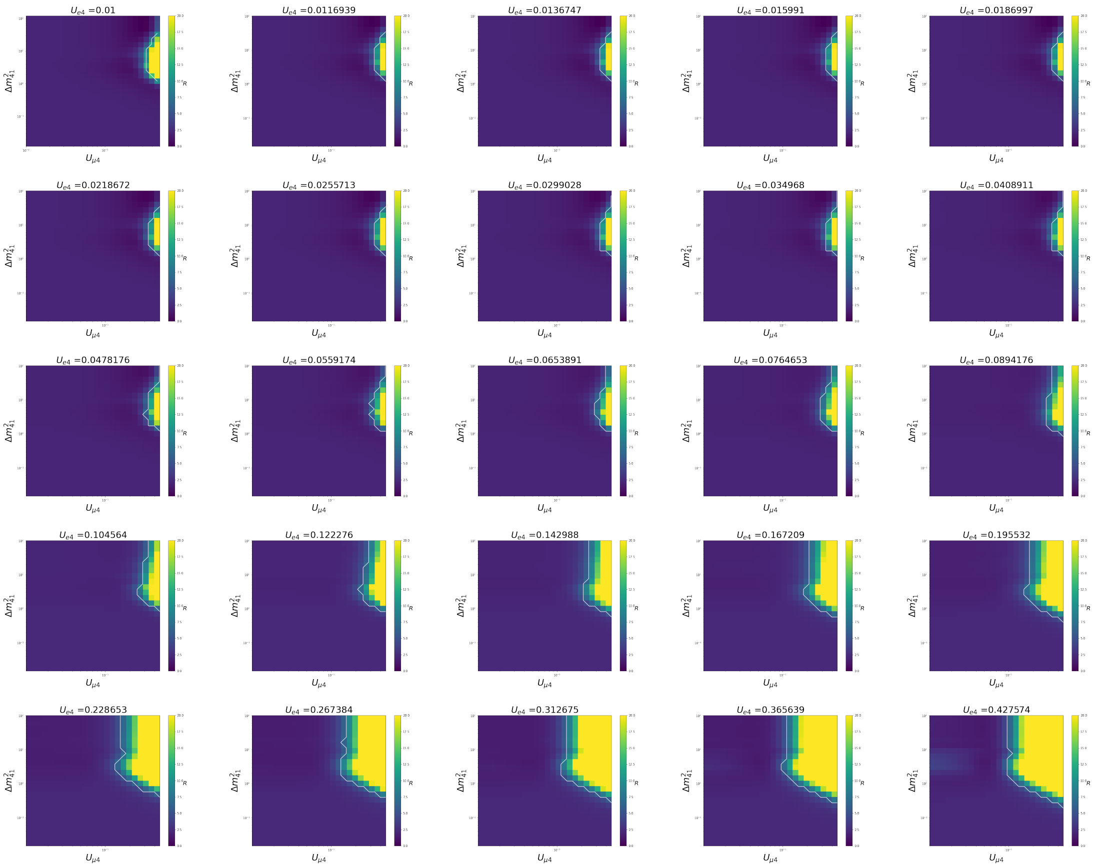

Figure 12.7: 2D slices for each U_{e4} value tested to construct the Wilks' 90% confidence excluded region (U_{e4} value indicated by the plot title).

shown again in Fig 12.9, with the global best fit point shown by the red star. Note that the 2D slices are not exactly at the global best fit, but at the closest parameter value tested. This point is not in the excluded region. This means that if the data matches the null model, then global best fit 3+1 model will not be excluded. When performing data/fake data studies, this region of parameter space will be of particular interest.

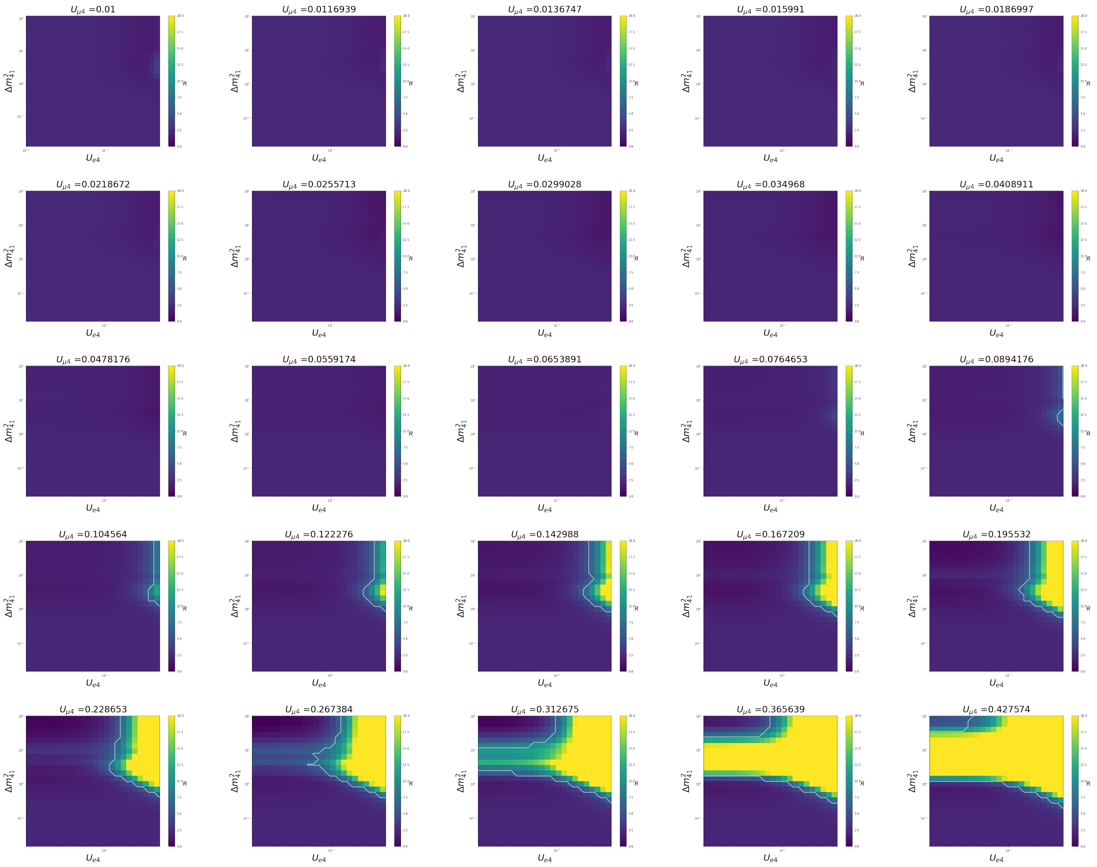

Figure 12.8: 2D slices for each $U_{\mu4}$ value tested to construct the Wilks' 90% confidence excluded region ($U_{\mu4}$ value indicated by the plot title).

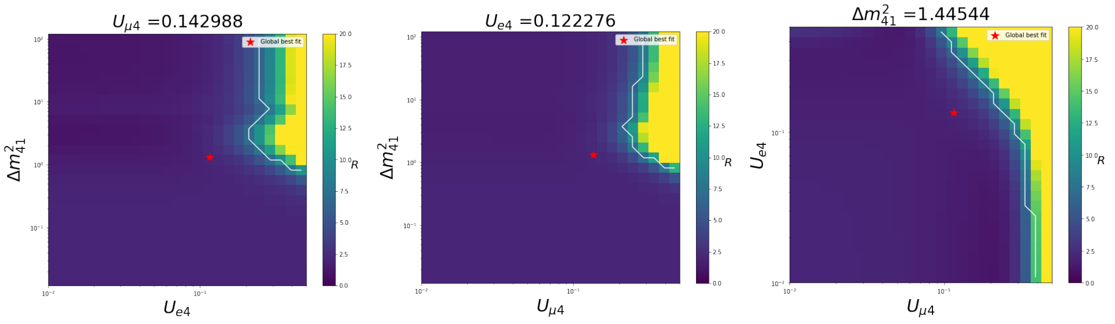

(a) $U_{\mu4}$ Slice (b) U_{e4} Slice (c) Δm^2_{41} Slice

Figure 12.9: 2D slices of the Wilks' theorem exclusion sensitivity at the grid points closest to the global best fit point. The global best fit parameters from Table 3.1 are indicated by the red star. The 90% confidence level is shown by the white line. The color scale (capped at 20) indicates the R value.

12.4 Signal Injection Test

A simple signal injection test has been performed to further verify performance. For this test, 1000 pseudo-experiments were thrown from a set of oscillation parameters. For each of these data sets the best fit parameters are found as in Section 12.2. Then the difference between the $-2\ln(L)$ from this best fit and the $-2\ln(L)$ at the null oscillation point was found. Following Wilks' theorem if this difference was greater than 6.251 the null is considered to have been excluded. Table 12.1 shows the results of this study. The percentage of the pseudo-experiments which excludes the null is given for each oscillation parameter set.

Table 12.1: Results of the simple signal injection test. Sens R is the R value of the model with the given oscillation parameters from the Wilks' theorem sensitivity study. 1000 pseudo-experiments were used for each oscillation point.

$\Delta m^2_{41}[MeV^2]$	$\lvert U_{e4}\rvert$	$\lvert U_{\mu4}\rvert$	Sens R	Null Excluded(%)
0.05	0.018	0.018	2.06	30.2
0.33	0.041	0.041	2.07	29.9
13.18	0.196	0.196	10.86	92.7
83.17	0.428	0.428	227.90	100.0

These results provide further validation of the methods. This test is almost the opposite of the test in Section 12.3. It measures how often the null oscillation hypothesis can be excluded at 90% confidence if the data arises from a set of oscillation parameters. If the data comes from a universe where there is near maximum oscillation, the null hypothesis is excluded 100% of the time. It is also notable that two sets of parameters with nearly identical R values in the sensitivity test in Section 12.3 are also nearly identical in how often they reject the null in this signal injection test (rows 1 and 2).

Figure 12.10 shows the 2D excluded regions of the first five pseudo-experiments. The 2D slices are slices of the parameters that the pseudo experiment was thrown from. The results shown in this Figure are from the first row in Table 12.1. Figures 12.11, 12.12, and 12.13 show the results of rows 2,3, and 4 respectively. The examples shown are the first 5 from each 1k set and were not cherry-picked.

In most pseudo experiments, the parameters the pseudo-experiment are thrown from are not excluded using Wilk's theorem (though it is not always the best fit point). Pseudo-experiment 5 in Figure 12.11 is an example where this is not case.

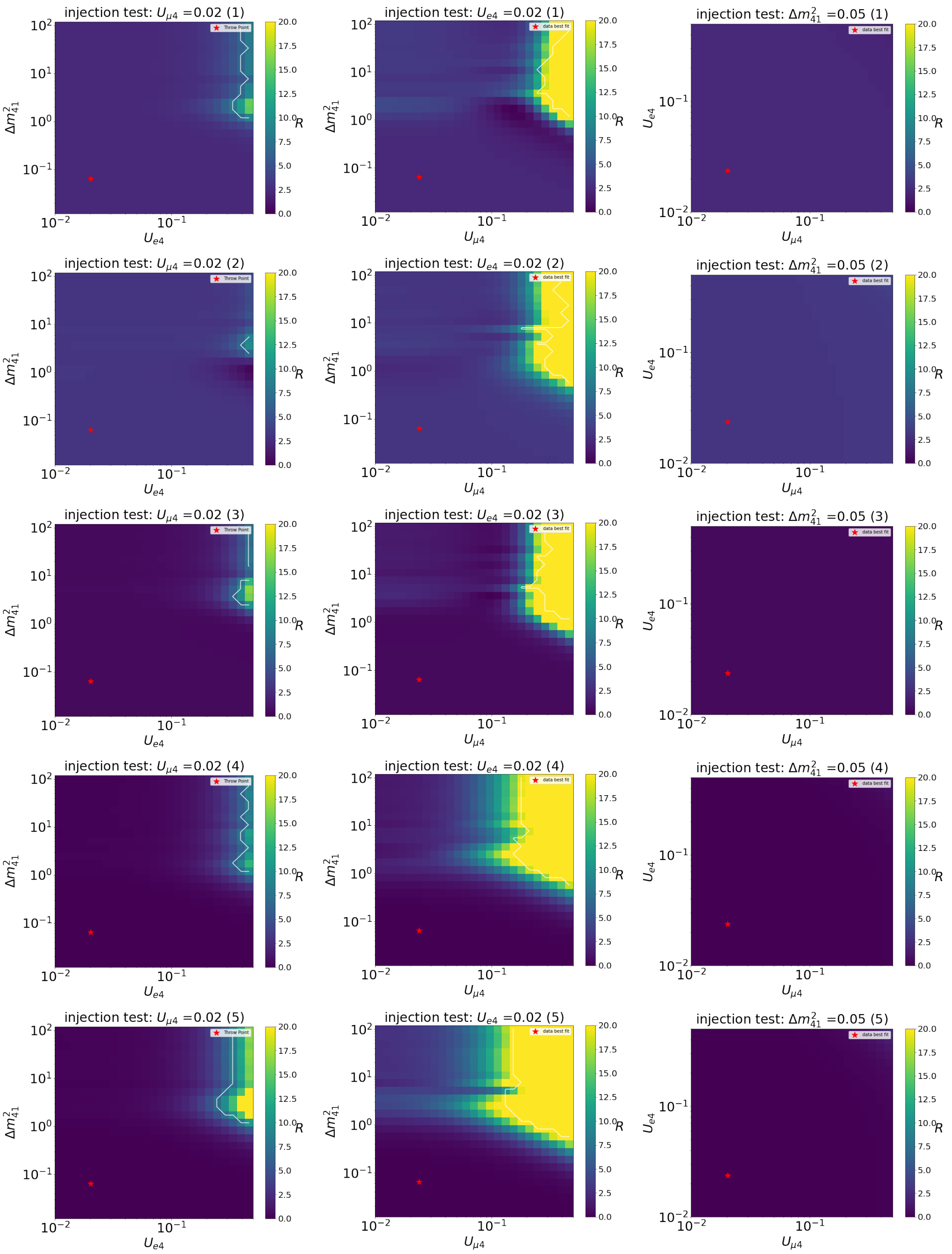

Figure 12.10: 2D slices of the Wilks' theorem exclusion for the first 5 pseudo-experiments thrown from $\Delta m^2_{41} = 0.05(MeV^2), U_{e4} = 0.018, U_{\mu4} = 0.018$. The 90% CL contour is shown by the white line. The red star indicates the parameters the pseudo experiment was thrown from.

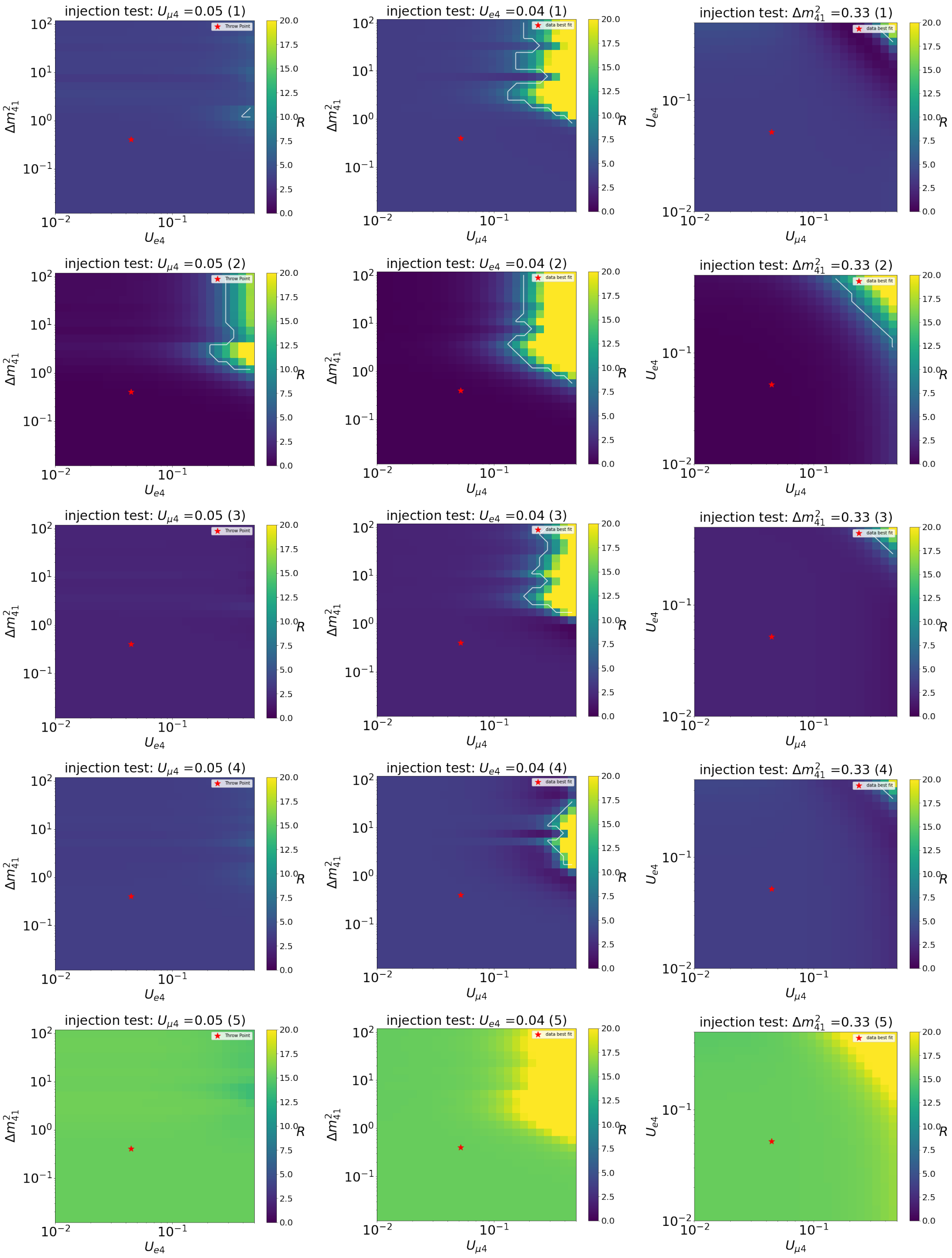

Figure 12.11: 2D slices of the Wilks' theorem exclusion for the first 5 pseudo-experiments thrown from $\Delta m^2_{41} = 0.33(MeV^2), U_{e4} = 0.041, U_{\mu4} = 0.041$. The 90% CL contour is shown by the white line. The red star indicates the parameters the pseudo experiment was thrown from.

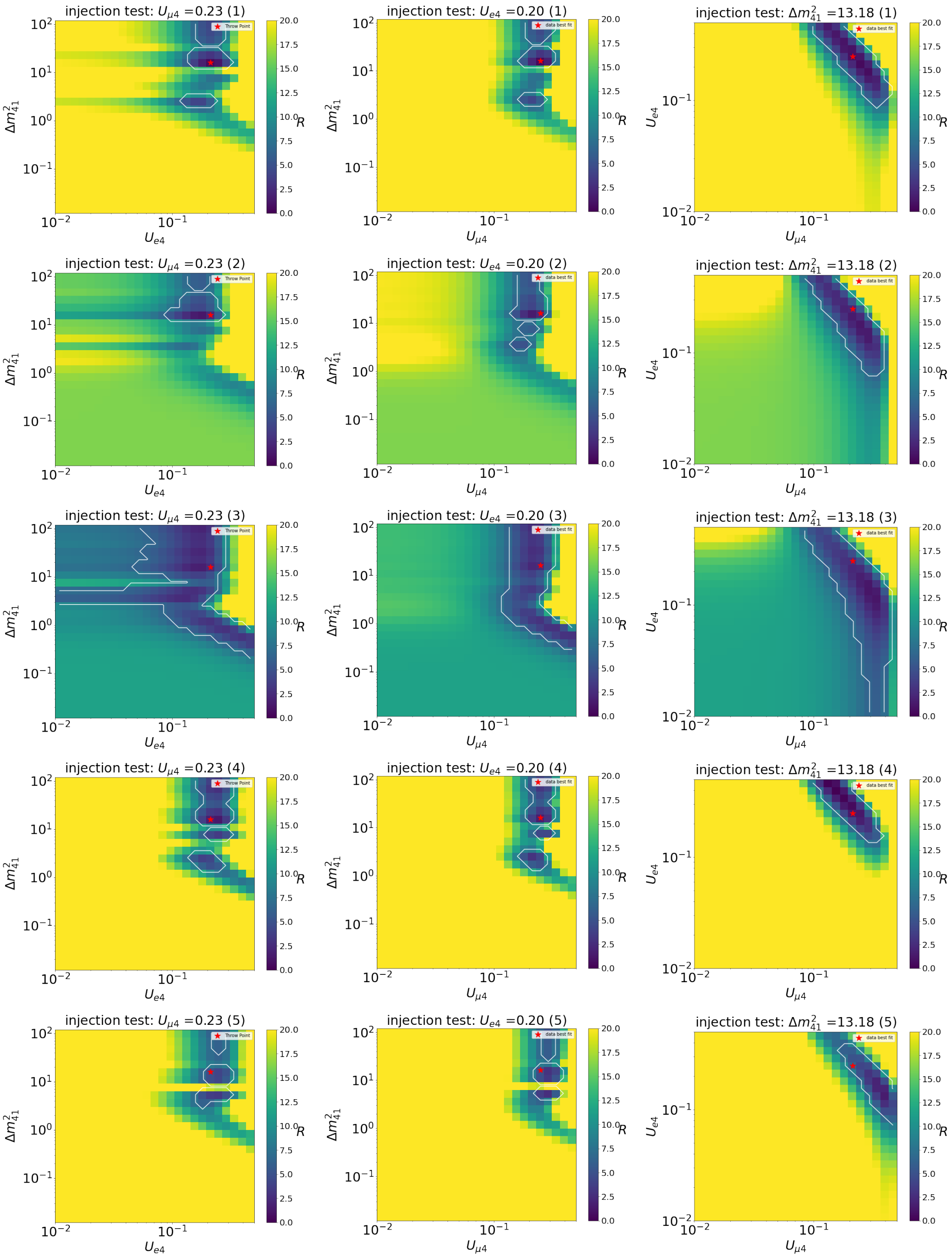

Figure 12.12: 2D slices of the Wilks' theorem exclusion for the first 5 pseudo-experiments thrown from $\Delta m^2_{41} = 13.18(MeV^2), U_{e4} = 0.196, U_{\mu4} = 0.196$. The 90% CL contour is shown by the white line. The red star indicates the parameters the pseudo experiment was thrown from.

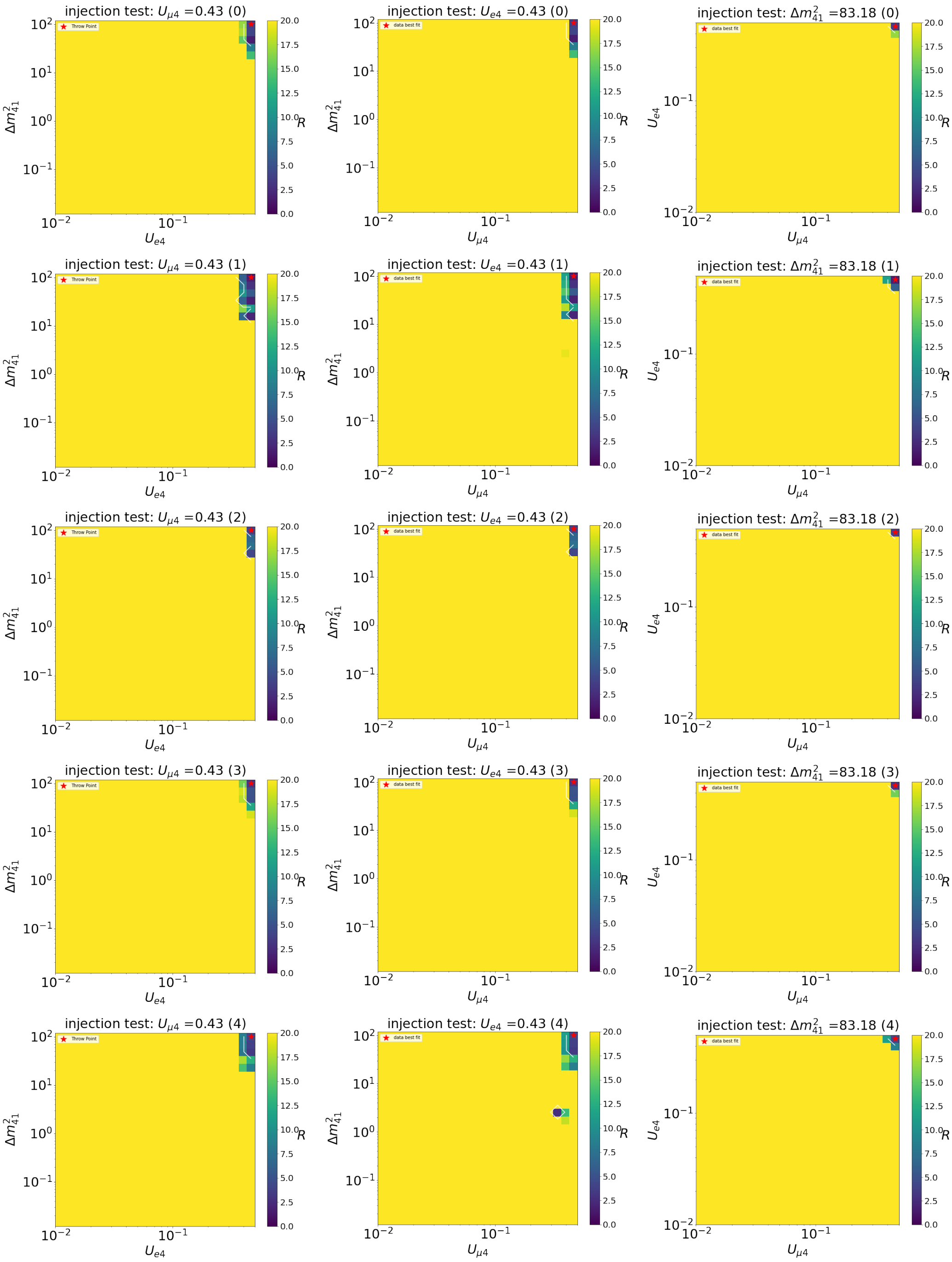

Figure 12.13: 2D slices of the Wilks' theorem exclusion for the first 5 pseudo-experiments thrown from $\Delta m^2_{41} = 83.17(MeV^2), U_{e4} = 0.428, U_{\mu4} = 0.428$. The 90% CL contour is shown by the white line. The red star indicates the parameters the pseudo experiment was thrown from.

12.5 Fake Data Tests

To test this analysis's machinery and performance on data, two fake data sets generated by the MicroBooNE collaboration were analyzed. These fake data sets were originally designed for the LEE analysis and are utilized here as a test before looking at the real data set. Both sets deviate with to a varying degree from the null spectrum used by this analysis. The properties of these data sets that differentiate them from the standard MicroBooNE simulation without sterile neutrinos are as follows. Fake data set 1:

1. used untuned GENIE v3 (instead of incorporating the MicroBooNE GENIE tune);
2. included an electron-LEE signal at 3.5x the median unfolded MiniBooNE signal;
3. included an enhanced NC Delta to gamma rate at 4.5x the standard model rate.

Fake data set 2:

1. enhanced normalization of QE and Meson exchange current (MEC) interactions;
2. increased final state interactions (FSI) for nucleons, such that nucleons created in the initial neutrino interaction are more likely to interact in the initial nucleus;
3. slight change to FSI for pions.

Based of the descriptions of these sets it is expected that fake data set 1 has a large excess of events in the $1e1p$ selection possibly mimicking sterile neutrino oscillation and fake data set 2 looks similar to the null prediction.

Each data set was analyzed with the following procedure which mirrors the analysis plan for the actual MicroBooNE data. First the set was run through the DL reconstruction and the $1l1p$ selection and the the number of events in each energy bin was calculated. Since this was fake data, the events were POT scaled to better match the POT from the actual data set to understand the performance at the expected POT.

Next the $-2\ln(L)$ value between data and the prediction was calculated at each point in parameter space. The smallest value from this grid search was used to initialize the minimizer which then found the parameters that give the best fit to the observation. The $-2\ln(L)$ of this best fit point was subtracted from the $-2\ln(L)$ at each grid point to find R. If the R of a parameter point was > 6.25, the point is excluded based of the data at 90% confidence.

Table 12.2 summarizes the results of the two fake data sets. For each data set, the % of grid points that are excluded, the best fit oscillation parameters, and the agreement with the data at the best fit are provided using the χ^2-CNP metric Eq. 4.8. The U parameters are also given in terms of $\sin^2(\theta_i)$. The conversion of the parameters can be derived from Eqs. 3.6,3.7, and 3.8.

Table 12.2: A summary of the fake data tests results showing the best fit oscillation parameters. "Excluded" is the number of grid points excluded with 90% confidence divided by the total number of grid points tested.

	Excluded	$\Delta m^2_{41} eV^2$	$\lvert U_{e4}\rvert$	$\lvert U_{\mu4}\rvert$	$\sin^2(2\theta_{\mu e})$	$\sin^2(2\theta_{ee})$	$\sin^2(2\theta_{\mu\mu})$	$\frac{\chi^2_{1e1p}}{11dof}$	$\frac{\chi^2_{1\mu1p}}{18dof}$
1	99.96%	0.278	0.475	0.488	0.214	0.698	0.725	8.18	1.21
2	14.16%	3.44	0.010	0.249	$2.5e^{-5}$	$4e^{-4}$	0.232	1.25	0.71

These results will now be analyzed in more detail starting with set 1. Fig. 12.14 shows 2D slices at the grid point closest to the best fit to the data (indicated by the red star). The allowed region is very small for this data set, indicating that there are few oscillation parameters that agree with this data set.

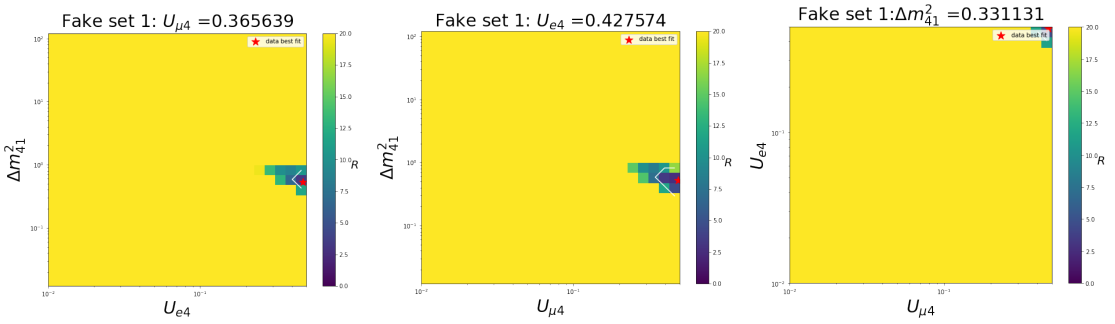

(a) $U_{\mu4}$ (b) U_{e4} (c) Δm^2_{41}

Figure 12.14: 2D slices of the Wilks' theorem exclusion close to the data best fit point for fake data set 1. This data set features a large low energy excess in ν_e . The 90% confidence level is shown by the white line. The color scale (capped at 20) indicates the R value.

Next Fig. 12.15 shows 2D slices at the global best fit point for this data set. This shows that the global best fit would be excluded if this were the actual data.

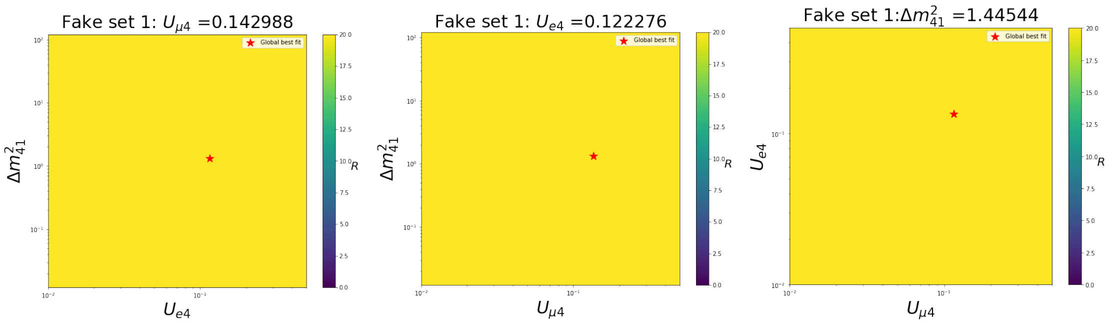

(a) $U_{\mu4}$ (b) U_{e4} (c) Δm^2_{41}

Figure 12.15: 2D slices of the Wilks' theorem exclusion close to the global best fit point for fake data set 1. The 90% confidence level is shown by the white line. The color scale (capped at 20) indicates the R value.

In order to compare to results from other experiments the 90% CL contours are next presented in terms of $sin^2(2\theta_{ee,\mu\mu,\mu e})$ to allow for comparison to other experiments. The oscillation probaility equations in this form are shown in Eq. 3.6, 3.7, and 3.8. For this test, a 2D parameter space is used of Δm^2_{41} vs $sin^2(2\theta_{ee,\mu\mu,\mu e})$ (one for each θ) and the other parameters are set to the best fit found previously in Table 12.2. The resulting R at each point in parameter space is then used to construct the exclusion contour in Δm^2_{41} vs. $sin^2(2\theta_{ee})$ 2D space. For this test the $sin^2(2\theta)$ values are 25 logarithmically spaced points in the range [0.0001, 1.0].

Figure 12.16 shows the result of this test for fake data set 1. The red star on these plots represents the best fit value as found by the minimizer in the 3 parameter fit in Table 12.2. The null oscillation result is still clearly excluded by this data set.

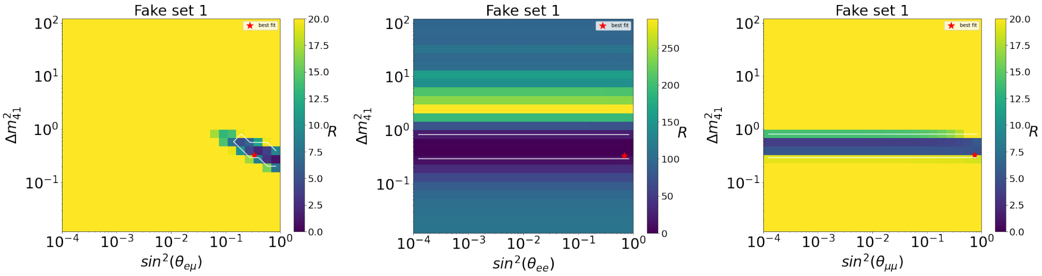

(a) $sin^2(2\theta_{\mu e})$ (b) $sin^2(2\theta_{ee})$ (c) $sin^2(2\theta_{\mu\mu})$

Figure 12.16: 2D slices of the Wilks' theorem exclusion in Δm^2_{41} vs $sin^2(2\theta_{ee,\mu\mu,\mu e})$, while setting the other two $sin^2(2\theta)$ terms to their best fit values in Table 12.2. The 90% CL is shown by the white line. The color scale (capped at 20) indicates the R value.

Finally, Fig. 12.17 (a) and (b) show the fake data spectrum in the $1e1p$ and $1\mu 1p$ selections respectively. This is compared to the null oscillation prediction (red dashed line) and the best fit oscillation prediction (stacked histogram). The Y axis represents the number of events in 100 Me ($1e1p$) or 50 MeV ($1\mu 1p$). The grey dashed line indicates the systematic + statistical uncertainty on the simulated spectrum. The categories shown in the stacked histograms are: BNB (ν_μ events from the beam), ν_e intrinsic (ν_e events from the beam), FullOsc (ν_μ events that oscillated into ν_e events), and extbnb (cosmic background. The $\chi^2/ndof$ between the data and the best fit spectrum is in Table 12.2.

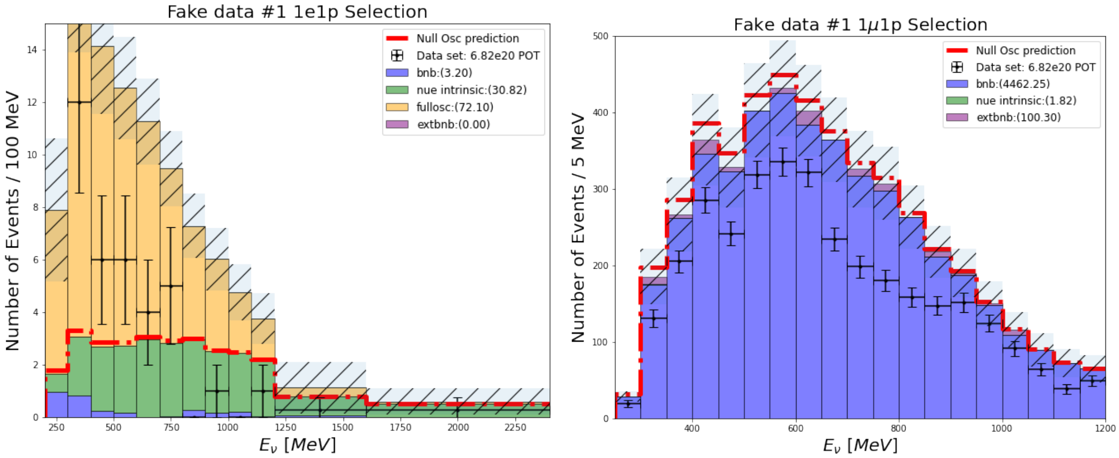

(a) $1e1p$ (b) $1\mu 1p$

Figure 12.17: Figure showing the fake data set 1 spectrum in the $1e1p$(a) and $1\mu 1p$(b) selections. The null oscillation prediction (red dashed line) and the best fit oscillation prediction (stacked histogram) are shown.The grey dashed line indicates the systematic + statistical uncertainty on the best fit simulated spectrum.

For this data set a strong 3+1 oscillation model is the best fit as seen from the large FullOsc contribution and the best fit parameter values. Additionally, the data is lower than the null oscillation spectrum in the $1\mu 1p$ channel, causing a ν_μ disappearance signal to be favored. However, the large $\chi^2/ndof$ of 6.22 in the $1e1p$ selection indicates that, though the best fit this model does not agree with the data. If this was seen in actual data one would conclude that no 3+1 sterile neutrino model with the tested oscillation parameters agrees with our data. This would hint that there is a different explanation for the observed excess. Since the underlying truth information is known, the explanation in this case is due to a large unfolded MiniBooNE excess signal rather than sterile neutrino oscillations.

Moving on to the second fake data set, the same analysis is performed. The best fit oscillation parameters are given in Table 12.2. As with fake data set 1, Figures 12.18 and 12.19 show 2D slices of the 90% excluded region at the data best fit and the global best fit respectively. However, unlike fake data set 1, there is a much smaller excluded region in this data set. 13.26% of the grid points tested are excluded. This is comparable to the 09.56% grid points excluded in the sensitivity study. For this data set, the global best fit point is not excluded.

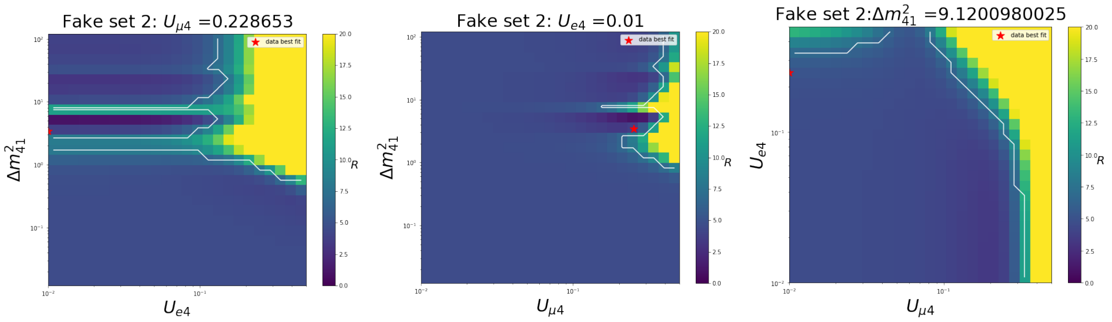

(a) $U_{\mu 4}$ (b) U_{e4} (c) Δm^2_{41}

Figure 12.18: 2D slices of the Wilks' theorem exclusion close to the data best fit point for fake data set 2. The 90% confidence level is shown by the white line. The color scale (capped at 20) indicates the R value.

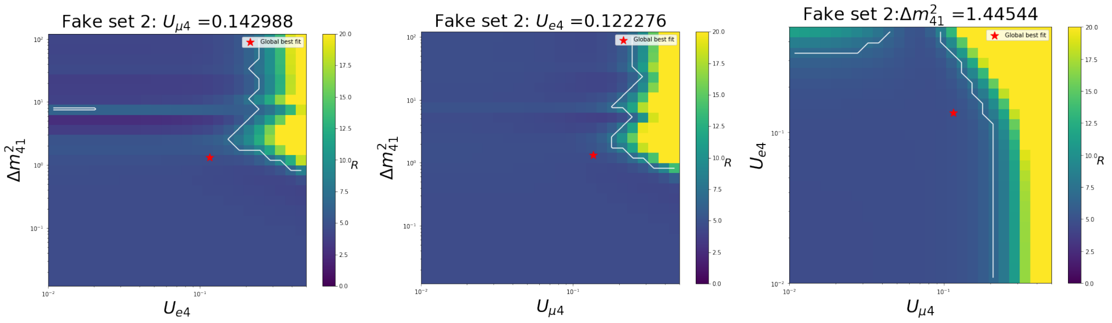

(a) $U_{\mu 4}$ (b) U_{e4} (c) Δm^2_{41}

Figure 12.19: 2D slices of the Wilks' theorem exclusion close to the global best fit point for fake data set 2. The 90% confidence level is shown by the white line. The color scale (capped at 20) indicates the R value.

Figure 12.20 shows the fit results in terms of Δm^2_{41} vs. $sin^2(2\theta)$. The null oscillation is still not excluded. The largest excluded region is seen in $sin^2(2\theta_{\mu e})$.

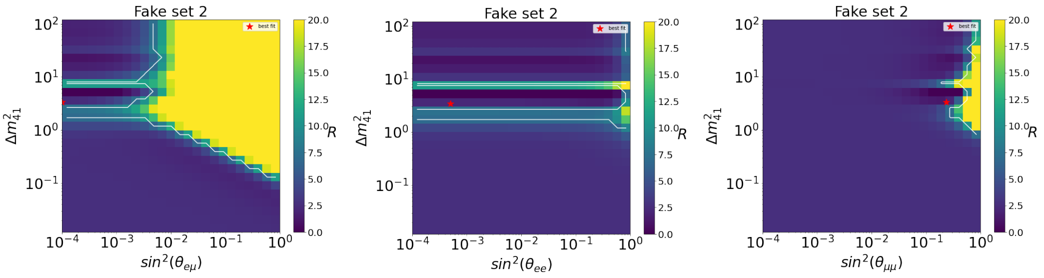

(a) $sin^2(2\theta_{\mu e})$ (b) $sin^2(2\theta_{ee})$ (c) $sin^2(2\theta_{\mu\mu})$

Figure 12.20: 2D slices of the Wilks' theorem exclusion in Δm^2_{41} vs $sin^2(2\theta_{ee,\mu\mu,\mu e})$, while marginalizing the other two $sin^2(2\theta)$ terms. The 90% CL is shown by the white line. The color scale (capped at 20) indicates the R value.

Fig. 12.21 (a) and (b) show the $1e1p$ and $1\mu1p$ spectra respectively. The plot format is the same as for fake data set 1. In this case, there is not much difference between the null oscillation and the best fit oscillation to this data. The $\chi^2/ndof$ for these spectra (Table 12.2) indicate good agreement. If this were real data it would be concluded that this sterile model is still potentially consistent with data. However, it is not conclusive evidence for the existence of sterile neutrinos as both the null model and the global best fit for sterile neutrinos are in the allowed region. This makes sense with the underlying truth model for this data set which did not contain sterile neutrino oscillations, but had slight modifications to the null model.

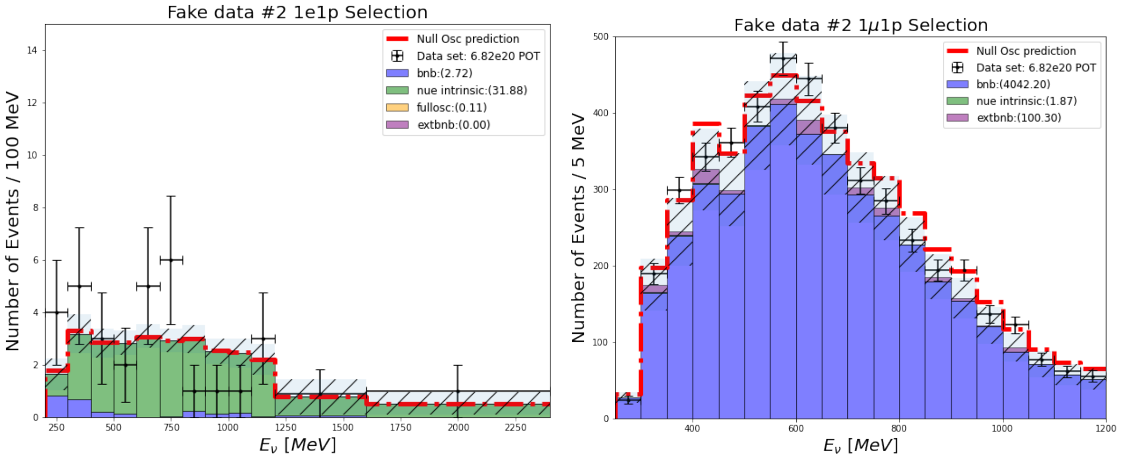

(a) $1e1p$ (b) $1\mu1p$

Figure 12.21: Figure showing the fake data set 2 spectrum in the $1e1p$(a) and $1\mu1p$(b) selections. The null oscillation prediction (red dashed line) and the best fit oscillation prediction (stacked histogram) are shown.The grey dashed line indicates the systematic + statistical uncertainty on the best fit simulated spectrum.

This chapter provided detailed documentation of the 3+1 sterile neutrino analysis strategy. The exclusion sensitivity utilizing Wilks' theorem when creating confidence levels was found. This showed what the excluded region will be if the data matches the null oscillation spectrum. It was notable that the global best fit is not excluded if this is the case. Next a minimizer to find the best fit oscillation parameters was described and verified. Finally, fake data studies were performed using the minimizer to find the best fit parameters. The excluded region was found using Wilk's theorem. This fake data studies validate the analysis strategy and provide results consistent with the truth information of the data sets.

Chapter 13

Results and Comparison to Global Best Fit

The event reconstruction and selection have been optimized and well vetted. The analysis method for comparing data to a 3+1 sterile neutrino oscillation model has been decided upon and carefully verified. It is finally time to look at the results on the MicroBooNE data set. Recall that the data shown here comes from the first 3 MicroBooNE run periods and corresponds to 6.67x10^{20} POT after processing. As in Chapter 12, the oscillation parameter values tested are: Δm^2_{41}, 25 logarithmic spaced values, range: [0.01,100] MeV^2; U_{e4}, 25 logarithmic spaced values, range: [0.01,0.5]; and $U_{\mu 4}$, 25 logarithmic spaced values, range: [0.01,0.5].

13.1 Results of Data Analysis

The analysis of the data set follows the same procedure used in Section 12.5 on the fake data sets. First, a grid search is be run to find the $-2ln(L(\theta))$ at each point in the oscillation parameter space. Next the minimizer will be run with the oscillation parameters with the minimum $-2ln(L(\theta))$ as the initial values. This provides the best fit oscillation parameters and the corresponding $-2ln(L(\theta_{bf}))$. R (Eq. 12.1) is then calculated for each tested set of oscillation parameters. If the R is greater than 6.251, that set of parameter values is considered to be excluded under

Wilks' theorem. Finally, the $1e1p$ and $1\mu1p$ spectra will be examined individually.

Table 13.1 provides a summary of the best fit values. Immediately a few pieces of this result stand out. The first is the calculated $sin^2(2\theta_{ee})$ is much higher than the other two $sin^2(2\theta)$ parameters. In other words the best fit model is one in which very few ν_μ 's from the beam oscillate into ν_e 's. However, the intrinsic ν_e backgrounds have a high disappearance rate in this best fit model. It is also notable that the exclusion region using Wilks' theorem is quite large. This will be examined later in this chapter.

Table 13.1: A summary of the MicroBooNE best fit oscillation parameters. "Excluded" is the number of grid points excluded with 90% confidence divided by the total number of grid points tested (15625).

Excluded	$\Delta m^2_{41} eV^2$	$\lvert U_{e4}\rvert$	$\lvert U_{\mu4}\rvert$	$\sin^2(2\theta_{\mu e})$	$\sin^2(2\theta_{ee})$	$\sin^2(2\theta_{\mu\mu})$
99.17%	3.57	0.432	0.010	7.5×10^{-5}	0.607	4×10^{-4}

Table 13.2 shows how well the data agrees with the model at two points, null oscillations and the best fit oscillation model. The first column $-2ln(L)$, is determined as in Eq. 4.7 and is the sum of $ln(|M|)$ and χ^2_{tot} in the table. The R value for null oscillation is 8.7 and is the difference of the two $-2ln(L)$ values. This R value has roughly equal contributions from the determinant term and the total χ^2 term.

Table 13.2: A summary of the best fit model and null model agreement with the data. The difference of $-2ln(L)$ for the two models leads to an R value of 8.7 at the null.

Model	$-2ln(L)$	$ln(\lvert M\rvert)$	$\chi^2_{tot}/31$ (ndof)
Null Model	215.08	124.09	90.99/31=2.94
Best Fit	206.34	119.57	86.79/31=2.80

Figure 13.1, 13.2, and 13.3 show the 2D slices of the 3D parameter space in slices of Δm^2_{41}, U_{e4}, and $U_{\mu4}$ respectively. R for each parameter is shown by the color scale (capped at 20 for visualization). The white lines show the 90% exclusion contours. An immediately obvious feature on these plots is the large portion of parameter space with values just above the 90% limit.

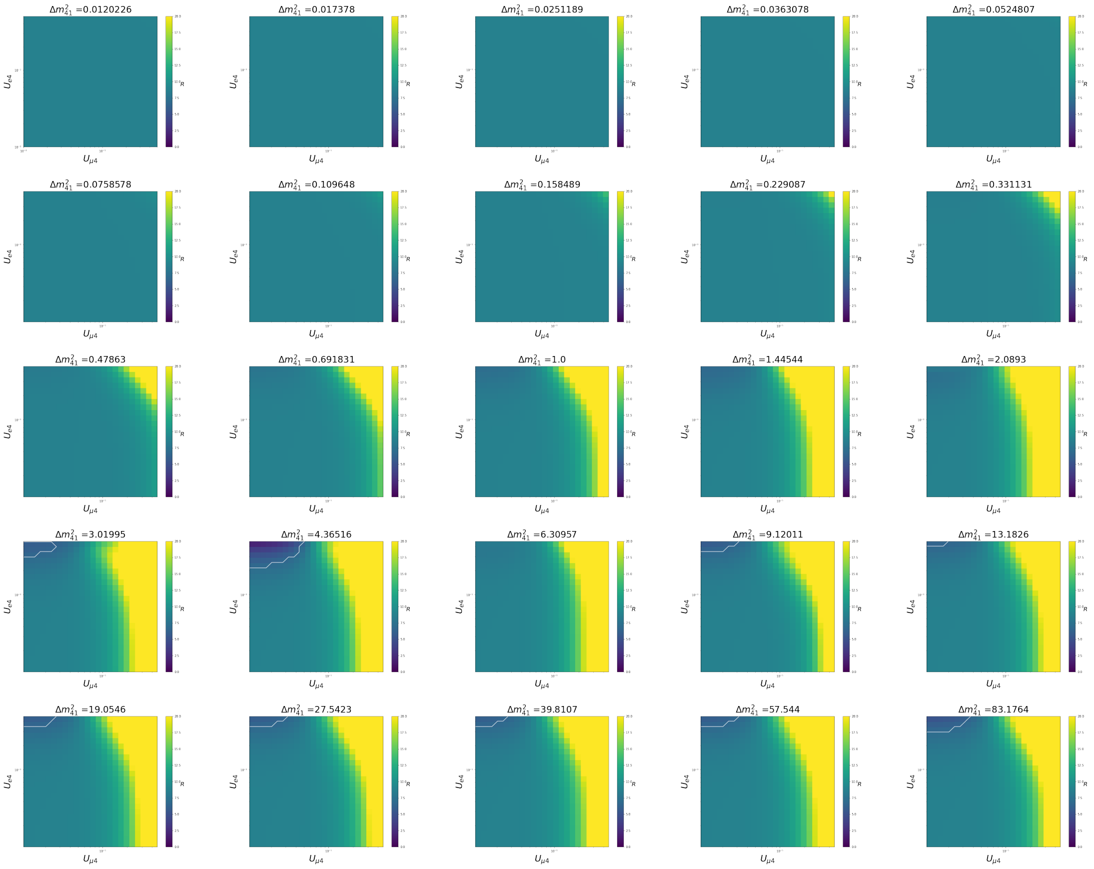

Figure 13.1: 2D slices for each Δm^2_{41} value tested to construct the Wilks' 90% confidence excluded region from data (Δm^2_{41} value indicated by the plot title).

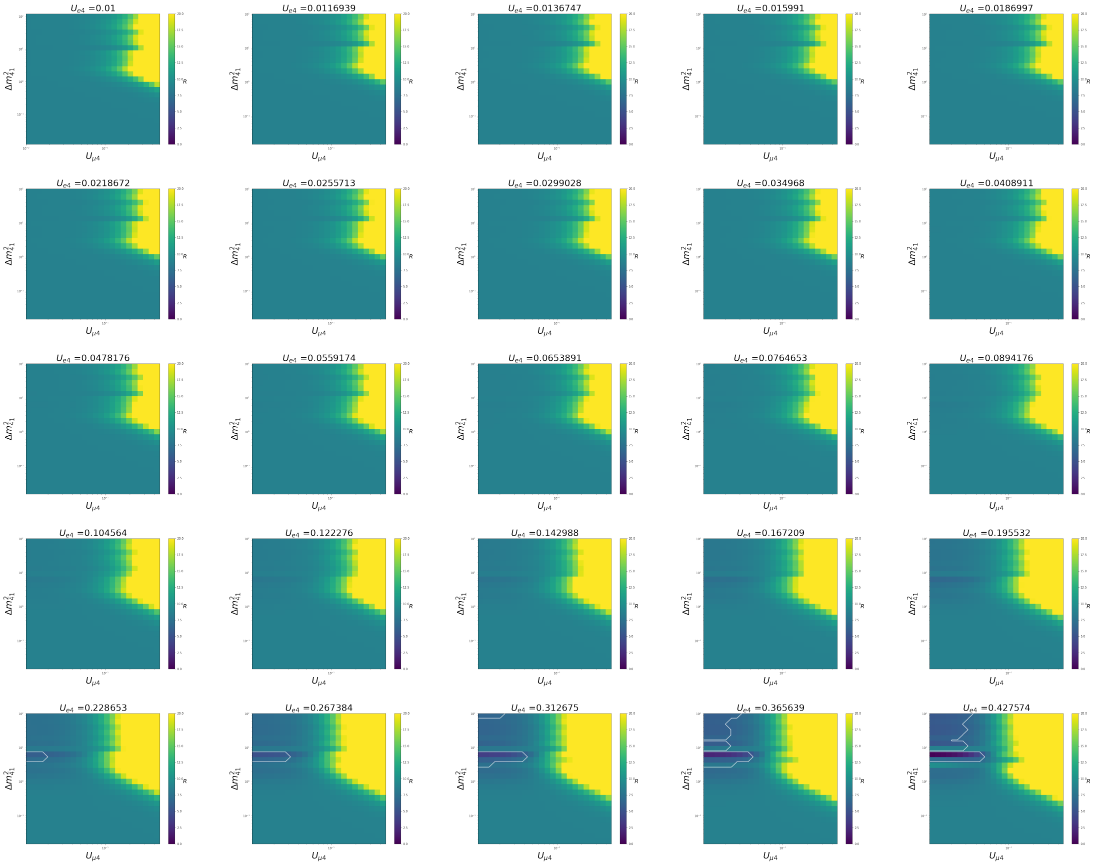

Figure 13.2: 2D slices for each U_{e4} value tested to construct the Wilks' 90% confidence excluded region from data (U_{e4} value indicated by the plot title).

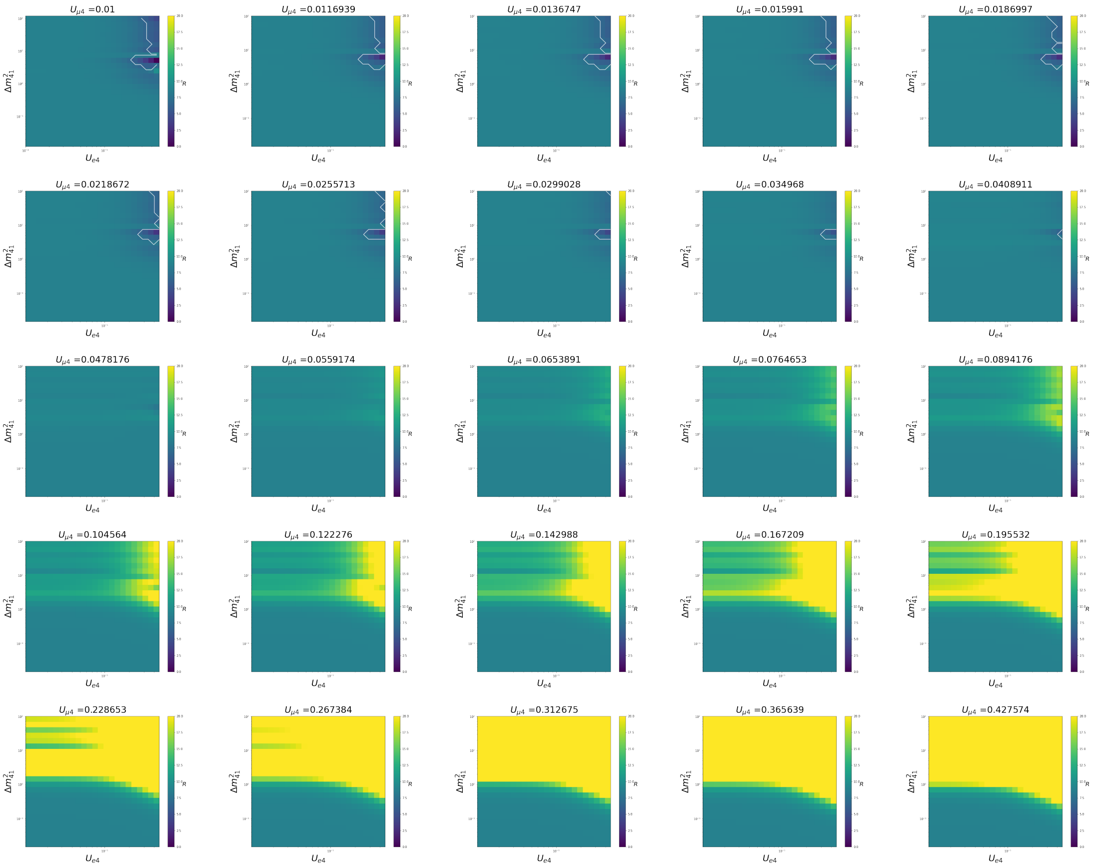

Figure 13.3: 2D slices for each $U_{\mu 4}$ value tested to construct the Wilks' 90% confidence excluded region with data ($U_{\mu 4}$ value indicated by the plot title).

Next, two particular slices are examined in more detail. The first, shown in Figure 13.4 are the 2D slices closest to the data best fit. The R values are indicated by the z axis and are evaluated at the centers of the bins. Recall that this is slightly offset from the values in Table 13.1, as those values were found by the minimizer. These slices highlight the small allowed region. The red star is the best fit from the minimizer of the two parameters shown in the slice. As such, the red star is slightly offset from the lowest R values in the 2D slice shown. The grid slices were decided upon before the minimizer was run and as such are slightly offset from the actual best fit values.

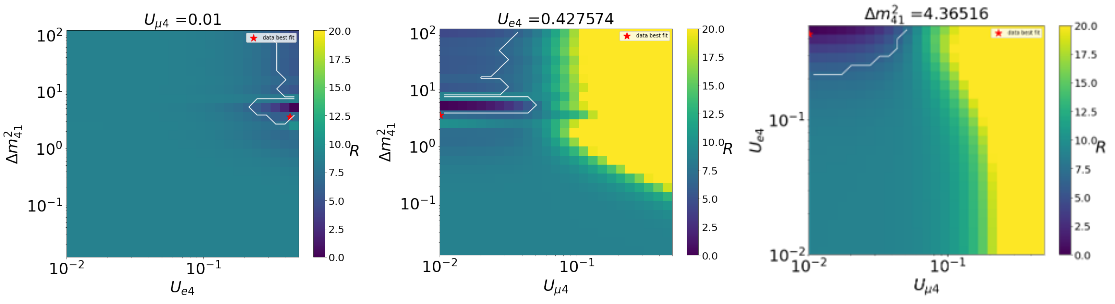

(a) $U_{\mu4}$ (b) U_{e4} (c) Δm^2_{41}

Figure 13.4: 2D slices of the Wilks' theorem exclusion close to the data best fit point. The 90% confidence level is shown by the white line. The color scale (capped at 20) indicates the R value.

Figure 13.5 highlights the 2D slices closest to the global best fit parameters (Table 3.1). No contour lines are shown on these slices because the entire region is considered excluded when using Wilks' theorem. However, the yellow region of the plot which indicates very high R values is similar to the shape of the yellow region observed when testing the MicroBooNE sensitivity in Figure 12.5.

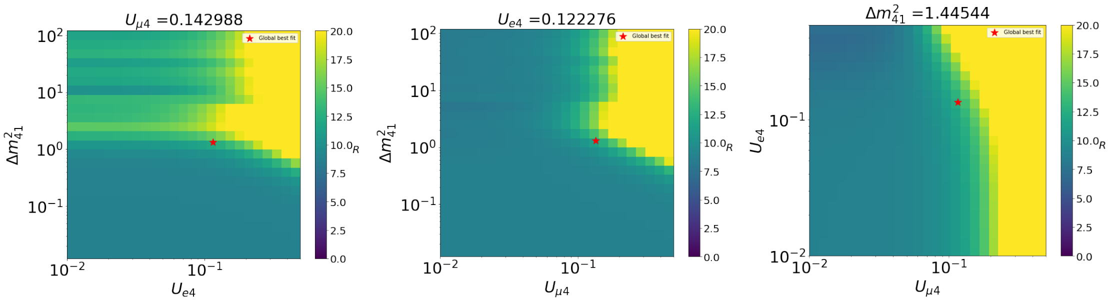

(a) $U_{\mu4}$ (b) U_{e4} (c) Δm^2_{41}

Figure 13.5: 2D slices of the Wilks' theorem exclusion close to the global best fit point for fake data set 1. The 90% confidence level is shown by the white line. The color scale (capped at 20) indicates the R value.

Next, Figure 13.6 shows 2D slices of R in $sin^2(2\theta)$ parameter space. As in the fake data studies, for each slice of Δm^2_{41} vs. $sin^2(2\theta_X)$, the other two $sin^2(2\theta_Y)$ terms have been set to their best fit value in Table 13.1. The red stars indicate the best fit points from this table. It is noted that the best fit value of $sin^2(2\theta_{\mu e})$ is below the minimum shown on this slice so is displayed in this plot as on the y-axis at the best fit Δm^2_{41}. As will be discussed in Section 13.2, while these contours show a large region excluded at 90% confidence, more work is required to fit them into the global picture.

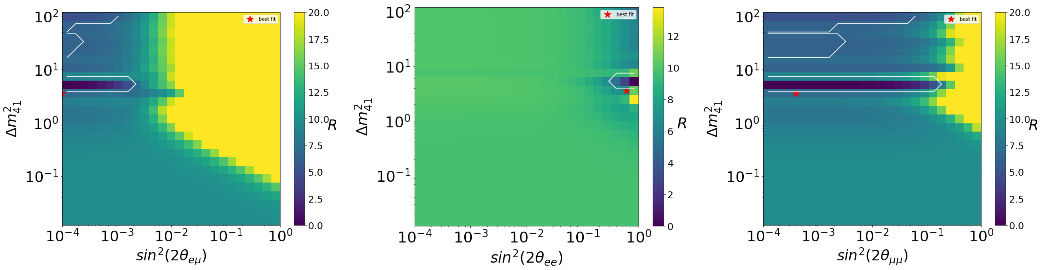

(a) $sin^2(2\theta_{\mu e})$ (b) $sin^2(2\theta_{ee})$ (c) $sin^2(2\theta_{\mu\mu})$

Figure 13.6: 2D slices of the Wilks' theorem exclusion in Δm^2_{41} vs $sin^2(2\theta_{ee,\mu\mu,\mu e})$, while setting the other two $sin^2(2\theta)$ terms to be their best fit as found in Table 13.1. The 90% CL is shown by the white line. The color scale (capped at 20) indicates the R value.

Finally, Figure 13.7 show the best fit model spectrum compared with data for both the $1e1p$ and $1\mu1p$ selections. The null oscillation model is indicated by the red dashed line. The best fit oscillation model is shown by the stacked colored histograms with the systematic uncertainty shown by the grey dashed boxes. The data with Poisson error bars is shown by the black points.

The strong ν_e disappearance is seen in Figure 13.7 (a). It is interesting that there the best fit oscillation parameters are such that there is large disappearance in the bins where no data is observed and less disappearance near where the data has bins above the null oscillation model. The data in the $1e1p$ bins does not match either the null oscillation or the best fit model well. This, along with the large excluded region, indicates that the 3+1 model in general does not agree well with the MicroBooNE $1e1p$ CCQE selection.

Figure 13.7 (b) shows the $1\mu1p$ selection. The observed data is slightly higher that the null oscillation which is what leads to the best fit oscillation model having minimal ν_μ disappearance. The data in the $1\mu1p$ selection agrees fairly well with the best fit model.

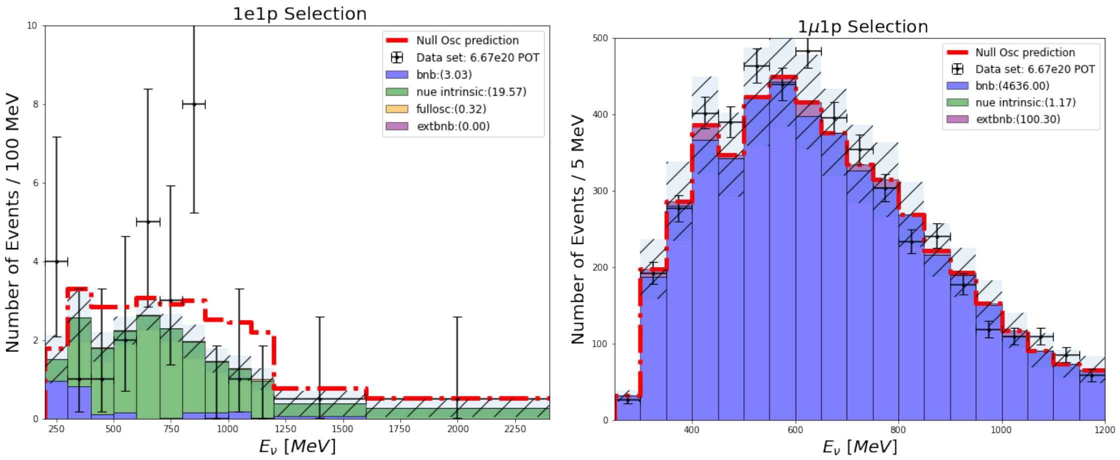

(a) $1e1p$ (b) $1\mu 1p$

Figure 13.7: A comparison of the data spectrum (black points), the null oscillation model (red dashed line), and the best fit oscillation model stacked histogram) in the $1e1p$(a) and $1\mu 1p$(b) selections. The grey dashed line indicates the systematic + statistical uncertainty on the best fit simulated spectrum.

13.2 Discussion of Statistical Method

The results in the previous section require further discussion. For this study Wilks' theorem has been used to determine whether various oscillation parameters are allowed by our data. For Wilks' theorem to correctly estimate the coverage of the confidence level contours, there are necessary conditions that must be met when applied both to this data and oscillation experiments. This section will look at these conditions and discuss a different method of determining whether parameters are excluded: the Feldman-Cousins method (FC) [85].

In order to use Wilks' theorem to determine the excluded region a number of conditions must be met as outlined by Ref. [90]. These are:

1. N (number of events) is sufficient;
2. the true values of the parameters should be in the interior of the parameter space tested;
3. different values of the parameters are identifiable (no degeneracy);
4. the null hypothesis is a limiting case of the model;

5. the systematic uncertainties are correctly estimated, are not too small, and can be approximated as a multivariate Gaussian;
6. the expectation varies approximately linearly as a function of the model parameters.

Of these conditions, the two that immediately require more consideration for this oscillation study are (1) and (5). Defining the necessary number events is difficult as in principle N should go to infinity for Wilks' theorem to hold. In practice one aims for >10 events per bin. It is clear that in our case, especially now that the $1e1p$ data selection has been observed, this assumption is not valid. Though it may have been more valid if the existence of a sterile neutrino caused a very large increase in the number of ν_e events. Additionally, this study is testing a theory that may not be true in nature, which could cause the observed tension throughout most of the parameter space. Even if a sterile neutrino exists, our model may be inaccurate if there was a problem in our simulation or uncertainty calculations.

As an alternate to Wilks' theorem, one may use the FC method to determine confidence level contours. This method does not make the assumptions that Wilks' theorem does in order to relate the test statistic to a frequentist confidence level, but instead explicitly calculates the explicit distribution of the test statistic using pseudo-experiments. In this method, one uses the same R value as calculated by Eq. 12.3 at each point in parameter space with the observed data. The best fit oscillation parameters are still the same. What changes is how a set of parameters is considered excluded. Instead of comparing to the 6.25 value, a new value is determined at each point in parameter space referred to as R_{crit}. This R_{crit} takes the place of 6.25 in that this is the value the R value is compared to. If $R > R_{crit}$ at a set of oscillation parameters that parameter set is considered excluded.

The first step of determining R_{crit} at a point in parameter space is to generate pseudo-experiments from that point as described previously in Section 12.2. The R value is calculated for each of these experiments. R_{crit} is set to be the R value which X% of experiments are less than. For example, in the case of the 90% exclusion limits analyzed for this analysis, R_{crit} is the value for with 90% of pseudo-experiments are less than. This process is repeated at each point in parameter space, which here would result in a 3D grid of parameter values. In other studies the FC method has been found to give a range of R_{crit} values that do not match the value from Wilks' theorem based on the number of degrees of freedom [85].

As may have been gleaned from this description, the reason this method was not used at first was the computational limits. To calculate the R value for a single experiment requires a grid-scan over all 15625 parameter sets followed by the use of the minimizer as was performed for the data. This currently takes $\sim$ 15 minutes of computer time. To perform a complete Feldman-Cousins' method, this is done for $\sim$ 1000 pseudo-experiments at each of the 15625 parameter sets. This was not feasible as a first analysis. However, current efforts within MicroBooNE to decrease the computational time are underway. Future oscillation studies as well as the one presented will be updated to use a full Feldman-Cousins' method.

In the meantime, in order to see what effect switching to an FC method for determining R_{crit} has, the method has been tested at a handful of oscillation parameters. The points chosen to be tested are the smallest oscillation parameters ($\sim$ null), the maximum oscillation parameters, the grid point closest to the global best fit parameters, and five points near the Wilk's 90% exclusion contour in the sensitivity shown in Section 12.3. Note that the first three of these points were already tested in this way in Section 12.2, but are now examined in the FC context instead of to verify the use of the minimizer. Figure 13.8 shows the distribution of these test points in Δm^2_{41} vs. $sin^2(2\theta)$ parameter space.

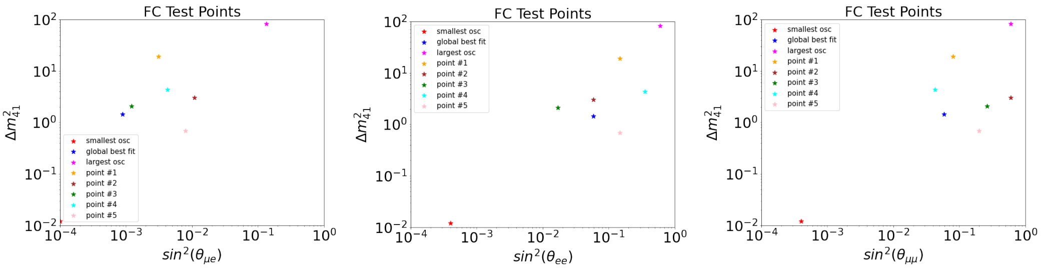

(a) $sin^2(2\theta_{\mu e})$ (b) $sin^2(2\theta_{ee})$ (c) $sin^2(2\theta_{\mu\mu})$

Figure 13.8: The location of the points used to test the Feldman-Cousins' method in Δm^2_{41} vs. $sin^2(2\theta)$ parameter space.

Figure 13.9 shows the result of this FC test. The red spectrum is the result using only a grid search. The blue spectrum is the result of using a grid search followed by the minimizer, which would be the ideal implementation of this method. The vertical lines in the corresponding color indicate R_{crit} for the given test point. The black line shows the Wilks' theorem 90% exclusion value of 6.25 for reference. It is clear just from this test, that a larger value of the oscillation parameter space would be allowed if using the Feldman-Cousins' method to determine the exclusion from the R values. In the future it will be informative to compare the exclusion contours from the two statistical methods.

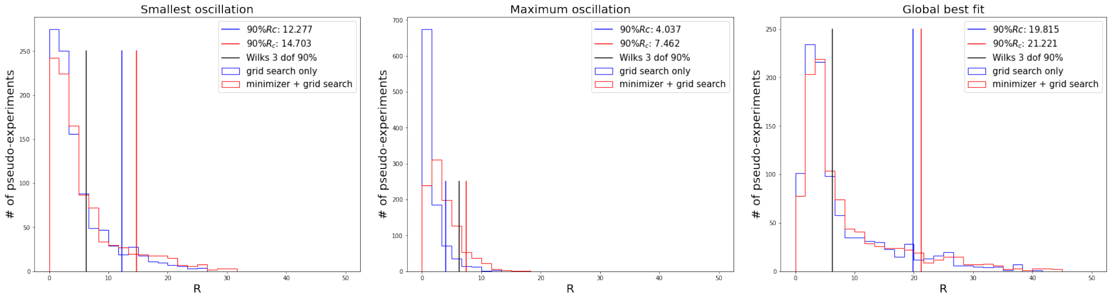

(a) Null Oscillation (b) Maximum Oscillation (c) Global best fit

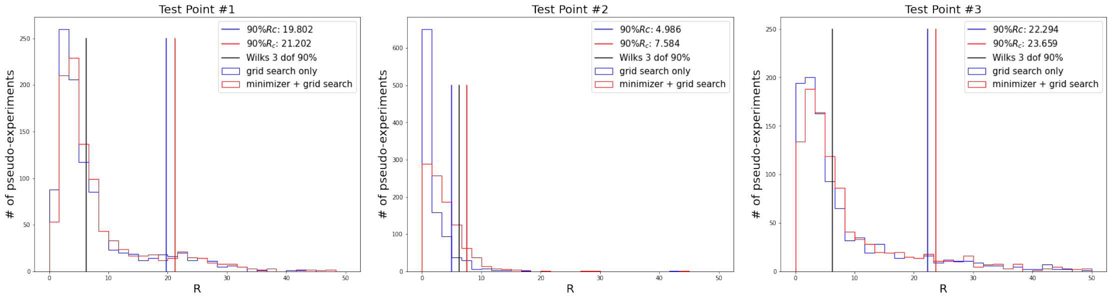

(d) Wilks' 90% point 1 (e) Wilks' 90% point 2 (f) Wilks' 90% point 3

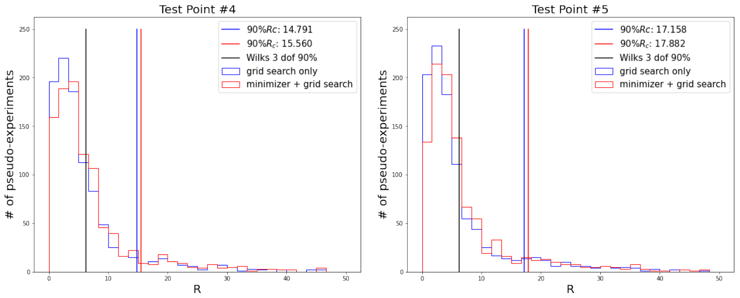

(g) Wilks' 90% point 4 (h) Wilks' 90% point 5

Figure 13.9: The R distribution for 1000 pseudo-experiments thrown from the specified set of oscillation parameters. The red spectrum is the result using only a grid search. The blue spectrum is the result of using a grid search followed by the minimizer. The Wilks' theorem 90% CL value is shown and compared to the 90% R_{crit} from the given spectrum.

A final useful metric for quantifying the agreement between data and the model is a p-value. The p-value is the probability of obtaining test results at least as extreme as the observed data. It is a way to quantify the statistical significance of the result. Smaller p-values are used as evidence against the model. In the FC method the p-value for given parameters is calculated by the number of pseudo-experiments with R values greater than data divided by the total number of pseudo-experiments generated from that point (1k in this test).

Table 13.3 summarizes the results of the FC test points. The new p-value using this method is shown. Three of these test points would be considered allowed. Critically, both the null model (smallest oscillation) and the global best fit points are allowed with this statistical methods. Recall that one limitation with using Wilks' is the assumption that the number of events are sufficiently large. Based on the FC test at maximum oscillation it appears that the assumption may hold for certain regions in parameter space with a large ν_e appearance contribution to the oscillation. At the maximum oscillation value tested, R_{crit} is much closer to 6.25. If more data is used in the future from the rest of the MicroBooNE runs or the other two detectors that are part of the Short-Baseline Neutrino program, Wilks' theorem may be valid through more of the parameter space.

Table 13.3: Results of using the Feldman-Cousins' method at various test points. Shown are the new R_{crit}, the R value of the data at that point, and the new resulting p-value of the data. The final column indicates if the oscillation parameters are allowed (✓) when using FC or still excluded (X) when using a 90% confidence exclusion cut-off.

Test Point	R_{crit}	R_{data}	p-value	Allowed?
Smallest Oscillation	14.70	8.73	0.20	✓
Maximum Oscillation	7.46	215.86	0.00	X
Global Best fit	21.22	16.32	0.17	✓
Near Wilks' 90% #1	21.20	20.43	0.11	✓
Near Wilks' 90% #2	7.58	220.70	0.00	X
Near Wilks' 90% #3	23.66	47.41	0.01	X
Near Wilks' 90% #4	15.56	20.02	0.07	X
Near Wilks' 90% #5	17.88	20.41	0.08	X

The Feldman-Cousins' method here appears to be a promising step forward. Other oscillation analyses in the field are exploring a variety of other methods to determine the allowed vs. excluded regions such as using Bayesian statistics. Regardless of which method is used, this chapter has found the best fit oscillation parameters for this selection in MicroBooNE. This best fit 3+1 sterile neutrino oscillation model still has tension with the data as indicated by the high χ^2. This implies that there is more to be understood about this data. It is entirely possible that the fluctuations seen in the $1e1p$ selection are just a statistical fluctuation. Alternatively, there may be some other beyond SM physics that may explain it such as a more complicated sterile neutrino model (i.e. 3+2, or 3+1 with a decaying sterile neutrino). Analyzing this result in context of other MicroBooNE selections as well as expanding to the full MicroBooNE data set will help shed light on the question of sterile neutrinos.

Chapter 14

Conclusions and Future Outlook

The standard model of particle physics is a very successful theoretical model, but it does not seem to completely explain neutrinos. Strong experimental evidence of three flavor neutrino oscillations has shown that neutrinos have non-zero mass. Even assuming non-zero mass and 3 flavor oscillations both in vacuum and through matter interactions, some experimental anomalies remain: in gallium solar neutrino experiments using a radioactive source, short-baseline reactor experiments, and two short-baseline accelerator experiments. One possible solution to these anomalies is a fourth, light sterile neutrino in a 3+1 model.

The MicroBooNE detector is the first in a series of three planned short-baseline accelerator experiments. It is on the same beam as MiniBooNE with a very similar baseline. The detector is a LArTPC which aims to have finer resolution event reconstruction and better background rejection than was possible in MiniBooNE.

The results in this thesis made use of novel deep-learning tools as well as traditional clustering algorithms to reconstruct the detector data with particular attention paid to shower reconstruction. The accurate reconstruction of shower particles (electrons and photons) proved critical to the utilized event selections.

The target event type used in this analysis are CCQE $1l1p$ events. An important sideband to these events are neutrino events which contain a π^0 in the final state. Using this sideband, a normalization disagreement was seen between the standard model prediction and data. Using this information, a method was developed to reweight the simulation events based on the π^0 momentum. π^0 backgrounds to the $1l1p$ selections have these weights applied.

The use of the two body scattering CCQE events as a target signal allowed for a pure event selection through the use of BDTs and other kinematic cuts. A first test compared these selection to a model of the MiniBooNE low energy excess to the MicroBooNE flux. It was observed that the MicroBooNE data more closely matched the standard model prediction than the MiniBooNE signal, though remaining tension was observed with the standard model prediction.

Using the joint selections of $1e1p$ and $1\mu1p$ events the 3+1 light sterile neutrino model was tested with MicroBooNE data. Three oscillation channels of: disappearance of the intrinsic ν_e background of the beam, disappearance of the ν_μ beam flux, and appearance of ν_e events due to the existence of a sterile neutrino were fit for simultaneously. 90% confidence levels were found assuming Wilks' theorem and the best fit oscillation parameters were found via the use of a minimizer algorithm, TMinuit.

The data presented here shows best fit oscillation parameters with high ν_e disappearance, and very little ν_e appearance or ν_μ disappearance. This best fit makes sense when looking at the spectra shown in Figure 13.7 in that this spectra matches the data more closely than the null oscillation model. However, it is still not a very good fit, especially in the $1e1p$ selection as indicated by the high χ^2 value at the best fit. Further, throughout much of the parameter space, the R value is just above the Wilks' theorem 90% exclusion value. The nature of the measurement and the model likely means that Wilks' theorem is inadequate to determine the confidence level contour lines. Future work may look at other methods for deciding which parameters are allowed by the MicroBooNE data such as the Feldman-Cousins' method that was explored here. These other methods are currently computationally time consuming but do not make the same assumptions as Wilks' theorem.

While Wilks' theorem indicates that the null model and the global best fit are excluded at 90% confidence, initial FC studies indicate that neither of these hypotheses are excluded by the data. More work will be needed to determine whether sterile neutrinos exist and if they do, what the oscillation parameters are. This can be strengthened in the future by the addition of the remaining MicroBooNE data (which will $\sim$ double the amount of data). Other ongoing MicroBooNE analyses are fitting 3+1 model to the data using different event reconstructions and target selections. Comparison to these other future results will be critical in understanding this puzzle. Different theoretical models besides sterile neutrinos to explain the remaining neutrino anomalies continue to be developed. Two more short-baseline accelerator detectors, SBND and ICARUS, will shortly come online to join MicroBooNE as part of the SBN. The combined results from all three experiments will be critical in understanding the short-baseline neutrino anomaly.

Appendix A

Abbreviations

This appendix outlines some of the abbreviations symbols used in this document for reference (listed alphabetically).

- $1e1p$: 1 electron 1 proton final state topology
- $1l1p$: 1 lepton 1 proton final state topology
- $1\mu 1p$: 1 muon 1 proton final state topology
- 3+1: shorthand for the standard model extended with one light sterile neutrino
- BDT: Boosted Decision Tree
- BNB: Boosted Neutrino Beam
- CC: Charged Current neutrino interaction
- CCQE: Charged Current Quasi-Elastic neutrino interaction
- CL: Confidence Level
- CV: Central Value (simulation weights used to model the standard model prediction)
- DIS: Deep Inelastic Scattering (neutrino interaction type)
- DL: Deep-learning
- DOF: Degrees Of Freedom
- FC: Feldman-Cousins' method of determining excluded regions in parameter space
- LAr(TPC): Liquid Argon (Time Projection Chamber)

- LEE: Low Energy Excess (referring to the MiniBooNE low energy excess signal)
- m_{e^-}: conversion factor to go from pixel intensity to shower energy
- NC: Neutral Current neutrino interaction
- PIU: Pixel Intensity Units
- PMT: PhotoMultiplier Tube used in light collection in the MicroBooNE detector and other experiments
- POT: Protons On Target, a measure of the beam flux
- RES: Resonant inelastic neutrino interaction
- SBN: Short-Baseline Neutrino program
- SM: Standard Model of particle physics (extended to include non-zero ν mass)

Appendix B

Contributions

The work shown here was performed with the aid of the entire MicroBooNE Collaboration. Specifically, the event reconstruction, selections, systematic uncertainty, and comparison to the MiniBooNE LEE was performed by the deep-learning analysis group in MicroBooNE. This appendix lists the work that was performed primarily by the author of the thesis for clarity. Though as part of the group, the author contributed to discussions, cross checks, and general assistance to portions that are not listed here. Contributions are listed in order of appearance.

- Sparse implementation and optimization of the algorithm performing direction and energy reconstruction of shower particles. Assisted performing the reconstructed PIU to MeV conversion using the algorithm results.
- The addition and optimization of a second shower search for events with multiple showers to the shower reconstruction algorithm.
- Design, implementation (including input formatting decisions), training, and testing of the Infill Network.
- Development of the π^0 event selection.
- The use of π^0 selection for the shower algorithm verification and combining this with the Michel electron verification.

- All π^0 sideband studies and determination of π^0 weights.
- Expansion of the 1e1p selection to higher energy bins for the 3+1 sterile neutrino study and the resulting updates to the systematic covariance matrix.
- Development of the joint $1e1p$ and $1\mu1p$ 3+1 sterile neutrino sensitivity study, analysis verification, and results on MicroBooNE data. (The principle measurement of this thesis).
- The author also contributed to MicroBooNE by taking shifts monitoring the detector and as a member of the data management team working to process data sets and simulation through various algorithms.

Appendix C

Further Studies on the π^0 Simulation Weights

This appendix presents further studies on the π^0 simulation weights discussed in Chapter 10.

C.1 NC Sample

As seen in Figure 10.11, the NC sample used for the π^0 weight functions has lower stats than the CC sample. Additionally, the weights for the NC result in a higher suppression than the weights for CC events. Further studies have been performed on this sample to understand both the agreement with the CV model and the effect on the NC π^0 backgrounds in the 1e1p selection.

Using the high POT MC NC π^0 sample for both runs 1 and 3, a comparison between the CV model and the π^0 weights was made. Simple selection cuts to isolate only NC events that make it through the reconstruction stage were applied.

1. Reconstructed vertex is in the fiducial volume.
2. Reconstructed vertex is $< 5\,\text{cm}$ away from the true vertex.
3. Reconstructed proton KE ¿ 50 MeV.

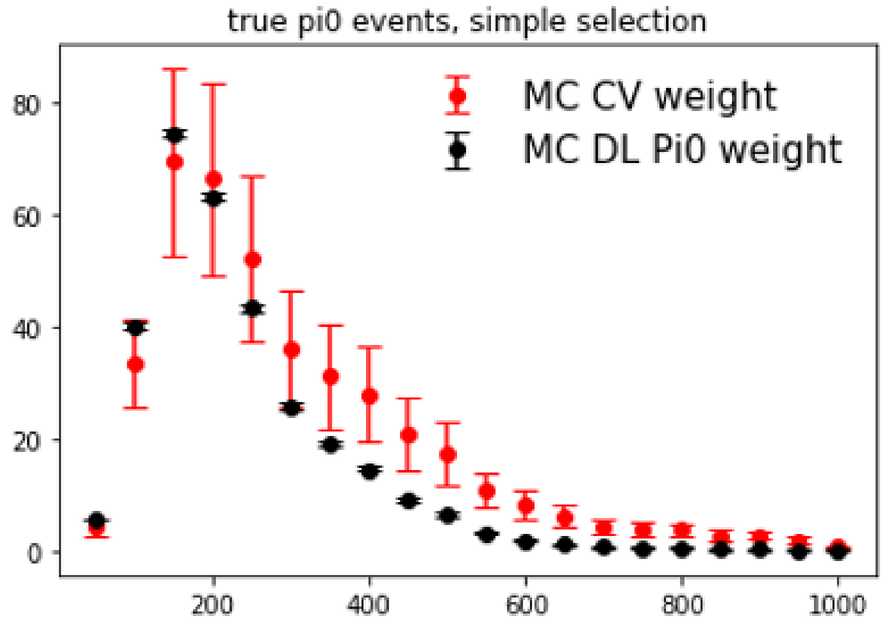

Figure C.1: Agreement with CV model and NC π^0 weights used in the DL analysis, using the high POT NC π^0 sample and simple cuts.

4. Both showers start inside the detector in truth.

Figure C.1 shows the agreement between the CV model and the NC π^0 weights. The CV model points include both statistical uncertainty and cross section systematics. The χ^2/ndof for the distributions is 34.46/20=1.72. This gives a P-value of 0.023. This means the disagreement between the CV model and the π^0 weights is 2.27σ. There is some tension, but the weights do not exclude the CV model.

I further tested various weight functions and present the results here. To summarize, we test 3 additional weight functions (polynomial, line + line, and a normalization) using 5 bins instead of 10 to account for the low stats. All three give worse agreement with the reconstructed data, but better agreement with the CV. Therefore, we have chosen to use the 10 bin polynomial fit as it gives the best agreement to the reconstructed data. We further show that switching between the various fit functions results in little change in the 1e1p background counts.

Figure C.2 shows the different fit functions that were tested. The agreement between the fit and the reconstructed data can be seen in Table C.1. It can be seen that the 10 bin polynomial fit used in the analysis gives the best agreement to the

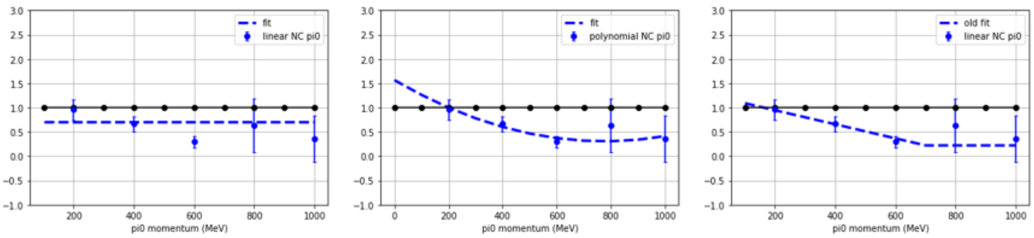

(a) 5 Bin Normalization (b) 5 Bin Polynomial (c) 5 Bin Line+Line

Figure C.2: Different fit functions tested for the NC π^0 sample: (a) 5 bin normalization, (b) 5 bin polynomial, (c) 5 bin line + line.

Fit Function	chi2/ndof	P-value
10 Bin polynomial	2.59/9 = 0.29	0.978
5 Bin normalization	6.88/4 = 1.72	0.142
5 Bin polynomial	12.54/4 = 3.13	0.014
5 Bin line + line	10.8/4 = 2.7	0.029

Table C.1: Table showing the agreement between the NC π^0 fit methods and the R distribution.

data.

We have tested the agreement with the CV for each of the fits. The results can be seen in Fig. C.3 and Table C.2 . The best agreement is with the normalization fit. This is by construction as the distributions have the same shapes.

C.2 CC Sample

We have also tested two further weight functions for the CC π^0 sample to verify that the function used in this analysis is an optimal choice. We have tested both an exponential fit and a two line fit. As seen in the following table, the best agreement

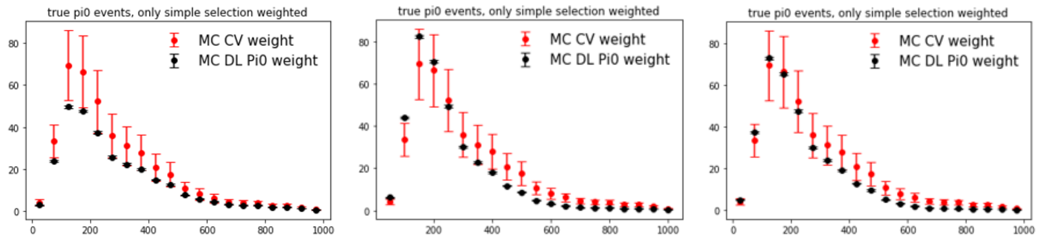

(a) 5 Bin Normalization (b) 5 Bin Polynomial (c) 5 Bin Line+Line

Figure C.3: Comparison with the CV for different fit functions tested for the NC π^0 sample: (a) 5 bin normalization, (b) 5 bin polynomial, (c) 5 bin line + line.

Fit Function	chi2/ndof	P-value
10 Bin polynomial	34.46/20=1.72	0.023
5 Bin normalization	1.22/20 = 0.067	0.999
5 Bin polynomial	27.6/20 = 1.38	0.11
5 Bin line + line	20.77/20 =1.04	0.41

Table C.2: Table showing the agreement between the NC π^0 fit and the CV model.

Fit Function	chi2/ndof
2nd degree polynomial	0.70/9 = 0.08
exponential	2.30/9 = 0.26
line +line	54.64/9 = 6.07

Table C.3: The agreement between the CC π^0 fit options and the data.

is the the 2nd degree polynomial used in the analysis.

C.3 Effect of Weights on Additional π^0 Kinematic Variables

The following set of plots show extra π^0 kinematic variables with the π^0 weights applied. The plots contain stat + flux + xsec + detector systematic uncertainties.

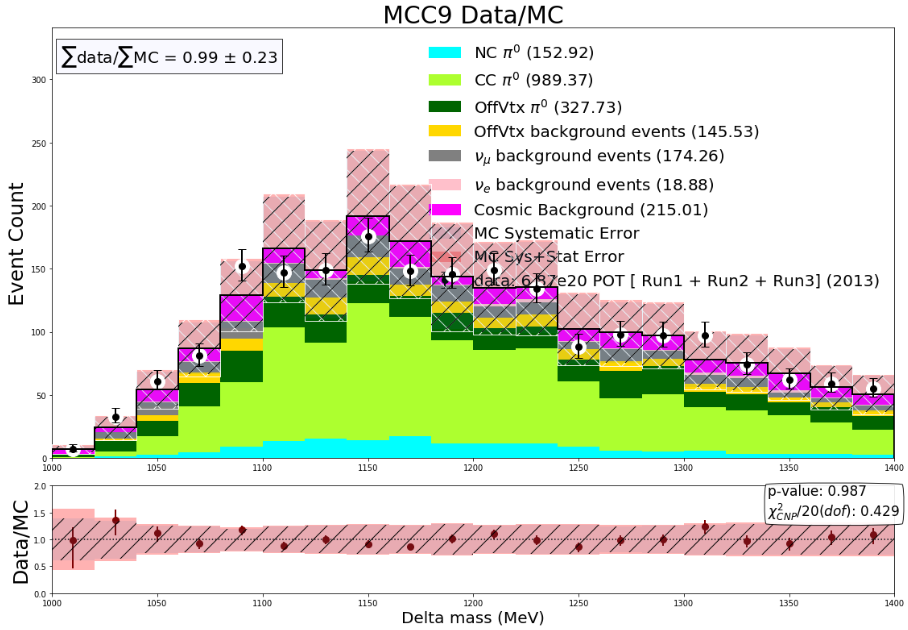

Figure C.4: The reconstructed delta mass distribution with the π^0 weights applied. The MC has been POT scaled to match runs 1+2+3 data.

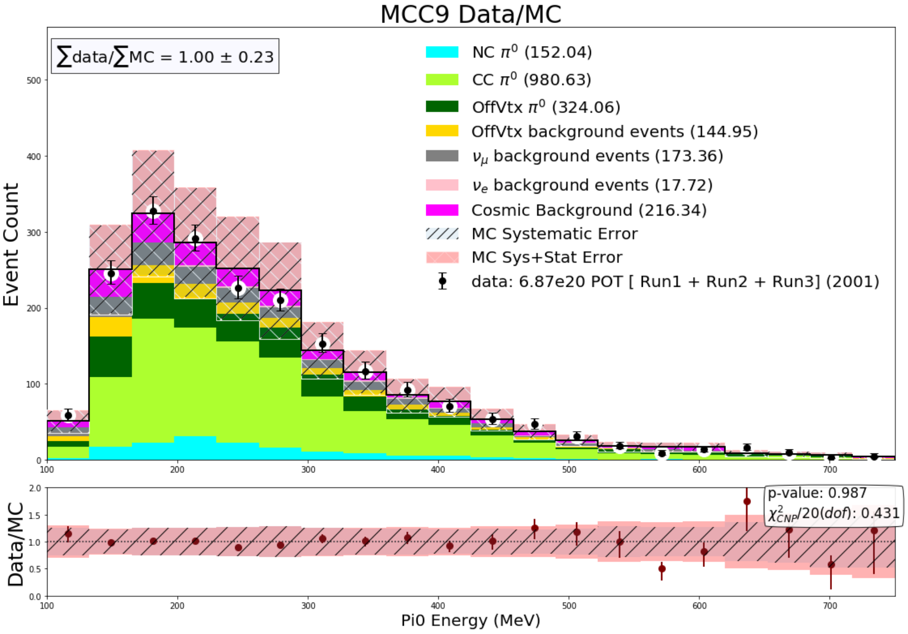

Figure C.5: The reconstructed pi0 energy distribution with the π^0 weights applied. The MC has been POT scaled to match runs 1+2+3 data.

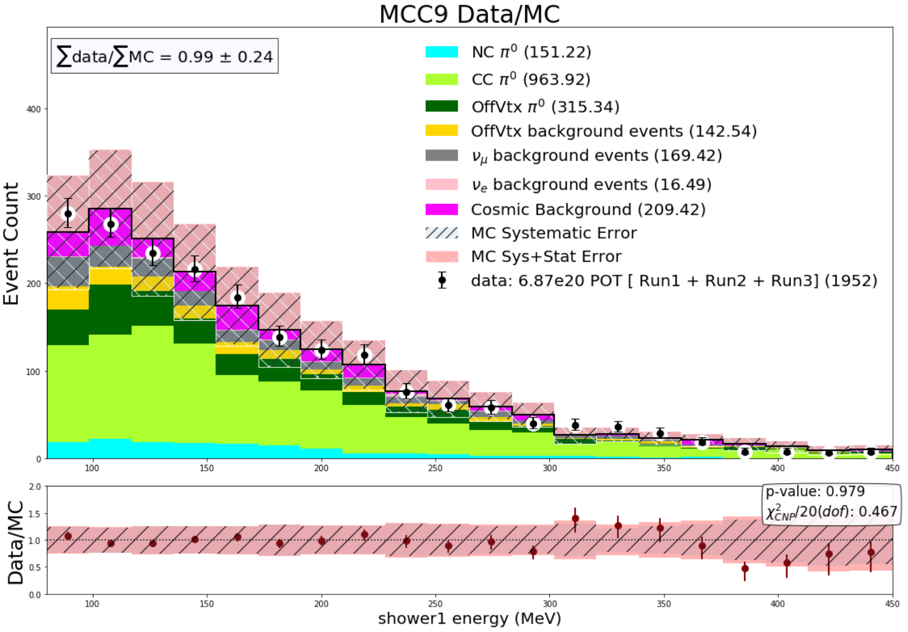

Figure C.6: The reconstructed leading photon energy distribution with the π^0 weights applied. The MC has been POT scaled to match runs 1+2+3 data.

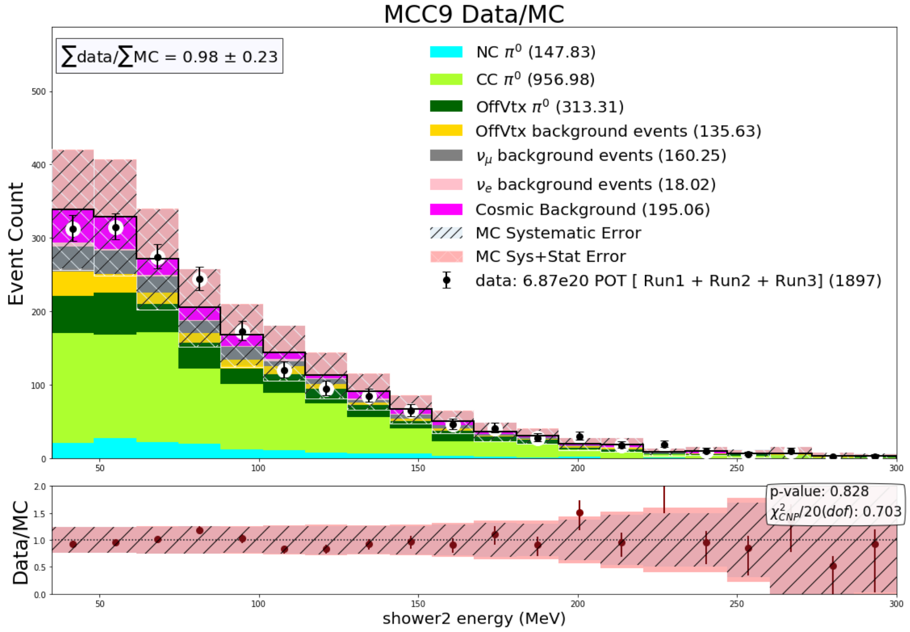

Figure C.7: The reconstructed sub leading photon energy distribution with the π^0 weights applied. The MC has been POT scaled to match runs 1+2+3 data.

Appendix D

High Energy 1e1p Bin Test

This appendix describes the series of studies performed to test the extension of the $1e1p$ selection energy range from 200-1200 MeV in 100 MeV bins (referred to as LEE binning) to 200-1200 MeV in 100 MeV bins 1 bin from 1200-1600 MeV + 1 bin from 1600-2400 MeV (referred 3+1 binning). Arriving at the chosen binning scheme involved a few intermediate tests. Everything shown in this section was performed on simulation only, while staying functionally blind to the data.

A variety of binning schemes to test were chosen that were similar to the LEE binning, but some of which added extra high energy bins of various sizes. The original LEE version was also tested. For each binning scheme the 90% Wilks' theorem excluded region was found (procedure described in Section 12.1). In this test, only a χ^2 metric was used instead of the full $-2\ln(L)$ metric described in Section **??**, as this test was performed before the $-2\ln(L)$ metric was decided upon. Only the $1e1p$ channel with ν_e appearance was used. The 1μ1p selection and the other two oscillation channels were ignored for simplicity. Before performing this study it was decided that the binning scheme with the largest 90% excluded region would be chosen for the rest of this analysis. A logarithmic grid of parameter values was used with Δm^2_{41} from 0-100 MeV and $\sin^2(2\theta_{\mu e})$ from 0-1. 100 values were tested for each parameter resulting in a parameter space of 10k bins.

Fig. D.1 shows the results of this test which are summarized in Table. D.1. Each plot shows the 2D parameter space with the χ^2 between the CV spectra and the oscillated spectra with the given parameters on the the z-axis. The Wilks' theorem 90% excluded region for 2 degrees of freedom ($\chi^2 > 4.25$) and 99% excluded region ($\chi^2 > 9.21$) boundaries are indicated by the white contour lines. All of the binning schemes have similar shapes, but the exact contour lines change.

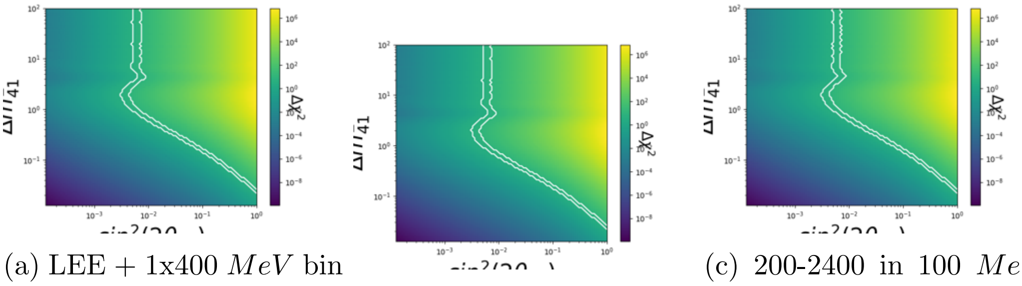

(a) LEE + 1x400 MeV bin + 1x800 MeV bin (b) LEE (c) 200-2400 in 100 MeV bins

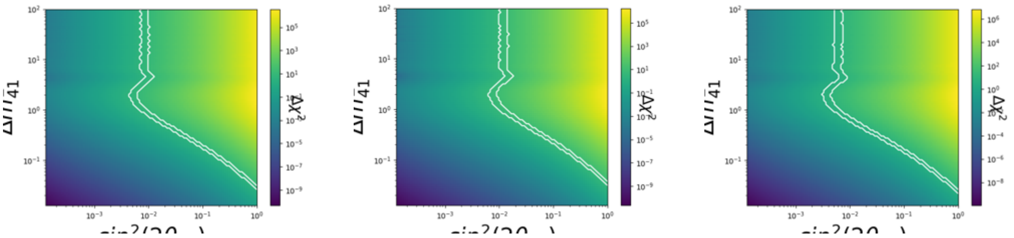

(d) 200-2400 in 200 MeV bins (e) 200-2400 in 400 MeV bins (f) LEE + 1x1200 MeV bin

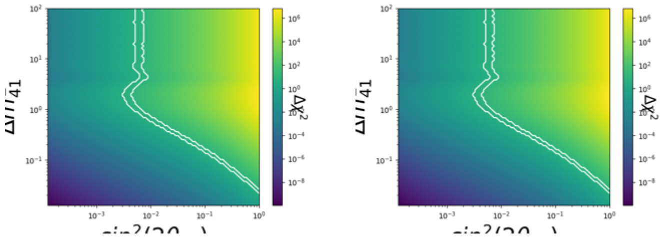

(g) LEE + 3x400 MeV bin (h) LEE + 2x600 MeV bin

Figure D.1: $1e1p$ bin test showing Wilks' theorem results using 1e1p only, ν_e appearance only, and a χ^2 test metric.

Based on the results of this test, using the previously designed metric, the binning for the 1e1p selection of 200-2400 MeV in 100 MeV bins was examined for this analysis. This binning scheme is very similar to the LEE binning, but with higher energy bins. No other part of the selection has been changed. Figure D.2 shows the new total CV spectrum as well as an example oscillation near maximum allowed oscillation. It can be seen that the 1e1p selection now captures the tail of the oscillation, even for the strong parameters used in this example.

Table D.1: A summary of binning schemes tested with the number of excluded bins with 90 % and 99% confidence out of the 10k test bins. LEE here means a binning scheme of 200-1200 MeV in 100 MeV bins.

Binning Scheme	90% excluded bins	99% excluded bins
LEE + 1x400 MeV bin + 1x800 MeV bin	4186	3863
LEE	4184	3862
200-2400 in 100 MeV bins	4194	3882
200-2400 in 200 MeV bins	3867	3564
200-2400 in 400 MeV bins	3548	3247
LEE + 1x1200 MeV bin	4184	3862
LEE + 3x400 MeV bins	4186	3863
LEE + 2x600 MeV bins	4185	3863

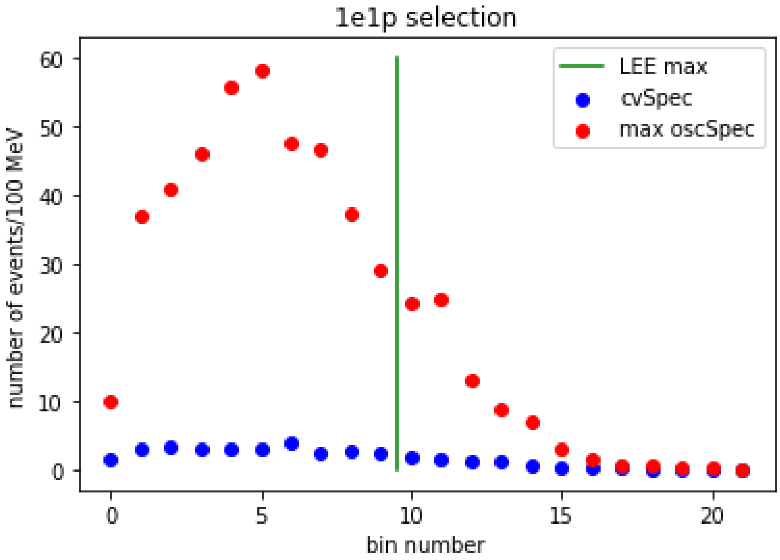

Figure D.2: Two example spectra in the 1e1p channel including the new bins. The green vertical line is the boundary of the original binning and the new binning for visualization. The blue spectrum is the zero oscillation prediction. The red spectrum is an example oscillation prediction.

However, upon closer inspection, various complications were found with this binning. The first, and most critical, is that the highest energy bins have $\sim O(0)$ expected events. Additionally, unexpected features were observed in the combined flux, neutrino–nucleus interaction model, and the hadron re-interaction model covariance matrix (here abbreviated to ”flux and cross-section covariance matrix”. These seem to be due to the very low simulation statistics in the high-energy bins.

Figure D.3 shows the flux and cross-section covariance matrix with both the null oscillation and maximal oscillation. The z-axis has been capped at to 0.25 to keep

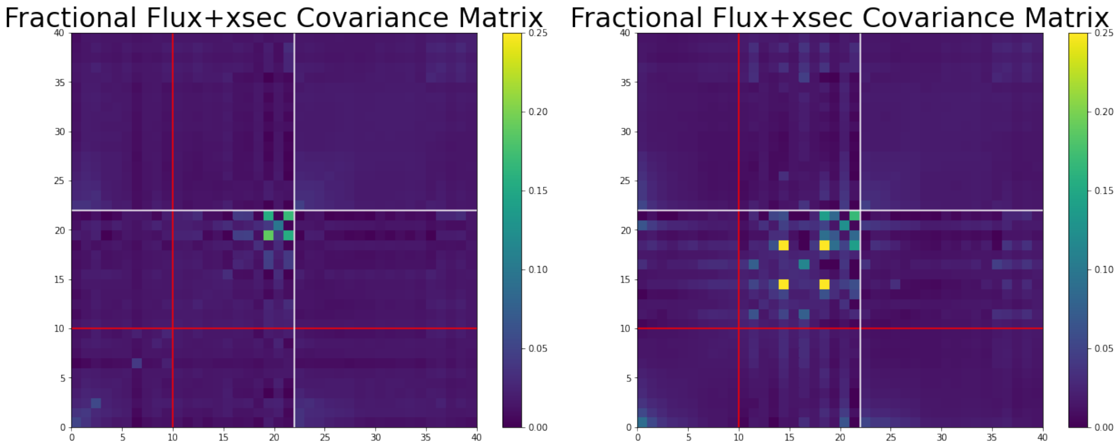

(a) Null oscillation (b) Maximum oscillation

Figure D.3: Two example flux and cross-section covariance matrices for (a) null oscillation and (b) maximum oscillation. Bins 0-9 are the original bins of the 1e1p selection (indicated by red line). Bins 10-21 are the additional high energy 1e1p bins (indicated by white line). Bins 22-40 are the 1μ1p bins. The z-axis has been capped at 0.25 for better visualization.

the scale the same for the purpose of visualization. In the high energy bins, a striped pattern is observed. This is due to low simulation statistics cause large uncertainty weights for certain events.

The solutions to these two problems (low number of expected events and large covariance matrix weights) is two-fold. The first is to put a cap on the uncertainty weights used to construct to the covariance matrix. An investigation into these weights found that 0.02% of the weights used were greater than 10. Of these large weights, ~90% were in the high energy bins of the 1e1p selection in the FullOsc simulation sample. An additional ~5% were in the high energy bins of the 1e1p selection in the nue intrinsic simulation sample. The final ~5% were scattered throughout the rest of the selection. Therefor the uncertainty weights used in calculating the flux and cross-section covariance matrix were capped at 10.

However, this did not completely fix the stripe behaviour seen in the covariance matrix and does not fix the problem of $\sim O(0)$ expected events in the highest energy bins. Therefore, a new binning was investigated from the previously defined list of options in Table D.1. The option chosen was [200-1200] in 100 MeV bins + [1200-1600] in 1 400 MeV bin + [1600-2400] in 1 800 MeV bin (first option in Table

D.1).

The spectrum with this binning can be seen in Fig. D.4. Now, only the highest bin has low expectation at maximum oscillation, instead of six bins in the previous proposal. As seen in Figure 9.7 in Chapter 9, the covariance matrix also has much smoother features using this final binning scheme, even at maximum oscillation.

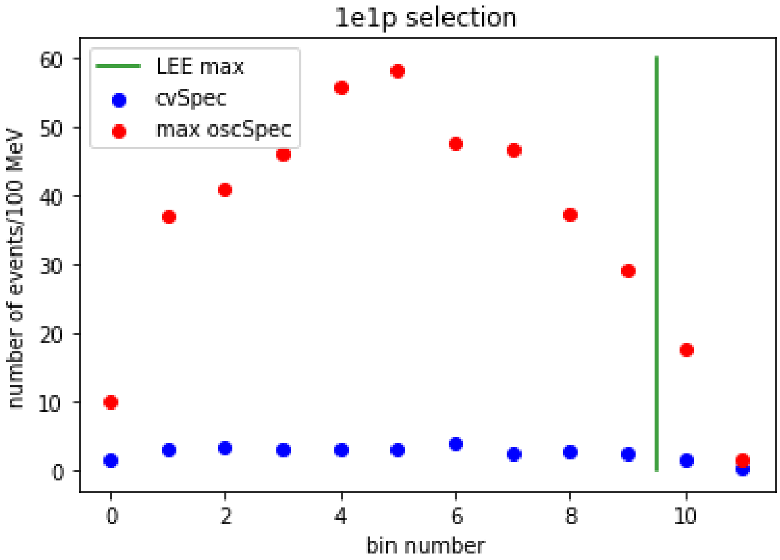

Figure D.4: Two example spectra in the 1e1p channel with the final binning scheme. The green vertical line is the boundary of the original binning and the new binning for visualization. The blue spectrum is the zero oscillation prediction. The red spectrum is an example oscillation prediction.

As mentioned previously, the test shown in Table D.1 was performed using 1e1p only, ν_e appearance only, and a χ^2 test metric instead of the more correct $-2\ln(L)$ test metric described in Section ??. Therefore, in order to analyze the difference in performance between the binning schemes, the test was repeated with 1e1p+1μ1p, all oscillation channels, and the $-2\ln(L)$ test metric. For each of the two binning schemes that were closely considered, the size of the Wilk's theorem 90% CL excluded region was found. The results are shown in D.2.

The performance between the two binning schemes is very similar. Therefore, the final binning chosen for this 3+1 sterile neutrino analysis is [200-1200] in 100 MeV bins + [1200-1600] in 1 400 MeV bin + [1600-2400] in 1 800 MeV bin. Though it doesn't have the maximum size excluded region, we have more confidence in the covariance matrix and the behaviour of our test metric when we don't have multiple

Table D.2: A summary of binning schemes tested with the number of excluded bins with 90% confidence out of the 15625 test bins (25x25x25). LEE here means a binning scheme of 200-1200 MeV in 100 MeV bins. Frac excluded is the number of 90% excluded bins/ total bins.

Binning Scheme	90% excluded bins	frac excluded
LEE + 1x400 MeV bin + 1x800 MeV bin	1494	0.0956
200-2400 in 100 MeV bins	1837	0.1175

bins at high energy with close to zero expectation.

Bibliography

[1] Mark Thomson. *Modern Particle Physics.* 4th ed. India: Cambridge University Press, 2013 (cit. on pp. 6, 13).

[2] M. Sajjad Athar and S. K. Singh. “Neutrinos and their interactions”. In: *The European Physical Journal Special Topics* 230.24 (Nov. 2021), pp. 4215–4220. DOI: `10.1140/epjs/s11734-021-00302-x`. URL: `https://doi.org/10.1140%2Fepjs%2Fs11734-021-00302-x` (cit. on pp. 8, 9).

[3] Donald H. Perkins. *Introduction to High Energy Physics.* 4th ed. India: Cambridge University Press, 2000 (cit. on p. 10).

[4] The KATRIN Collaboration. “Direct neutrino-mass measurement with sub-electronvolt sensitivity”. In: *Nature Physics* 18 (Feb. 2022). DOI: `10.1038/s41567-021-01463-1` (cit. on p. 13).

[5] A. Bellerive et al. “The Sudbury Neutrino Observatory”. In: *Nuclear Physics B* 908 (July 2016), pp. 30–51. ISSN: 0550-3213 (cit. on pp. 14, 15).

[6] P.A. Zyla et al. “Review of Particle Physics”. In: *PTEP* 2020.8 (2020), p. 083C01 (cit. on pp. 14–18, 31, 91, 99, 148, 158).

[7] Christopher W. Walter. “The Super-Kamiokande Experiment”. In: *Neutrino Oscillations* (Mar. 2008), pp. 19–43 (cit. on p. 15).

[8] K. S. Hirata et al. “Observation of a small atmospheric muon-neutrino / electron-neutrino ratio in Kamiokande”. In: *Phys. Lett. B* 280 (1992), pp. 146–152 (cit. on p. 16).

[9] D. Casper et al. “Measurement of atmospheric neutrino composition with the IMB-3 detector”. In: *Phys. Rev. Lett.* 66 (20 May 1991), pp. 2561–2564. DOI: `10.1103/PhysRevLett.66.2561`. URL: `https://link.aps.org/doi/10.1103/PhysRevLett.66.2561` (cit. on p. 16).

[10] Fréjus Collaboration. “Determination of the atmospheric neutrino spectra with the Fréjus detector”. In: *Zeitschrift für Physik C Particles and Fields* 66 (Sept. 1995), pp. 417–428. DOI: `10.1007/BF01556368` (cit. on p. 16).

[11] The NUSEK Collaboration et al. “Experimental Study of Atmospheric Neutrino Flux in the NUSEX Experiment”. In: *Europhysics Letters (EPL)* 8.7 (Apr. 1989), pp. 611–614. DOI: `10.1209/0295-5075/8/7/005`. URL: `https://doi.org/10.1209/0295-5075/8/7/005` (cit. on p. 16).

[12] R.Jeffrey Wilkes. “Results on neutrino oscillations from Super-Kamiokande”. In: *Advances in Space Research* 26.11 (2000), pp. 1813–1822. ISSN: 0273-1177. DOI: `https://doi.org/10.1016/S0273-1177(99)01228-4`. URL: `https://www.sciencedirect.com/science/article/pii/S0273117799012284` (cit. on p. 16).

[13] P. F. de Salas et al. "2020 global reassessment of the neutrino oscillation picture". In: *Journal of High Energy Physics* 2021.2 (Feb. 2021). ISSN: 1029-8479. DOI: `10.1007/jhep02(2021)071` (cit. on p. 19).

[14] CernCourier. *Neutrino production moves to an industrial scale.* 2012. URL: `https://cerncourier.com/a/neutrino-production-moves-to-an-industrial-scale/` (cit. on p. 20).

[15] A. Diaz et al. "Where are we with light sterile neutrinos?" In: *Physics Reports* 884 (Nov. 2020), pp. 1–59. ISSN: 0370-1573. DOI: `10.1016/j.physrep.2020.08.005` (cit. on pp. 22, 31–33).

[16] D. Cianci et al. "Prospects of light sterile neutrino oscillation and CP violation searches at the Fermilab Short Baseline Neutrino Facility". In: *Physical Review D* 96.5 (Sept. 2017). ISSN: 2470-0029. DOI: `10.1103/physrevd.96.055001` (cit. on p. 24).

[17] J. N. Abdurashitov et al. "Measurement of the solar neutrino capture rate with gallium metal. III. Results for the 2002–2007 data-taking period". In: *Physical Review C* 80.1 (July 2009). ISSN: 1089-490X. DOI: `10.1103/physrevc.80.015807` (cit. on pp. 24, 25).

[18] F. Kaether et al. "Reanalysis of the Gallex solar neutrino flux and source experiments". In: *Physics Letters B* 685.1 (Feb. 2010), pp. 47–54. ISSN: 0370-2693. DOI: `10.1016/j.physletb.2010.01.030`. URL: `http://dx.doi.org/10.1016/j.physletb.2010.01.030` (cit. on pp. 24, 25).

[19] G. Mention et al. "Reactor antineutrino anomaly". In: *Physical Review D* 83.7 (Apr. 2011). ISSN: 1550-2368. DOI: `10.1103/physrevd.83.073006`. URL: `http://dx.doi.org/10.1103/PhysRevD.83.073006` (cit. on pp. 24–26).

[20] A. Aguilar et al. "Evidence for neutrino oscillations from the observation of $\overline{\nu}_e$ appearance in a $\overline{\nu}_\mu$ beam". In: *Phys. Rev. D* 64 (11 Nov. 2001), p. 112007. DOI: `10.1103/PhysRevD.64.112007` (cit. on pp. 24, 26, 27).

[21] A. A. Aguilar-Arevalo et al. "Updated MiniBooNE neutrino oscillation results with increased data and new background studies". In: *Physical Review D* 103.5 (Mar. 2021). ISSN: 2470-0029. DOI: `10.1103/physrevd.103.052002` (cit. on pp. 24, 28, 99).

[22] A. A. Aguilar-Arevalo et al. "Improved Search for $\overline{\nu}_\mu \to \overline{\nu}_e$ Oscillations in the MiniBooNE Experiment". In: *Phys. Rev. Lett.* 110 (16 Apr. 2013), p. 161801. DOI: `10.1103/PhysRevLett.110.161801`. URL: `https://link.aps.org/doi/10.1103/PhysRevLett.110.161801` (cit. on pp. 24, 29–32).

[23] A.A. Aguilar-Arevalo et al. "The MiniBooNE detector". In: *Nuclear Instruments and Methods in Physics Research Section A: Accelerators, Spectrometers, Detectors and Associated Equipment* 599.1 (Feb. 2009), pp. 28–46. DOI: `10.1016/j.nima.2008.10.028`. URL: `https://doi.org/10.1016%2Fj.nima.2008.10.028` (cit. on p. 28).

[24] Joseph Grange and Teppei Katori. "Charged current quasi-elastic cross-section measurements in MiniBooNE". In: *Modern Physics Letters A* 29.12 (Apr. 2014), p. 1430011. DOI: `10.1142/s0217732314300110`. URL: `https://doi.org/10.1142%2Fs0217732314300110` (cit. on p. 29).

[25] A. A. Aguilar-Arevalo et al. “Measurement of ν_μ and $\overline{\nu}_\mu$ induced neutral current single π^0 production cross sections on mineral oil at $E_\nu \sim \mathcal{O}$ (1 GeV)”. In: *Phys. Rev. D* 81 (1 Jan. 2010), p. 013005. DOI: `10.1103/PhysRevD.81.013005`. URL: `https://link.aps.org/doi/10.1103/PhysRevD.81.013005` (cit. on pp. 29, 31, 32).

[26] B. Armbruster et al. “Upper limits for neutrino oscillations $\overline{\nu}_\mu \rightarrow \overline{\nu}_e$ from muon decay at rest”. In: *Phys. Rev. D* 65 (11 June 2002), p. 112001. DOI: `10.1103/PhysRevD.65.112001`. URL: `https://link.aps.org/doi/10.1103/PhysRevD.65.112001` (cit. on pp. 31, 32).

[27] Xiangpan Ji et al. “Combined Neyman–Pearson chi-square: An improved approximation to the Poisson-likelihood chi-square”. In: *Nuclear Instruments and Methods in Physics Research Section A: Accelerators, Spectrometers, Detectors and Associated Equipment* 961 (May 2020), p. 163677. ISSN: 0168-9002 (cit. on pp. 39, 99, 124, 150).

[28] R. et al. Acciarri. “Design and construction of the MicroBooNE detector”. In: *Journal of Instrumentation* 12.02 (Feb. 2017), P02017–P02017. ISSN: 1748-0221 (cit. on pp. 41, 46, 47, 49).

[29] A. A. Aguilar-Arevalo et al. “The Neutrino Flux prediction at MiniBooNE”. In: *Phys. Rev. D* 79 (2009), p. 072002. DOI: `10.1103/PhysRevD.79.072002`. arXiv: `0806.1449 [hep-ex]` (cit. on pp. 41–46, 116).

[30] Fermilab. *Fermilab’s Accelerator Complex.* Oct. 2020. URL: `https://www.fnal.gov/pub/science/particle-accelerators/accelerator-complex.html` (cit. on p. 42).

[31] P. Abratenko et al. “First Measurement of Inclusive Muon Neutrino Charged Current Differential Cross Sections on Argon at $E_\nu \sim$0.8 GeV with the MicroBooNE Detector”. In: *Phys. Rev. Lett.* 123.13 (2019), p. 131801. DOI: `10.1103/PhysRevLett.123.131801`. arXiv: `1905.09694 [hep-ex]` (cit. on pp. 45, 116).

[32] T Katori. “The MicroBooNE light collection system”. In: *Journal of Instrumentation* 8.10 (Oct. 2013), pp. C10011–C10011. ISSN: 1748-0221. DOI: `10.1088/1748-0221/8/10/c10011` (cit. on pp. 49, 50).

[33] R. Acciarri et al. “Noise Characterization and Filtering in the MicroBooNE Liquid Argon TPC”. In: *Journal of Instrumentation* 12.08 (Aug. 2017), P08003–P08003. ISSN: 1748-0221 (cit. on pp. 52, 57, 67).

[34] Jarrett Moon. “Using Deep Learning Techniques to Search for the MiniBooNE Low Energy Excess in MicroBooNE with $> 3\sigma$ Sensitivity”. PhD thesis. Massachusetts Institute of Technology, 2020 (cit. on pp. 52, 68, 94).

[35] Davio Cianci. “A Deep-Learning-Based ν_μ CCQE Selection for Searches Beyond the Standard Model with MicroBooNE”. PhD thesis. Columbia University, 2021 (cit. on p. 52).

[36] “A Method to Extract the Charge Distribution Arriving at the TPC Wire Planes in MicroBooNE”. In: (July 2016). DOI: `10.2172/1573049` (cit. on pp. 53, 54).

[37] P. Abratenko et al. *Search for an anomalous excess of charged-current quasi-elastic ν_e interactions with the MicroBooNE experiment using Deep-Learning-based reconstruction.* 2021. arXiv: `2110.14080 [hep-ex]` (cit. on pp. 55, 60, 71, 115, 130, 136–138, 149, 150, 152).

[38] P. Abratenko et al. "Search for an anomalous excess of charged-current ν_e interactions without pions in the final state with the MicroBooNE experiment". In: arXiv: `2110.14065 [hep-ex]` (cit. on pp. 57, 153).

[39] P. Abratenko et al. "Search for an anomalous excess of inclusive charged-current ν_e interactions in the MicroBooNE experiment using Wire-Cell reconstruction". In: arXiv: `2110.13978 [hep-ex]` (cit. on pp. 57, 153).

[40] MicroBooNE Collaboration. "Ionization electron signal processing in single phase LArTPCs. Part I. Algorithm Description and quantitative evaluation with MicroBooNE simulation". In: *Journal of Instrumentation* 13.07 (July 2018), P07006–P07006. ISSN: 1748-0221 (cit. on p. 58).

[41] MicroBooNE Collaboration. "Ionization electron signal processing in single phase LArTPCs. Part II. Data/simulation comparison and performance in MicroBooNE". In: *Journal of Instrumentation* 13.07 (July 2018), P07007–P07007. ISSN: 1748-0221 (cit. on p. 58).

[42] C. Andreopoulos et al. "The GENIE Neutrino Monte Carlo Generator". In: *Nucl. Instrum. Meth. A* 614 (2010), pp. 87–104. DOI: `10.1016/j.nima.2009.12.009`. arXiv: `0905.2517 [hep-ph]` (cit. on p. 58).

[43] Costas Andreopoulos et al. "The GENIE Neutrino Monte Carlo Generator: Physics and User Manual". In: (Oct. 2015). arXiv: `1510.05494 [hep-ph]` (cit. on pp. 58, 118).

[44] Luis Alvarez-Ruso et al. "Recent highlights from GENIE v3". In: (June 2021). arXiv: `2106.09381 [hep-ph]` (cit. on p. 58).

[45] Júlia Tena-Vidal et al. "Neutrino-Nucleon Cross-Section Model Tuning in GENIE v3". In: (Apr. 2021). arXiv: `2104.09179 [hep-ph]` (cit. on pp. 58, 118).

[46] J. Nieves, I. Ruiz Simo, and M. J. Vicente Vacas. "Inclusive charged-current neutrino-nucleus reactions". In: *Phys. Rev. C* 83 (4 Apr. 2011), p. 045501. DOI: `10.1103/PhysRevC.83.045501`. eprint: `1102.2777` (cit. on p. 58).

[47] A.A. Aguilar-Arevalo et al. "First Measurement of the Muon Neutrino Charged Current Quasielastic Double Differential Cross Section". In: *Phys. Rev. D* 81 (2010), p. 092005. DOI: `10.1103/PhysRevD.81.092005`. arXiv: `1002.2680 [hep-ex]` (cit. on p. 58).

[48] K. Abe et al. "Measurement of double-differential muon neutrino charged-current interactions on C_8H_8 without pions in the final state using the T2K off-axis beam". In: *Phys. Rev. D* 93 (11 June 2016), p. 112012. DOI: `10.1103/PhysRevD.93.112012`. URL: `https://link.aps.org/doi/10.1103/PhysRevD.93.112012` (cit. on p. 59).

[49] P. Abratenko et al. "New Theory-driven GENIE Tune for MicroBooNE". In: (2021). DOI: `10.48550/ARXIV.2110.14028`. URL: `https://arxiv.org/abs/2110.14028` (cit. on pp. 59, 117, 118, 130).

[50] S. Agostinelli et al. “GEANT4–a simulation toolkit”. In: *Nucl. Instrum. Meth. A* 506 (2003), pp. 250–303. DOI: `10.1016/S0168-9002(03)01368-8` (cit. on p. 59).

[51] P. Abratenko et al. “Neutrino event selection in the MicroBooNE liquid argon time projection chamber using Wire-Cell 3D imaging, clustering, and charge-light matching”. In: *Journal of Instrumentation* 16.06 (June 2021), P06043. DOI: `10.1088/1748-0221/16/06/p06043`. URL: `https://doi.org/10.1088/1748-0221/16/06/p06043` (cit. on p. 60).

[52] P. Abratenko et al. “Cosmic Ray Background Rejection with Wire-Cell LArTPC Event Reconstruction in the MicroBooNE Detector”. In: *Phys. Rev. Applied* 15.6 (2021), p. 064071. DOI: `10.1103/PhysRevApplied.15.064071`. arXiv: `2101.05076 [physics.ins-det]` (cit. on p. 60).

[53] C. Adams et al. “Reconstruction and Measurement of $\mathcal{O}(100)$ MeV Energy Electromagnetic Activity from $\pi^0 \to \gamma\gamma$ Decays in the MicroBooNE LArTPC”. In: *JINST* 15.02 (2020), P02007. arXiv: `1910.02166 [hep-ex]` (cit. on pp. 61, 65).

[54] P. Rocca and Francesco Riggi. “The Use of Avalanche Photodiodes in High Energy Electromagnetic Calorimetry”. In: Mar. 2011. ISBN: 978-953-307-163-3. DOI: `10.5772/14574` (cit. on p. 74).

[55] P. Abratenko et al. “Semantic segmentation with a sparse convolutional neural network for event reconstruction in MicroBooNE”. In: *Physical Review D* 103.5 (Mar. 2021). ISSN: 2470-0029 (cit. on pp. 62, 63, 83).

[56] Olaf Ronneberger et al. “U-Net: Convolutional Networks for Biomedical Image Segmentation”. In: *Medical Image Computing and Computer-Assisted Intervention – MICCAI 2015*. Cham: Springer International Publishing, 2015, pp. 234–241 (cit. on pp. 62, 83).

[57] Kaiming He et al. “Deep Residual Learning for Image Recognition”. In: *2016 IEEE Conference on Computer Vision and Pattern Recognition (CVPR)*. 2016, pp. 770–778. DOI: `10.1109/CVPR.2016.90` (cit. on p. 62).

[58] C. Adams et al. “Deep neural network for pixel-level electromagnetic particle identification in the MicroBooNE liquid argon time projection chamber”. In: *Physical Review D* 99.9 (May 2019). ISSN: 2470-0029 (cit. on pp. 62, 83).

[59] P. Abratenko and et al. “Vertex-finding and reconstruction of contained two-track neutrino events in the MicroBooNE detector”. In: *Journal of Instrumentation* 16.02 (Feb. 2021), P02017–P02017. ISSN: 1748-0221 (cit. on pp. 63, 64, 148).

[60] Victor Genty. “The MicroBooNE Search For Anomalous Electron Neutrino Appearance Using Image Based Data Reconstruction”. PhD thesis. Columbia University, 2019 (cit. on p. 63).

[61] P. Abratenko et al. “Electromagnetic shower reconstruction and energy validation with Michel electrons and $\pi 0$ samples for the deep-learning-based analyses in MicroBooNE”. In: *Journal of Instrumentation* 16.12 (Dec. 2021), T12017 (cit. on pp. 65, 89, 109, 148).

[62] P. Abratenko et al. “Convolutional neural network for multiple particle identification in the MicroBooNE liquid argon time projection chamber”. In: *Physical Review D* 103.9 (May 2021). ISSN: 2470-0029 (cit. on p. 68).

[63] Artur M. Ankowski and Jan T. Sobczyk. “Argon spectral function and neutrino interactions”. In: *Phys. Rev. C* 74 (2006), p. 054316. arXiv: `nucl-th/0512004` (cit. on pp. 69, 148).

[64] Benjamin Graham and Laurens van der Maaten. *Submanifold Sparse Convolutional Networks*. 2017. arXiv: `1706.01307 [cs.NE]` (cit. on p. 82).

[65] Sebastian Ruder. *An overview of gradient descent optimization algorithms*. 2017. arXiv: `1609.04747 [cs.LG]` (cit. on p. 84).

[66] S. S. Wilks. “The Large-Sample Distribution of the Likelihood Ratio for Testing Composite Hypotheses”. In: *The Annals of Mathematical Statistics* 9.1 (1938), pp. 60–62 (cit. on pp. 102, 110, 158).

[67] R. Acciarri et al. “Michel electron reconstruction using cosmic-ray data from the MicroBooNE LArTPC”. In: *Journal of Instrumentation* 12.09 (Sept. 2017), P09014–P09014. ISSN: 1748-0221 (cit. on p. 105).

[68] Claude Bouchiat and Louis Michel. “Theory of μ-Meson Decay with the Hypothesis of Nonconservation of Parity”. In: *Phys. Rev.* 106 (1 Apr. 1957), pp. 170–172. DOI: `10.1103/PhysRev.106.170` (cit. on p. 108).

[69] Lauren Yates. “Using the MicroBooNE Liquid Argon Detector to Search for Electron Neutrino Interactions and Understand the MiniBooNE Anomaly”. PhD thesis. Columbia University, 2021 (cit. on pp. 115, 117).

[70] J. Calcutt et al. “Geant4Reweight: A Framework for Evaluating and Propagating Hadronic Interaction Uncertainties in GEANT4”. In: *JINST* 16.08 (Aug. 2021), P08042. DOI: `10.1088/1748-0221/16/08/p08042`. arXiv: `2105.01744 [physics.data-an]`. URL: `https://doi.org/10.1088/1748-0221/16/08/p08042` (cit. on p. 118).

[71] P. Abratenko et al. In: `https://microboone.fnal.gov/wp-content/uploads/MICROBOONE-NOTE-1075-PUB.pdf` (cit. on p. 119).

[72] David W. Scott. “Kernel Density Estimation”. In: *Wiley StatsRef: Statistics Reference Online*. American Cancer Society, 2018, pp. 1–7. ISBN: 9781118445112. DOI: `https://doi.org/10.1002/9781118445112.stat07186.pub2` (cit. on p. 120).

[73] V. T. Nguyen et al. “NC pi0 Production in the MiniBooNE Antineutrino Data”. In: *AIP Conference Proceedings* (2008). ISSN: 0094-243X (cit. on pp. 128, 129).

[74] Qudsia Gani and Waseem Bari. “Cross-sections for ν_μ and $\bar{\nu}_\mu$ induced single pion production processes in the few GeV using NuWro”. In: 2017 (cit. on p. 129).

[75] J. Mousseau et al. “Measurement of partonic nuclear effects in deep-inelastic neutrino scattering using MINERvA”. In: *Phys. Rev. D* 93 (7 Apr. 2016), p. 071101. DOI: `10.1103/PhysRevD.93.071101`. URL: `https://link.aps.org/doi/10.1103/PhysRevD.93.071101` (cit. on p. 129).

[76] MicroBooNE Collaboration et al. *Search for Neutrino-Induced Neutral Current Δ Radiative Decay in MicroBooNE and a First Test of the MiniBooNE Low Energy Excess Under a Single-Photon Hypothesis.* 2021. DOI: `10.48550/ARXIV.2110.00409` (cit. on pp. 132, 152).

[77] Tim Adye. "Unfolding algorithms and tests using RooUnfold". In: (2011). DOI: `10.48550/ARXIV.1105.1160` (cit. on p. 136).

[78] Robert E. Schapire. "The Strength of Weak Learnability". English (US). In: *Machine Learning* 5.2 (June 1990), pp. 197–227. ISSN: 0885-6125. DOI: `10.1023/A:1022648800760` (cit. on p. 144).

[79] Byron P. Roe et al. "Boosted decision trees as an alternative to artificial neural networks for particle identification". In: *Nuclear Instruments and Methods in Physics Research Section A: Accelerators, Spectrometers, Detectors and Associated Equipment* 543.2-3 (May 2005), pp. 577–584. DOI: `10.1016/j.nima.2004.12.018`. URL: `https://doi.org/10.1016%2Fj.nima.2004.12.018` (cit. on p. 145).

[80] Yasser Ganjisaffar, Rich Caruana, and Cristina Videira Lopes. "Bagging gradient-boosted trees for high precision, low variance ranking models". In: *Proceedings of the 34th international ACM SIGIR conference on Research and development in Information Retrieval.* 2011, pp. 85–94 (cit. on p. 145).

[81] XGBoost developers. *Introduction to Boosted Trees.* 2021. URL: `https://xgboost.readthedocs.io/en/latest/tutorials/model.html` (cit. on p. 145).

[82] A. A. Aguilar-Arevalo et al. "Significant Excess of Electron-Like Events in the MiniBooNE Short-Baseline Neutrino Experiment". In: *Phys. Rev. Lett.* 121.22 (2018), p. 221801. DOI: `10.1103/PhysRevLett.121.221801`. arXiv: `1805.12028 [hep-ex]` (cit. on p. 150).

[83] A. A. Aguilar-Arevalo et al. "A Search for Electron Neutrino Appearance at the $\Delta m^2 \sim 1eV^2$ Scale". In: *Phys. Rev. Lett.* 98 (2007), p. 231801. DOI: `10.1103/PhysRevLett.98.231801`. arXiv: `0704.1500 [hep-ex]` (cit. on p. 150).

[84] Davio Cianci and Mark Ross-Lonergan. *SBNfit.* Available at `https://github.com/NevisUB/whipping_star`(2021) (cit. on pp. 151, 162).

[85] Gary J. Feldman and Robert D. Cousins. "Unified approach to the classical statistical analysis of small signals". In: *Physical Review D* 57.7 (Apr. 1998), pp. 3873–3889. ISSN: 1089-4918. DOI: `10.1103/physrevd.57.3873`. URL: `http://dx.doi.org/10.1103/PhysRevD.57.3873` (cit. on pp. 152, 163, 187, 189).

[86] MicroBooNE collaboration et al. *Search for an Excess of Electron Neutrino Interactions in MicroBooNE Using Multiple Final State Topologies.* 2021. arXiv: `2110.14054 [hep-ex]` (cit. on p. 153).

[87] William Navidi. *Principles of Statistics for Engineers and Scientists.* 2nd ed. New York City, United States: McGraw Hill Higher Education, 2010 (cit. on p. 159).

[88] F. James. *Minuit Function Minimization and Error Analysis Reference Manual.* Report 94.1. CERN, 1994 (cit. on p. 161).

[89] D. Cianci et al. "Prospects of light sterile neutrino oscillation and CP violation searches at the Fermilab Short Baseline Neutrino Facility". In: *Physical Review D* 96.5 (Sept. 2017). ISSN: 2470-0029. DOI: `10.1103/physrevd.96.055001`. URL: `http://dx.doi.org/10.1103/PhysRevD.96.055001` (cit. on p. 164).

[90] S. Algeri et al. "Searching for new phenomena with profile likelihood ratio tests". In: *Nature reviews physics* 2 (Apr. 2020). URL: `https://www.nature.com/articles/s42254-020-0169-5#citeas` (cit. on p. 187).